Identification of Multiple Cracks in a Shaft System

A Thesis Submitted in
Partial Fulfilment of the Requirements
for the Degree of

DOCTOR OF PHILOSOPHY

by

Sachin Kumar Singh

Department of Mechanical Engineering
Indian Institute of Technology Guwahati
November 2012

CERTIFICATE

It is certified that the work contained in this thesis entitled **Identification of Multiple Cracks in a Shaft System** by **Sachin Kumar Singh (Roll no. 05610310)** has been carried out under our supervision and that the work has not been submitted elsewhere for a degree.

Dr. Rajiv Tiwari
Professor
Department of Mechanical Engineering
Indian Institute of Technology Guwahati
Guwahati - 781 039, INDIA

Dr. Sudip Talukdar
Professor
Department of Civil Engineering
Indian Institute of Technology Guwahati
Guwahati - 781 039, INDIA

Dedicated to my parents

for

their love and support.

Acknowledgments

I would like to express my gratitude to my supervisors, Professor R. Tiwari and Professor S. Talukdar for their guidance and support throughout my thesis work. I have benefitted a lot from them in the area of machinery condition monitoring. I am obliged for being introduced to such a relevant research area. I am especially thankful to Professor R. Tiwari for providing me the financial assistantship through a research project.

I would like to express my sincere thanks to my doctoral committee members, Professor S. K. Kakoty, Dr. K. S. R. K. Murthy, and Dr. S. R. M. Prasanna for reviewing my work and for the helpful observations and suggestions.

I would like to thank Mr. D. J. Bordoloi for helping me in conducting the experiments and the staffs of the central workshop of the institute for fabrication of the experimental setup. I am thankful to Dr. M. Karthikeyan for helping me to understand the mathematical model of the cracked shaft at the initial stage of my thesis.

I would like to thank my friends in IITG campus for they made the campus life really memorable. Finally, I am grateful to my family members for their love, patience and constant support.

Sachin Kumar Singh

ABSTRACT

Fatigue cracks present in the shaft of a machine make it susceptible to the catastrophic failure. Hence, it is important to detect all the potentially dangerous cracks present in the shaft before failure occurs. Assessment of damage severity is also important to predict the remaining life, to schedule the maintenance and to prepare the inventory. In the present work, an identification methodology has been developed; which identifies the number of cracks, their locations on the shaft, their sizes, and the orientation angle of cracks. The methodology uses transverse forced responses of the shaft system at different frequencies of a harmonic excitation. First, a *multi-crack detection and localization algorithm* (MCDLA) is developed. Transverse forced vibrations of a non-rotating cracked shaft in two orthogonal planes are analyzed with the help of the finite element method by using the Timoshenko beam theory. The presence of a crack in a shaft introduces a slope discontinuity in the elastic line of the shaft. This causes a jump in the value of the curvature of the shaft elastic line, and it is difficult to measure in the presence of measurement noise. In the present work, the shaft curvature is obtained by approximating forced responses of the shaft at consecutive axial measurement locations by a quadratic polynomial. The effect of noise is reduced by utilising forced responses of the shaft at several frequencies. This stage of the algorithm gives the number of cracks and their approximate locations over the shaft. Information obtained from the first algorithm is used in the second algorithm, the *multi-crack localization and sizing algorithm* (MCLSA), to find out the size and more accurate location of cracks. The MCLSA uses the multi-objective genetic algorithms to solve an optimization problem giving the size and accurate location of the cracks. Responses of the shaft at several frequencies are used to define objective functions in the genetic algorithm (GA). The proposed two stage methodology is tested with numerically simulated noisy forced responses from the finite element modeling of a simply supported shaft having two cracks. The

methodology identifies very well the presence of cracks and also estimates quite accurately the location and the size of cracks on the shaft.

Initially, the identification algorithm is tested with cracks of known orientation, i.e. assuming that all the cracks have the same and known orientation angle. Hence, the identification algorithm is developed for identifying two unknowns per crack, i.e. the size and the location. Later, the crack orientation angle is introduced as another crack parameter and the identification algorithm is tested with cracks of unknown orientation angle. First, the algorithm is tested for open cracks then for breathing cracks. From numerical simulations, it is shown that the first algorithm, i.e. the MCDLA, work well in these situation also. It gives the number of cracks present in the shaft and its approximate location over it. A new method is proposed to find out the crack orientation angle for open cracks as well as for breathing cracks. It consists of taking measurements of the shaft deflection at regular angular orientations of the shaft.

Next, the MCDLA is tested for a real cracked shaft in a laboratory test set-up. Initially, measurements were taken using eddy current sensors, which did not give good results. Next, to reduce the noise in measurements, the laser vibrometer was used for measuring the shaft vibrations. With this the algorithm is able to detect some of the cracks present over the shaft. Performance of the algorithm is improved further by implementing a scheme to reduce the effect of measurement noise.

Table of Contents

ABSTRACT v

LIST OF FIGURES xiii

LIST OF TABLES xxi

LIST OF SYMBOLS xxiii

1 INTRODUCTION 1

1.1 Importance of Study 1

1.2 Background and Literature Review 2

1.2.1 Background 2

1.2.2 Literature review 4

(a) Modeling of transverse fatigue crack 6

(b) Identification of cracks 15

(c) Identification of multiple cracks 27

1.3 Present Work 35

1.4 Organization of the Thesis 37

2 MATHEMATICAL MODEL OF THE SHAFT SYSTEM 39

2.1 Model of a Shaft Element with a Crack 39

2.2 System Equations of Motion 41

2.3 Response of a Shaft System 44

3 DETECTION AND LOCALIZATION OF CRACKS 47

3.1 Introduction 47

3.2 The MCDLA 47

3.3 Numerical Experiments of the MCDLA 54

  3.3.1 Simulation-I 56

  3.3.2 Simulation-II 61

4 ESTIMATION OF ACCURATE LOCATION AND SIZE OF CRACKS 67

4.1 Introduction 67

4.2 Introduction to Genetic Algorithm 67

4.3 Working Principles of Genetic Algorithms 67

  4.3.1 Binary Coding of the Strings 68

  4.3.2 Fitness Function 69

  4.3.3 The Selection Operator 70

  4.3.4 The Crossover Operator 71

  4.3.5 The Mutation Operator 73

  4.3.6 The Elitism Operator 74

  4.3.7 Termination Criterion 75

4.4 The Multi-Objective Genetic Algorithm 75

  4.4.1 Non-Dominated Sorting 75

  4.4.2 Crowding Distance 77

4.5 Multi-Objective Optimization for Crack Parameters Estimation 77

4.6 The MCLSA 79

4.7 Numerical Experiments for the MCLSA 81

4.8 Normalization of the Quadratic Coefficients using "Equivalent Reduced Stiffness" 88

5 IDENTIFICATION OF CRACK ORIENTATION ANGLE 95

5.1 Introduction 95

5.2 Identification of Open Cracks 96

5.2.1 Shaft Response with Rotated Open Crack 96

5.3 Detection and Localization of Breathing Cracks 98

5.3.1 Estimation of the Crack Orientation Angle 99

5.3.2 Identification of the Crack Size 104

5.4 Identification of Breathing Cracks 106

5.4.1 Shaft Responses for Breathing Cracks 106

5.4.2 Detection and Localization of Breathing Cracks 109

5.4.3 Estimation of Crack Orientation Angle of Breathing Cracks 111

5.4.4 Identification of Crack Size 115

5.5 Detection and Localization of Cracks in a Stepped Shaft 116

6 EXPERIMENTAL VERIFICATION OF THE MCDLA 123

6.1 Introduction 123

6.2 Experimental Setup and Instrumentation 123

6.2.1 Experimental Setup 124

6.2.2 The Excitation Unit 126

6.2.3 Signal Generator and Power Amplifier 126

6.2.4 Force Transducer 127

6.2.5 Proximity Transducers 127

6.2.6 Laser Vibrometer 128

6.2.7 Data Acquisition System 129

6.3 Stages for Conducting the Experiments 130

6.4 Experimentation using Proximity Sensors 131

6.4.1 Procedure 131

6.4.2 Signal Processing of Measured Signals 131

6.4.3 Experimental Results 136

6.5 Experimentation using Laser Vibrometer 138

6.5.1 Procedure 138

6.5.2 Signal Processing of the Measured Signal 139

6.5.3 Experimental Results 144

6.6 Scheme for Better Estimation of the Quadratic Coefficients 151

6.6.1 The Scheme 151

6.6.2 Numerical Simulation of the Scheme 152

6.7 Implementation of the Scheme to Actual Measurements 156

7 CONCLUSIONS AND SCOPES FOR FUTURE WORK 167

7.1 Conclusions 167

7.2 Limitations and Applicability 170

7.3 Scopes for the Future Work 170

APPENDIX 173

Appendix A: Flexibility Coefficients of an Open Crack 173

Appendix B: Rayleigh damping 174

Appendix C: Elemental Mass and Stiffness Matrices for Transverse Vibrations 175

C.1: Elemental Mass Matrices 175

C.2: The element stiffness matrix 177

C.3 Elemental Displacement Vector for Transverse Vibrations 178

Appendix D: Addition of noise to simulated cracked shaft deflection 178

REFERENCES **179**

Publications from the Present Work **193**

LIST OF FIGURES

Figure 2.1: A shaft element with a crack subjected to a transverse loading. 39

Figure 2.2: A geometry of a beam section with a transverse crack. 40

Figure 2.3: Crack orientation angle of a rotated crack. 41

Figure 2.4: The finite element discretisation of the shaft with multiple cracks............. 41

Figure 2.5: Variation of shaft displacement amplitude with excitation frequency......... 45

Figure 2.6: Shaft response amplitudes at 110 rad/s. 46

Figure 2.7: Shaft response amplitudes at 430 rad/s. 46

Figure 3.1: Measurement locations along the shaft. 54

Figure 3.2: Cracked shaft response amplitudes at 110 rad/s... 57

Figure 3.3: Variation of coefficients, $a_{cv_{i,j}}$ and $a_{ch_{i,j}}$ with measurement locations. 57

Figure 3.4: Variation of the coefficients $a^{\mathrm{I}}_{cv_{i,j}}$ —, $a^{\mathrm{I}}_{wcv_{i,j}}$ - -, with measurement locations. 58

Figure 3.5: Variation of coefficients $a^{\mathrm{II}}_{v_{i,j}}$ and $a^{\mathrm{II}}_{h_{i,j}}$ with measurement locations. 59

Figure 3.6: Variation of coefficients $a^{\mathrm{III}}_{v_j}$ and $a^{\mathrm{III}}_{h_j}$ along the measurement locations...... 60

Figure 3.7 Crack probability functions for Simulation-I. 61

Figure 3.8: Cracked shaft response amplitudes at 430 rad/s... 62

Figure 3.9: Variation of coefficients, $a_{cv_{i,j}}$ and $a_{ch_{i,j}}$ with measurement location. 62

Figure 3.10: Variation of the coefficients $a^{\mathrm{I}}_{cv_{i,j}}$ —, $a^{\mathrm{I}}_{wcv_{i,j}}$ - -, with measurement location.. 63

Figure 3.11: Variation of coefficients $a^{\mathrm{II}}_{v_{i,j}}$ and $a^{\mathrm{II}}_{h_{i,j}}$ with measurement location. 64

Figure 3.12: Variation of coefficients $a^{\mathrm{III}}_{v_j}$ and $a^{\mathrm{III}}_{h_j}$ along the measurement locations.... 64

Figure 3.13: Crack probability functions for Simulation-II. 65

Figure 4.1: The crossover between two strings. 72

Figure 4.2: The mutation of the strings. 73

Figure 4.3: Dominance of strings in objective space. 76

Figure 4.4: Cracked shaft responses in the vertical direction. 79

Figure 4.5: Variation of crack parameters with number of generations for simulation example I. 85

Figure 4.6: Variation of crack parameters with number of generations for simulation example II. 86

Figure 4.7: A combined flowchart of the MCDLA as well as the MCLSA. 87

Figure 4.8: Plot of coefficients $a^{\mathrm{I}}_{wcv_{i,j}}$ (—) and $a^{\mathrm{I}}_{cv_{i,j}}$ (− −) with measurement locations for excitation frequency of 120 rad/s. 89

Figure 4.9: Plot of *CPF* values with measurement locations at 120 rad/s, (with *ERS* —), without *ERS* − −). 90

Figure 4.10: CPF values at 120 rad/s (with *ERS* —), (without *ERS* − −), with deviation in the (a) density (b) diameter (c) elastic constant *E*. 91

Figure 4.11: Plot of coefficients $a^{\mathrm{I}}_{wcv_{i,j}}$ (—) and $a^{\mathrm{I}}_{cv_{i,j}}$ (− −) with measurement locations for excitation frequency of 490 rad/s. 92

Figure 4.12: Plot of *CPF* values with measurement locations for excitation frequency of 490 rad/s, (with *ERS* —), (without *ERS* − −). 92

Figure 4.13: CPF values at 490 rad/s (with *ERS* —), (without *ERS* − −), with deviation in the (a) density (b) diameter (c) elastic constant *E*. 93

Figure 5.1: Crack orientation angle ϕ, (a) $\phi = 0$ (b) $\phi > 0$ 96

Figure 5.2: Cracked shaft response for the crack orientation angle of $\varphi = 45°$ 98

Figure 5.3: Crack probability functions for the shaft with a single crack of the crack depth ratio of 0.7 and the crack orientation angle of $\phi = 45^{\circ}$ 98

Figure 5.4: Crack probability functions for the shaft with two crack of crack depth ratio 0.6 and 0.7, and crack orientation angle of $\phi = 45^{\circ}$ 99

Figure 5.5: Coefficients a_v^{II} and a_h^{II} from responses at the excitation frequency of 100 rad/s. 100

Figure 5.6: Peak value variations in coefficients at excitation frequency of 100 rad/s for (a) a_v^{II} and (b) a_h^{II} 101

Figure 5.7: Peak value variations in coefficients at excitation frequency of 50 rad/s (a) a_v^{II} and (b) a_h^{II} 101

Figure 5.8: Estimation of crack orientation angle ϕ. (a) $\phi = 0°$, (a) $\phi \neq 0°$.................. 102

Figure 5.9: The cracked shaft response for the crack orientation angle $\phi = 45°$ and $\phi = 225°$ (the two responses are same hence they are overlapping). 103

Figure 5.10: Convergence of crack parameters for numerical Simulation-I with the crack orientation angle $\varphi = 45°$ 105

Figure 5.11: Fully closed and fully open states of a breathing crack. 107

Figure 5.12: The variation of the stiffness of the cracked element with the shaft angular position... 108

Figure 5.13: Cracked shaft responses for the crack orientation angle of 45° for a single crack of the crack depth ratio 0.6. 108

Figure 5.14: Coefficients a_v^{II} and a_h^{II} at the excitation frequency of 100 rad/s. 109

Figure 5.15: Peak value variations in coefficients a_v^{II} and a_h^{II} at the excitation frequency of 110 rad/s. 109

Figure 5.16: Crack probability functions for a shaft with a crack of the crack orientation angle, 45°. 110

Figure 5.17: Crack probability functions for a shaft with two cracks. 110

Figure 5.18: Coefficients a_v^{II} for a shaft with a single crack at 50 rad/s of excitation frequency, (a) variation with the shaft length, (b) variation of peak value in a_v^{II} with the angular position of the shaft. 111

Figure 5.19: The variation of peak value in a_v^{II} with the angular position of the shaft for a crack of the crack orientation angle = -90°. 113

Figure 5.20: Variation of peak values of the coefficients a_v^{II} with the angular position of the shaft (a) Crack orientation angle of the second crack is changed (b) Crack orientation angle of the first crack is changed. 113

Figure 5.21: Convergence of crack parameters for numerical Simulation-I. 116

Figure 5.22: A stepped shaft with two cracks. 117

Figure 5.23: Quadratic coefficients for the first example (step near 7th location, one crack of crack depth ratio 0.6 near the 11th measurement location). 118

Figure 5.24: Quadratic coefficients for the second example (step near 7th location, two cracks of crack depth ratios 0.6 each and located near the 7th and11th measurement location. 119

Figure 5.25: Normalized quadratic coefficients for (a) the first example (b) the second example. 120

Figure 5.26: Crack probability functions for (a) first example (b) second example. 121

Figure 6.1: The test rig for the experimental crack detection. 124

Figure 6.2: A close view of one end of the shaft, supported by a deep-groove ball bearing. 125

Figure 6.3 A close view of the slit-type crack. ... 125

Figure 6.4: An electromagnetic exciter connected to the shaft through a stringer via a transducer. ... 126

Figure 6.5: Measurement of shaft displacements using proximity sensors. ... 128

Figure 6.6: Laser head of the rotational laser vibrometer. ... 129

Figure 6.7: A sample forcing time history at 10 Hz. ... 132

Figure 6.8: A sample response time history at the 9th measurement location and the excitation frequency of 10 Hz. ... 132

Figure 6.9: The filtered (- -) and unfiltered (-) signals for the sample forcing time history of Figure 6.7. ... 133

Figure 6.10: The filtered (- -) and unfiltered (-) signals for the sample response time history of Figure 6.8. ... 134

Figure 6.11: A sample filter characteristics for excitation at 20 Hz. ... 134

Figure 6.12: The cracked shaft deflections at 24 Hz. ... 136

Figure 6.13: The crack probability functions for Shaft-I with single crack neat 11th measurement location (first set of measurements). ... 137

Figure 6.14: The crack probability functions for Shaft-I with single crack near 11th measurement location (second set of measurements). ... 137

Figure 6.15: Reflecting films on the shaft surface for response measurements using the laser vibrometer. ... 139

Figure 6.16: A sample sine-sweep forcing. ... 140

Figure 6.17: A sample response to a sine-sweep forcing. ... 140

Figure 6.18: Variation of force amplitude with time. ... 141

Figure 6.19: A sample response amplitude at 6th measurement location. ... 142

Figure 6.20 The response amplitude at various measurement locations, *j*. ... 142

Figure 6.21 The response per unit force at the measurement location 4. 143

Figure 6.22: The shaft deflection at the excitation frequency of 20 Hz. 144

Figure 6.23: Crack probability functions for the Shaft-I with a crack near 11th measurement location (first set of measurements). 145

Figure 6.24: Crack probability functions for the Shaft-I with a crack near 11th measurement location (second set of measurements). 145

Figure 6.25: Crack probability functions for the Shaft-II with a single crack near 13th measurement location (first set of measurements). 146

Figure 6.26: Crack probability functions for the Shaft-II with a single crack near 13th measurement location (second set of measurements). 147

Figure 6.27: Crack probability functions for the Shaft-I with two cracks (one near 11th measurement location and the other near 15th measurement location, first set of measurements). 148

Figure 6.28: Crack probability functions for the Shaft-I with two cracks (one near 11th measurement location and the other near 15th measurement location, second set of measurements). 148

Figure 6.29: Crack probability functions for the Shaft-II with two cracks (one near 13th measurement location and the other near 7th measurement location, first set of measurement). 149

Figure 6.30: Crack probability functions for the Shaft-II with two cracks (one near 13th measurement location and the other near 7th measurement location, second set of measurement). 150

Figure 6.31: Estimation of the slope from measured shaft deflections. 152

Figure 6.32: Estimation of quadratic coefficients, (actual values, without noise: —), (1% noise and distance between measurement locations is 5 cm: $*$), (1% noise and distance between measurement locations is 10 cm: $\times$) 153

Figure 6.33: Crack probability functions for simulation A (19 measurement locations and 1% noise). ... 155

Figure 6.34: Crack probability functions for simulations B (19 measurement locations and 5% noise). ... 155

Figure 6.35: Crack probability functions for simulation C (9 measurement locations and 5% noise). ... 156

Figure 6.36: Crack probability functions for the Shaft-I with a single crack near 6th measurement location (first set of measurements). ... 157

Figure 6.37: Crack probability functions for the Shaft-I with a single crack near 6th measurement location (second set of measurements). ... 158

Figure 6.38: Crack probability functions for the Shaft-II with a single crack near 7th measurement location of the shaft (first set of measurements). ... 159

Figure 6.39: Crack probability functions for the Shaft-II with a single crack near 7th measurement location of the shaft (second set of measurements). ... 160

Figure 6.40: Crack probability functions for the Shaft-I with two cracks. First crack near 6th measurement location and the second crack near the 8th measurement location (first set of measurements). ... 161

Figure 6.41: Crack probability functions for the Shaft-I with two cracks. First crack near 6th measurement location and the second crack near the 8th measurement location (second set of measurements). ... 161

Figure 6.42: Crack probability functions for the Shaft-II with two cracks. First crack is near the 7th measurement location and the second crack is near the 4th measurement location (first set of measurements). 162

Figure 6.43: Crack probability functions for the Shaft-II with two cracks. First crack near 7th measurement location and the second crack near the 4th measurement location (second set of measurements). 163

LIST OF TABLES

Table 2-1: System parameters for Figure 2.4 and Figure 2.5 44

Table 3-1: Parameters for the numerical simulations of the multi-crack detection and localization algorithm. 55

Table 3-2: Crack parameters for the numerical simulations of the multi-crack detection and localization algorithm. 55

Table 4-1: Parameters used for the multi-objective optimization using NSGA-II. 84

Table 6-1: Physical parameters of the cracked shaft for the experimentation. 130

Table 6-2: Different parameters for numerical simulations.. 154

LIST OF SYMBOLS

$a_{cv_{i,j}}$, $a_{wcv_{i,j}}$,	Quadratic coefficients
a_0, a_1	Rayleigh damping factors
A	Cross sectional area of the shaft
b	Half width of the crack cross section
$c_{22}, c_{33}, \ldots, c_{55}$	Flexibility coefficients of the crack
$[C]$	Total flexibility matrix of the cracked shaft element
$[C_c]$	Flexibility matrix of the crack
$[C_o]$	Flexibility matrix of the un-cracked shaft element
CPF	Crack probability function
d	Crack size
$[D]$	Assembled damping matrix
$[D_c]^{(e)}$	Damping matrix of a finite element with a crack
$[D_{wc}]^{(e)}$	Damping matrix of a finite element without crack
E	Young’s modulus of shaft material
EI	Flexural rigidity of the shaft cross section
ERS	Equivalent reduced stiffness
$\{f(t)\}^{(e)}$	Elemental force vector
$\{F\}$	Assembled force vector
F	Force amplitude
h	Height of the crack elemental strip
k	Number of excitation frequencies

k_{sc}	Shear correction factor
$[K]$	Assembled stiffness matrix
$[K_c]^{(e)}$	Elemental stiffness matrix with crack
$[K_{wc}]^{(e)}$	Elemental stiffness matrix without crack
$[K_\eta]$	Fitting compliance matrices
l	Length of a finite element
l_1, l_2	Crack locations
$[M]$	Assembled mass matrix
$[M]^{(e)}$	Element mass matrix
n	Number of measurement locations
nc	Number of cracks in the shaft for the optimization problem
ne	Number of elements in finite element model of the shaft for the optimization problem
NSGA-II	Non-dominated sorting genetic algorithms-II
P_1	Axial force
P_2, P_3	Shearing force
P_4, P_5	Bending moments
P_6	Torque
$\{Q\}$	Assembled displacement vector
$\{q(t)\}^{(e)}$	Elemental displacement vector
$q_{cv_{i,j}}$	Cracked shaft deflections
$q_{wcv_{i,j}}$	Intact shaft deflections

R	Radius of the shaft
s	Binary coding of strings
$[T]$	Transformation matrix
v_1	Linear degree of freedom at element node 1
v_2	Linear degree of freedom at element node 2
x_j	Distance of measurement locations from left support
$X^{'}$	Response amplitude
X-Y-Z	Stationary Rectilinear coordinate system
X'-Y'-Z'	Rectilinear coordinate system aligned with the crack front

Greek

β_i	Decision variables for GA
ν	Poisson's ratio
ω	Excitation frequency
ϕ	Crack orientation angle
θ	Angular displacements of the shaft
θ_1	Rotational degree of freedom at element node 1
θ_2	Rotational degree of freedom at element node 2

Superscripts

c	With crack
h	Horizontal
v	Vertical
wc	Without crack

Superscript

(e)	elemental

Abbreviations

FEM	Finite element method
MCDLA	Multi-crack detection and localization algorithm
MCLSA	Multi-crack localization and sizing algorithm
NSGA-II	Non-dominated sorting genetic algorithm-II

1 INTRODUCTION

1.1 Importance of Study

Rotating machineries play an important role in many industries. Its applications include turbines and generators in power plants, airplanes, ships, automobile, household and medical appliances, etc. The shaft is a critical part of the rotating machinery because the power is transmitted through the rotating shaft. Fatigue cracks in the shaft are a potential source for their catastrophic failure. The machine failure because of rotating shaft would result in the increase in maintenance cost, loss of safety at workplace, and increase in the downtime. Hence, it is important to assess the health of shaft continuously for its safe operation.

The Electric Power Research Institute in 1997 reported that turbine breakdowns cost power generation industries and consumers $200 million per year as mentioned in the work by Boonyaprapasorn (1997). Also, as rotating machines surpass main working age, non-destructive testing is often necessary to estimate their remaining useful life.

There are different types of crack detection techniques and each of them has their own advantages and limitations depending upon the situation. There are several non-destructive techniques (NDT) available which are suitable for detecting cracks such as radiographic testing, ultrasonic testing, and X-ray. But these techniques have their own limitation to be used for detecting cracks in shaft; mainly because the shaft is not easily accessible. Then there are other reasons such as the radiographic testing can be used only for specimen with limited thickness and with the ultrasound techniques, if the crack surface is parallel to the ultrasonic beam the crack will go unnoticed.

Presence of cracks in a shaft changes the flexibility locally and hence its dynamic behavior globally. This gives a means for the identification of cracks in a shaft by measurement of cracked shaft vibrations. Advantage with the vibration based crack identification techniques is that it is non–destructive as well as it can be used for inaccessible machine components.

A shaft can have more than one potentially dangerous crack and a crack detection technique should take this fact into account. Lots of work has been done for a shaft with single crack. In the present work, identification of cracks in a multi-cracked shaft is studied.

The present chapter discusses the various causes for the development of cracks in machine elements and also the advantages and limitations of different crack detection techniques. The background and literature review on the vibration based techniques have been presented. The scope of the present investigation has been stated. An outline of the thesis has been given with brief description on the contents of each chapter.

1.2 Background and Literature Review

1.2.1 Background

In the high-speed rotating machinery, the high torsional and radial loads, together with a complex pattern of rotor motion, can create severe mechanical stress conditions and may eventually lead to the development of a rotor crack. Among the various faults like unbalances in a rotor, reciprocating unbalances, misalignments, mechanical looseness, run–outs, faults in gears, rolling element bearing faults, rubs, etc., the rotor crack is considered as one of the most serious fault.

The crack in a shaft can arise because of several reasons. The fluctuating load in the shaft leads to fatigue cracks. Normally, these cracks arise at the location of stress concentration. Hence, these cracks may appear near the region of discontinuity, such as oil holes, keyways, screw threads; or near any other abrupt change in the cross section of shaft, such as steps cut on the shaft to mount gears, pulleys and bearings. Microscopic and submicroscopic discontinuity, such as, inclusions of foreign materials, alloy segregation, and crystal discontinuity can also give rise to stress concentration. Then there are conditions that accelerate the crack initiation such as residual tensile stresses, elevated temperatures, temperature cycling, and a high corrosive environment.

A rotating shaft is subjected to fatigue loadings. A high level of fatigue stresses lead to development of the micro and macro cracks near the mechanical stress raisers such as keyways and steps notches, slits, etc. Apart from these, metallurgical faults like forging flaws, small voids, and the matrix porosity may also cause the crack initiation. Once a crack is developed, the high stress intensity around the crack tip will cause the crack to propagate. In terms of time scales, the crack will grow over long periods and the failure occurs very rapidly once the crack(s) reaches a critical size.

The failure of a shaft leads to the plant shutdown with associated various losses and sometimes accident. A cracked shaft must be replaced or repaired to prevent equipment from possible damages and losses. Hence, the presence of cracks should be identified well before it goes critical and leads to the catastrophic failure. If a crack is detected and localized at an early stage, the shaft may be repaired at a relatively low cost and within a short period of time.

For the identification of damage in structures, a non-destructive technique (NDT) is preferred over the destructive techniques (DT) since it is not always feasible to dismantle a structure for using a destructive testing. The dismantling is undesirable also. Various non-destructive techniques (NDT) are the liquid penetrant testing, radiographic testing, ultrasonic inspection, visual and optical testing, electromagnetic testing, eddy-current testing, acoustic emission testing, infrared and thermal testing, laser testing, etc., can be used for the detection of cracks. However, these methods usually require that the system under investigation to be taken out of service for inspection at pre-set time intervals (Bachschmid 2010). The inspection procedure can be very expensive and time consuming, especially when it involves components at inaccessible locations. This has led to the development and continued research on vibration based methods that examine the changes in the vibration characteristics of complex structures. These methods can be applied to in-service structures, reducing maintenance costs, ensuring safety and improving system performance. With the development of non-contact sensors, the method finds useful application in the case of moving parts of the machine.

According to Rytter (1993), the problem of damage diagnostics in general can be categorized as four different levels:

Level 1: Detecting the existence of damage in the structure;

Level 2: Level 1 plus determination of the damaged site, i.e. localisation;

Level 3: Level 2 plus quantification of severity of damage;

Level 4: Level 3 plus prediction of remaining service life of the structure.

The present work has been done up to Level 3. The prediction of remaining service life can be made using fracture mechanics and fatigue life analysis which is a forward problem, while the problem up to Level 3 is an inverse problem. Hence, the problem of prediction of the remaining service life can be treated uncoupled from the problem up to Level 3.

1.2.2 Literature review

There is plenty of literature dealing with the identification of cracks in a shaft system. Many techniques have been proposed, out of which some are tested experimentally. Extensive reviews on crack identification methods are presented by Wauer (1990a), Gasch (1993), Dimarogonas (1996), Doebling et al. (1998), Sabnavis et al. (2004), Heng et al. (2009) and Feldman (2011).

In this section, the state of the art of the 'vibration based techniques for the condition monitoring of shaft' is presented. As per the literature review by Sabnavis *et al.* (2004), the methods for the identification of cracks in rotors can be divided in three groups. These methods can be grouped as

1) Vibration-based methods (VBM)
    1.1) Model-based methods
    1.2) Signal-based methods
2) Modal testing
3) Non-traditional methods

In signal based methods, the vibration signature of the machine is compared with some reference vibration signature of the machine. The reference vibration signature is taken when there is no crack in the shaft. Transient or steady state vibration data are analysed for known indicators of cracks.

"Model-based methods are based on analytical or numerical models to simulate the behaviour of cracked shafts during operation and attempts to correlate the observed vibration signature with the presence of a crack at discrete locations on the shaft" as stated by Sabnavis *et al.* (2004).

In modal testing, changes in system modal characteristics such as changes in mode shapes and system natural frequencies, response to specially applied excitation (other than unbalance), etc. due to the presence of a crack, are employed for the crack detection.

Techniques like, genetic algorithms, neural networks, fuzzy logic along with signal processing techniques such as wavelet techniques, Hilbert transfer come in the non–traditional methods for the crack identification.

With multiple cracks in a shaft, number of unknown variables is more, and often a crack identification method uses a combination of different features and techniques. For example some recent works (Chasalevris and Papadopoulos, 2006) on multiple crack identification techniques have used wavelet transform (non-traditional methods) along with the change in natural frequencies (modal testing). A literature review on the identification of cracks is presented in the following sections. It is divided in three parts: (a) modeling of transverse fatigue cracks; (b) identification of single crack; (c) identification of multiple cracks.

(a) Modeling of transverse fatigue crack

Subnavis et al. (2004), in their review paper, defined the crack as any unintentional discontinuities in the shaft material. Based upon the geometry, cracks are classified as:

a) Cracks perpendicular to the shaft axis are known as “transverse” cracks. These are the most common and most serious as they reduce the cross-section, and thereby weaken the rotor. The most of past and current research focuses on the detection of such cracks. They introduce a local flexibility in the stiffness of the shaft due to strain energy concentration in the vicinity of the crack tip.
b) Cracks parallel to the shaft axis are known as “longitudinal” cracks.
c) Slant cracks are cracks at an angle to the shaft axis.
d) Cracks that open when the affected part of the material is subjected to tensile stresses and close when the stress is reversed are known as “breathing” cracks.

e) Cracks that always remain open are known as “gaping” cracks or open cracks. They are more correctly called “notches”. Gaping cracks are easy to mimic in a laboratory environment and hence most experimental work is focused on this particular crack type.

f) Cracks that open on the surface are called “surface” cracks.

g) Cracks that do not show on the surface are called “subsurface” cracks.

Mathematical modeling of a crack is an important part of the research work involved in the identification of cracks in a shaft. Modeling of a crack mainly involves three factors: stiffness, damping and non-linearity. Among these, researchers have concentrated more on the stiffness and the non-linearity for the modeling of a crack. Few researchers have considered other factors such as: thermal effect is considered by Bachschmid et al. (2004), and damping properties of crack was discussed by Wauer (1990b). All the formulations involve reduction in the stiffness at the location of crack. A review on modeling a crack, based on the strain energy release rate was presented by Papadopoulos (2008).

Thomson (1943) and Kirmsher (1944) were the first who attempted to quantify the local damage in a structure. They simulated the effect of notch on the structural flexibility by using the reduced section of the structure, and discussed the effect of location and size of notch on the change in natural frequencies of the damaged beam. The presence of a crack in a shaft introduces the local flexibility. Irwin (1957) was the first to relate the local flexibility to the stress intensity factor. The stress intensity factor is used in fracture mechanics to relate the stress state near the crack tip to macroscopic characteristics (such as the geometry of a body and loading). Adams et al. (1978) modelled the damage in a bar by a linear spring of infinitesimal length. The elastic stiffness was determined from the change in first two natural frequencies.

Dimarogonas and Massouros (1981) considered the effect of a crack on the torsional dynamic behavior of a shaft. They used the strain energy release rate approach to calculate the local flexibility of the shaft due to the presence of the crack. A continuous shaft with a circumferential crack was analyzed. They found strong dependence of the fundamental natural frequency on the crack depth. The analysis was verified by experimental results. The dimension of the flexibility matrix depends on the number of DOFs considered. Dimarogonas and Paipetis (1983) introduced a matrix for beams of the rectangular cross section with the transverse surface crack. They showed a beam with a transverse crack, in general, could be modelled in the vicinity of the crack by way of a local flexibility (compliance) matrix, connecting the longitudinal, bending, and shear forces, and corresponding displacements. They established a 5×5 matrix neglecting the torsion. It has off-diagonal terms that indicate coupling of the respective forces and displacements, and therefore the coupling of respective motions. This matrix is a diagonal matrix in absence of the crack.

Gudmundson (1983) represented the crack by a consistent, static flexibility matrix. He calculated the flexibility matrix by two different methods. He showed that if the static stress intensity factors are known, the flexibility matrix can be determined from an integration of these stress intensity factors. Alternatively, the static finite element calculations can be used for the determination of the flexibility matrix. Christides and Barr (1984) used variational principle to develop vibration equations for cracked beams. They developed a cracked beam theory by deriving the differential equation and associated boundary conditions for a uniform Euler-Bernoulli beam containing one or more pairs of symmetric cracks. They proposed a local empirical function decaying exponentially with the distance from the crack, to model the stress field induced due to the crack. They used the extended Hu-Washizu variational principle

(Christides and Barr, 1986) for derivation of equation of motion for the cracked Euler-Bernoulli beam.

Papadopoulos and Dimarogonas (1987) investigated the coupling of the longitudinal and bending vibrations of a rotating shaft due to an open transverse surface crack. They assumed that the open crack leads to a system with behaviour similar to that of a rotor with dissimilar moments of inertia along two perpendicular directions. They represented the local flexibility due to the presence of the crack by a matrix of size 6×6, including torsion. This matrix has off diagonal terms, which cause the coupling along the bending in two transverse directions and the extension along the longitudinal direction. The existence of the coupling due to the crack was used for the crack identification in rotating shafts together with the sub-critical resonance. They excited the beam by giving longitudinal harmonic excitation. They found that for small crack, the peaks occurred at the natural frequency of the longitudinal vibrations but as the crack size increased, other peaks appeared due to coupling with bending vibrations. Gounaris and Dimarogonas (1988) used the FEM to model the structure and developed a finite element for the cracked prismatic beam. The element was used to evaluate the dynamic response of a cracked cantilever beam to the harmonic force excitation. They showed that resonant frequencies and vibration amplitudes were considerably affected by the existence of moderate crack.

Shen and Pierre (1990) presented an approximate Galerkin solution to the one dimensional cracked beam theory developed by Christides and Barr (1984) for the free transverse motion of beams with pairs of symmetric cracks. To validate the theoretical results, a two dimensional finite element approach was developed, which also allowed determining the parameter that controls the stress concentration profile near the crack tip in the theoretical formulation without requiring the use of experimental results. Lee et al. (1992) proposed a switching crack model with two different stiffness states, depending upon whether the crack is open or close. The necessary conditions for the crack opening and closing were analytically derived from the simple rotor with the switching crack.

Sukumar et al. (2000) presented a FEM based three-dimensional crack modeling. A discontinuous function and a two-dimensional asymptotic crack tip displacement field were added to the finite element approximation to account for the crack using the notion of partition of unity. They discussed computational geometry issues associated with the representation of the crack and presented stress intensity factors for planar three-dimensional cracks. Chondros et al. (1997) developed a consistent continuous cracked bar vibration theory. The stress and displacement fields about the crack were used to modify the stress and displacement fields throughout the bar. The reduction to one spatial dimension was achieved by integrating the stress and displacement fields throughout the bar cross-sections. The resulting linear differential equation with variable coefficients had the modified displacement field due to the crack imbedded in it.

Chondros et al. (1998) developed a continuous cracked beam vibration theory for the lateral vibration of cracked Euler-Bernoulli beams with single edge or double edge open cracks. They used the Hu-Washizu-Barr (Christides and Barr, 1986) variational formulation to develop the differential equation and boundary conditions of the cracked beam as a one-dimensional continuum. The crack was modeled as a continuous flexibility using the displacement field in the vicinity of the crack, that is found with fracture mechanics methods. Carneiro and Inman (2002) proposed a continuous mathematical model of a cracked Timoshenko beam. The Hu-Washizu-Barr variational principle (Christides and Barr, 1986) was used for the systematic derivation of continuous models and the stress concentration effects was represented by an exponential disturbance function acting both on the axial and shear stresses.

Irretier (1999) gave mathematical foundations for the experimental model analysis of rotating structures which characterised by time-variant matrices. Equations of motion were solved by the modal transformation to obtain the impulse and frequency response functions. Wang et al. (2004) compared the performance of recurrent neural networks (RNNs) and neuro-fuzzy (NF) systems as a machine fault prognostic systems for the rotary machinery. They found that if an NF system is properly trained, it performs better than RNNs system in both forecasting accuracy and training efficiency. Consequently, they developed an on-line machine fault prognostic system based upon NF Systems. The performance of the developed prognostic system is evaluated by using three test cases including a worn gear, a chipped gear, and a cracked gear.

Di and Law (2007) presented different types of damage models of a frame element, whose elemental matrices were decomposed into their eigenvalue and eigenvector matrices. These eigen-parameters were included in a flexibility-based and sensitivity-based model-updating algorithm for the condition assessment of a plane frame structure.

For a rotating shaft with a crack, if the static deflection of the shaft is more than the vibration of the shaft, the crack will open and close periodically with the rotation of the shaft. The opening and closing of the crack depends upon the bending stresses in the shaft. The crack will remain open when the bending stresses are tensile while the crack will remain closed when the bending stresses are compressive. For the intermediate locations (some part of the crack is in the tensile region and some of the crack part is in compressive region), the crack is partly closed and partly open. This is normally the case with large rotors. If the shaft vibration is more than the static deflection, the problem will become non-linear and the shaft response, for this case, can be obtained by numerical integration (Papadopoulos, 2008).

In earlier works on modelling the crack breathing behaviour, the crack is modelled by bi-level stiffness of the rotor corresponding to open and closed state of the crack. Gasch (1976) modelled the breathing crack by a spring-loaded hinge, and numerically demonstrated a sub-harmonic resonance. In this model the crack remains open for one half and closed for the other half of a revolution of the rotor. Transition of the crack from the open state to close state (and vice-versa) occurs abruptly as the rotor turns. Grabowski (1984) suggested switching of the stiffness values from those of an uncracked rotor (closed crack state) to those of cracked rotor (fully open state) at a particular rotor angular position. Mayes and Davies (1976) studied the behaviour of a cracked shaft model, which took into account opening and closing of the crack as a stiffness step function. Later, they extended their work and suggested a method for calculation of change in stiffness due to a deep crack (1984). Breathing of the crack is modelled by assuming sinusoidal variation of stiffness.

Nelson and Nataraj (1986) developed the finite element formulation of a crack element. The presence of crack was taken into account by a rotating stiffness variation. The stiffness variation was considered as a function of the rotor's bending curvature at the crack location. Papadopoulos and Dimarogonas (1988) used truncated cosine series approximation to calculate the compliance of a crack at any orientation angle. The fitting compliance matrices are determined from the known behavior of the stiffness matrix at certain angular orientation and the slopes of the stiffness at fully open and fully closed states of the cracks. Changhe et al. (1989) represented the crack as a hinge with variable stiffness in two rotor-fixed lateral directions. The crack is introduced at a node of the finite element model. The stiffness change was assumed to be dependent on the direction of bending moment at the crack cross-section.

Abraham and Brandon (1995) proposed a substructure approach for modelling breathing behaviour of crack using Lagrange multipliers. They used time varying connection matrices to relate the two segments of the cracked beam, separated by the crack. The connection matrices are expanded in a Fourier series leading to a classical eigenvalue problem. Darpe *et al.* (2004) presented a response-dependent non-linear crack model. The flexibility matrix was constructed through the stress intensity factors. In their work, the boundary of opening of the cracked surfaces needs to be known to define the limits of integration in the process of finding the flexibility. Therefore, they developed a crack closure line (CCL) algorithm that provides the position of the crack closure line for each value of the rotating angle.

Chasalevris and Papadopoulos (2006) calculated the compliance matrix for a crack as a function of both the crack depth and its orientation in a transverse plane. They used *B-spline* curves to interpolate the known values of the compliance, as stress intensity functions do not give good approximation of the compliance at all the rotation angle of the crack. Darpe (2007) presented a finite element model of a rotor with a slant crack. He derived a new flexibility matrix for the slant crack that accounts for the additional stress intensity factors due to orientation of the crack compared to the transverse crack. Comparison between the rotor with a slant and transverse crack was made with regard to stiffness coefficients and coupled vibration response characteristics. The influence of angle of orientation of the slant crack on the stiffness values was investigated. It was shown that, compared to the transverse crack, the stiffness matrix for the slant crack is more populated with additional cross coupled coefficients. Also, cross-coupled stiffness values are larger for the slant crack, which leads to stronger cross-coupling in the bending–torsional–longitudinal vibrations compared to the transverse crack.

Han and Chu (2011) calculate the additional local flexibility due to an elliptical crack in the shaft under the bending and axial tension loads. The results were compared with the flexibility of crack with the straight crack front, which was reported by Dimarogonas and Papadopoulos (1983), and Papadopoulos and Dimarogonas (1987). Al-Shudeifat and Butcher (2011) presented two breathing functions to represent the breathing effect on the cracked element stiffness matrix. Breathing functions were used in formulating the time-varying finite element stiffness matrix of the cracked element. The finite element equations of motion were then formulated for the cracked rotor system and solved via the harmonic balance method for response, whirl orbits and the shift in the critical and subcritical speeds.

Several crack model has been evolved in past few years. Some researchers have used the variational formulation to obtain the cracked bar theory. This requires modelling of the stress field near the crack. Some parameters of the model have to be evaluated experimentally. Some other researchers have used the lumped flexibility approach, where the additional flexibility due to a crack is obtained using the fracture mechanics approach. In this method, the flexibility due to a crack can be obtained as a function of the crack size. Hence, a separate model for the stress field is not required. Still some limitations are there such as: it does not consider any friction on the cracked area during the breathing. An accurate model of a cracked shaft is needed to study the key features of a cracked shaft which will help in the diagnostic of the cracked shaft. Modelling of the crack should include the modelling of the stress and strain due to the crack, the breathing of cracks, the friction between cracked surfaces, and thermal effects. This gives future scopes of the research in the area of crack modelling.

Some other researchers have used the two- and three-dimensional FEM to model a cracked beam. The generation of time response with the fine mesh resolution is demanding in terms of the computational time. Since the crack depth is unknown, auto re-meshing capability is required, which makes the modelling task more complicated (Carneiro and Inman 2002). As per work of Friswell and Penny (2002), these two- and three-dimensional approaches produce detailed and accurate models but are a complicated and computational-intensive approach to model simple structures like beams, and are unlikely to lead to practical algorithms for the damage identification. Furthermore, FEA models contain modelling errors. As a result, these detailed models do not substantially improve simplified models.

(b) Identification of cracks

The occurrence of a crack in a structure introduces the local flexibility, which changes the dynamics of the structure as a whole. Thus the inverse problem can be solved by using the changes in modal parameters and the free and forced responses of the cracked structures. But a more accurate crack model is needed for identifying the key features of a cracked shaft dynamic behaviour. These key features include: the coupling between different motions such as the bending, longitudinal and torsional vibrations, the splitting of natural frequency due to presence of crack, the non linearity in stiffness due to breathing, and the friction between the cracked surfaces. These key features, along with modal parameters and the free and forced vibrations have been explored by several researchers for development of cracked-shaft diagnostic methods.

For weight dominated shafts, the crack open and closes as the shaft rotates. When the crack is fully closed the stiffness of the shaft is maximum, and when the crack is fully open the stiffness of the shaft is minimum. During the rotation of the shaft the stiffness of the shaft varies between these two limits. Hence, a transverse crack causes a shaft to have asymmetric stiffness. Dimentberg (1961) showed that the total motion of an asymmetric shaft center is the sum of a vector that turns with the angular velocity and a vector that turns with twice the angular velocity. The result is a spiral like orbit that is determined by relative lengths of two vectors. This is because the shaft crosses the two limiting stiffness twice during one revolution. The weight of shaft is balanced by this varying stiffness. The shaft will rest at a higher position when the stiffness is more and vice versa. This oscillation causes the 2X component in the frequency spectrum. Hence, 2X component in the frequency spectrum is a strong indication of the presence of a crack in the shaft. Although the bearing misalignment could also result in 2X and 3X components in the spectrum. The bow in a rotor introduces 1X component in the spectra and the mass unbalance also introduces 1X component.

Liebowitz et al. (1967), and Okamura (1969) studied the effects of the reduced rigidity on the load carrying capacity, deflection, and fracture load of a slender column with a single edge crack based on the column theory together with the relationship between the compliance and the stress intensity factor of a cracked beam. This study indicated that the bending and compression stress intensity factors of the same mode could be superimposed. Dimarogonas and Papadopoulos (1983) investigated uncoupled bending vibration of a de Laval rotor with a transverse surface crack. With the open crack the assumption, analytical solution for the de Laval rotor based on the theory of rotating shaft with dissimilar moments of inertia were obtained. An important aspect of the analytical solution was the near-half-critical speed. This speed has been used as the primary source of information for the identification of the existence of a crack in turbomachinery rotors. Also, an analytical approach is presented for closing cracks for the weight dominated rotor leading to equations with periodic coefficients.

Imam et al. (1989) presented a crack identification technique based upon the vibration analysis approach. They developed a 3-dimensional finite element crack model and a nonlinear rotor dynamic code to model a cracked rotor system. They developed variety of vibration signatures indicating a rotor crack. Both the analytical crack model and the crack signature analysis techniques were experimentally validated. This paper described steps of the development, starting from the technical concept to the commercial field applications. Rajab and Sabeeh (1991) investigated vibration characteristics of a cracked Timoshenko shaft. The local flexibility due to a crack in the presence of bending moment and shear loads is modelled by using fracture mechanics concepts. It was shown that the knowledge of changes in the first three natural frequencies relative to the uncracked shaft was sufficient to estimate the crack depth and the crack location in a single crack. Each additional crack in the shaft requires the knowledge of the changes in the next two higher natural frequencies.

Pandey et al. (1991) used the curvature mode shape as an indicator of the presence of cracks in beams. They derived the curvature mode shape using the central difference approximation. The change in the curvature mode shapes increase when the size of damage increases. This information can be used to obtain the amount of damage in the structure. Morassi (1993) derived an explicit expression of the sensitivity of a natural frequency to an open crack in a beam in the bending vibration for a simple spring-line model of a crack. He concluded that the sensitivity was proportional to the potential energy stored in the corresponding mode shape, evaluated for the undamaged beam at the damaged cross-section.

Sekhar and Prasad (1997) analyzed flexural vibrations of a rotor-bearing system by including a shaft having a slant crack that resulted from the fatigue of the shaft due to the torsional moment. They developed a stiffness matrix of a slant cracked element, which could be used in the FEM analysis of the rotor–bearing system. At an interval, the frequency corresponding to the torsional frequency, the presence of sub-harmonic frequency components in the frequency spectrum of the steady state response was used for the crack detection. Friswell et al. (1998) used a combined genetic algorithm and eigen sensitivity method to identify the location and magnitude of a damage from measured vibration data. The genetic algorithm was used to optimize the discrete damage location variables and to identify the damage location, and the eigen sensitivity was used to identify the extent of damage. Wu and Huang (1998) investigated the dynamic response of rotating shaft containing a transverse crack and supported over speed dependent bearings. From the FFT analysis of displacement responses, the 2X component was extracted that served as a good index to detect the crack location and depth. Response amplitudes to variations of the crack depth and the crack location are then discussed and a technique of the crack identification is introduced with the aid of response contour maps of two sensing probes.

Sekhar (1999) used the finite element (FEM) to study flexural vibrations of a rotor system by considering open cracks. They studied the influence of one crack over the other for eigen frequencies, mode shapes and for threshold speed limits. Vyas and Satishkumar (2001) used a neural network simulator for the prediction of faults in the rotating machinery. A back-propagation learning algorithm and a multi-layer network were employed. The layers were constituted of nonlinear neurons and an input vector normalization scheme was built into the simulator.

Sekhar and Srinivas (2002) presented an analysis on the slotted shaft, including compensatory inertia slots. The slotted composite shaft was modelled based on the first order shear deformation theory using the finite element method with shell elements. Slot parameters, stacking sequences and material properties were found to influence to great extent on the vibrational characteristics of rotors. The results were compared with those of isotropic slotted shaft. It was found that the difference between eigen frequencies of a shaft in two orthogonal directions increases due to the presence of slots. Hong et al. (2002) used the continuous wavelet transform to estimate the Lipschitz exponent. The magnitude of the Lipschitz exponent was found to be indicator of damage extent. The continuous wavelet transform (CWT) by a Mexican hat wavelet having two vanishing moments was utilized for the estimation of the Lipschitz exponent. However, the magnitude of the Lipschitz exponent depends upon sampling distance and the location of the crack along the shaft length also that makes the inverse problem depending upon more factors.

Bachschmid et al. (2002) presented a model-based identification method for multiple faults by a least-squares fitting approach in the frequency domain, by means of the minimization of a multi-dimensional residual between vibrations in some measuring planes on the machine and the calculated vibrations due to the acting faults. The method required the definition of the models of the elements that compose the system; i.e., the rotor, bearings and the foundation, as well as the models of the faults, which could be represented by harmonic components of the equivalent force or moment systems. The identification procedure was validated with experimental results obtained on a test-rig.

Yang et al. (2002) developed a wavelet based algorithm to determine the nonlinear dynamical characteristics of a cracked rotor. This investigation reported the correlation of surface crack breathing with rotor chaotic motions. The effectiveness of the algorithm in detecting rotor-dynamic instability induced by mechanical faults as contrast to algorithms that were based on nonlinear dynamics was discussed. Sinha et al. (2002) presented a method for the estimation of crack locations and sizes in a beam based on minimizing the difference between the measured and predicted natural frequencies via the model updating. The methodology used a baseline FE model along with the modal test data in a gradient-based model updating method. Three experimental examples were demonstrated and it was observed that the estimation of the crack location was more accurate than the estimation of the crack depth.

Dilena and Morassi (2004) used damage-induced changes in natural frequencies and anti-resonant frequencies for the identification of a single open crack in a vibrating beam, either under axial or bending vibration. It was shown that an appropriate use of frequencies and anti-resonances may be useful to avoid the non-uniqueness of the damage location problem, which occurs in symmetrical beams when only frequency data are used. From a series of dynamic tests on cracked steel beams, it was found that the noise and the modelling errors on anti-resonances were usually amplified strongly with respect to cases in which only frequency data were used. Based upon this behaviour, they suggested that the damage identification techniques based on anti resonance data should be carried out with some caution when mechanical systems of greater complexity are considered.

Sekhar (2004a) used the continuous wavelet transform (CWT) to extract sub-harmonics from the coast-down time domain vibration signal from journal locations of cracked rotors on fluid film bearings. The coast-down phenomenon was analysed by considering the dissipation through the journal film and by evaluating the deceleration for each speed. The CWT of a time-varying function was defined as the sum over all time of the signal multiplied by the scaled shifted versions of the wavelet function. Characteristic sub-harmonic peaks, which could not be detected by the normal fast Fourier transform (FFT) due to the non-stationary nature of the signals, could be detected by CWT. Darpe et al. (2004) studied the coupled longitudinal, bending, and torsional vibrations for a rotating cracked shaft using a response dependent non-linear breathing crack model. Bending natural frequencies and the sum and difference frequencies are observed in the lateral vibration spectrum due to the interaction of the torsional excitation frequency and rotational frequency, when torsional excitation with a frequency equal to the bending natural frequency is applied to the cracked rotor.

Sekhar (2004b) presented a model-based method for the on-line identification of cracks in a rotor. The fault-induced change of the rotor system was taken into account by equivalent loads in the mathematical model. The crack was identified for its depth and location on the shaft. The nature and symptoms of the fault were ascertained using the fast Fourier transform. However, it was found that the estimation of crack depth, to a good extent, was dependent on the number of measurement locations. Nahvi and Jabbari (2005) proposed a method based on measured frequencies and mode shapes of the beam. They used contours of normalized frequency in terms of normalized crack depth and location to detect the crack in cantilever beams. The intersection of contours with the constant modal natural frequency planes was used to relate the crack location and depth. A minimization approach was employed for identifying the cracked element within the cantilever beam. The method was based on measured frequencies and mode shapes of the beam.

Dharmaraju et al. (2004) developed an algorithm for estimating crack flexibility coefficients and subsequently the estimation of the equivalent crack depth based on the forced response information. The algorithm used the Euler-Bernoulli beam theory in the beam model without considering the damping in the system and required the crack location and the force to the beam to be known. The standard static reduction scheme was incorporated in the identification algorithm to eliminate some of DOFs so as to overcome the problem of measurements of all DOFs at all nodal locations. Since the static reduction scheme is suitable only for low frequency excitations, the same authors, Dharmaraju et al. (2005) used the standard dynamic reduction scheme in the identification algorithm. However, it had limitation in that it required the measurement of the rotational DOFs at least at the crack element nodes. Hence, they outlined a “high frequency” condensation scheme for eliminating the rotational DOFs at crack element nodes. However, this reduction scheme could be applied only for high frequency operations and this limitation was overcome by Tiwari and Dharmaraju (2006). They used a hybrid reduction scheme in the identification algorithm to eliminate all the rotational DOFs and retain some of the linear DOFs for which measurements could be available. The hybrid reduction scheme was suitable for low, moderate, and high frequency operations.

Hadjileontiadis et al. (2005) presented a technique for the crack identification in beam structures based on the fractal dimension analysis. The fundamental vibration mode of a cracked cantilever beam was analysed and the location of the crack was determined by the sudden changes in the spatial variation of the analysed response, while the size of the crack was related to the fractal dimension measure. The technique was validated by experiments on cracked plexi-glass beams. A noise test was performed on simulated data to show the ability of the method to accurately identify cracks in presence of noise in the signal. Han et al. (2005) proposed a damage detection index called the wavelet packet energy rate index for the damage detection of beam structures. Measured dynamic signals were decomposed into the wavelet packet components, and the wavelet energy rate index was computed to indicate the structural damage.

Sekhar et al. (2005) presented the detection and monitoring of a slant crack in the rotor system using the mechanical impedance. It was shown that the effect of slant crack parameters on the normalized impedance is the same as transverse cracks, but a transverse crack is highly sensitive to the mechanical impedance compared to a slant crack. They also observed that the changes in the rotor impedance due to cracks were significant as compared to that of natural frequencies of the rotor-bearing system. Jaishia and Ren (2006) presented a sensitivity-based finite element model updating method for the damage detection. The proposed procedure was firstly illustrated with a simulated example of a simply supported beam. The effect of noise on the updating algorithm was studied also. Afterwards, the procedure was applied for a tested reinforced concrete beam. It was shown that the modal flexibility was sensitive to damage.

Rucka and Wilde (2006a) used the continuous wavelet transform for estimating the damage location in beam and plate structures. A plexi-glass cantilever beam and a steel plate with four fixed boundary conditions were tested experimentally. The location of the damage was indicated by a peak in the spatial variation of the transformed response. Rucka and Wilde (2006b) presented a method for the crack detection in cantilever beams. The selection of the wavelet transform for the crack localization was discussed. The measurement of the static deflection of the beam in a large number of spatially distributed points was obtained by processing digital photographs of the beams. The wavelet transforms of static deflection lines of the beam was determined and a peak in the spatial variation of the transformed response indicated the location of the crack.

Solbeck and Ray (2006) investigated a coherence approach for locating the structural damage using modal frequencies. Transfer function parameters were identified from the input-output data using the Observer/Kalman filter identification method on extraction of modal properties. Using the coherence approach, a damage parameter vector was hypothesized for each damage case, using either identified or analytic structural models. The method was evaluated experimentally using a three-degree-of-freedom torsional system and a space-frame truss. Liu and Yang (2006) presented a decoupled damage identification algorithm. The method approached the damage identification problem in three steps: determining the number of damaged elements, localizing the damaged elements, and quantifying the extent of damage. The method was shown to be accurate and robust in the structural damage identification when the number of measured modes is more than the number of damaged elements with or without noise.

Pennacchi et al. (2006) presented a model based transverse crack identification method. The method was validated by experimental results obtained on a large test rig, designed for investigating the dynamical behaviour of cracked horizontal rotors. Three types of cracks were analyzed: the first was a slot, the second was a small crack (14% of the diameter) and the third was a deep crack (47% of the diameter). Darpe (2007) presented a crack identification procedure in a rotating shaft by analyzing transient features of the resonant bending vibrations by wavelet transforms. He utilized both the nonlinear breathing phenomenon of the crack and the coupling of bending–torsional vibrations due to the presence of a crack.

Karthikeyan at al. (2007) developed an algorithm for the crack localisation and sizing in a beam from the free and forced response measurements. The algorithm was iterative in nature. The iteration starts with an initial guess for the crack depth ratio and iteratively estimates the crack location and the crack depth until getting the desired convergence for both the crack location and the crack depth. For estimation of bounded flexibility coefficients, a regularisation technique was adopted. The method was illustrated through numerical examples. Morassi (2007) proposed a damage identification procedure for a beam vibrating either under the axial or bending vibration based on change in natural frequencies. The method was based on assumptions that the damaged configuration of the beam is a perturbation of the undamaged one. The frequency shifts caused by the damage are correlated with generalized Fourier coefficients of the unknown stiffness variation caused by the damage. The reconstruction procedure they proposed was based on an iterative algorithm.

Pennacchi et al. (2007) proposed the M-estimators, which could be used for defining weights automatically in the least square based algorithms for solving inverse problems. This method is general and can be applied in every problem of regression or estimation, not necessarily related to rotor dynamics. Perera and Ruiz (2008) presented a multistage scheme for the damage detection for large structures based on the experimental modal data and on finite element (FE) model updating methods. In the first stage, occurrence and approximate location of damage was estimated. In the second stage, the specific damaged members and the extent of damage was determined by considering only the members belonging to the regions detected as damaged in the first stage. The two objective functions formulated were based on the modal flexibility, and on mode shapes and natural frequencies.

Babu et al. (2008) used Hilbert–Huang transform (HHT) for the detection of crack in a cracked rotor. They applied the HHT to transient responses from a cracked rotor. It was found that the HHT performs better than fast Fourier transform and continuous wavelet transform for the crack detection in a transient rotor. It was observed that the HHT is particularly useful for identifying very small crack depths, where even CWT fails to detect them. Patel and Darpe (2008) studied the influence of the crack breathing models on the nonlinear vibration characteristics of cracked rotors. They investigated nonlinear dynamics of the cracked rotor using two crack models, i.e. the switching crack model and the response-dependent breathing crack model. Through numerical simulations, the dynamic response for both crack models was compared for the subcritical speed region for the rotor. Distinct differences were found in the bifurcation, amplitude, orbit and Poincaré map when two crack models were compared for assumed rotor parameters. The switching crack modeling revealed chaotic, quasi-periodic and subharmonic vibration response for deeper cracks. Contrary to this, more realistic breathing crack model revealed no evidence of chaotic, quasi-periodic and subsynchronous vibrations in the response.

Karthikeyan et al. (2008) developed a model based method for the crack identification in beam, which utilized forced responses and the change in natural frequencies. The algorithm was iterative in nature. The algorithm starts with a presumption that a crack is present in the beam. For an assumed crack location, flexibility coefficients are estimated with the help of forced responses. These crack flexibility coefficients are used to obtain the crack size by minimizing an objective function. With the help of the estimated crack size and measured natural frequency, the crack location is updated. The procedure iterates till the crack size and location get stabilized up to the desired level of accuracy. Karthikeyan and Tiwari (2010) presented an experimental verification of the identification algorithm presented by Karthikeyan et al. (2007). The experimental setup consisted of a circular beam, which was supported by rolling bearings at both ends. A harmonic force of continuously varying frequency was applied to excite the beam specimen. The actual force applied to the beam was measured by a piezoelectric force transducer. Displacement responses in the horizontal and vertical directions were measured at various locations of the beam by using four proximity sensors. Estimated flaw parameters were found to be in good agreement with the measured data in different frequency ranges.

Chasalevris and Papadopoulos (2009) investigated the coupled bending vibrations in a cracked rotor mounted in resilient bearings. Governing equations are coupled in two main directions, and the partial solution is obtained by solving a linear system of equations, for each time step, taking into account the non-linearity due to the breathing crack. The coupling is introduced in three different ways: equations of motion, the coupling due to breathing crack and the coupling due to cross-coupled bearing coefficients for stiffness and damping. They found, through the resilient bearing analysis that the coupling due to a crack is negligible in respect to the coupling that bearings introduce. Kim and Lee (2010) proposed a damage identification method for beam-like structures with a fatigue crack, which did not require comparative measurement on an intact structure. The method needed several measurements at different level of excitation forces on the cracked structure. Second spatial derivatives of frequency response functions along the longitudinal direction of a beam were used as the indicator of crack existence. The damage identification method was verified with experiments as well as by finite element modeling.

Quek et al. (2001) studied the effectiveness of different wavelet technique in identification of cracks with respect to crack parameters like, the size, orientation, and width of the crack. Yang (2011) presented a method for the structural damage identification based on the flexibility disassembly. The basic idea of the method was to decompose a structural flexibility matrix into a matrix representation of the connectivity between degrees-of-freedom and a diagonal matrix containing the magnitude information. Using the flexibility disassembly, a new damage detection scheme was presented to approach the damage identification problem in three steps. The scheme has a unique advantage that it can accurately compute the stiffness perturbation parameter without any higher-order sensitivity analysis or iteration. Sawicki et al. (2011) proposed the use of auxiliary excitation of rotor using active magnetic bearings (AMB) for detection of cracks in rotors. They used the harmonic balance method to simulate the cracked rotor system. It was shown that a sinusoidal force from the AMB produces combinational frequencies based on the AMB frequency, and the rotational speed, that could be used to detect cracks in a rotor. Jun (2012) simulated behavior of cracked rotor by using the response including bending moment and the additional slope recursively. In the linearized equation of motion expressed using complex transfer matrix the additional slope is included as an excitation source.

(c) Identification of multiple cracks

Number of unknown crack parameters, such as the location, crack size, and crack orientation angle increases with the number of cracks present in a shaft. This makes the inverse problem of ‘multi-crack parameter estimation’ more difficult. For this, the diagnostic techniques for such cracked shaft are more complex and researchers are now using increasingly more powerful soft computing techniques (such as the multi-objective genetic algorithm, artificial neural networks, the fuzzy logic, etc.) along with a combination of cracked shaft features (natural frequencies, mode shapes, free and forced vibrations, breathing mechanism). Sekhar (2008) presented a review paper on the identification of multiple cracks in beam rotors, pipes, etc.

Springer et al. (1987) studied the longitudinal vibration of a bar with free ends. They considered two cracks that were located symmetrically at the centre. Cracks were modelled by two methods, i.e., one by springs and the other by reduced cross-section area. Changes in first three natural frequencies are found to be matched very well with experimental values. Messina et al. (1998) presented the sensitivity- and statistical-based method called the multiple damage location assurance criterion to localize structural damages. Their effectiveness was illustrated using numerical data for two truss structures and algorithms were validated experimentally using a three-beam test structure. Shifrin and Ruotolo (1999) presented a technique for calculating natural frequencies of a vibrating beam with an arbitrary finite number of transverse open cracks. The main feature of this method was related to decreasing the dimension of the matrix involved in the calculation, so as to reduce the computation time for evaluating natural frequencies.

Khiem and Lien (2001) used the transfer matrix method to develop a method for the natural frequency analysis of a beam with an arbitrary number of cracks. The resulted frequency equation of the multiple cracked beam was general in respect to boundary conditions including the more realistic (elastic) end supports. The frequency equation was used to investigate the effect of crack position and depth, number of cracks and elastic end constraints on natural frequencies of a beam. Darpe et al. (2003) derived the stiffness of two crack Jeffcott rotor using fracture mechanics concept. They investigated the effect of interaction of the two cracks on the breathing behaviour and on the unbalance response of the rotor.

Sekhar (2004c) presented a model-based method for the on-line identification of two cracks in a rotor. The fault-induced change of the rotor system was taken into account by equivalent loads in the mathematical model. Cracks were identified for their depths and locations on the shaft. The nature and symptoms of the cracks were ascertained using the FFT. Khiem and Lien (2004) formulated a non-linear optimisation problem for the multi-crack detection based upon natural frequencies. The spring model of the crack was applied to establish the frequency equation based on the dynamic stiffness of the multiple cracked beam. They presented numerical simulation results for a cantilever with one, two and three cracks. Loutridis et al. (2004) presented a method for the crack identification in double-cracked beams based on the wavelet analysis. The fundamental vibration mode of a double-cracked cantilever beam was analysed using the continuous wavelet transform and both the location and depth of cracks were estimated. Locations of cracks were determined by the sudden changes in the spatial variation of the transformed response. To estimate the relative depth of cracks, an intensity factor was established that relates the size of cracks to coefficients of the wavelet transform. The proposed technique was validated both by analytically and experimentally in the case of a double-cracked cantilever beam having cracks of varying depths at different positions.

Patil and Maiti (2005) verified experimentally a method for the prediction of the location and the size of multiple cracks based on the measurement of natural frequencies for slender cantilever beams, with two and three normal edge cracks. The analysis was based on the energy method and the crack was represented by a rotational spring. For theoretical prediction the beam was divided into a number of segments and each segment was considered to be associated with a damage index. Law and Lu (2005) proposed a time dependent method in which parameters of a crack in a structural member were identified from the strain or displacement measurements. The crack was modelled as a discrete open crack represented mathematically by the Dirac delta function. Dynamic responses were calculated based on the modal superposition and the optimization technique coupled with the regularization on the solution was used to identify cracks. The formulation for identification was extended to the case of multiple cracks. A general orthogonal polynomial function was used to generate derivatives of the strain or displacement time responses to eliminate the error due to the measurement noise. The identification algorithm was verified experimentally from impact hammer tests on a beam with a single crack. Chang and Chen (2003) presented a technique for the identification of cracks in a multiple cracked beam using the spatial wavelet analysis. First, locations of cracks were determined using the wavelet transform of the mode shape and then knowing the location, the size of the cracks were determined using the change in natural frequencies.

Chasalevris and Papadopoulos (2006) used the wavelet transform to get the location of cracks present in a beam. Then, the diagrams of the first three eigen values versus both the crack depth and the rotational angle, are used to identify the remaining unknown parameters for both cracks. They found that a signal to noise ratio of 50dB or higher is sufficient for the method to be applied in real field problems, which is possible if such measurements are carried out at or near eigen frequencies. Zhong and Oyadiji (2007) proposed a wavelet based method for the detection of cracks in beam-like structures. The method was based on finding the difference between two sets of detail coefficients obtained by the use of the stationary wavelet transform (SWT) of two sets of mode shape data of the beam-like structure. These two sets of mode shape data, which constitute two new signal series, were obtained and reconstructed from the modal displacement data of a cracked simply supported beam. Hence, the proposed method did not require modal parameters of an uncracked beam as a baseline for the crack detection.

Chasalevris and Papadopoulos (2008) studied the dynamic behavior of a cracked beam with two transverse surface cracks. They studied the horizontal and vertical plane motions of a cracked shaft that is excited by the vertical excitation. When crack orientations are not symmetrical to the vertical plane, a response in the horizontal plane is observed due to the presence of cracks. The experimental coupled response and eigen frequency measurements for the corresponding planes were presented. Saridakis et al. (2008) used neural networks, genetic algorithms and fuzzy logic for identification of two cracks in a shaft. Both cracks were considered to lie along arbitrary angular positions with respect to the longitudinal axis of the shaft and at some distance from the clamped end. The compliance matrix was calculated using stress intensity factor expressions for all rotation angles through a function that incorporates the crack depth and position as parameters. In the inverse problem, a genetic algorithm produces values for the cracks' attributes (position, depth and angle) as input arguments to the neural network, and searches for a solution comparing the outputs with experimentally measured values of responses. The artificial neural network was used to replace the analytical model in the inverse problem.

Guo and Li (2009) presented a two-stage method of determining the location and extent of multiple structural damages by using the information fusion technique and the genetic algorithm. In the first stage, evidence theory integrating the natural frequencies and mode shapes are used to find out the location of damage. Then in the second stage, a micro-search genetic algorithm (MSGA) was used to determine the damage extent. From numerical examples on a cantilever beam, it was found that the evidence theory are better than both of the frequency multiple damage location assurance criterions method and the mode shape multiple damage location assurance criterions method (Messina et al., 1998), and the MSGA is also more accurate and effective than simple genetic algorithms. JianPing and Meng (2009) proposed blind source separation (BSS) technique to separate the vibrational features produced by several faults existed in a rotor. The BSS algorithm requires source signals to be independent or slightly correlative with each other. However, some amount of correlation always exists between faults in a rotor and different faults may be correlative in different extent. This correlation leads to some errors in the signal separation of multi-fault. For this, a statistic variable-based algorithm, decorrelation method, is employed to analyze the signals of the rotors with multi-faults. The separation results using the numerical and experimental methods showed good separation of the typical feature components of the frequency spectrum of each fault.

Nguyen and Tran (2010) used wavelet transform for detection and localization of multi-cracks in beam like structures. The dynamic response of the bridge–vehicle system is measured directly from the moving vehicle. Locations of cracks were determined by positions of peaks of the wavelet transform and the velocity of the moving vehicle. Mazanoglu and Sabuncu (2012) used frequency contours to determine the location and size of two cracks in a beam. Natural frequencies were determined by using the theoretical model for different depths and locations of a single crack. The ratios of cracked and un-cracked beam's natural frequencies constituted the prediction tables scaled in two axes as the crack location and the crack depth.

With multiple cracks in a shaft, the inverse problem becomes more involved. Researchers have used the advanced signal processing technique, such as the wavelet technique and the Hilbert transform, and soft computing techniques such as genetic algorithms, fuzzy logic, and neural networks to solve the inverse problem. Among these, some of the wavelet based techniques are two stage techniques (Chasalevris and Papadopoulos, 2006; Chang and Chen, 2003). In the first stage, number of cracks and their locations are determined using the wavelet transform and then in the second stage, change in system dynamic parameters (for example natural frequencies) is used to get the orientation angle and size of cracks. Hence, the first stage will work for any number of cracks present in the shaft, since the wavelet transform checks the slope discontinuity locally. But in the second stage of these algorithms, there are few natural frequencies that can be used in the inverse problem. Hence, the second stage of these techniques is useful for few unknown only, hence limited number of cracks only. Some more wavelet based works were reported where estimation of the crack size has been obtained from the wavelet transform itself. Hong et al. (2002) proposed the use of magnitude of Lipschitz exponent for the estimation of crack size. But the discontinuity in the wavelet transform will depend upon the sampling distance, the measurement noise and the location of the crack along the shaft length. Hence, in the forward problem, although a bigger crack at a given location will give bigger discontinuity in the wavelet transform, the inverse problem to get crack size using the wavelet transform will need to consider these factors.

The inverse problem with multiple cracks in structures is difficult because different combination of crack parameters (like the crack size, location and relative orientation) may produce similar free and forced responses. The problem is more complicated because of the measurement noise. This means that solving the inverse problem with more number of unknown (crack) parameters is difficult with help of few global parameters (modal values). Researchers have used change in first few natural frequencies of transverse vibrations for the identification of multiple cracks in shafts (Chang and Chen 2003, and Khiem and Lien 2004). Some of them have been verified in laboratory conditions also (Patil and Maiti, 2005; Owolabi et al., 2003). But for an industrial application, where measurements have to be taken over large time scales, the change in natural frequency of transverse vibrations can be due to some more reasons such as change in bearing properties, seal ring locking and rub (Maynard et al., 2001). This means that the drop in lateral natural frequency may not be associated with a crack in a shaft. Effect of environmental factors such as temperature and humidity on the change in natural frequency on civil structure is discussed by Salawu (1997). For a weight dominated axial-symmetric shaft where crack breaths with the angular position of shaft, the periodic variation of natural frequencies is a good indicator of the presence of crack (Bachschmid et al. 2010). This is due to the gradual opening and closing of the crack. This means that the periodic change in the natural frequency is a good indicator of presence of a crack in a shaft. Algorithms such as wavelet based methods work by searching the effect of crack locally, i.e., detecting the slope discontinuity in the elastic line of shaft. The application of wavelet transforms to spatial vibrations of the shaft give the number of cracks and its locations. For a successful application of the wavelet transform, the signal-to-noise ratio in the measured vibration signal should be high (Chasalevris and Papadopoulos, 2006). Curvature mode shapes, presented by Pandey (1991), give sudden high value (peak) in the mode shape at the location of crack in a shaft. But the algorithm did not consider the effect of measurement noise. Also curvature mode shapes were obtained from mode shapes that are difficult to measure experimentally.

In summary based on the literature survey, the identification of cracks in a multi-cracked shaft is still a challenge. This is because the number of unknown parameters is more. And most of the papers (reviewed) are using the change in natural frequencies at some stage in their algorithm. Some have used the mode shape, which is again difficult to measure experimentally. Methods based upon the wavelet transform have the advantage that it can detect any number of cracks present in a shaft and its locations but for the estimation of crack size, it has to rely over some other feature such as change in natural frequencies. Also the signal-to-noise ratio of the measurement should be high.

In the present work, a multi-crack identification algorithm has been developed which uses the forced response from a cracked shaft at several frequencies to reduce the effect of measurement noise. The outline of the present work is briefed in the next section.

1.3 Present Work

In the present work, an identification methodology has been developed for the detection of cracks in a multi-cracked shaft. It identifies the number of cracks, their locations over the shaft length, their sizes and the crack orientation angle of cracks. The work is briefed in subsequent paragraphs.

First, the *multi-crack detection and localization algorithm* (MCDLA) is developed based on forced responses from the cracked shaft. The Timoshenko beam theory is used to model the shaft by using the FEM. The slope discontinuity at locations of cracks causes a jump in values of the shaft curvature. In the present work, the shaft curvature is obtained by fitting forced responses of the shaft, at consecutive axial locations, in a quadratic polynomial. The discontinuity in the elastic line of the shaft is found out from the coefficient of the quadratic term in the polynomial, which is proportional to the curvature. The jump in the value of curvature at the crack location is difficult to identify in the presence of measurement noise. For this, the algorithm uses shaft responses at several frequencies. A novel technique is used to normalize coefficients at each frequency so that they can be combined to enhance the discontinuity in the curvature at the crack location. Subsequently, c*rack probability functions* have been defined that gives the number of cracks and its approximate locations on the shaft.

The *multi-crack localization and sizing algorithm* (MCLSA) is developed to obtain the size and accurate locations of the cracks. The information, obtained from the MCDLA, is used in a multi-objective optimization by using the genetic algorithm (GA) to get crack sizes and its accurate location along the shaft. Objective functions for the GA are defined as the norm of the difference between the measured and the FEM predicted responses at different measurement locations. Since different combination of crack parameters, like its size and location, can give almost the same response, objective functions for the multi-objective GA is derived from response of the shaft at several frequencies to converge the GA to actual crack parameters. This ensures contribution of several modes of vibrations of interest in the estimation of nearly unique crack parameters.

Subsequently, cracks are assumed to be oriented with unknown crack orientation angle, but the crack remains open for any orientation angle. A new method is suggested to find out the crack orientation angle. This reduces the number of unknown in solving the inverse problem of crack parameter identification. Next, a breathing crack model is taken and the algorithm is verified numerically for a shaft with two breathing cracks. It is shown that for a multi-cracked shaft, the crack orientation angle for a crack can be identified independently of crack parameters of other cracks present in the shaft.

Next, experimentation has been done on real cracked shaft for the verification of the proposed algorithm. First, eddy current transducers are used for the measurement of shaft deflection due to a sine-swept external excitation at regular axial distances. This did not give satisfactory result. Next, to improve the accuracy of measurements, laser vibrometer was used to measure the shaft deflections. The algorithm was tested for single crack as well as double crack. It was found that the algorithm could identify the presence of cracks in few cases. A scheme is proposed to reduce the effect of measurement noise in the performance of the algorithm. The algorithm performed better after implementation of the scheme.

1.4 Organization of the Thesis

The introduction and the literature review are presented in **Chapter 1**. The finite element formulation for both the cracked shaft as well as the intact shaft is presented in **Chapter 2**. Development of the MCDLA along with its application to the simulated cracked shaft response is presented in **Chapter 3**. Development of the MCLSA along with its application to the simulated cracked shaft response is presented in **Chapter 4**. Development of algorithms for estimation of crack orientation angles for both the open as well as the breathing cracks is presented in **Chapter 5**. Experimentation results on the real cracked shaft are presented in **Chapter 6**. Conclusions and future works have been presented in **Chapter 7**.

2 MATHEMATICAL MODEL OF THE SHAFT SYSTEM

The mathematical model of a multi-cracked shaft is developed in the present chapter. Finite element formulation of the shaft using the Timoshenko beam theory is presented. Model of the open crack is provided and the additional flexibility due to crack is obtained. Finally, equations of motion of the intact shaft as well as the cracked shaft are obtained. The effect of the proportionate damping is included. Transverse surface crack are considered for the crack model. Cracks are assumed to be open cracks. The shaft is assumed to be non-rotating.

2.1 Model of a Shaft Element with a Crack

Figure 2.1 shows a shaft element with a crack subjected to a general loading. Let P_2 and P_3 are shearing forces, P_4 and P_5 are bending moments; l is the shaft element length, d is the crack depth, and *X*-*Y*-*Z* is a rectilinear coordinate system.

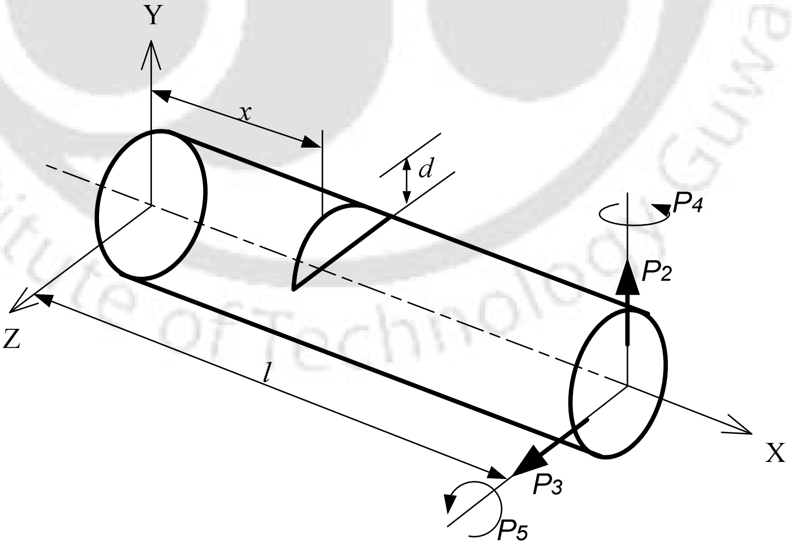

Figure 2.1: A shaft element with a crack subjected to a transverse loading.

For the transverse loading of the shaft, neglecting the axial and torsional loadings, the flexibility matrix of the crack could be expressed as (Dimarogonas and Paipetis, 1983),

$$[C_c] = \begin{bmatrix} c_{22} & 0 & 0 & 0 \\ 0 & c_{33} & 0 & 0 \\ 0 & 0 & c_{44} & c_{45} \\ 0 & 0 & c_{54} & c_{55} \end{bmatrix} \tag{2.1}$$

Where $c_{22}, c_{33}, \ldots, c_{55}$ are the six non-zero flexibility coefficients of the crack, in which four are direct coefficients and remaining two, c_{45} and c_{54} are cross-coupled coefficients. Detailed expressions of flexibility coefficients, for a transverse crack (see Figure 2.2) of negligible thickness, are given in Appendix A. The crack orientation angle ϕ of a rotated crack is shown in Figure 2.3.

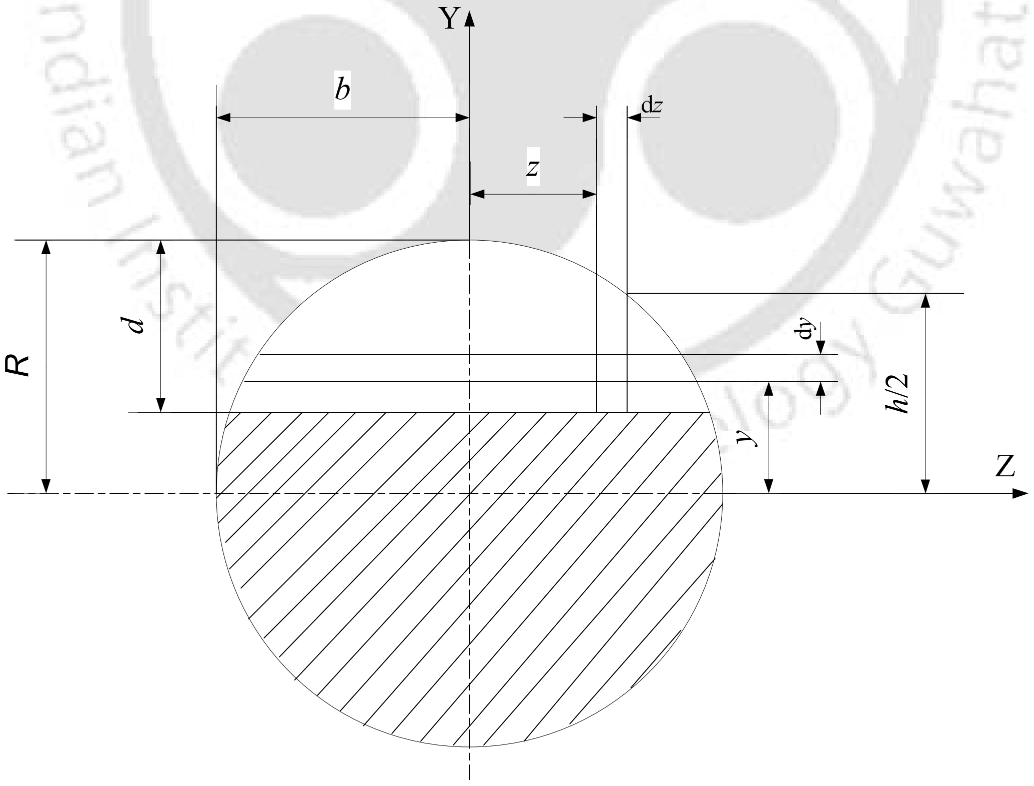

Figure 2.2: A geometry of a beam section with a transverse crack.

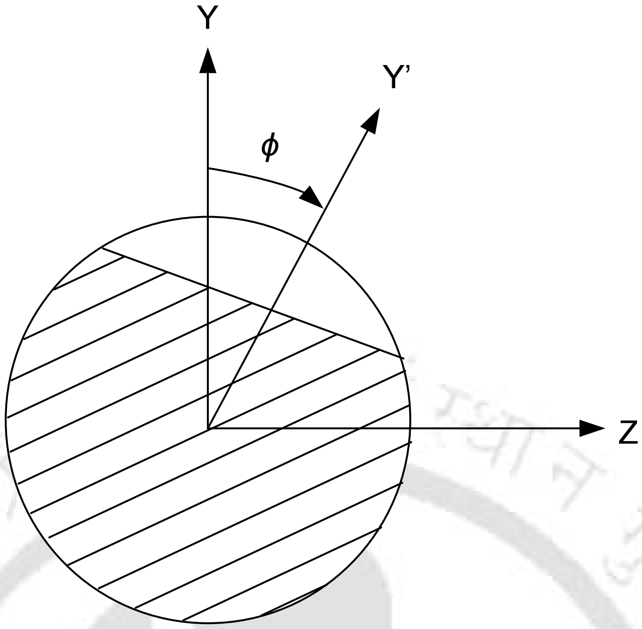

Figure 2.3: Crack orientation angle of a rotated crack.

2.2 System Equations of Motion

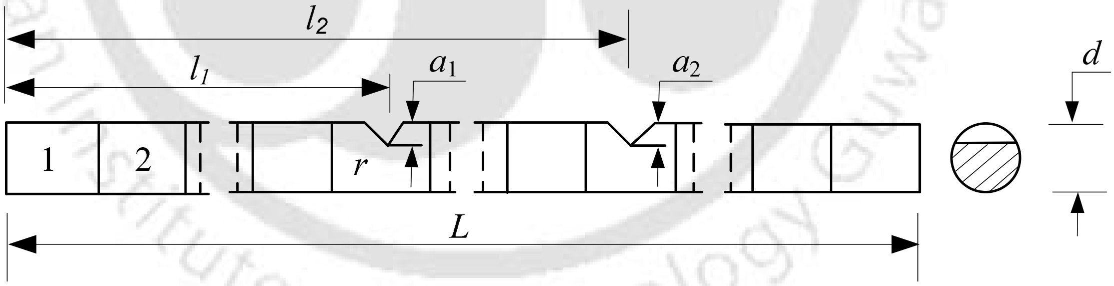

Figure 2.4: The finite element discretisation of the shaft with multiple cracks.

Figure 2.4 shows the finite element discretization of the shaft with multiple cracks. The equation of motion for the shaft element with and without crack (intact), respectively, can be written as

$$[M]^{(e)}\{\ddot{q}(t)\}^{(e)}+[D_c]^{(e)}\{\dot{q}(t)\}^{(e)}+[K_c]^{(e)}\{q(t)\}^{(e)}=\{f(t)\}^{(e)}, \tag{2.2}$$

and

$$[M]^{(e)}\{\ddot{q}(t)\}^{(e)}+[D_{wc}]^{(e)}\{\dot{q}(t)\}^{(e)}+[K_{wc}]^{(e)}\{q(t)\}^{(e)}=\{f(t)\}^{(e)}, \tag{2.3}$$

where subscripts, c and wc, are used to represent the cracked and intact shaft elements, respectively. Matrices $[M]^{(e)}$, $[D]^{(e)}$, and $[K]^{(e)}$, are the elemental mass, damping and stiffness matrices, respectively; and vectors $\{f(t)\}^{(e)}$ and $\{q(t)\}^{(e)}$ are the elemental force and response vectors, respectively. The damping is assumed to be proportional damping. Damping matrices for the uncracked element and the cracked element can be expressed as follows,

$$[D_{wc}]^{(e)}=a_0[M]^{(e)}+a_1[K_{wc}]^{(e)}, \tag{2.4}$$

and

$$[D_c]^{(e)}=a_0[M]^{(e)}+a_1[K_c]^{(e)} \tag{2.5}$$

Where a_0 and a_1 are the Rayleigh damping factors (expressions for a_0 and a_1 are given in Appendix B). $[K_c]^{(e)}$ is the stiffness matrix of the beam element with crack, and it is given as

$$[K_c]^{(e)}=[T][C]^{-1}[T]^{\mathrm{T}} \tag{2.6}$$

with

$$[C]=[C_o]+[C_c] \tag{2.7}$$

and

$$[C_o]=\begin{bmatrix} l^3/3EI+SF & 0 & 0 & l^2/2EI \\ 0 & l^3/3EI+SF & -l^2/2EI & 0 \\ 0 & l^2/2EI & l/EI & 0 \\ l^2/2EI & 0 & 0 & l/EI \end{bmatrix} \tag{2.8}$$

$$\text{Here} \quad SF = l/(k_{sc}AG); \quad \text{with} \tag{2.9}$$

$$k_{sc} = 6(1+\nu)/(7+6\nu); \; A = (\pi D^2)/4; \quad \text{and} \quad G = 0.5E/(1+\nu); \tag{2.10}$$

Here $[C_o]$ is the flexibility matrix of the beam element without crack, $[C_c]$ is the additional flexibility of the cracked beam element due to crack, and it is defined in Eq. (2.1). $[C]$ is the total flexibility matrix of the beam element with crack, $[D_c]^{(e)}$ is the damping matrix of the beam element with crack, *EI* is the flexural rigidity of the beam, *l* is the element length, and ν is the Poisson's ratio. $[T]$ is the transformation matrix, and it can be expressed as (Darpe et. al., 2004)

$$[T]^{\mathrm{T}} = \begin{bmatrix} -1 & 0 & 0 & -l & 1 & 0 & 0 & 0 \\ 0 & -1 & l & 0 & 0 & 1 & 0 & 0 \\ 0 & 0 & -1 & 0 & 0 & 0 & 1 & 0 \\ 0 & 0 & 0 & -1 & 0 & 0 & 0 & 1 \end{bmatrix} \tag{2.11}$$

Damping matrices are different for the cracked and intact element because they are proportional to stiffness matrices also and the stiffness matrices are different for cracked beam element and uncracked beam element. The elemental mass matrix of the cracked element is assumed to be same as that of the intact element. For a harmonic transverse excitation $\{f(t)\} = \{F\}e^{\mathrm{j}\omega t}$, the shaft response vector is expressed as $\{q(t)\} = \{Q\}e^{\mathrm{j}\omega t}$; and system equations on assembly of elemental equations and after the application of boundary conditions reduce to

$$\left(-\omega^2[M]+j\omega[D]+[K]\right)\{Q\}=\{F\}. \tag{2.12}$$

Eq. (2.12) can be used to get the forced response of the intact and cracked shaft systems.

2.3 Response of a Shaft System

For numerical simulations, a steel shaft of 0.01m diameter and 1 m span is considered with simply supported boundary conditions. External harmonic excitation to the shaft is assumed to be in vertical direction (i.e. along Y-axis in Figure 2.3). System parameters for numerical experiments are summarized in Table 2-1.

Table 2-1: System parameters for numerical simulations.

Parameters	Values for Figure 2.6	Values for Figure **2.7**
Number of finite elements	80	80
Location of the first cracked element	21	21
Location of the second cracked element	35	35
Depth of first crack	0.0030 m	0.0030 m
Depth of second crack	0.0035 m	0.0035 m
Crack orientation angle (in deg)	0	0
Excitation frequencies, ω_i (in rad/s)	110	430

Variation of the shaft response amplitude with excitation frequency is given in Figure 2.5. From standard eigen value analysis the first two natural frequencies of the intact shaft are found to be 126.78 rad/sec and 506.93 rad/sec.

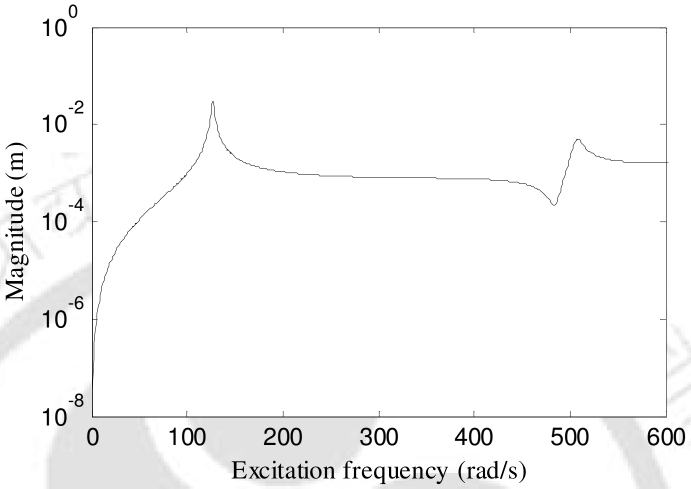

Figure 2.5: Variation of shaft displacement amplitude with excitation frequency.

Shaft deflections in the vertical and horizontal directions at various axial positions for a harmonic excitation of frequency 110 rad/s (i.e., below and near the first natural frequency) is given in Figure 2.6. From Figure 2.6 (a), the intact shaft deflection is different than the cracked shaft deflection in the vertical direction. The vertical and horizontal plane motions are independent for the intact shaft, hence the intact shaft response in horizontal direction is zero (Figure 2.6 (b)). For the cracked shaft, the vertical and horizontal plane motions are coupled so an excitation in vertical direction results in shaft displacements in horizontal plane also. Shaft deflections for a harmonic excitation of frequency of 430 rad/s are given in Figure 2.7. The excitation frequency is below the second natural frequency.

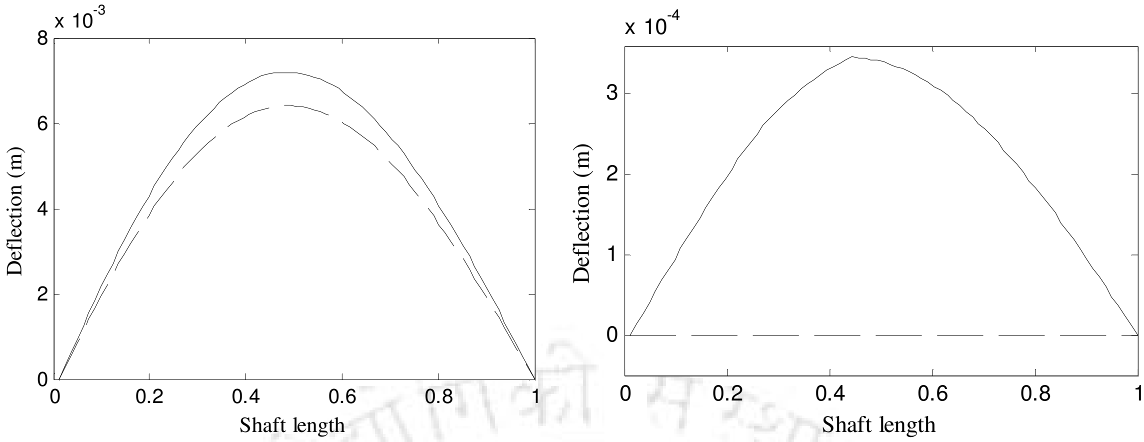

(a) Vertical response of the shaft

(cracked shaft —; intact shaft - -)

(b) Horizontal response of the shaft

(cracked shaft —; intact shaft - -)

Figure 2.6: Shaft response amplitudes at 110 rad/s.

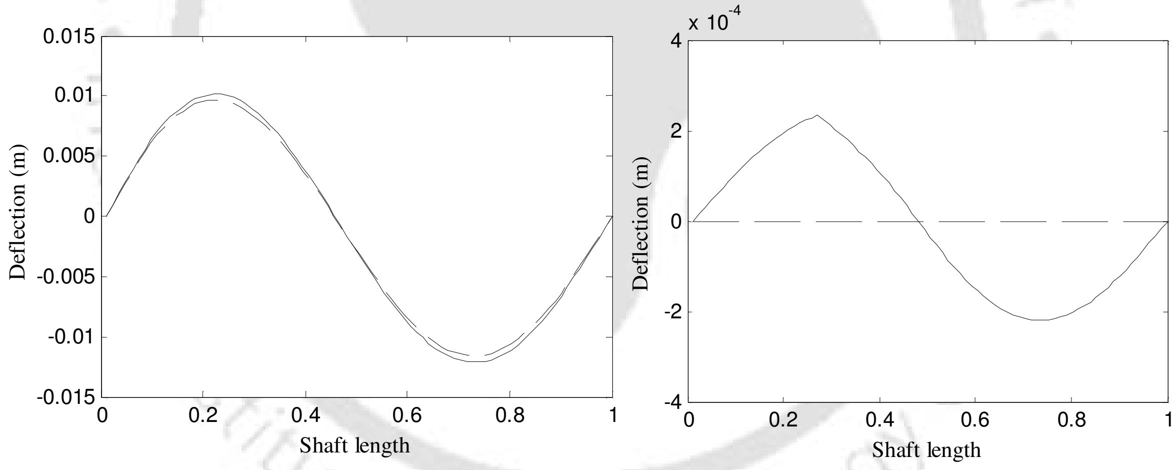

(a) Vertical response of the shaft

(cracked shaft —; intact shaft - -)

(b) Horizontal response of the shaft

(cracked shaft —; intact shaft - -)

Figure 2.7: Shaft response amplitudes at 430 rad/s.

Development of the MCDLA and its numerical simulations are presented in the following chapter. The algorithm gives the number of cracks present in a shaft and the approximate locations of the cracks along the shaft length.

3 DETECTION AND LOCALIZATION OF CRACKS

3.1 Introduction

The presence of a crack in the shaft causes a slope discontinuity in the elastic line of the shaft when vibrating due to a harmonic force. This slope discontinuity is not easy to identify especially in the presence of measurement noise. However, once the slope discontinuity is identified, it could be used to identify both the number of cracks and its location. In the present chapter, the MCDLA has been developed. In the algorithm, effect of noise in the signal has been averaged by utilizing the response of the shaft at several frequencies. This also ensures participation of various modes of vibrations in the identification algorithm. To find out the discontinuity in the slope of the vibrating shaft, measured forced responses are fitted with a second degree polynomial. Estimated coefficients of polynomials of the cracked shaft are normalized by the corresponding polynomial coefficients obtained for the intact shaft. The detailed development of the algorithm is presented in following section.

3.2 The MCDLA

For a shaft system, let the number of equidistant locations at which linear DOFs are known (obtained from the measurements and boundary conditions both), be n, and the number of frequencies at which the system is excited be k. Let us denote the measured deflection of the cracked shaft at frequency, ω_i, and at location, x_j, by $q_{cv_{i,j}}$ in the vertical plane, and similarly $q_{ch_{i,j}}$ in the horizontal plane (the first place of the subscript *c* represents the crack, the second place subscript *v* (or *h*) represents the vertical (or horizontal), the first place subsubscript *i* corresponds the frequency and the second place subsubscript corresponds the axial location of the shaft). It should be noted that the horizontal plane motion takes place due to cross-coupled crack flexibility coefficients. In actual tests, shaft deflections can be measured with displacement sensors. Also let the deflection predicted by the FE model of the intact shaft is $q_{wcv_{i,j}}$ in the vertical plane (here the subscript *wc* represents the without crack or the intact shaft). There is no response in the horizontal plane for the vertical forcing of the intact shaft. Deflections at three consecutive axial positions are selected to find out coefficients of the quadratic polynomial between them. Let a response, q, be expressed as a quadratic polynomial of the form

$$q = ax^2 + bx + c, \tag{3.1}$$

where a, b and c are coefficients of the quadratic polynomial. Coefficients of the quadratic polynomial from cracked shaft deflections could be found at frequency, ω_i, as

$$q_{cv_{i,j-1}} = a_{cv_{i,j}} x_{j-1}^2 + b_{cv_{i,j}} x_{j-1} + c_{cv_{i,j}}, \tag{3.2}$$

$$q_{cv_{i,j}} = a_{cv_{i,j}} x_j^2 + b_{cv_{i,j}} x_j + c_{cv_{i,j}}, \tag{3.3}$$

and

$$q_{cv_{i,j+1}} = a_{cv_{i,j}} x_{j+1}^2 + b_{cv_{i,j}} x_{j+1} + c_{cv_{i,j}}. \tag{3.4}$$

Here, $q_{cv_{i,j-1}}$, $q_{cv_{i,j}}$, and $q_{cv_{i,j+1}}$ are deflections at frequency, ω_i, in the vertical direction at measurement locations, x_{j-1}, x_j, and, x_{j+1}, respectively. In matrix notations, Eqns. (3.2)-(3.4) could be written as

$$\begin{Bmatrix} a_{cv_{i,j}} \\ b_{cv_{i,j}} \\ c_{cv_{i,j}} \end{Bmatrix} = \begin{bmatrix} x_{j-1}^2 & x_{j-1} & 1 \\ x_j^2 & x_j & 1 \\ x_{j+1}^2 & x_{j+1} & 1 \end{bmatrix}^{-1} \begin{Bmatrix} q_{cv_{i,j-1}} \\ q_{cv_{i,j}} \\ q_{cv_{i,j+1}} \end{Bmatrix}, \quad \text{for} \quad i = 1, \ldots, k; \quad j = 2, \ldots, (n-1). \tag{3.5}$$

In the similar way, coefficients, $a_{ch_{i,j}}$, $b_{ch_{i,j}}$, and $c_{ch_{i,j}}$ corresponding to cracked shaft deflections in the horizontal direction, $q_{ch_{i,j-1}}$, $q_{ch_{i,j}}$, and $q_{ch_{i,j+1}}$ could be written as

$$\begin{Bmatrix} a_{ch_{i,j}} \\ b_{ch_{i,j}} \\ c_{ch_{i,j}} \end{Bmatrix} = \begin{bmatrix} x_{j-1}^2 & x_{j-1} & 1 \\ x_j^2 & x_j & 1 \\ x_{j+1}^2 & x_{j+1} & 1 \end{bmatrix}^{-1} \begin{Bmatrix} q_{ch_{i,j-1}} \\ q_{ch_{i,j}} \\ q_{ch_{i,j+1}} \end{Bmatrix}, \text{ for } \quad i = 1, \ldots, k; \quad j = 2, \ldots, (n-1). \tag{3.6}$$

Similarly, polynomial coefficients $a_{wcv_{i,j}}$, $b_{wcv_{i,j}}$, $c_{wcv_{i,j}}$ corresponding to the vertical deflections for the intact shaft could be written as

$$\begin{Bmatrix} a_{wcv_{i,j}} \\ b_{wcv_{i,j}} \\ c_{wc_{i,j}} \end{Bmatrix} = \begin{bmatrix} x_{j-1}^2 & x_{j-1} & 1 \\ x_j^2 & x_j & 1 \\ x_{j+1}^2 & x_{j+1} & 1 \end{bmatrix}^{-1} \begin{Bmatrix} q_{wc_{i,j-1}} \\ q_{wcv_{i,j}} \\ q_{wc_{i,j+1}} \end{Bmatrix}, \text{ for } \quad i = 1, \ldots, k; \quad j = 2, \ldots, (n-1). \tag{3.7}$$

Polynomial coefficients corresponding to the quadratic term, a, in the polynomial are used in the algorithm to get the slope discontinuity. Here, the curvature of the shaft is proportional to the coefficient of the quadratic term in the polynomial, as

$$\frac{\mathrm{d}^2 q}{\mathrm{d}\, x^2} = 2a \tag{3.8}$$

Pandey et al. (1991) used *curvature mode shape* as an indicator of presence of cracks in beams. They derived the curvature mode shape using the central difference approximation and did not consider the effect of measurement noise. However, in the present work, forced vibration is used. The shaft curvature obtained from the quadratic polynomial has the advantage that the two segments of the shaft formed from the three consecutive measurement locations need not be of equal length. This flexibility allows the condition monitoring system to avoid a few inaccessible measurement locations on the shaft. The change in shaft curvature is localized and it can be used as an indicator of presence of cracks in shaft if the shaft response signal is free from any noise. Also in actual measurements, there will always be noise in the signal. The MCDLA uses shaft responses at several frequencies to amplify the discontinuity in the shaft curvature and hence reducing the effect of noise in the signal.

In the algorithm, polynomial coefficients obtained from the cracked shaft responses are normalized by dividing it with polynomial coefficients obtained from the intact shaft responses. In the denominator during the normalization of the cracked shaft polynomials, very low values of polynomial coefficients of the intact shaft at some of the measurement locations may lead to a singularity. Hence, to avoid this, polynomial coefficients needed to be shifted by adding suitable term to them. Hence, let p_{a_i} be defined at each frequency, ω_i, as the difference of the maximum and minimum values of the coefficient, $a_{wcv_{i,j}}$, at all measurement locations from $j=2$ to $j=n-1$, as

$$p_{a_i} = \frac{\max(a_{wcv_{i,2}},\ldots,a_{wcv_{i,n}}) - \min(a_{wcv_{i,2}},\ldots,a_{wcv_{i,n}})}{k_a}, \quad \text{for} \quad i=1,\ldots,k; \qquad (3.9)$$

where k_a is a constant, and the choice of it depends upon the noise in the signal and the number of excitation frequencies. It is needed to avoid singularity during the subsequent normalization step (Eqn. (3.12)). Here p_{a_i} is also defined in terms of the shaft response. Hence, it will have different values at different excitation frequencies. A single term at all frequencies is not sufficient for the shift of p_{a_i} because the relative magnitude of coefficients at different excitation frequencies will be of different order. Shift these coefficients, $a_{wcv_{i,j}}$ and $a_{cv_{i,j}}$, at all the measurement locations for a given frequency such that its minimum value is p_{a_i}. Hence, define $a^{\mathrm{I}}_{wcv_{i,j}}$ and, $a^{\mathrm{I}}_{cv_{i,j}}$ by

$$a^{\mathrm{I}}_{wcv_{i,j}} = a_{wcv_{i,j}} - \min(a_{wcv_{i,2}}, \ldots, a_{wcv_{i,n}}) + p_{a_i}, \quad \text{for} \quad i = 1, \ldots, k; \quad j = 2, \ldots, (n-1) \tag{3.10}$$

and

$$a^{\mathrm{I}}_{cv_{i,j}} = a_{cv_{i,j}} - \min(a_{cv_{i,2}}, \ldots, a_{cv_{i,n}}) + p_{a_i}, \quad \text{for} \quad i = 1, \ldots, k; \quad j = 2, \ldots, (n-1). \tag{3.11}$$

Polynomial coefficients obtained from the measured cracked shaft responses are now ready to be normalized, so as to make it ready to be added with the normalized coefficients obtained at other excitation frequencies. This normalization will make the relative magnitude of the co-efficients at different frequencies to be of same order while keeping the curvature discontinuity information at crack locations. This step is explained in more detail in the numerical simulation. For this purpose, divide polynomial coefficients, $a^{\mathrm{I}}_{cv_{i,j}}$ of the cracked shaft by corresponding polynomial coefficients, $a^{\mathrm{I}}_{wcv_{i,j}}$ of the intact shaft obtained from the shaft deflection in the vertical direction. Hence, define $a^{\mathrm{II}}_{v_{i,j}}$ by,

$$a^{\mathrm{II}}_{v_{i,j}} = \frac{a^{\mathrm{I}}_{cv_{i,j}}}{a^{\mathrm{I}}_{wcv_{i,j}}}, \quad \text{for} \quad i = 1, \ldots, k; \quad j = 2, \ldots, (n-1). \tag{3.12}$$

Since there is no response in the horizontal direction due to the vertical forcing of the intact shaft, hence, corresponding polynomial coefficients are not defined. Hence, polynomial coefficients obtained from the cracked shaft response in the horizontal direction are normalized in different way. They are normalized by dividing the individual coefficients by their mean (i.e.

the mean of deflections at all locations). Again, this will make the relative magnitude of the coefficients at different frequencies of same order. Hence, define $a^{\mathrm{II}}_{h_{i,j}}$ by,

$$a^{\mathrm{II}}_{h_{i,j}} = \frac{a_{ch_{i,j}}}{\mathrm{mean}\left(a_{ch_{i,2}},\ldots,a_{ch_{i,n}}\right)}, \qquad \text{for} \quad i=1,\ldots,k; \quad j=2,\ldots,(n-1). \tag{3.13}$$

Coefficients $a^{\mathrm{II}}_{v_{i,j}}$ and $a^{\mathrm{II}}_{h_{i,j}}$ are defined at different measurement locations of the shaft and at various excitation frequencies. Now for each measurement location, modified coefficients $a^{\mathrm{II}}_{v_{i,j}}$ and $a^{\mathrm{II}}_{h_{i,j}}$, at different excitation frequencies, ω_i, are added to get respective new coefficients $a^{\mathrm{III}}_{v_j}$ and $a^{\mathrm{III}}_{h_j}$ as,

$$a^{\mathrm{III}}_{v_j} = a^{\mathrm{II}}_{v_{1,j}} + a^{\mathrm{II}}_{v_{2,j}} + \ldots. + a^{\mathrm{II}}_{v_{k,j}}, \qquad \text{for } j=2,\ldots,(n-1) \tag{3.14}$$

and

$$a^{\mathrm{III}}_{h_j} = a^{\mathrm{II}}_{h_{1,j}} + a^{\mathrm{II}}_{h_{2,j}} + \ldots. + a^{\mathrm{II}}_{h_{k,j}}, \qquad \text{for } j=2,\ldots,(n-1). \tag{3.15}$$

These coefficients give a measure of change in the vibration response with respect to excitation frequency at a particular location of the shaft. By adding them for various frequencies at a particular location gives a measure of change in the response at various mode of excitations. As we know for different mode of vibrations the same point may have entirely different response trend. The magnitude of the above coefficients will depend upon the number of excitation frequencies and its range. To make the magnitude of coefficients independent of number of excitation frequencies, scale them down to vary between 0 and 1. For this purpose, let us define $a^{\mathrm{IV}}_{v_j}$ and $a^{\mathrm{IV}}_{h_j}$ by,

$$a_{v_j}^{\mathrm{IV}} = \mathrm{abs}\left\{ \frac{a_{v_j}^{\mathrm{III}} - \min\left(a_{v_2}^{\mathrm{III}}, a_{v_3}^{\mathrm{III}}, \ldots, a_{v_n}^{\mathrm{III}}\right)}{\max\left(a_{v_2}^{\mathrm{III}}, a_{v_3}^{\mathrm{III}}, \ldots, a_{v_n}^{\mathrm{III}}\right) - \min\left(a_{v_2}^{\mathrm{III}}, a_{v_3}^{\mathrm{III}}, \ldots, a_{v_n}^{\mathrm{III}}\right)} \right\}, \quad \text{for } j = 2, \ldots, (n-1), \tag{3.16}$$

and

$$a_{h_j}^{\mathrm{IV}} = \mathrm{abs}\left\{ \frac{a_{h_j}^{\mathrm{III}} - \min\left(a_{h_2}^{\mathrm{III}}, a_{h_3}^{\mathrm{III}}, \ldots, a_{h_n}^{\mathrm{III}}\right)}{\max\left(a_{h_2}^{\mathrm{III}}, a_{h_3}^{\mathrm{III}}, \ldots, a_{h_n}^{\mathrm{III}}\right) - \min\left(a_{h_2}^{\mathrm{III}}, a_{h_3}^{\mathrm{III}}, \ldots, a_{h_n}^{\mathrm{III}}\right)} \right\}, \quad \text{for } j = 2, \ldots, (n-1). \tag{3.17}$$

Expressions in Eqns. (3.16) - (3.17) are basically for quantification of the discontinuity in the coefficients. Now the jump in values of coefficients, $a_{v_j}^{\mathrm{IV}}$ and $a_{h_j}^{\mathrm{IV}}$, at the crack location may appear above or below of their mean value, hence we define, *crack probability functions,* CPF_{v_j} and CPF_{h_j}, as the absolute distance of coefficients $a_{v_j}^{\mathrm{IV}}$ and $a_{h_j}^{\mathrm{IV}}$ from their mean as,

$$CPF_{v_j} = \mathrm{abs}\left\{ a_{v_j}^{\mathrm{IV}} - \mathrm{mean}\left(a_{v_2}^{\mathrm{IV}}, a_{v_3}^{\mathrm{IV}}, \ldots, a_{v_n}^{\mathrm{IV}}\right) \right\}, \quad \text{for } j = 2, \ldots, (n-1), \tag{3.18}$$

and

$$CPF_{h_j} = \mathrm{abs}\left\{ a_{h_j}^{\mathrm{IV}} - \mathrm{mean}\left(a_{h_2}^{\mathrm{IV}}, a_{h_3}^{\mathrm{IV}}, \ldots, a_{h_n}^{\mathrm{IV}}\right) \right\}, \quad \text{for } j = 2, \ldots, (n-1). \tag{3.19}$$

Here, crack probability functions CPFs, at location, x_j, give the probability of presence of a crack between locations x_{j-1} and x_{j+1}. A high value of CPF at a location x_j indicates a high probability of the presence of crack near that location. It should be noted that the present algorithm relies on forced response measurements for which literatures are not in abundance as against modal parameters (e.g., natural frequencies and mode shapes, etc.) for which very rich literature is available.

Illustration of the MCDLA, using the simulated cracked shaft response obtained from Eq. (2.12), is presented in the next section.

3.3 Numerical Experiments of the MCDLA

The MCDLA is numerically tested for a simply supported shaft. Any other boundary conditions could be incorporated without much difficulty since the FEM is used in modeling of the system. Figure 3.1 shows locations of measurements over a simply supported shaft. For experiments over real shafts, the shaft vibrations in the vertical as well as in the horizontal direction can be measured using displacement sensors. However for numerical experiments presented in this section, response of the simply supported shaft is obtained by Eqn. (2.12). The external forcing is assumed to be in the vertical direction only. In these measurements 1% noise is added to mimic the actual measurement noise. The algorithm uses the intact shaft response also, which is generated by Eqn. (2.12). But noise is not added in intact shaft responses since the intact shaft response, in the algorithm, comes anyway from mathematical modeling of the shaft system.

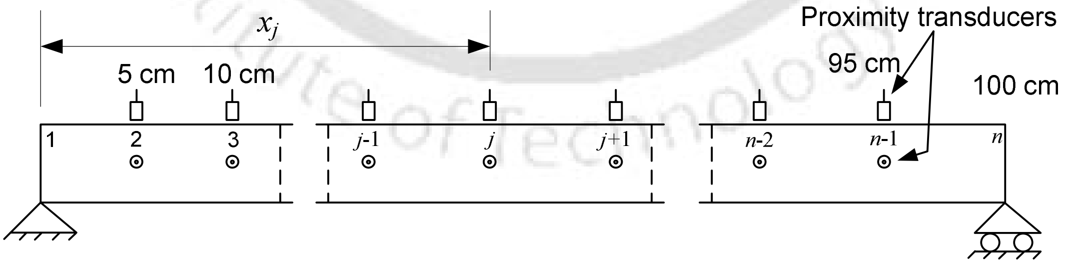

Figure 3.1: Measurement locations along the shaft.

A steel shaft of 0.01m diameter and 1 m span is considered. For the response generation by using FEM, the shaft is divided into 80 elements. However, shaft deflections at 19 equidistant points are considered as measured data. System parameters for numerical experiments are summarized in Table 3-1 and Table 3-2. First two natural frequencies of the intact shaft are 126.78 rad/s and 506.93 rad/s.

Table 3-1: Parameters for the numerical simulations of the MCDLA.

Parameters	Values for Simulation-I	Values for Simulation-II
Shaft length (m)	1	1
Shaft diameter (m)	0.01	0.01
Number of finite elements	80	80
Number of sensor locations	19 (= n-2)	19
Measurement noise	1 %	1 %
Excitation frequencies, ω_i (in rad/s)	5, 10, …, 110	360, 365, …, 430

Table 3-2: Crack parameters for the numerical simulations of the MCDLA.

Parameters	Values for Simulation-I	Values for Simulation-II
Location of the first cracked element	21	21
Location of the second cracked element	35	51
Depth of first crack (m)	0.0030	0.0030
Depth of second crack (m)	0.0035	0.0035
Crack orientation angle of the first crack (deg)	0	0
Crack orientation angle of the second crack (deg)	0	0

With 80 finite elements and 19 equidistant measurement locations, number of finite elements between two consecutive measurement locations is four. Thus the measurement locations are at 5th, 9th, 13th, ..., 77th nodes of the FE model. Also, in the present crack model, the location of crack is assumed to be in the middle of the finite element. Hence, the distance of a particular crack from the neighboring measurement locations can be obtained if location of the cracked element is known. In Table 3-2, the closest distance of all four cracks from its neighboring measurement locations is half of the length of a finite element, i.e. 0.00625m.

3.3.1 Simulation-I

Two cracks are introduced in the shaft. Cracked shaft parameters are given in Table 3-1 and Table 3-2. Responses of the intact shaft and the cracked shaft for a forcing of $0.0024 r\omega_i^2 \cos(\omega_i t)$ are obtained from Eqn. (2.12). Here 0.0024 is the product of m (the unbalance mass) and r (the radial distance of the centre of the shaft to the unbalance mass m). The forcing represents a sinusoidal forcing of frequency ω_i which, in the actual case, can be given by an exciter. The cracked shaft steady-state forced response at frequency ω_i = 110 rad/s for various axial positions in the vertical and horizontal directions are plotted in Figure 3.2.

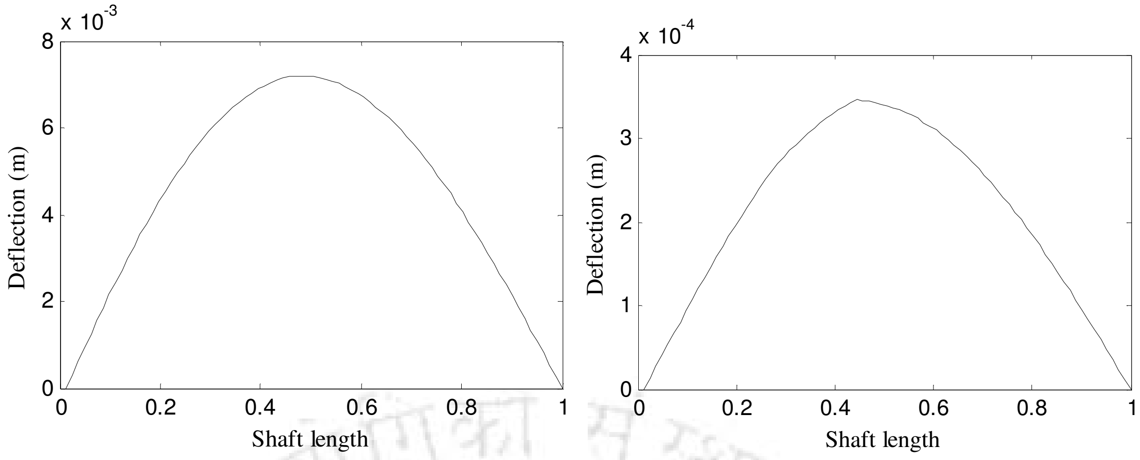

(a) Vertical response (b) Horizontal response

Figure 3.2: Cracked shaft response amplitudes at 110 rad/s.

The forced response simulated from FE modeling of the cracked shaft is treated as the measured response after adding 1% noise (Appendix D) in the response. Coefficients of the quadratic polynomial, $a_{cv_{i,j}}$, obtained from the deflection of the shaft in the vertical direction are plotted in Figure 3.3(a) while those obtained from the horizontal direction, $a_{ch_{i,j}}$, are plotted in Figure 3.3 (b).

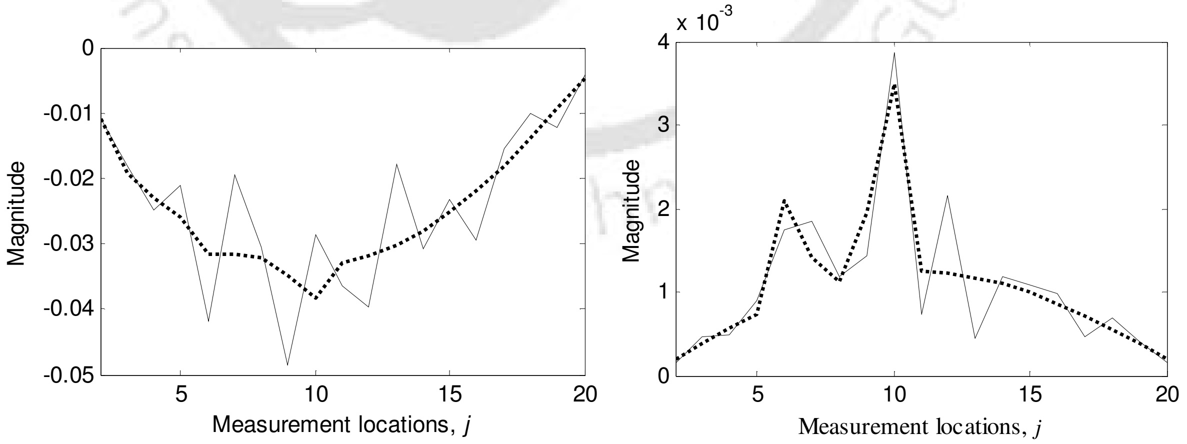

(a) $a_{cv_{i,j}}$ (with noise —; without noise - -) (b) $a_{ch_{i,j}}$ (with noise —; without noise - -)

Figure 3.3: Variation of coefficients, $a_{cv_{i,j}}$ and $a_{ch_{i,j}}$ with measurement locations.

In Figure 3.3, coefficients $a_{cv_{i,j}}$ and $a_{ch_{i,j}}$ are plotted by dotted line for the case of no noise in the signal. They have discontinuity at the location of cracks. Hence, presence of cracks is observable. But with the noise added in the signal, this information is lost because of the high sensitivity of these parameters. Polynomial coefficients $a^{\mathrm{I}}_{cv_{i,j}}$ and $a^{\mathrm{I}}_{wcv_{i,j}}$ obtained from the vertical direction response of the cracked and intact shafts, respectively, are plotted in Figure 3.4. These two coefficients are used to get the normalized coefficients $a^{\mathrm{II}}_{v_{i,j}}$ in the vertical direction.

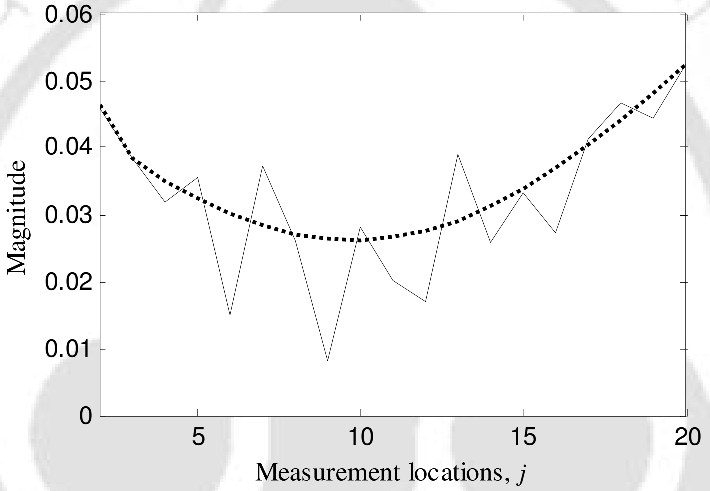

Figure 3.4: Variation of the coefficients $a^{\mathrm{I}}_{cv_{i,j}}$ —, $a^{\mathrm{I}}_{wcv_{i,j}}$ - -, with measurement locations.

Coefficients $a_{wch_{i,j}}$, from the deflection of the intact shaft in the horizontal direction, are not defined because the forcing is in the vertical direction and there is no horizontal direction response when shaft is intact and symmetric. When the shaft is cracked, there is a coupling in the vertical and horizontal direction motions, which gives motion in the horizontal direction as well for a force in the vertical direction. Now, to minimize the effect of noise in coefficients obtained from the vertical direction response, coefficients are normalized in special way as given in Eqn. (3.12). Coefficients of the cracked shaft are divided by the corresponding coefficients of the intact shaft, for the same vertical force, to obtain new coefficients $a^{\mathrm{II}}_{v_{i,j}}$. These are plotted in Figure 3.5(a).

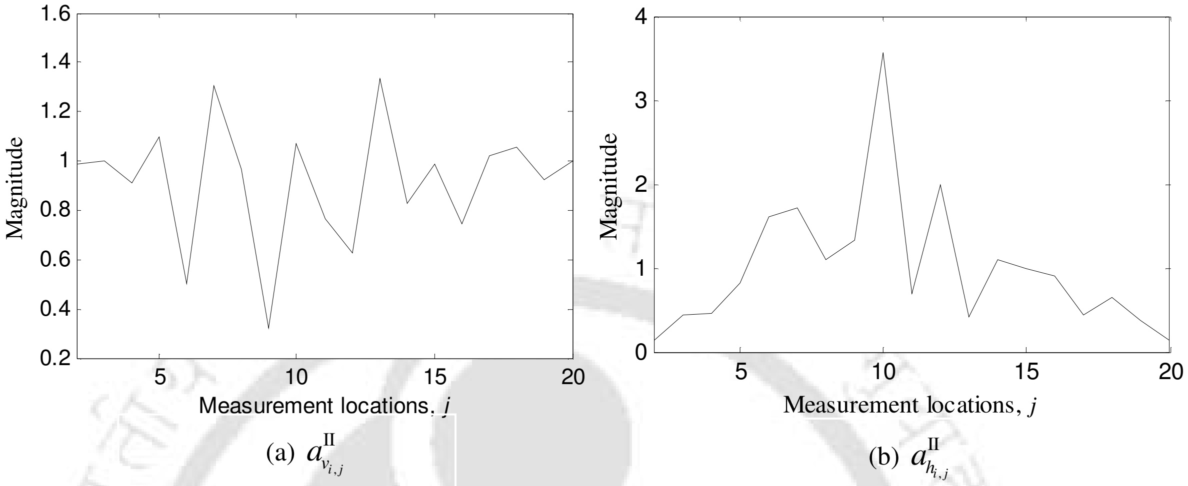

(a) $a^{\mathrm{II}}_{v_{i,j}}$ (b) $a^{\mathrm{II}}_{h_{i,j}}$

Figure 3.5: Variation of coefficients $a^{\mathrm{II}}_{v_{i,j}}$ and $a^{\mathrm{II}}_{h_{i,j}}$ with measurement locations.

In Figure 3.5 (a), we can observe that coefficients, $a^{\mathrm{II}}_{v_{i,j}}$, are now almost normalized in the sense that their mean is near one and the plot is almost flat. Now these coefficients at different frequencies are ready to be added. For the normalization of coefficients obtained from the horizontal direction response, they are divided by their mean as given in Eqn. (3.13). Here we need different type of normalization because firstly, we don't have intact shaft coefficients (they are not defined) and secondly, the slope discontinuity is more here. It can be observed from Figure 3.3. The new coefficients, $a^{\mathrm{II}}_{h_{i,j}}$, are plotted in Figure 3.5 (b).

After normalizing all the coefficients, add the corresponding coefficients $a^{\mathrm{II}}_{v_{i,j}}$ and $a^{\mathrm{II}}_{h_{i,j}}$ at all the frequencies to get the new coefficients $a^{\mathrm{III}}_{v_j}$ and $a^{\mathrm{III}}_{h_j}$. Hence, now the index, i, used for the frequency, is eliminated from these new coefficients. These are defined in Eqns.(3.14) - (3.15). The resulting coefficients are plotted in Figure 3.6.

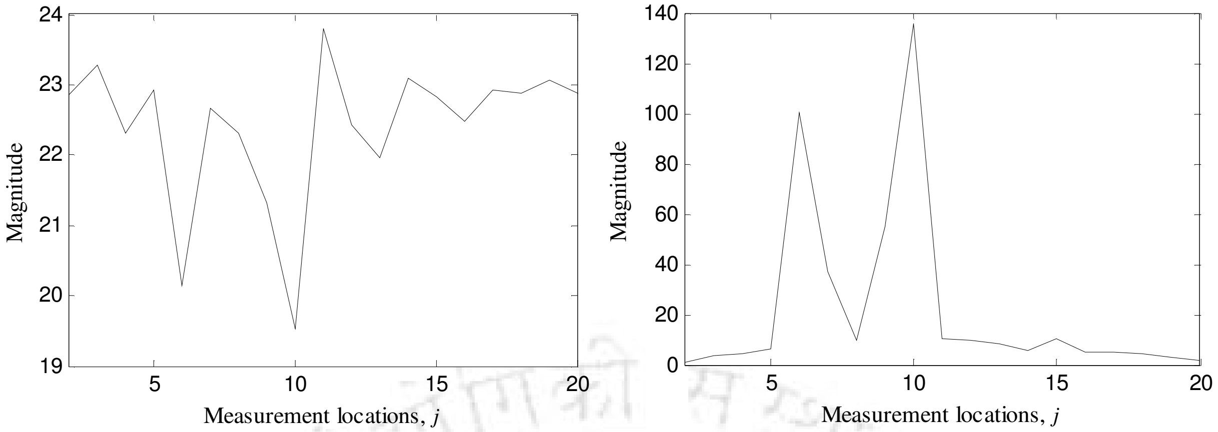

(a) $a_{v_j}^{\text{III}}$ (b) $a_{h_j}^{\text{III}}$

Figure 3.6: Variation of coefficients $a_{v_j}^{\text{III}}$ and $a_{h_j}^{\text{III}}$ along the measurement locations.

Now presence of cracks in the shaft is evident from Figure 3.6 in a sense that peaks are appearing (inverted or upright) at crack locations. But, the algorithm may use different number of excitation frequencies and also the peaks due to cracks may appear above the mean or below the mean, depending upon the mode of vibration. So, for cracks to be identifiable through more logical way; first compress these coefficients to vary between zero and one, and then find out the distance of resulting individual coefficients from their mean at all measurement locations. These two steps are performed in Eqns. (3.16)-(3.19). Resulting *crack probability functions* obtained are plotted in Figure 3.7.

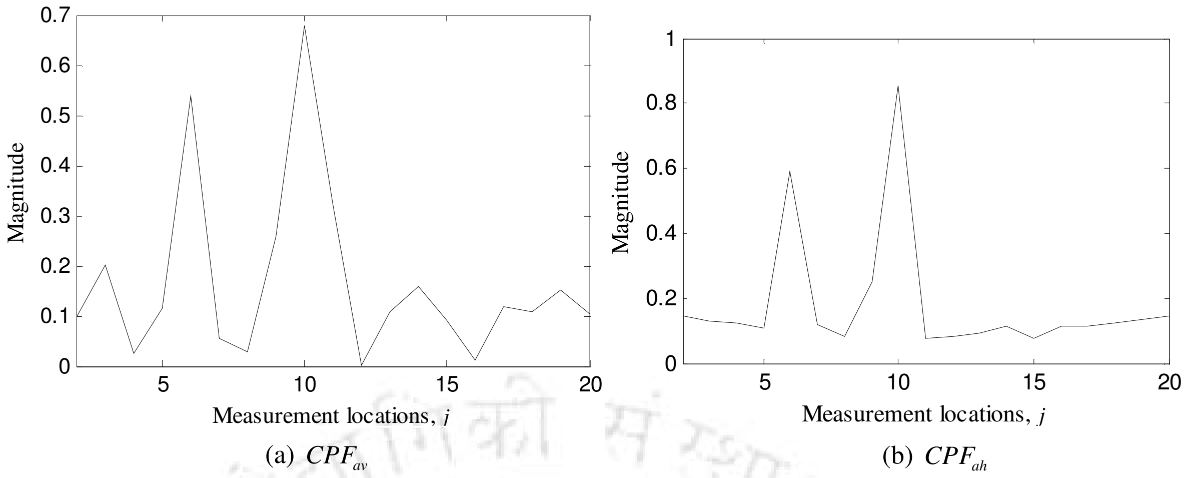

(a) CPF_{av} (b) CPF_{ah}

Figure 3.7 Crack probability functions for Simulation-I.

Crack probability functions have relatively high values at measurement locations those are near to the cracked element, e.g. at measurement locations x_6 and x_{10}. Hence, it indicates presence of two cracks in the shaft, one between locations x_5 and x_7, while the other between locations x_9 and x_{11}.

3.3.2 Simulation-II

The identification algorithm is sensitive to excitation frequencies that are to be considered. For simulation example I (see Table 3-1), excitation frequencies are chosen in such a way that the first mode will dominate in the shaft response and hence it will give more amplification to those peaks in CPFs, which are caused by cracks near middle of the beam. In simulation example II, excitation frequencies are chosen in such a way that the beam vibration is dominated by the second mode, so that it will amplify more peaks caused by cracks near 1/4th of the shaft length from both ends of the shaft. The cracked shaft steady-state forced response at frequency ω_i = 430 rad/s for various axial positions in the vertical and horizontal directions are plotted in Figure 3.8.

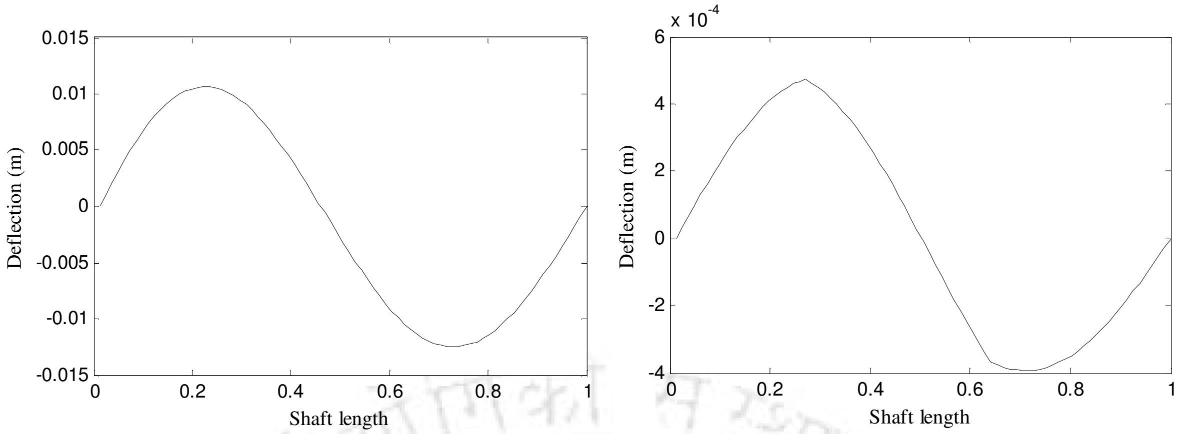

(a) Vertical response

(b) Horizontal response

Figure 3.8: Cracked shaft response amplitudes at 430 rad/s.

Coefficients of the quadratic polynomial, $a_{cv_{i,j}}$, obtained from the deflection of the shaft in the vertical direction are plotted in Figure 3.9(a) while those obtained from the horizontal direction, $a_{ch_{i,j}}$, are plotted in Figure 3.9(b). As was the case with Simulation-I the crack information contained in coefficients $a_{cv_{i,j}}$ is lost. However, the crack information contained in coefficients $a_{ch_{i,j}}$ is retained.

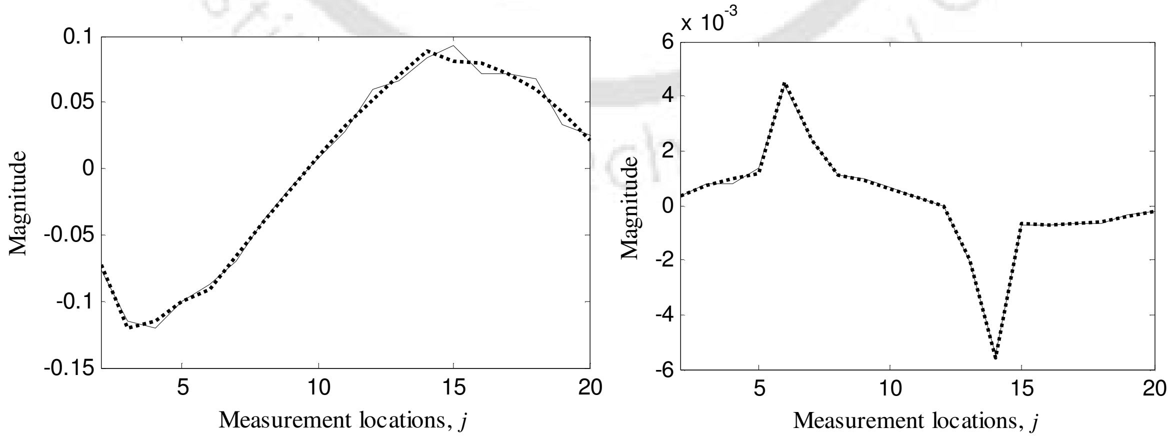

(a) $a_{cv_{i,j}}$ (with noise —; without noise -

(b) $a_{ch_{i,j}}$ (with noise —; without noise - -)

Figure 3.9: Variation of coefficients, $a_{cv_{i,j}}$ and $a_{ch_{i,j}}$ with measurement location.

Polynomial coefficients $a^{\mathrm{I}}_{cv_{i,j}}$ and $a^{\mathrm{I}}_{wcv_{i,j}}$ obtained from the vertical direction response of the cracked and intact shafts, respectively, are plotted in Figure 3.10. These two coefficients are used to get normalized coefficients $a^{\mathrm{II}}_{v_{i,j}}$ in the vertical direction.

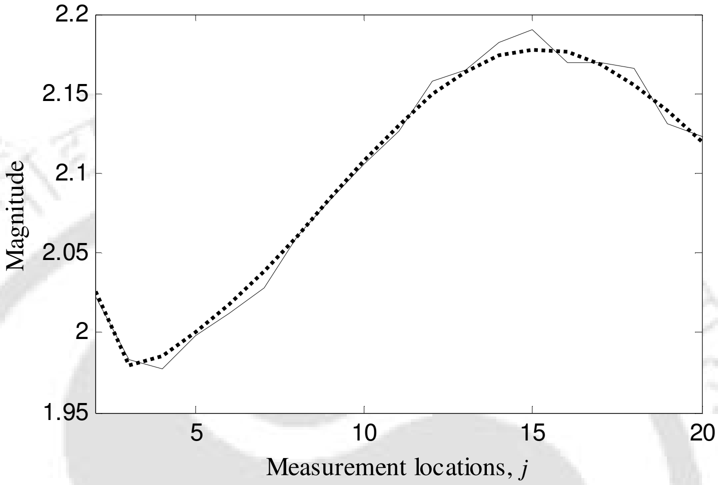

Figure 3.10: Variation of the coefficients $a^{\mathrm{I}}_{cv_{i,j}}$ —, $a^{\mathrm{I}}_{wcv_{i,j}}$ - -, with measurement location.

The normalized coefficients $a^{\mathrm{II}}_{v_{i,j}}$, are then obtained by dividing coefficients of the cracked shaft $a^{\mathrm{I}}_{cv_{i,j}}$, by corresponding coefficients of the intact shaft $a^{\mathrm{I}}_{wcv_{i,j}}$, for the same vertical force, (Eqn. (3.12)). These are plotted in Figure 3.11 (a). For getting coefficients $a^{\mathrm{II}}_{h_{i,j}}$, coefficients $a_{ch_{i,j}}$ are divided by their mean (Eqn. (3.13)). They are plotted in Figure 3.11(b).

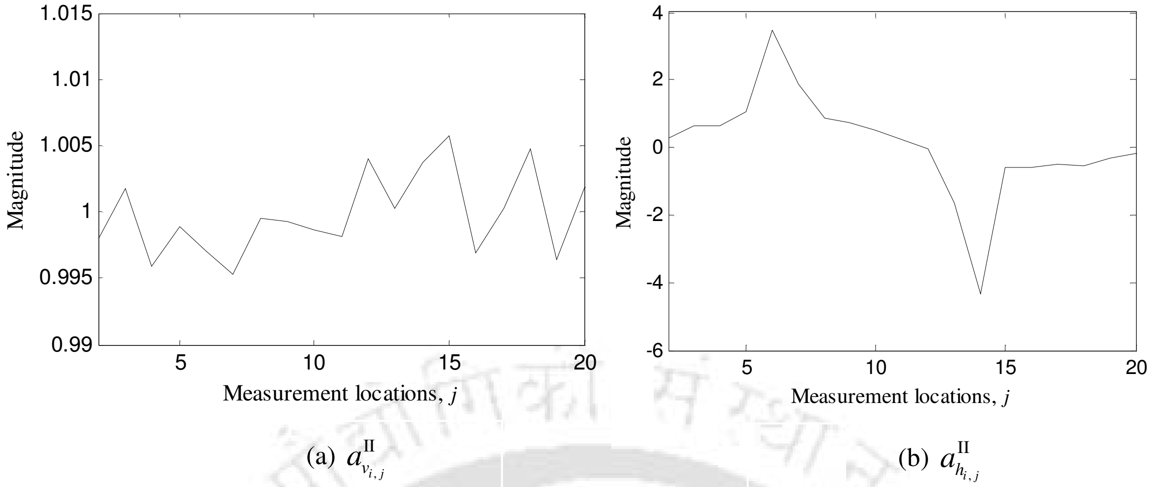

(a) $a_{v_{i,j}}^{\mathrm{II}}$ (b) $a_{h_{i,j}}^{\mathrm{II}}$

Figure 3.11: Variation of coefficients $a_{v_{i,j}}^{\mathrm{II}}$ and $a_{h_{i,j}}^{\mathrm{II}}$ with measurement location.

The new coefficients, $a_{v_j}^{\mathrm{III}}$ and $a_{h_j}^{\mathrm{III}}$, are obtained by adding corresponding coefficients $a_{v_{i,j}}^{\mathrm{II}}$ and $a_{h_{i,j}}^{\mathrm{II}}$ at all the frequencies. These are defined in Eqns.(3.14) - (3.15). Resulting coefficients are plotted in Figure 3.12.

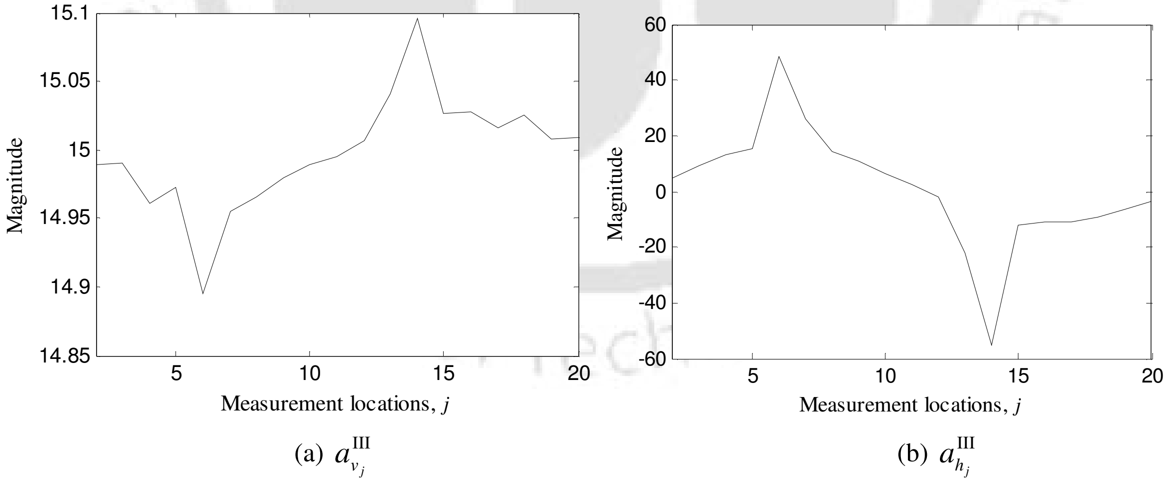

(a) $a_{v_j}^{\mathrm{III}}$ (b) $a_{h_j}^{\mathrm{III}}$

Figure 3.12: Variation of coefficients $a_{v_j}^{\mathrm{III}}$ and $a_{h_j}^{\mathrm{III}}$ along the measurement locations.

Now the *crack probability functions* are obtained by first compressing these coefficients to vary between zero and one (Eqns. (3.16) - (3.17)), and then find out the distance of resulting individual coefficients from their mean at all measurement locations (Eqns. (3.18) - (3.19)). The resulting *crack probability functions* are plotted in Figure 3.13. It suggests presence of two cracks in the shaft, one between locations x_5 and x_7, while the other between locations x_{13} and x_{15}.

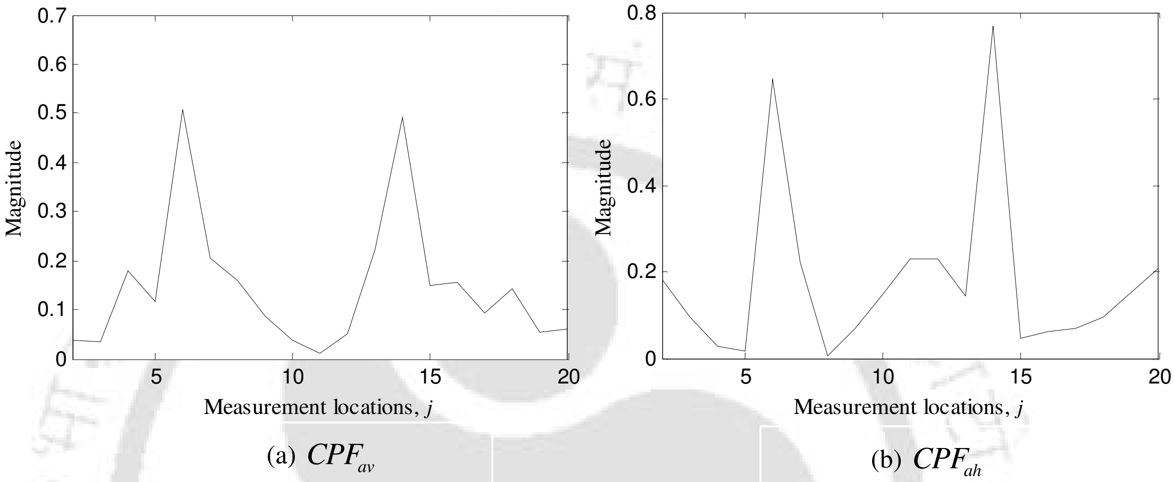

(a) CPF_{av} (b) CPF_{ah}

Figure 3.13: Crack probability functions for Simulation-II.

In the present chapter, the MCDLA has been developed. The algorithm gives the number of cracks present in the shaft and its locations over the shaft. Working of the algorithm is illustrated with simulated cracked shaft response using FEM. Two simulation examples are presented and the algorithm detects the location of cracks in both the cases. In the next chapter, an optimization problem is presented for the estimation of size and accurate location of cracks.

4 ESTIMATION OF ACCURATE LOCATION AND SIZE OF CRACKS

4.1 Introduction

Number of cracks and their approximate locations are obtained from the method presented in the MCDLA, i.e. in Section 3.3. In this chapter, the MCLSA is developed to find the accurate locations and size of cracks. An optimization problem is defined using measured forced responses from a cracked shaft and forced responses of the cracked shaft using the finite element modeling. The optimization problem is solved by using a multi-objective genetic algorithm. Information obtained from the identification algorithm of previous sections is used to define the decision variable space for the optimization problem.

4.2 Introduction to Genetic Algorithm

Genetic algorithms (GAs) are the random search and optimization techniques based on natural selection and genetics. They use a combination of the selection, crossover and mutation operators to search for the optimized solution. GAs discretise the search space by coding the variables in strings, traditionally in the binary coding. Since the GAs use a population of strings created over all the variable space, rather than a single string as in traditional optimization methods (such as gradient search methods), chances are more that the GA solution is a global one. The working principle of the genetic algorithm is explained briefly in the following section.

4.3 Working Principles of Genetic Algorithms

Area of genetic algorithm has evolved considerably since concepts of GAs were first presented (Holland, 1975) and nowadays there exist a large number of variations to the basic genetic algorithms. Working of the basic genetic algorithm is explained in the present section (Deb and Agrawal, 2005; Rao, 2010).

Let us consider a single objective optimization problem:

Minimize

$$f(\boldsymbol{\beta}), \qquad \beta_i^L \le \beta_i \le \beta_i^U, \; i = 1, 2, \ldots, N, \tag{4.1}$$

where $\boldsymbol{\beta} = \{\beta_1, \beta_2, \ldots, \beta_N\}$.

Domain of the function $f(\boldsymbol{\beta})$, given by the inequality relation in Eqn. (4.1), is the design space or the decision variable space for the optimization problem and $\boldsymbol{\beta}$ is the design vector or the decision variable vector.

4.3.1 Binary Coding of the Strings

First the variables β_i are coded in string structures. Normally binary-coded strings are used. However some GAs work with real variable itself (real-coded GA). Length of the binary coded string is determined by the desired accuracy in the solution. For an optimization problem with two variables (N = 2 in Eqn. (4.1)), if 5 bits are used to code each variable, the strings (00000 00000) and (11111 11111) would represent the points (β_1^L, β_2^L) and (β_1^U, β_2^U), respectively. Then the mapping rule between the variable β_i and its binary coded substring s_i of length l_i is given by

$$\beta_i = \beta_i^L + \frac{\beta_i^U - \beta_i^L}{2^{l_i} - 1} \times \text{Decoded value}\,(s_i). \tag{4.2}$$

There are three GA operators: (i) *Selection*, (ii) *crossover* and (iii) *mutation*. Although the *crossover* and *mutation* operators need the binary representation of variables, the *selection* operator needs real variables (i.e., the decoded value of binary substrings) to evaluate the objective function. The decoded value of the binary string can be calculated by

$$\text{Decoded value}(s_i) = \sum_{j=0}^{l-1} 2^j (s^j)_i \ . \qquad (4.3)$$

Here $(s^j)_i$ are the bits (binary digits) of the string s_i. Hence, the string s_i is represented by

$$s_i = (s^{l-1}, s^{l-2}, ..., s^j, ..., s^1, s^0) \qquad (4.4)$$

For example, the decoded value for a string $s_i = (10111)$, using Eqn. (4.3), would be equal to $\{(1)2^0 + (1)2^1 + (1)2^2 + (0)2^3 + (1)2^4\}$. A string such as (11001 10110) is known as chromosome also. They represents a particular value for all the design variables according to the mapping rule given in Eqn.(4.2).

4.3.2 Fitness Function

During the selection stage, every string is assigned a fitness function F_{fit}. Normally the fitness function is derived from the objective function. For binary-coded strings, strings are decoded to get real variables. For the minimization problem, the fitness function may be considered to be same as the objective function $F_{fit} = f(\boldsymbol{\beta})$, while a maximization problem can be converted to a minimization problem by defining the fitness function by $F_{fit} = 1/\{1 + f(\boldsymbol{\beta})\}$. More number of such fitness functions for the maximization problem as well as the minimization problem can be defined.

The genetic algorithm is an iterative process. First an initial population of strings is generated. The initial population is distributed all over the design space. Each string of the initial population is assigned a fitness value depending upon the fitness function. The initial population is then operated by three GA operators: *selection*, *crossover*, and *mutation*. The fitness value is used at the *selection* stage. After applying three operators, the resulting population is tested for a convergence criterion. If the convergence criteria are not satisfied, the three GA operators are applied again to the resulting population. The process is repeated till the convergence criterion is satisfied.

4.3.3 The Selection Operator

Job of the selection operator is to select the better strings from the population and make the mating pool. The crossover operator is operated over strings in the mating pool. A string is selected to the mating pool depending upon its fitness. There are different type of selection operator namely, the *proportional* selection, the *tournament* selection, and the *ranking* selection. In the proportional selection, a string is selected to the mating pool with a probability proportional to the fitness of the string. One way of implementing the proportionate selection is to use a Roulette wheel selection. Circumference of the Roulette wheel is divided in proportion to the fitness of each string. The wheel is spun the same number of times as the number of strings needed in the mating pool, each time selecting one string to the mating pool. Strings with the higher fitness cover more part of the wheel circumference and hence have more chances of getting selected to the mating poll. This way more copies of better strings are copied to the mating pool.

In the Roulette wheel selection, if the fitness of the best string is 80%, it will occupy 80% of the circumference. This will give multiple copy of a single string only in the mating pool, discarding the other strings. This way the GA will not be able to search for the solution over all the design space. In ranking selection, strings are sorted based upon their fitness value and a rank is given to each string. Compared to Roulette wheel selection it gives slow convergence and but it preserves diversity.

In the tournament selection, a number of sub-tournaments are used that produce the required size of strings in the mating pool. It involves two stages: (i) forming subgroups for the sub-tournaments and (ii) selecting a string as the winner of the tournament. The winner string will go to the mating pool. Normally, two strings are selected in each tournament and a winner is decided based upon the fitness value of the string.

4.3.4 The Crossover Operator

The crossover operator is operated over strings in the mating pool. This result in new strings called child strings. Two strings are chosen randomly from the mating pool and some part of one string is exchanged with the other string. A crossover probability, p_c, is used to decide whether a chosen pair of chromosome will go through the crossover operator. The job of the crossover probability is to keep some of strings in the mating pool unchanged after the crossover. This way some of the good strings in the mating pool is brought unchanged to the new generation. Two strings from the mating pool that take part in the crossover operation is called parent strings, and two strings formed after the crossover is called the child string. During the crossover, a crossover point in the string is selected randomly and bits of strings right to the crossover point are exchanged. The crossover between two strings is shown in Figure 4.1.

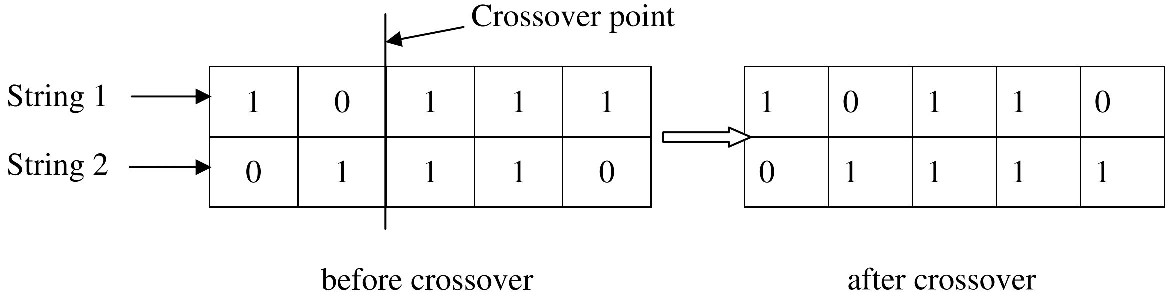

Figure 4.1: The crossover between two strings.

Selection of the crossover point is chosen randomly. If the resulting child strings are good, their fitness will be more and chances of survival of these good strings will be more in subsequent generations, whereas if the resulting child strings have lower fitness level, chances of survival of the strings will be less and they will be eliminated in subsequent generations. For a real-coded GA, different crossover operators are available such as: simulated binary crossover (Deb and Agrawal, 1995), unimodal normally distributed crossover operator (Ono and Kobayashi, 1997), simplex crossover (Tsutsui et al., 1999), etc. In the present work, simulated binary crossover is used. The simulated binary crossover is explained in following paragraphs.

Suppose $\beta_i^{(1,n_g+1)}$ and $\beta_i^{(2,n_g+1)}$ are the offspring from parents $\beta_i^{(1,n_g)}$ and $\beta_i^{(2,n_g)}$. Here i in β_i are defined in Eqn. (4.1), n_g is the number of generations, and 1 and 2 are used for two solutions participating in the crossover. The offspring are expressed as (Deb and Agrawal, 1995)

$$\beta_i^{(q,n_g+1)} = 0.5(a_c + \gamma_i b_c), \qquad q = 1,2 \tag{4.5}$$

where a_c is the sum of parent solutions and b_c is the difference of parent solutions. The parameter, γ_i, is expressed as

$$\gamma_i = \begin{cases} (2u_i)^{1/(\eta_c+1)}, & \text{if } u_i \le 0.5 \\ \left(\dfrac{1}{2(1-u_i)}\right)^{1/(\eta_c+1)}, & \text{otherwise} \end{cases} \tag{4.6}$$

where u_i is a random number between 0 and 1, and η_c is the crossover distribution index. A high value of η_c gives high probability of creating offspring near parent springs.

4.3.5 The Mutation Operator

The mutation operator is used after the application of crossover operator. A small probability called mutation probability, p_m, is used to decide whether a selected string will go through mutation. If the selected string has to go through the mutation then the site of the mutation can be obtained through generating random numbers. The mutation can be applied bitwise also. The mutation operator will change from 1 to 0 and vice versa. A mutation operator is helpful in maintaining diversity in the solution by introducing a new genetic structure by modifying the string (or chromosome) randomly.

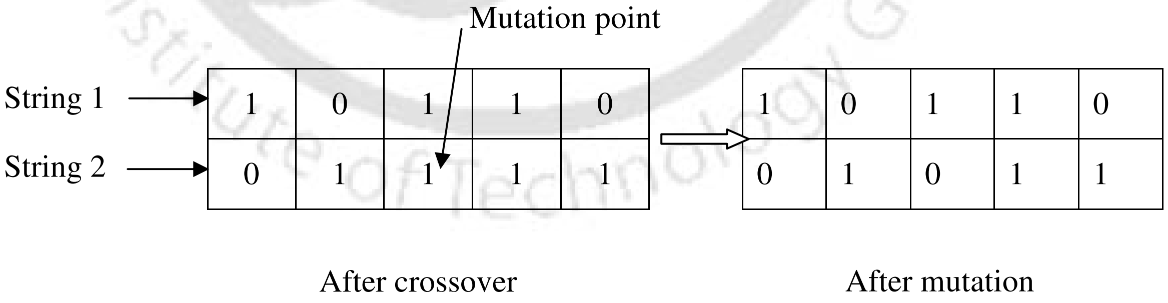

Figure 4.2: The mutation of the strings.

A single point mutation is shown in Figure 4.2, where string 1 remains unchanged while the string 2 is mutated at the 3rd bit of the string from the left. For the real coded GA, different mutation operators are available such as: non-uniform mutation (Michalewicz, 1992) and polynomial mutation (Deb and Goyal, 1996). In the present work the real-coded GA with a polynomial mutation is used. The polynomial mutation is explained in following paragraphs.

Suppose $\beta_i^{(n_g+1)}$ is obtained from the application of crossover operator on $\beta_i^{(n_g)}$, and $\psi_i^{(n_g+1)}$ is obtained from the application of polynomial mutation on $\beta_i^{(n_g+1)}$. Then the relation between $\beta_i^{(n_g+1)}$ and $\psi_i^{(n_g+1)}$ is given by

$$\psi_i^{(n_g+1)} = \beta_i^{(n_g+1)} + (\beta_i^U - \beta_i^L)\delta_i \tag{4.7}$$

where δ_i is determined from,

$$\delta_i = \begin{cases} (2u_i)^{\frac{1}{\eta_m+1}} - 1 & \text{if } u_i \le 0.5, \\ 1 - [2(1-u_i)]^{\frac{1}{\eta_m+1}} & \text{otherwise.} \end{cases} \tag{4.8}$$

Here u_i is a random number between 0 and 1, and η_m is the mutation distribution index. The mutation operator is applied on decision variables with a probability $1/N$, where N is the number of decision variables.

4.3.6 The Elitism Operator

The main purpose of the elitism operator is to prevent the good strings from earlier generations from being lost. A few best strings from parent strings are copied to child strings. These good strings can be lost if they are not selected during the selection operator or if the crossover and mutation operators destroy them.

4.3.7 Termination Criterion

One generation of a GA comprises of the application of selection, crossover and mutation operators over the current population. After each generation of the GA, a termination criterion is tested and if the criterion is satisfied the GA is terminated otherwise it will go for next generation. Different termination criterion can be used. Sometimes, maximum number of generations is used as the termination criterion; in that case the search will terminate after a given number of generations. Sometimes the search is stopped when there is no significant change in fitness value over subsequent generations.

4.4 The Multi-Objective Genetic Algorithm

Multi-objective genetic algorithms have been used in the present work. There are several multi-objective genetic algorithms such as: (1) niched pareto genetic algorithms (NPGA) (Horn et al., 1994), (2) vector evaluated genetic algorithm (VEGA) (Schaffer, 1985), (3) non-dominated sorting genetic algorithms (NSGA) (Srinivas and Deb, 1994) and (4) non-dominated sorting Genetic Algorithms-II (NSGA-II) (Deb et al., 2002). Among these, NSGA-II has been used for wide range of problems. Both the NSGA and NSGA-II use non-dominated sorting for preliminary assigning fitness values. However, the computational complexity for the non-dominated sorting in NSGA-II is less than that in NSGA. Also, elitism and diversity preservation mechanisms (crowding distance) are introduced in NSGA-II, which has improved the algorithm.

4.4.1 Non-Dominated Sorting

NSGA-II uses non-dominated sorting of strings to assign rank to parent strings. Non-dominated sorting is explained with an optimization problem of two objective function and two decision variables. Let us consider an optimization problem

Minimize

$$f_j(\boldsymbol{\beta}), \qquad \beta_i^L \le \beta_i \le \beta_i^U,\ i=1,2 \quad j=1,2 \tag{4.9}$$

A string in the objective space is shown in Figure 4.3. Since the optimization problem in Eqn. (4.9) is a minimization problem, point A dominates all the points in quadrant-I and all the points in quadrant-III dominates the point A. Considering the objective function $f_2(\boldsymbol{\beta})$, point A has higher fitness than point D whereas considering the objective function $f_1(\boldsymbol{\beta})$, point D has higher fitness than point A. Hence any point in quadrant-II is not inferior to point A. Similarly, any point in quadrant-IV is also not inferior to point A.

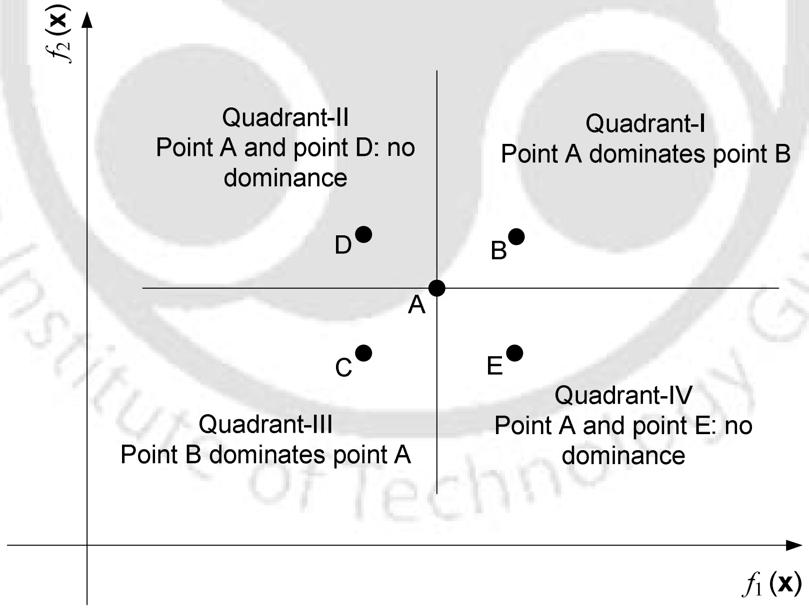

Figure 4.3: Dominance of strings in objective space.

In non-dominated sorting of the parent population, first those strings are identified which are not dominated by any other strings in the population. Non-dominated strings are those strings which are not inferior to any other string in the population. All non-dominated strings are given rank 1. New non-dominated set of strings are then formed after neglecting, temporarily, the strings with rank 1. The new set of strings is given rank 2. This process is continued till last string in the parent population is assigned rank.

4.4.2 Crowding Distance

The crowding distance in NSGA-II is a diversity preservation mechanism. For a particular string it is the average side length, in the objective space, of a cuboid formed by using the nearest neighbours of the particular string. It is calculated for strings of same rank.

In NSGA-II, initially a random population is created. Each solution is assigned a rank according to its non-domination level (1 is the best rank). The tournament selection is used to select the individuals to the mating pool. Among two feasible solutions, the one belongs two lower rank is decided to be winner of the tournament selection. If the two individuals are of the same rank, the one with higher crowding distance will be the winner. All other operators such as: the crossover operator, the mutation operator and the elitism operator are same as explained in Section 4.3.

4.5 Multi-Objective Optimization for Crack Parameters Estimation

Different combination of crack parameters may produce very similar responses. For more number of variables arising from more number of cracks, it is difficult to get actual crack parameters in the inverse problem of identification of multi-crack parameters from system responses. This point is explained with Figure 4.4. Eq. (2.12) is used to generate responses of the cracked shaft. To exaggerate the effect, excitation frequencies are chosen to be near natural frequencies of the shaft. A response of a shaft, having a single crack, for different combination of crack parameters is plotted in Figure 4.4. From Figure 4.4(a), response of the shaft for combination I (the crack depth ratio of 0.6 and the cracked element of 59), is almost same as that for combination II (the crack depth ratio of 0.5 and the cracked element at 51). There could be many more other combinations possible, which may give almost the same response. The response of the shaft at 515 rad/s is plotted in Figure 4.4(b). The above two combinations of crack parameters, i.e. combination I and combination II, do not give the same response. Actually, now combination III (the crack depth ratio of 0.73 at the element number 51) produces a similar response as that of combination I. Hence, more number of objective functions made from shaft responses at several excitation frequencies helps to get the GA convergence towards actual crack parameters.

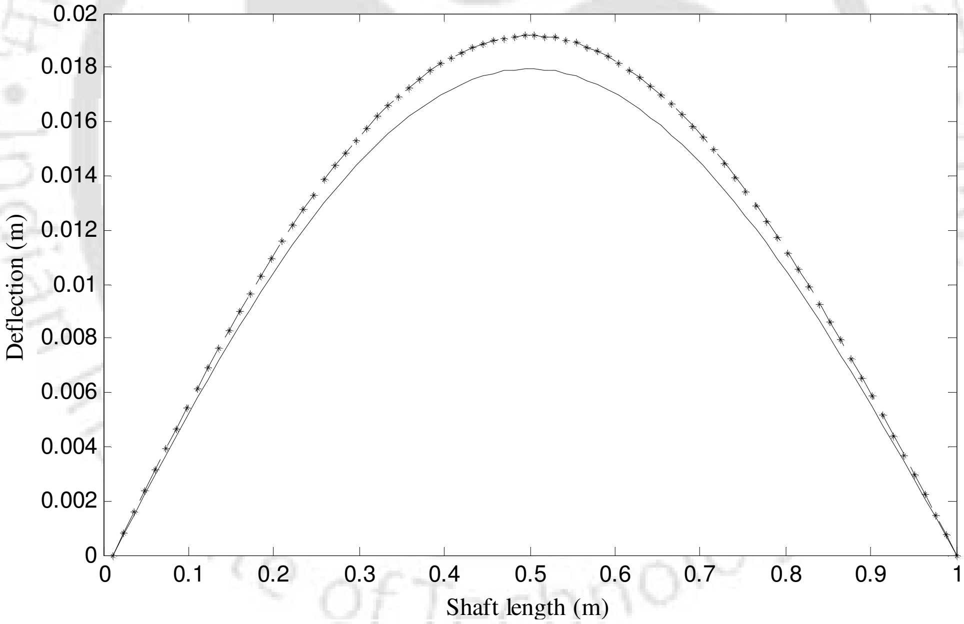

(a) Response at 120 rad/s, (uncracked —), (crack depth ratio 0.6, cracked element 59 − −), (crack depth ratio 0.5, cracked element 51 **)

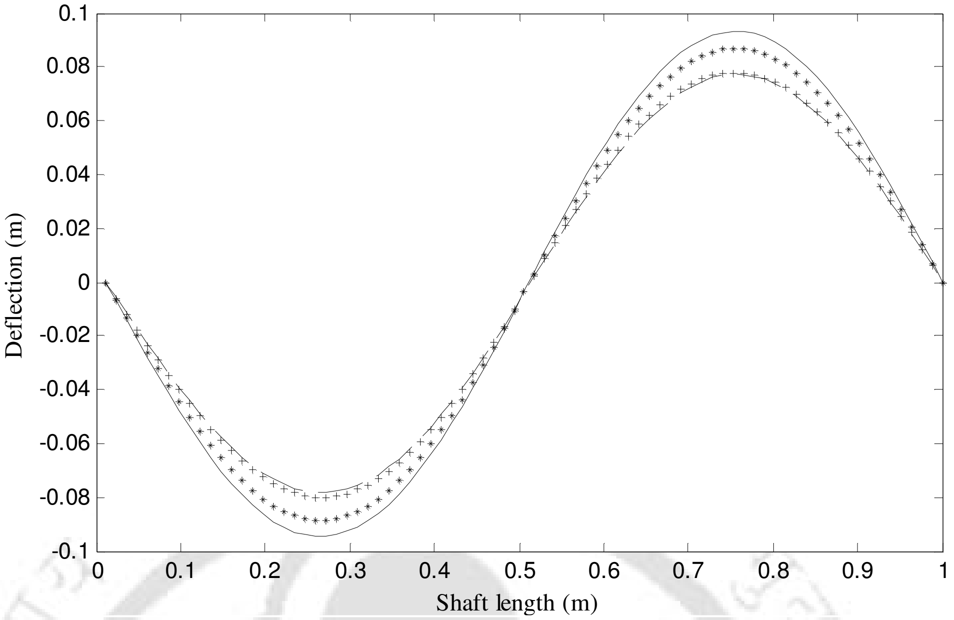

(b) Response at 515 rad/s, (uncracked —), (crack depth ratio 0.6, cracked element 59 −−), (crack depth ratio 0.5, cracked element 51 **), (crack depth ratio 0.73, cracked element 51 ++)

Figure 4.4: Cracked shaft responses in the vertical direction.

Also, from Figure 3.2, the response in the horizontal direction is very less due to coupling effect than the response in the forcing direction, i.e. the vertical direction. To give a sufficient weighting to the response in the horizontal direction, separate objective functions are made out of it: one for the vertical direction response and other for the horizontal direction response.

4.6 The MCLSA

The present identification algorithm for the accurate localization and sizing makes use of the following: (i) measured forced response from the cracked shaft and (ii) forced response obtained from the FE modeling of the intact shaft, using Eqn. (2.12).

Let the number of measurement locations at which measurements are taken be n and that the number of frequencies at which the system is excited be k, let us denote the measured deflection of the shaft at frequency, ω_i, and node , j , by $q_{mv_{i,j}}$ in the vertical plane and $q_{mh_{i,j}}$ in the horizontal plane. Similarly, that the deflection predicted by the cracked shaft model by $q_{pv_{i,j}}$ in the vertical plane, and $q_{ph_{i,j}}$ in the horizontal plane. Now, define

$$q_{1,i,j} = \left(q_{mv_{i,j}} - q_{pv_{i,j}}\right)^2; \quad i = 1,\dots,k; \quad j = 1,\dots,n; \tag{4.10}$$

and

$$q_{2,i,j} = \left(q_{mh_{i,j}} - q_{ph_{i,j}}\right)^2; \quad i = 1,\dots,k; \quad j = 1,\dots,n; \tag{4.11}$$

Now an optimization problem can be stated as

Minimize

$$f_{r,i}(\boldsymbol{\beta}) = \sum_{j=1}^{n} q_{r,i,j}; \quad i = 1,\dots,k; \quad r = 1,2; \tag{4.12}$$

Where $\boldsymbol{\beta} = \{\beta_1, \beta_2, \dots, \beta_{nc}, \beta_{nc+1}, \beta_{nc+2}, \dots, \beta_{2nc}\}$

subject to

$$\beta_s \in [1, ne]; \qquad \text{for } s = 1, 2, \dots, nc;$$

$$\beta_s \in [0,1]; \qquad \text{for } s = nc+1, nc+2, \dots, 2\times nc;$$

where $\beta_s = d_s / R,$ for $s = nc+1, nc+2, \dots, 2\times nc;$

Here, nc is the number of cracks present in the shaft, ne is the number of finite elements used to model the shaft, d_s is the size of the s^{th} crack, and R is the radius of the shaft. Hence, d_s / R is the crack depth ratio of the s^{th} crack. Difference between the measured cracked shaft response and the FEM predicted cracked shaft response is obtained in Eqns. (4.10) and (4.11). Eqn. (4.10) is used for shaft responses in vertical direction while Eqn. (4.11) is used for the shaft responses in horizontal direction. Eqn. (4.12) defines objective functions for the optimization problem. Number of objective functions is two times the number of excitation frequencies (Eqn.(4.12)). Design variables $\boldsymbol{\beta}$ in Eqn. (4.12) are the location and size of the cracks. For a shaft with nc number of cracks, the number of design variables would be $2 \times nc$. β_s for $s = 1, 2, ..., nc$; are the location of finite elements with cracks, which will vary from 1 to ne. β_s for $s = nc+1, nc+2, ..., 2 \times nc$; are the crack depth ratio of cracks which will vary from 0 to 1. Hence, the location and the size of a $(s=i)^{\text{th}}$ crack is represented by β_i and β_{nc+i}, respectively.

4.7 Numerical Experiments for the MCLSA

The numerical simulation has been done for the MCLSA. Shaft system parameters for present numerical simulations are chosen to be same as given in Table 3-1. The previous algorithm of Section 3.3 gives the number of cracks, nc, present in the shaft and their approximate locations along the shaft length. This information is used to define the decision variable space, β_s for $s = 1, 2, ..., nc$.

In the simulation example I, the *CPF*s (Figure 3.7) indicates presence of two cracks in the shaft, hence $nc = 2$. Also, since total 80 elements are used in FE model of the shaft, $ne = 80$.

Decision variable space β_1 and β_2 would be locations of two cracks. Decision variable space β_3 and β_4 would be the sizes of two cracks. From Figure 3.7, *CPF*s have high values at measurement locations x_6 and x_{10}. Hence, one crack is between measurement locations x_5 and x_7, and the other crack is between locations x_9 and x_{11}. Since the number of finite elements between two consecutive measurement locations is 4, the measurement location x_5 corresponds to 16th finite element and the measurement location x_7 corresponds to 24th finite element. Similarly, measurement locations x_9 and x_{11} corresponds to 32nd and 40th finite elements. Hence, the decision variable space for β_1 and β_2 are chosen to be [16, 24] and [32, 40], respectively. It means that the location of the first crack is restricted within 16th and 24th finite elements and the location of the second crack is restricted within 32nd and 40th finite elements. Decision variable space for both β_3 and β_4 will remain [0, 1] as there is no a prior estimation of size of cracks.

For the simulation example II, the *CPF*s (Figure 3.13) indicate presence of two cracks. The first peak is at measurement location x_6 and the second peak is at measurement location x_{14}. Hence the first crack is located between measurement locations x_5 and x_7 while the second crack is located between measurement locations x_{13} and x_{15}. Thus the decision variable space β_1, for the first crack is [16, 24] and the design variable space β_2, for the second crack is [48, 56].

The NSGA-II is used to solve the optimization problem stated in Eqn. (4.12). Different parameters used for the NSGA-II are listed in Table 4-1. Convergence criteria used for the GA is defined as follows

$$(i > 30) \quad \text{and} \quad \left(\left|\gamma_i - \gamma_{i-1}\right| < \varepsilon_1\right), \tag{4.13}$$

with

$$\gamma_i = (\beta_1 / ne + \beta_2 / ne + \beta_3 + \beta_4)_{i-4} +, \ldots, +(\beta_1 / ne + \beta_2 / ne + \beta_3 + \beta_4)_i \tag{4.14}$$

where i is number of generations and decision variables appearing in brackets with subscripts i denote their mean values after i^{th} generation. From Eqn. (4.13), minimum number of generations required for convergence is 30. γ_i in Eqn. (4.14) is normalised decision variables, summed over last 5 generations. β_1 and β_2 are normalized by dividing it by ne, the number of finite elements used to model the shaft. After this normalization, values of β_1 / ne and β_2 / ne varies between 0 and 1 which is comparable to values of β_3 and β_4. For convergence, γ_i is compared with γ_{i-1} (Eqn. (4.13)). The value of small parameter ε_1 is taken to be 0.01.

Table 4-1: Parameters used for the multi-objective optimization using NSGA-II.

Parameters	Values for simulation I	Values for simulation II
Number of cracks, f	2	2
Population size	20	20
Crossover probability	0.9	0.9
Mutation probability	0.1	0.1
Crossover distribution index	20	20
Mutation distribution index	20	20
Range for β_1	[16, 24]	[16, 24]
Range for β_2	[32, 40]	[48, 56]
Range for β_3	[0, 1]	[0, 1]
Range for β_4	[0, 1]	[0, 1]
Excitation frequencies (rad/s)	10,20,30,150,160, 170,360,370,380, 520,530,540	10,20,30,150,160, 170,360,370,380, 520,530,540

The simulation results by the GA for two simulation examples are presented in Figure 4.5 and Figure 4.6. Application of MCLSA to real shaft would need the measurement of forced responses of the real shaft and the FEM generated cracked shaft responses (Eq. (2.12)). For numerical simulations, however, forced responses of the real shaft is also obtained using Eq. (2.12). To mimic the actual experiments 1% noise is added in shaft responses. For the first example, converged results for crack parameters are $(\beta_1, \beta_2, \beta_3, \beta_4)_{31} = (21, 36, 0.61, 0.70)$ and actual crack parameters are $(21, 35, 0.60, 0.70)$. For the second example, the converged values of crack parameters are $(\beta_1, \beta_2, \beta_3, \beta_4)_{50} = (19, 51, 0.61, 0.68)$, and actual crack parameters are $(21, 51, 0.60, 0.70)$. For both simulated examples, converged values of crack parameters from the GA are very close to actual crack parameters.

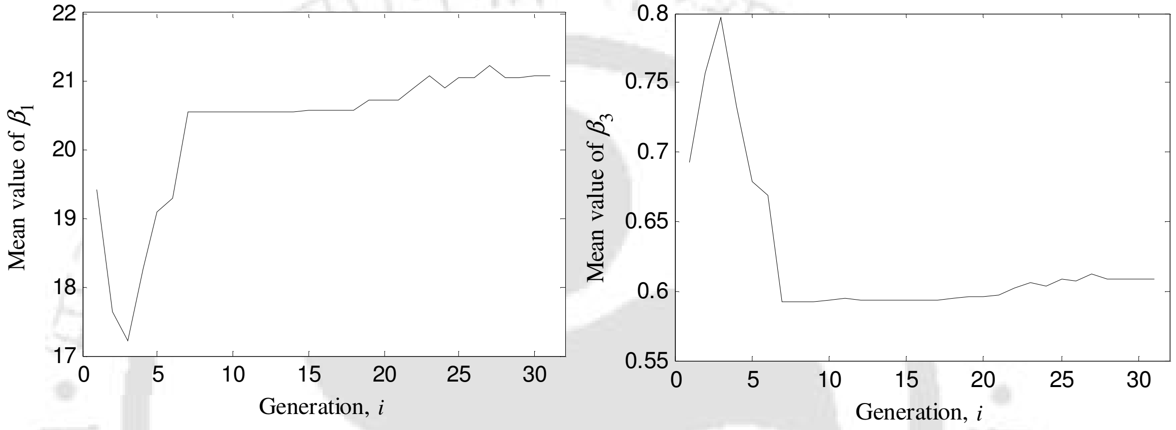

(a) First crack location, β_1

(b) First crack size, β_3

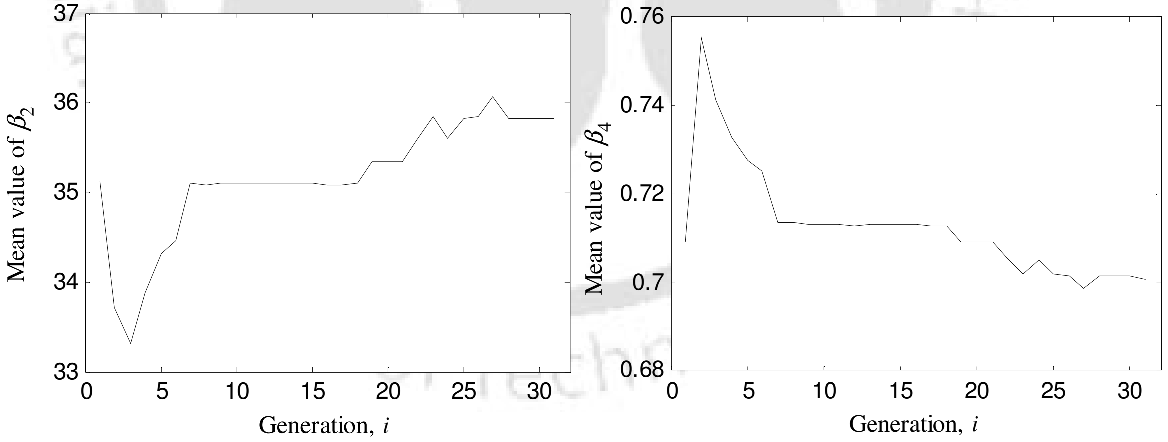

(c) Second crack location, β_2

(d) Second crack size, β_4

Figure 4.5: Variation of crack parameters with number of generations for simulation example I.

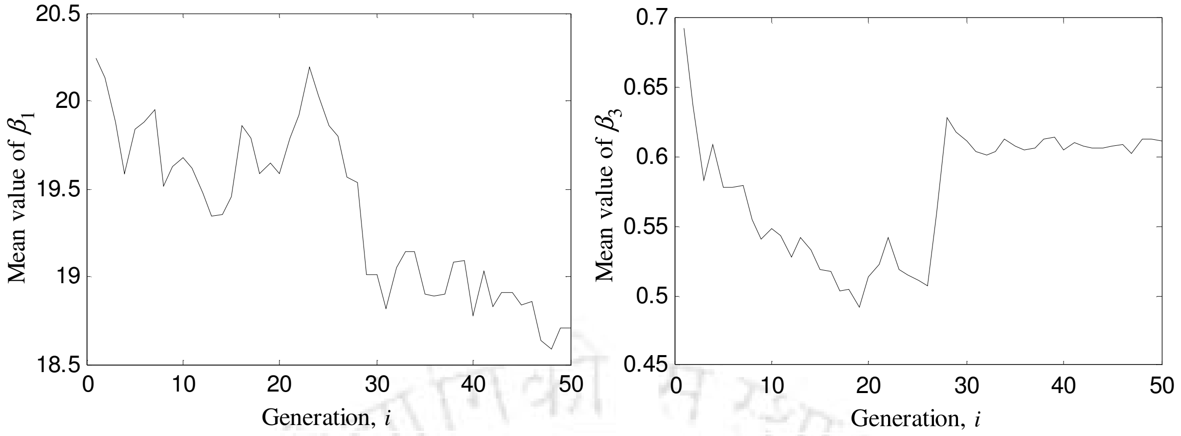

(a) First crack location, β_1 (b) First crack size, β_3

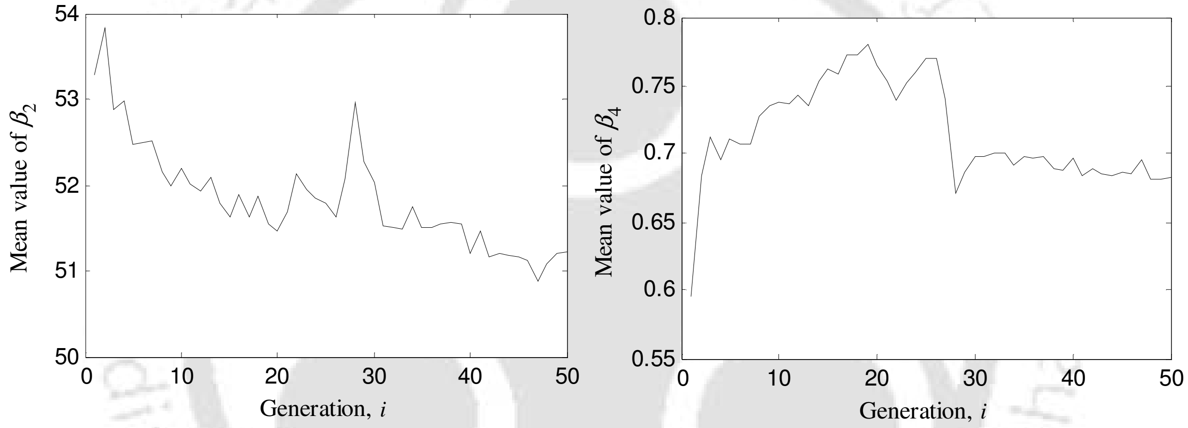

(c) Second crack location, β_2 (d) Second crack size, β_4

Figure 4.6: Variation of crack parameters with number of generations for simulation example II.

A flowchart of the above two-stage identification algorithm (the MCDLA and the MCLSA) is summarized in Figure 4.7.

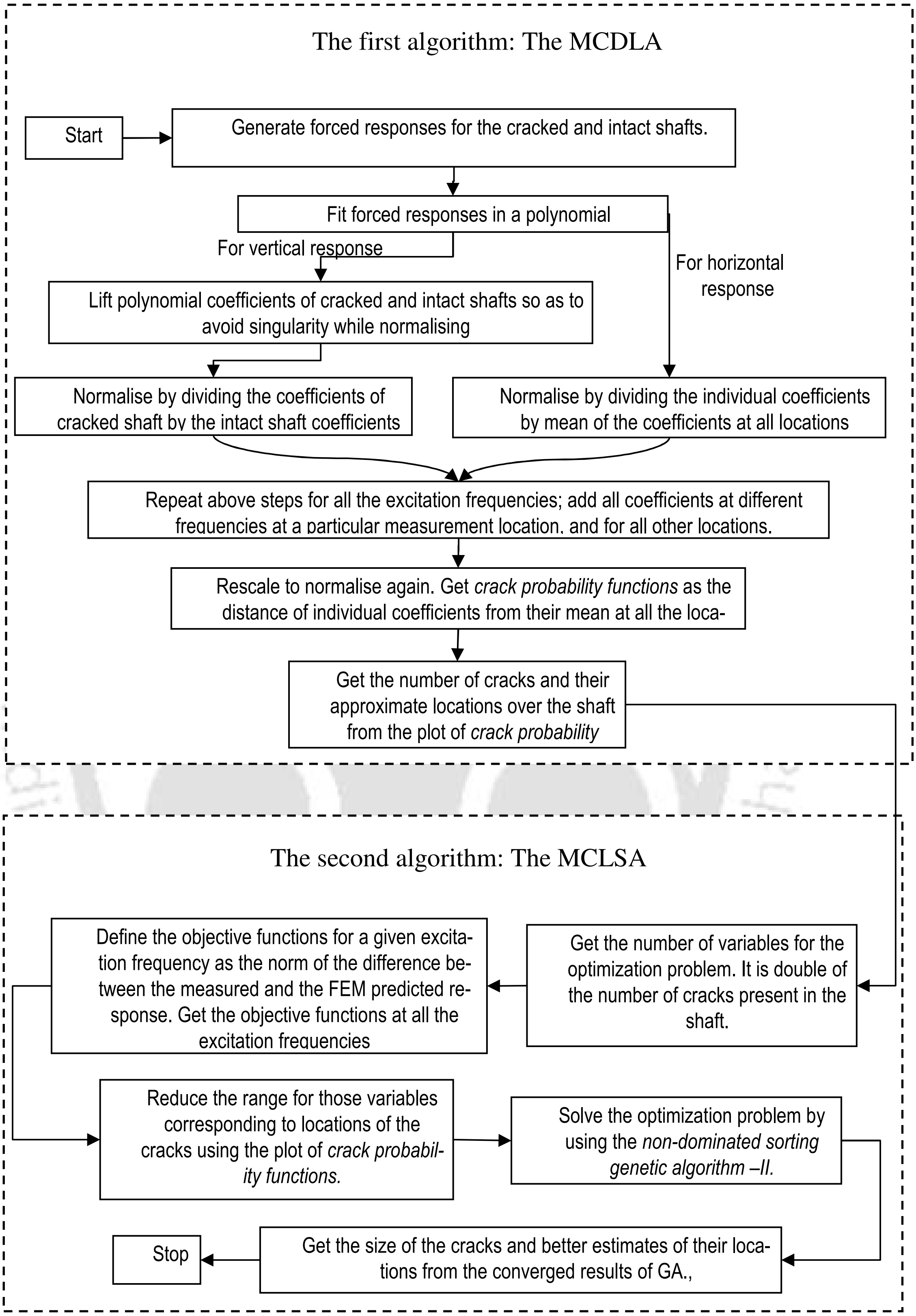

Figure 4.7: A combined flowchart of the MCDLA as well as the MCLSA.

In above sections, the MCLSA is tested numerically with two simulation examples. NSGA-II is used to solve the optimization problem which gives the sizes and accurate locations of the cracks. Estimated crack parameters (the size and location of the cracks) are in good agreement with actual crack parameters. The concept of *Equivalent Reduced Stiffness* (ERS) is introduced in the next section. It improves the normalization step of the MCDLA presented in Section 3.2.

4.8 Normalization of the Quadratic Coefficients using "Equivalent Reduced Stiffness"

The *multi-crack detection and normalization algorithm* is presented in Section 3.2. In the algorithm, coefficients $a^{\mathrm{I}}_{cv_{i,j}}$ obtained from the cracked shaft are normalised in Eqn. (3.12) by the corresponding coefficients $a^{\mathrm{I}}_{wcv_{i,j}}$ obtained from intact shaft deflections. The elasticity constant *E* of the intact shaft was assumed to be same as that of cracked shaft. Now a new parameter *equivalent reduced stiffness* (*ERS*) is defined which is expected to improve the normalization of the coefficients. The *ERS* will replace the elasticity constant *E*, while producing the intact shaft response in the vertical direction. The *ERS* is defined in the following way

$$f\left(ERS\right)=0, \tag{4.15}$$

with

$$f(ERS)=\operatorname{abs}\left\{\left(a_{wcv_{i2}}-a_{cv_{i2}}\right)+\left(a_{wcv_{i3}}-a_{cv_{i3}}\right)+\ldots+\left(a_{wcv_{in}}-a_{cv_{in}}\right)\right\},$$

where $a_{wcv_{i2}}, a_{wcv_{i3}}, \ldots, a_{wcv_{in}}$ are obtained from the intact shaft response with its elasticity constant *E*, replaced by the *ERS*. While $a_{cv_{i2}}, a_{cv_{i3}}, \ldots, a_{cv_{in}}$ are obtained from the cracked shaft response with elasticity constant *E*. It is reminded that these coefficients (i.e. a_{wcv} and a_{cv}) are proportional to the bending moment in the shaft. For the practical implementation of Eqn. (4.15), following expression is used to get the *ERS*.

$$f\left(ERS\right) < \varepsilon_2. \tag{4.16}$$

For the present simulation examples, value of small parameter ε_2 is taken to be 10^{-6}. Coefficients $a^{\mathrm{I}}_{wcv_{i,j}}$ and $a^{\mathrm{I}}_{cv_{i,j}}$ are plotted in Figure 4.8. The excitation frequency is taken to be 120 rad/s, whereas the fundamental natural frequency of the shaft is 126.78 rad/sec. The noise is not added in the signal and other parameters for the crack are same as the simulation example I in Table 3-1. The *CPF* values for the above simulation are plotted in Figure 4.9. Value of the *ERS* is found to be 2.009×10^{11} N/m^2 while the elasticity constant of the shaft material was taken to be 2.060×10^{11} N/m^2.

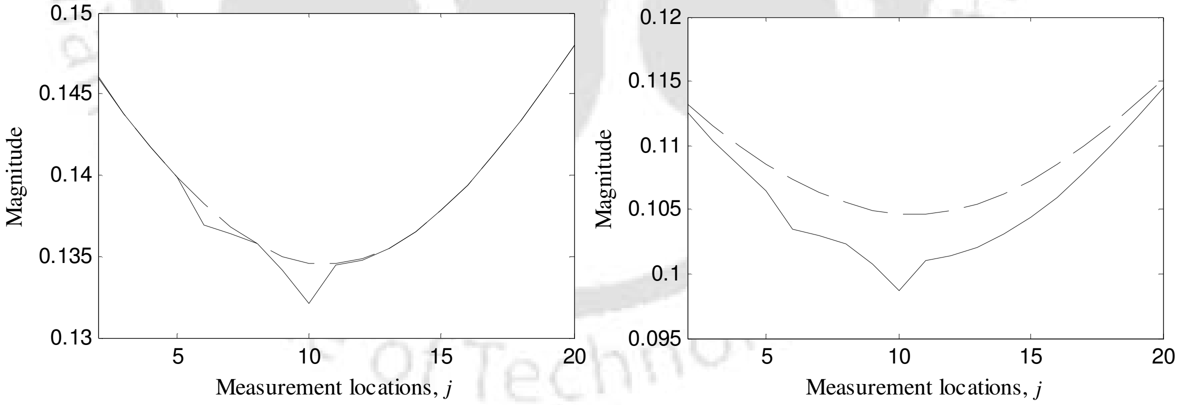

(a) With *ERS*

(b) Without *ERS*

Figure 4.8: Plot of coefficients $a^{\mathrm{I}}_{wcv_{i,j}}$ (—) and $a^{\mathrm{I}}_{cv_{i,j}}$ (– –) with measurement locations for excitation frequency of 120 rad/s.

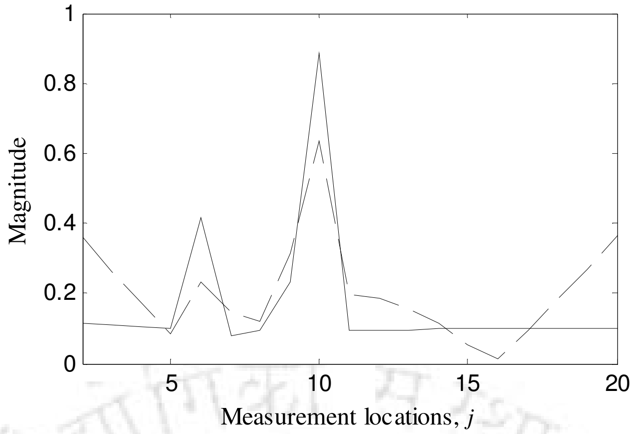

Figure 4.9: Plot of *CPF* values with measurement locations at 120 rad/s, (with *ERS* —), without *ERS* − −).

Use of *ERS* would reduce the need for updating of model, which is used to tune a few natural frequencies of interest from the numerical model to that of the measurement data. To show this, the algorithm is tested for the case when the density, diameter, and elastic constant used to generate the intact shaft response are not the same as that used to generate the cracked shaft response. Measured responses of the cracked shaft is generated with 2% change (reduction) in values of the density, the diameter and the elastic constant *E* (not all simultaneously, but one at a time).

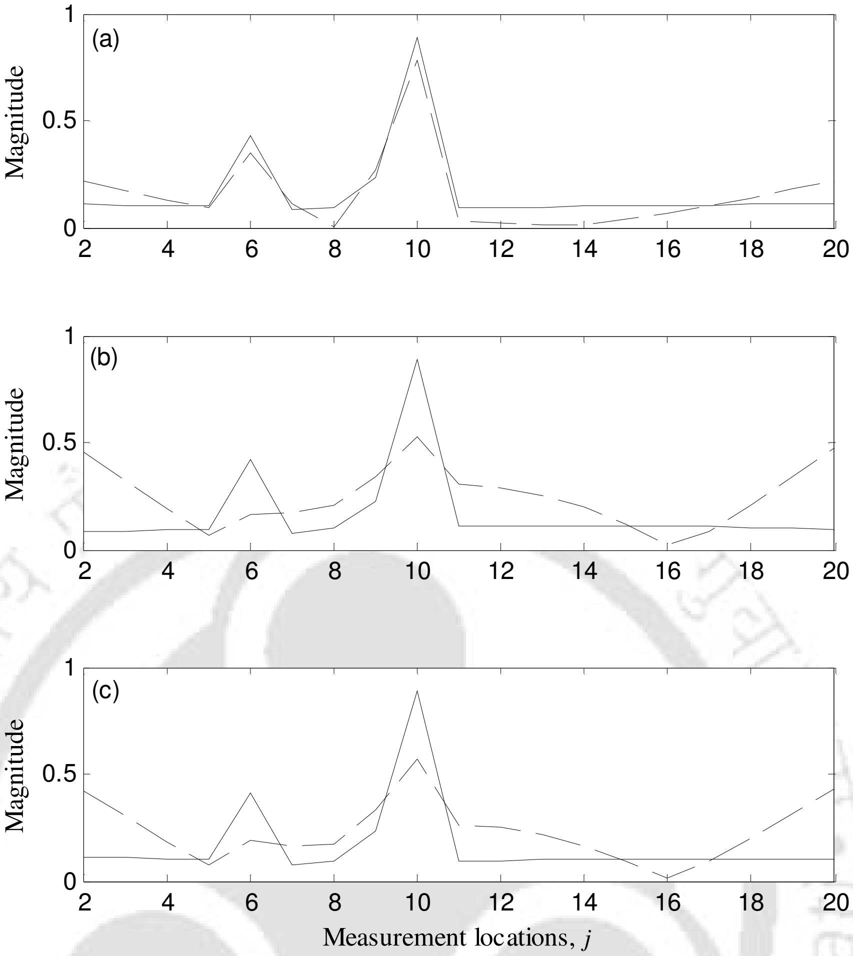

Figure 4.10: CPF values at 120 rad/s (with *ERS* —), (without *ERS* – –), with deviation in the (a) density (b) diameter (c) elastic constant *E*.

The *CPF* values obtained from simulation example I are plotted in Figure 4.10. In all the three cases, the *CPF*s using *ERS* are better than the *CPF*s using the elastic constant *E*. Next, the algorithm is tested for simulation example II (Table 3-1). Coefficients $a^{\mathrm{I}}_{wcv_{i,j}}$ and $a^{\mathrm{I}}_{cv_{i,j}}$ are plotted in Figure 4.11 and *CPF*s are plotted in Figure 4.12. The excitation frequency is taken to be 490 rad/s. The second natural frequency of the system is 506.93 rad/s. For simulation example II also, *CPF*s obtained using the ERS is better than that using the elastic constant, *E*. The *ERS* for the simulation example II is found to be 2.00×10^{11} N/m^2.

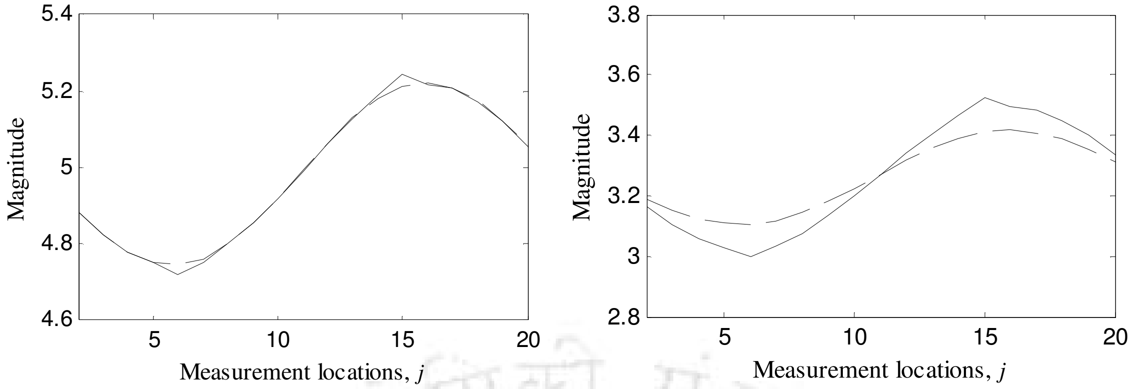

(a) With *ERS*

(b) Without *ERS*

Figure 4.11: Plot of coefficients $a^{\mathrm{I}}_{wcv_{i,j}}$ (—) and $a^{\mathrm{I}}_{cv_{i,j}}$ (− −) with measurement locations for excitation frequency of 490 rad/s.

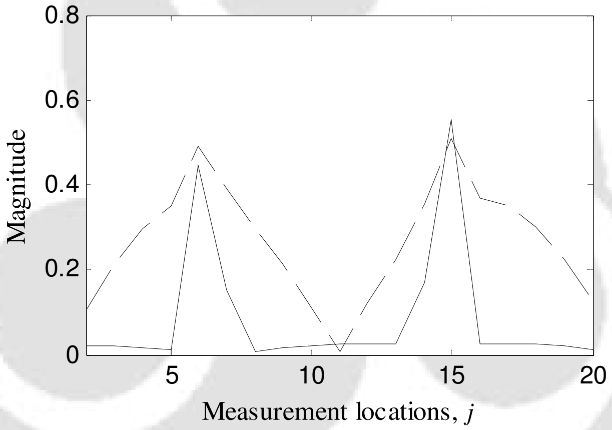

Figure 4.12: Plot of *CPF* values with measurement locations for excitation frequency of 490 rad/s, (with *ERS* —), (without *ERS* − −).

Now the algorithm is tested for simulation example II for the case when the density, diameter, and elastic constant of the cracked shaft and that of the intact shaft are not same. Cracked shaft responses are generated with 2% change (reduction) in values of the density, diameter and elastic constant. Resulting *CPF*s are plotted in Figure 4.13. In all the three cases, *CPF*s using the *ERS* are better than *CPF*s using the elastic constant, *E*.

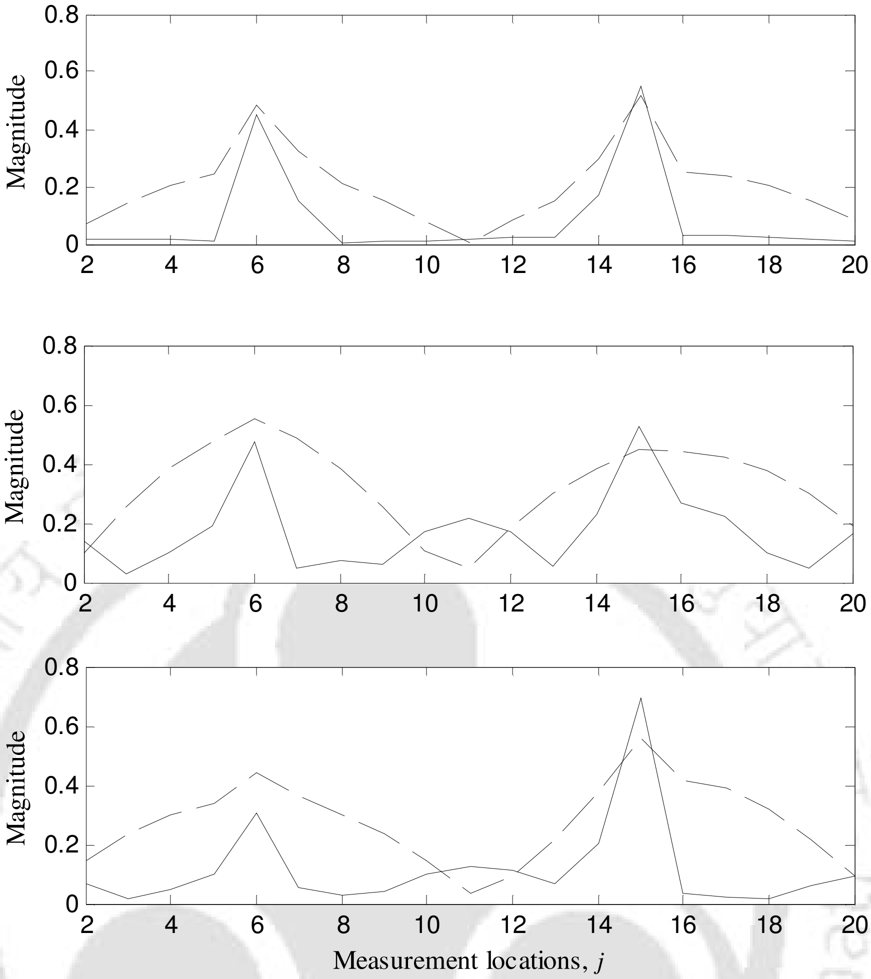

Figure 4.13: CPF values at 490 rad/s (with *ERS* —), (without *ERS* – –), with deviation in the (a) density (b) diameter (c) elastic constant *E*.

In the present chapter, a multi-objective optimization problem is presented for the estimation of location and size of multiple cracks in a shaft. The NSGA-II is used to solve the multi-objective optimization problem. Two simulation examples are presented to show the working of the algorithm. Range of the decision variable space is reduced by the information obtained from the MCDLA, presented in Section 3.2.

Up to now, cracks were assumed to be aligned with the forcing direction, i.e., the vertical direction. In actual case, however, the crack orientation with respect to the forcing direction will not be known. Algorithms for estimation of crack orientation angles are presented in the next chapter.

5 IDENTIFICATION OF CRACK ORIENTATION ANGLE

5.1 Introduction

The crack in a shaft can have any orientation with respect to the forcing direction. Hence, even for a shaft with single crack, the crack orientation angle of the crack is an unknown quantity. For solving the inverse problem, the *crack orientation angle* of the crack should be taken into account.

In Chapter 3, the *crack orientation angles* of the cracks were assumed to be known. Also, the cracks were assumed to be aligned with the forcing direction, i.e., the Y-axis (Figure 2.3). In this section this assumption is relaxed. Cracks are assumed to be aligned at any unknown orientation with respect to the $X-Y-Z$ co-ordinate system (Figure 2.3).

Fatigue cracks are very thin and for heavy shafts, with more static deflection due to gravity, the crack would gradually open and close during the rotation of the shaft. Hence, they are known as breathing cracks. If the crack is on the concave part of the deflected shaft the crack will be closed and if the crack is on the convex part of the deflected shaft the crack will be open. In intermediate positions, the crack will be partially open and partially closed. However, for a crack made by a saw in a light shaft, the crack remains open for all the angular positions of the shaft, and it is called the open crack. In the present chapter, first the cracks are assumed to be the open crack. A method is proposed to find out the crack orientation angle for open cracks. Next, cracks are assumed to be breathing cracks and a method is proposed for estimation of crack orientation angles for the breathing cracks. Subsequently, the MCDLA (Section 3.2) and the MCLSA (optimization problem, Section 4.6) is tested for rotated open cracks as well as breathing cracks.

5.2 Identification of Open Cracks

In the present section, the open crack model is used to get the stiffness of a rotated crack. First, the MCDLA (Section 3.2) is tested for cracked shaft with rotated open cracks. Thereafter, a method is proposed for the estimation of crack orientation angle of the rotated cracks. Finally, the MCLSA (Section 4.6) is used for the estimation of size and accurate location of the cracks.

5.2.1 Shaft Response with Rotated Open Crack

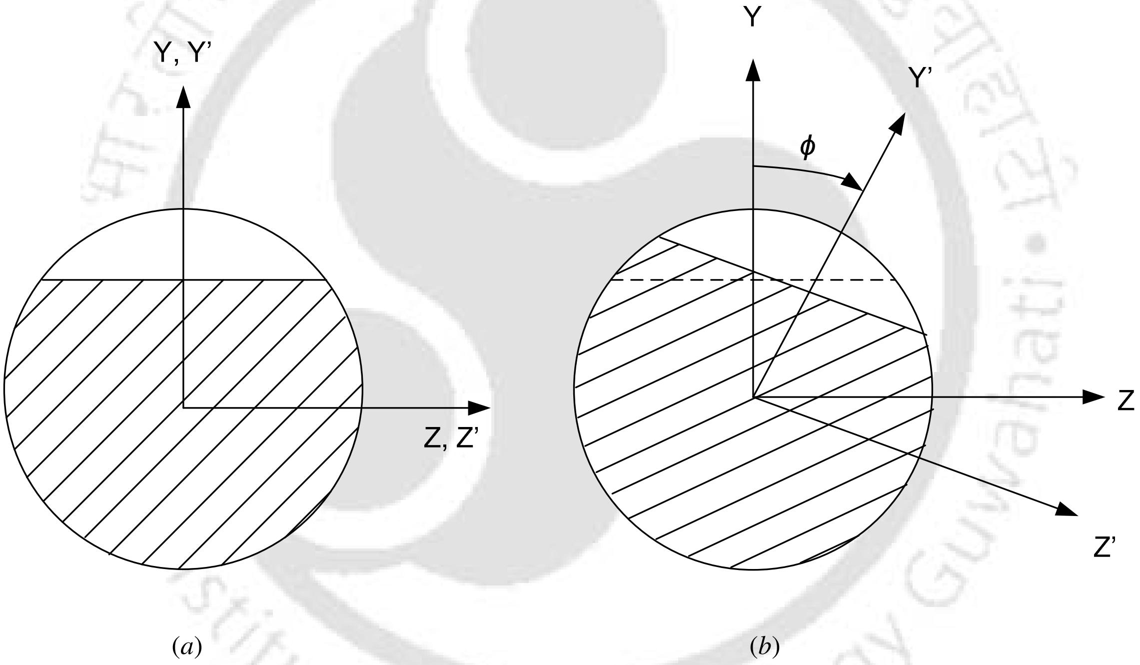

Figure 5.1: Crack orientation angle ϕ, (a) $\phi = 0$ (b) $\phi > 0$.

The co-ordinate axis $X - Y - Z$ in Figure 5.1 is the stationary co-ordinate system. The forcing to the system is applied along the *Y*-axis. The rotating co-ordinate axis $X^{'} - Y^{'} - Z^{'}$ is fixed with the crack orientation front. The angular displacement of $X^{'} - Y^{'} - Z^{'}$ with respect to $X - Y - Z$ is the crack orientation angle, ϕ , of a crack. The forcing f_y applied in the Y direction in $X-Y-Z$ co-ordinate system and its components can be represented in $X^{'}-Y^{'}-Z^{'}$ co-ordinate system by,

$$\begin{Bmatrix} f_y \\ 0 \end{Bmatrix} \rightarrow \begin{Bmatrix} f_y \cos\phi \\ -f_y \sin\phi \end{Bmatrix}. \tag{5.1}$$

The flexibility matrix of the cracked element in the $X^{'}-Y^{'}-Z^{'}$ co-ordinate system is same as Eqn. (2.8). Hence, the response of the shaft in the $X^{'}-Y^{'}-Z^{'}$ co-ordinate system can be generated for a forcing given by Eqn. (5.1) and governing Eqn. (2.12). Let the deflection of the shaft in $Y^{'}$ direction is represented by $q_{y'}$ and the deflection of the shaft in the $X^{'}$ direction is represented by $q_{x'}$. Shaft deflections in the $X-Y-Z$ co-ordinate system could be obtained as,

$$\begin{Bmatrix} q_y \\ q_x \end{Bmatrix} = \begin{bmatrix} \cos\phi & -\sin\phi \\ \sin\phi & \cos\phi \end{bmatrix} \begin{Bmatrix} q_{y'} \\ q_{x'} \end{Bmatrix}. \tag{5.2}$$

Responses for a cracked shaft with a single crack of crack depth ratio 0.7, crack orientation angle $\varphi = 45°$, and located at finite element 35, are given in Figure 5.2. Forcing is along the *Y*-axis (vertical direction). The shaft has horizontal direction response also because motions in two orthogonal planes (i.e., the vertical and horizontal planes) are coupled due to the crack.

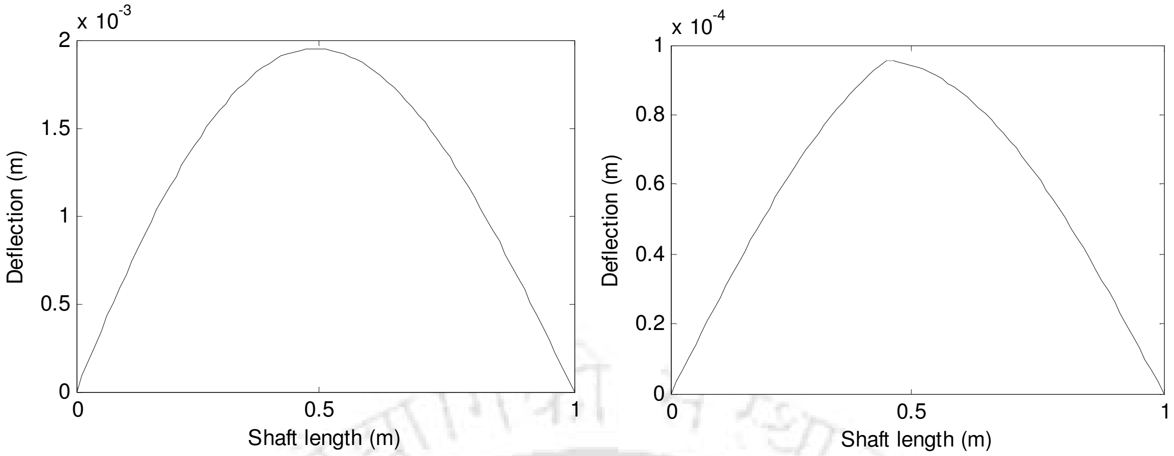

(b) Vertical response of the shaft.

(b) Horizontal response of the shaft.

Figure 5.2: Cracked shaft response for the crack orientation angle of $\varphi = 45°$.

5.3 Detection and Localization of Breathing Cracks

In this section, the MCDLA of Section 3.2 is tested for a shaft with rotated cracks. Crack probability functions, for a shaft with a single crack of crack depth ratio of 0.7, located at finite element number of 35, and the crack orientation angle of $\phi = 45^{\circ}$ is shown in Figure 5.3. Other system parameters in simulation are same as of Simulation-I in Table 3-1. Peak in the *CPF* values are coming at the crack location.

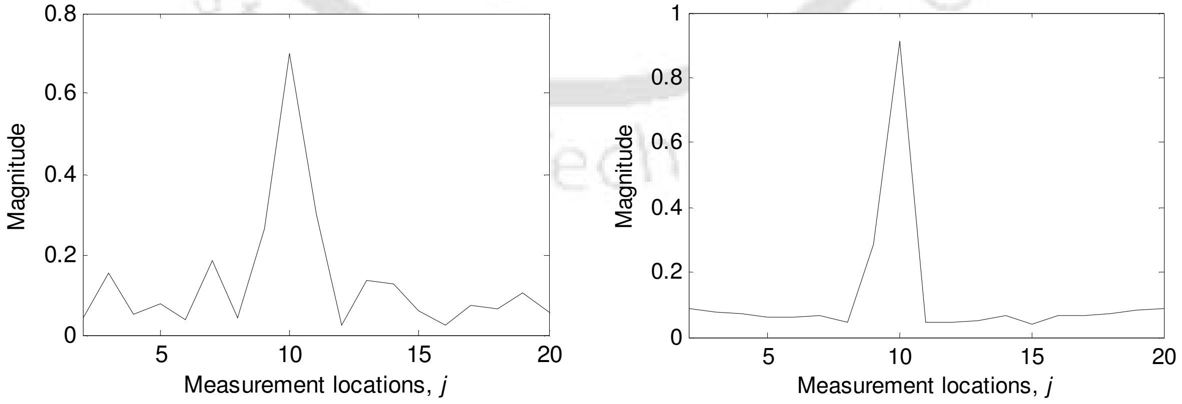

(a) CPF_v

(b) CPF_h

Figure 5.3: Crack probability functions for the shaft with a single crack of the crack depth ratio of 0.7 and the crack orientation angle of $\phi = 45^{\circ}$.

Crack probability functions for a shaft with two cracks are shown in Figure 5.4. The crack orientation angle of both the cracks is taken to be $\phi = 45^{\circ}$. Other parameters are same as for Simulation-I in Table 3.1 and Table 3-2. Again, peaks in the *CPF* values came at the crack locations.

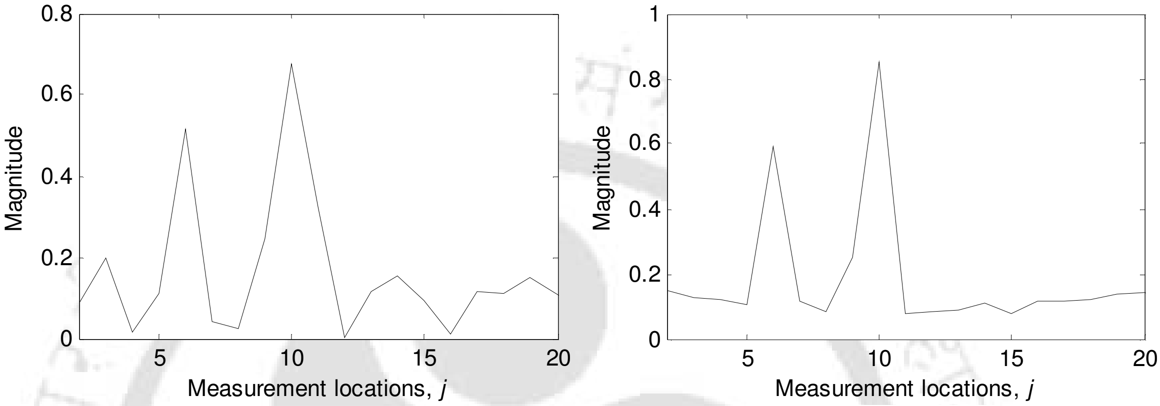

(a) CPF_v (b) CPF_h

Figure 5.4: Crack probability functions for the shaft with two crack of crack depth ratio 0.6 and 0.7, and crack orientation angle of $\phi = 45^{\circ}$.

Hence, the MCDLA (Section 3.2) is working fine for a shaft with rotated cracks. In the next section, a method is proposed for the estimation of crack orientation angle of open rotated cracks.

5.3.1 Estimation of the Crack Orientation Angle

For cracks with unknown orientations, the MCDLA (Section 3.2) will give the approximate location of the cracks. The optimization problem, defined in Section 4.6, handles two variables per crack (the size and the location of cracks). Also, objective functions (Eqn. (4.12)) of the optimization problem involve FEM predicted cracked shaft responses and measured cracked shaft responses. FEM predicted cracked shaft responses can be obtained if crack orientation angles are known. In the present section, a method is presented for estimation of the crack orientation angle of cracks. It uses the MCDLA, presented in Section 3.2.

Coefficients a_v^{II} and a_h^{II} for a cracked shaft, with a crack at the element number 35 and the crack depth ratio of 0.7, are plotted in Figure 5.5. Other system parameters such as length and diameter of the shaft remain same as in Simulation-I of Table 3-1. However, the noise is not added in the shaft response.

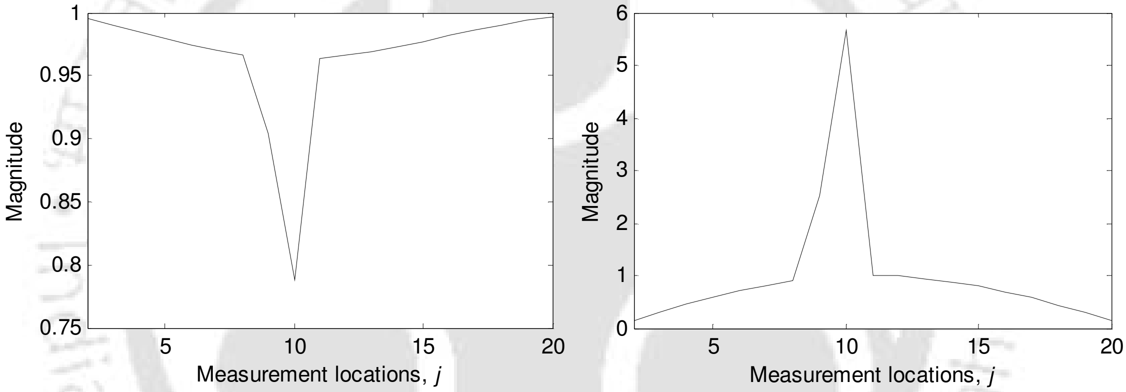

(a) a_v^{II} (b) a_h^{II}

Figure 5.5: Coefficients a_v^{II} and a_h^{II} from responses at the excitation frequency of 100 rad/s.

From Figure 5.5, coefficients a_v^{II} and a_h^{II} have peaks at the location of crack. This indicates presence of a single crack in the shaft. The magnitude of peaks in Figure 5.5 (a) and Figure 5.5 (b) vary with the crack orientation angle. These variations (i.e. the magnitude of the peak versus the crack orientation angle) are plotted in Figure 5.6. The coefficients a_v^{II} show a sinusoidal variation with the crack orientation angle, while coefficients a_h^{II} show a stepwise variation with the crack orientation angle. The coefficients a_v^{II} attain minimum at angles 23° and (180+23)°

whereas maximum at angles (90+23)° and (270+23)°. Also, the coefficient, a_h^{II}, changes its sign at angles 23°, (90+23)°, (180+23)°, and (270+23)°.

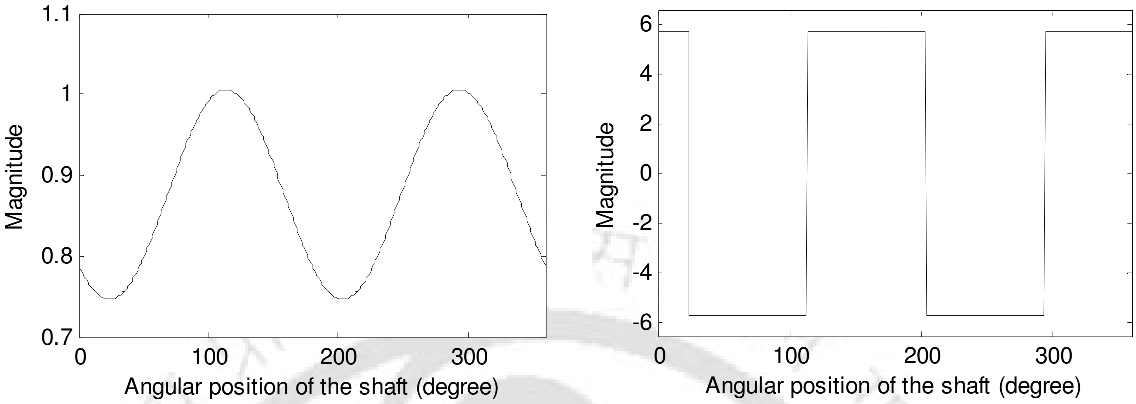

(a) a_v^{II} (b) a_h^{II}

Figure 5.6: Peak value variations in coefficients at excitation frequency of 100 rad/s for (a) a_v^{II} and (b) a_h^{II}

Peak value variations of coefficients a_v^{II} and a_h^{II} with angular position of the shaft at the excitation frequency of 50 rad/s is plotted in Figure 5.7. Again the angle at which the coefficient a_v^{II} attains minimum and coefficient a_h^{II} changes sign remain the same. Hence, it does not depend upon the excitation frequency.

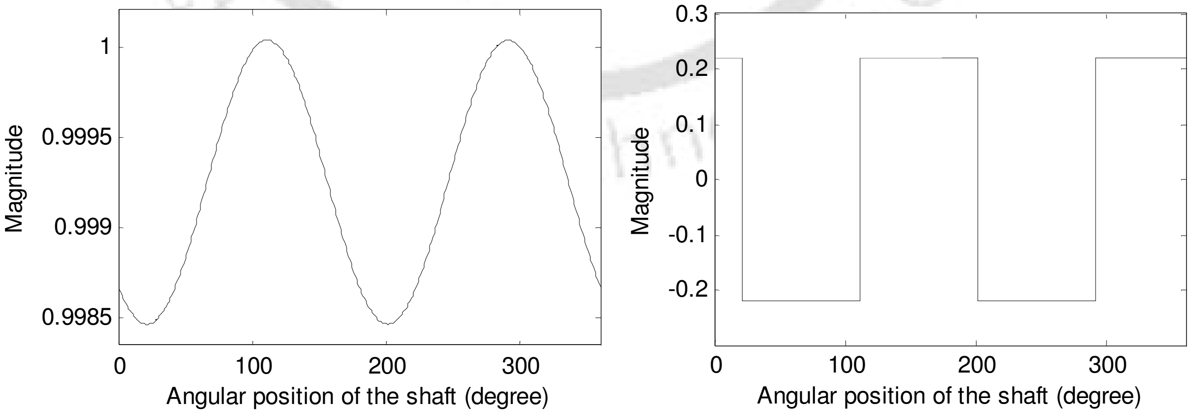

(a) a_v^{II} (b) a_h^{II}

Figure 5.7: Peak value variations in coefficients at excitation frequency of 50 rad/s (a) a_v^{II} and (b) a_h^{II}

Peaks in coefficients a_v^{II} and a_h^{II} have highest values for the crack orientation angle of $\phi = 23°, (180+23)°$ and the lowest value for $\phi = (90+23)°, (270+23)°$. From Figure 5.5 (b) and Figure 5.6 (b), coefficients a_h^{II}, obtained from the shaft response in the horizontal direction, have positive values at $\phi = 23°, (180+23)°$ and negative values at $\phi = (90+23)°, (270+23)°$. This information can be used to find out the orientation of cracks. For this, it is proposed to get the coefficients a_v^{II} and a_h^{II} at regular angular positions of the shaft. This can be obtained by either rotating the shaft by small incremental angles or by rotating the exciter (by which the shaft is getting the sinusoidal excitation).

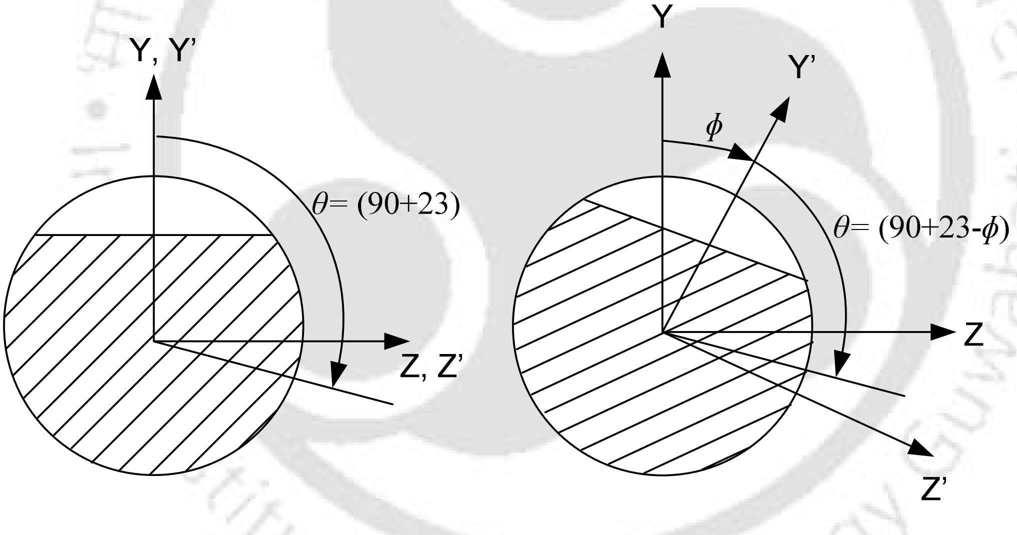

(a) (b)

Figure 5.8: Estimation of crack orientation angle ϕ. (a) $\phi = 0°$, (a) $\phi \neq 0°$.

Let the shaft is rotated gradually with small increments and the shaft response is measured after each increment. If the crack front is initially aligned with the *Y*-axis (Figure 5.8 (a)), it would take θ = (90+23)° rotation of the shaft to get the maximum in the coefficients a_v^{III}. Whereas if the initial angular displacement of the crack front with respect to *Y*-axis is ϕ (Figure

5.8 (b)), it would take $\theta = (90+23- \phi)°$ rotation of the shaft to get the minimum in coefficients a_v^{III}. Hence if minimum of the coefficients a_v^{III} are obtained after θ rotation of the shaft, initially the crack front must be at an angular position of $(90+23- \theta)°$ with respect to the *Y*-axis. Since there are two maxima in the coefficients a_v^{III}, the two possible values for the initial angular position of the crack would be $(90+23- \theta)°$ and $(270+23- \theta)°$. But the shaft response for the two possible initial angular positions would be same. It is explained in Figure 5.9. For $\theta = 68°$, the shaft responses are plotted for $\phi = (90+23- 68 = 45)°$ and $\phi = (270+23- 68 = 225)°$. The two shaft responses are exactly same. Hence, it is expected that with known orientation of the cracks, the optimization problem (Section 4.6) will give the size and accurate locations of the cracks, since the number of variables remained the same.

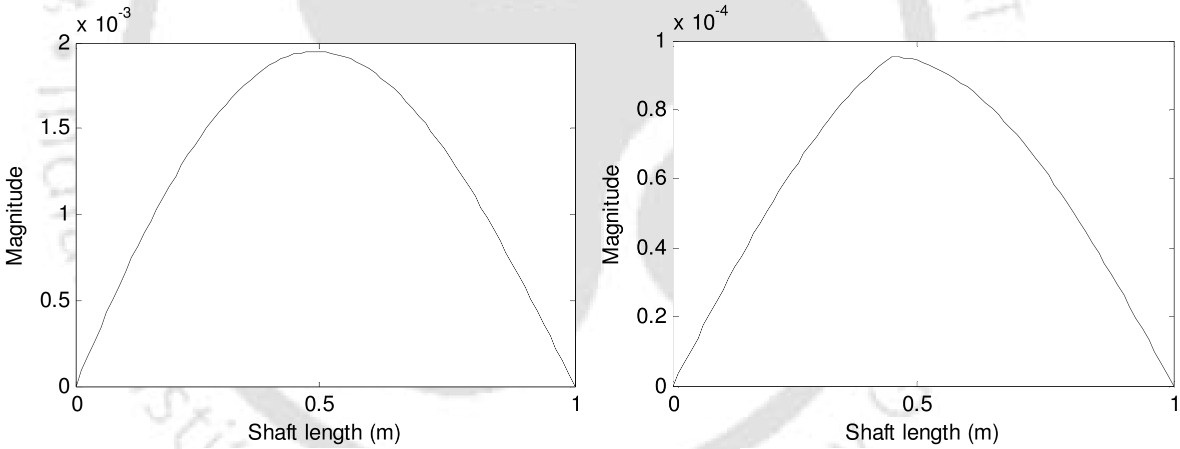

(a) Vertical response (b) Horizontal response

Figure 5.9: The cracked shaft response for the crack orientation angle $\phi = 45°$ and $\phi = 225°$ (the two responses are same hence they are overlapping).

Finding the orientation of cracks alone is not a very important issue, but with crack orientation unknown, it takes one extra variable (per crack) to be solved to get the crack size information which is the most vital. The crack model considered for the present case is an open crack, which remains open for all degree of shaft rotation. For actual fatigue cracks, when displacements due to weight of the shaft dominates the vibration amplitude, cracks will be breathing cracks which open and closes depending upon its angular orientation. When cracks are fully in compression region, the cracks will be fully closed and the stiffness of the shaft element containing the crack would be same as that of the intact shaft. Hence, cracks would go undetected by any vibration based condition monitoring system and this can be dangerous. Also when the shaft is partially open and partially closed, the effect of cracks would be less in the dynamics of the shaft motion compared to when cracks are fully open. All the symptoms like the reduction in natural frequencies and the change in model parameters would be less. Because of this small change in system parameters, detection of cracks will be even more difficult. Hence, it is important to get the shaft response at several angular positions. At some of the angular orientation when the crack is open, the effect of crack would be more on dynamics of the shaft which will help the condition monitoring system to find out crack parameters. Hence, taking the shaft response at several angular positions of the shaft, to get the crack orientation angle, is justified.

5.3.2 Identification of the Crack Size

Assuming that the crack orientation angle of the rotated cracks is known, the optimization problem (Section 4.6) can be attempted again to get the size of the cracks and their locations. *CPF*s, for the cracked shaft parameters of Simulation-I (Table 3-1 and Table 3-2) and with crack orientation angles of both the cracks $\phi = 45°$, are plotted in Figure 5.4. Results of the optimization problem (Section 4.6) are plotted in Figure 5.10. Here β_1 and β_2 are locations of the first crack and the second crack respectively, β_3 and β_4 are sizes of the first crack and the second crack respectively. The converged values of crack parameters are

$(\beta_1, \beta_2, \beta_3, \beta_4)_{31} = (21, 35, 0.61, 0.70)$ which is very close to the actual crack parameters $(\beta_1, \beta_2, \beta_3, \beta_4) = (21, 35, 0.60, 0.70)$.

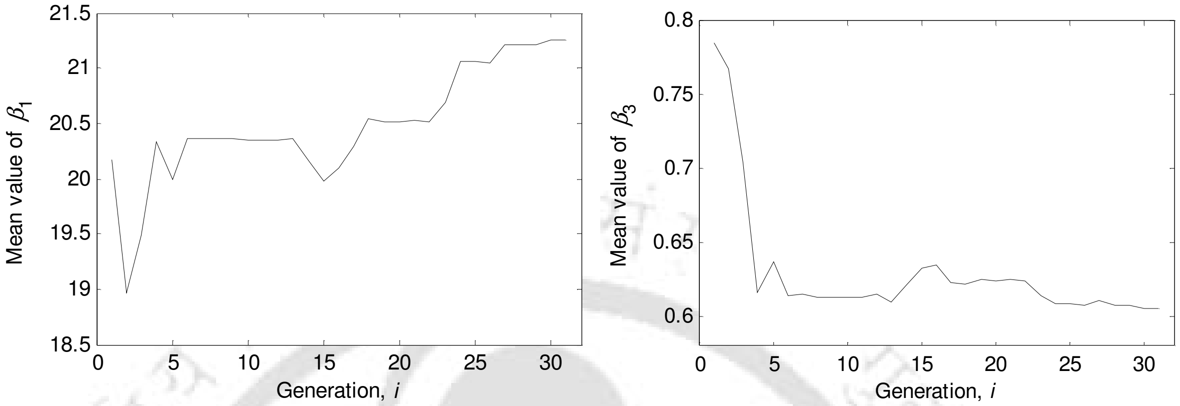

(a) First crack location, β_1

(a) First crack size, β_3

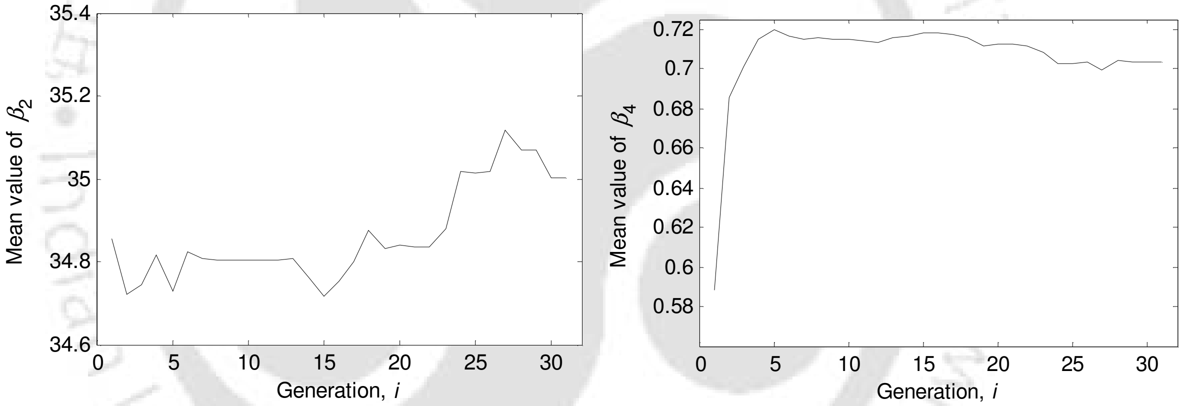

(a) Second crack size, β_2

(a) Second crack size, β_4

Figure 5.10: Convergence of crack parameters for numerical Simulation-I with the crack orientation angle $\varphi = 45°$.

For weight dominated rotors, the fatigue cracks show breathing behavior, i.e. the crack will open and close gradually with the rotation of the shaft. In the next section, shaft responses are generated by calculating the stiffness of a rotated crack by using the breathing crack model.

5.4 Identification of Breathing Cracks

In the present section, the breathing crack model is used to get the stiffness of a rotated crack. In the present work, since the shaft is non-rotating the crack does not breathe. Breathing model is used to find the stiffness of the shaft at a particular angular position. For a heavy shaft, since a portion of the crack which is open, and hence the flexibility due to the crack will depend upon the angular position of the crack. The MCDLA (Section 3.2) is tested for the single-cracked shaft and the double-cracked shaft. A method is proposed for the estimation of crack orientation angle of the rotated cracks. Finally, the MCLSA (Section 4.6) is used for the estimation of size and location of cracks.

5.4.1 Shaft Responses for Breathing Cracks

In Sections 5.2.1 and 5.3.1, cracks are assumed to be open, i.e. cracks will remain open for all the angular positions of the shaft. For actual fatigue cracks, the crack will open and close according to the rotation (i.e., the angular position) of the shaft. The crack will be fully open when it is entirely in the tension region, while the crack will be fully closed when it is entirely in the compression region (Figure 5.11). The local compliance of the crack varies periodically with the rotation of the shaft. This model of crack is good for modeling the breathing behavior of the crack when the static deflection due to weight of the rotor is more than vibrations due to unbalanced forces. This is valid for most of the turbine and generator shafts. In other case, when the vibration amplitude dominates the displacements due to gravity, the problem becomes non-linear and that case is not considered here.

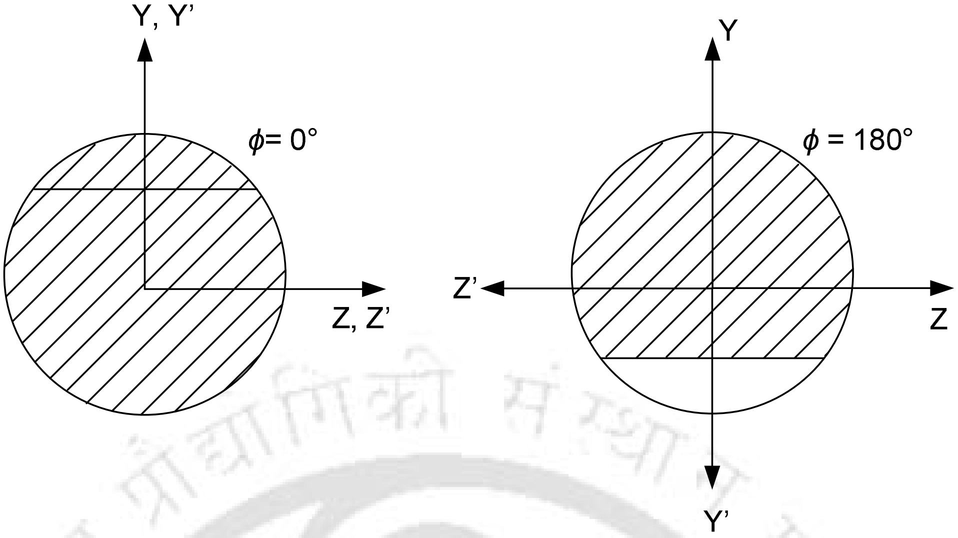

Figure 5.11: Fully closed and fully open states of a breathing crack.

Papadopoulos and Dimarogonas (1988) represented the variation of the stiffness of the cracked element by truncated cosine series.

$$[K]=[K_0]+[K_1]\cos\phi+[K_2]\cos 2\phi+[K_3]\cos 3\phi+[K_4]\cos 4\phi \tag{5.3}$$

$[K_\eta]$, $\eta=0,\ 1,\ \ldots,\ 4,$ are fitting compliance matrices determined from the known behavior of the stiffness matrix at certain angular orientations and slopes of the stiffness at the fully open and fully closed states of crack. For the breathing crack model presented here, the reference axis is chosen in such a way that the crack orientation angle is 180°, when the crack is fully open. Variation of the stiffness of cracked element with the angular position of the shaft is given in Figure 5.12. The cracked-shaft response of a shaft with a single crack of crack depth ratio 0.6, located at finite element number 35, and for the crack orientation angle of $\phi=45^\circ$ is shown in Figure 5.13. Coefficients a_v^{II} and a_h^{II} are plotted in Figure 5.14. Variation of peaks of coefficients a_v^{II} and a_h^{II} with the angular position of the shaft is plotted in Figure 5.15.

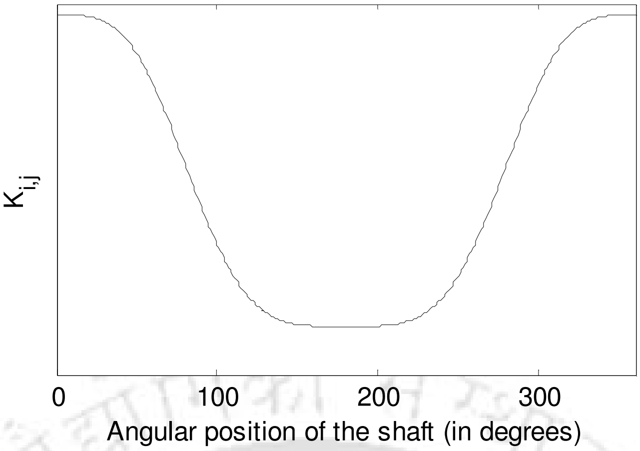

Figure 5.12: The variation of the stiffness of the cracked element with the shaft angular position.

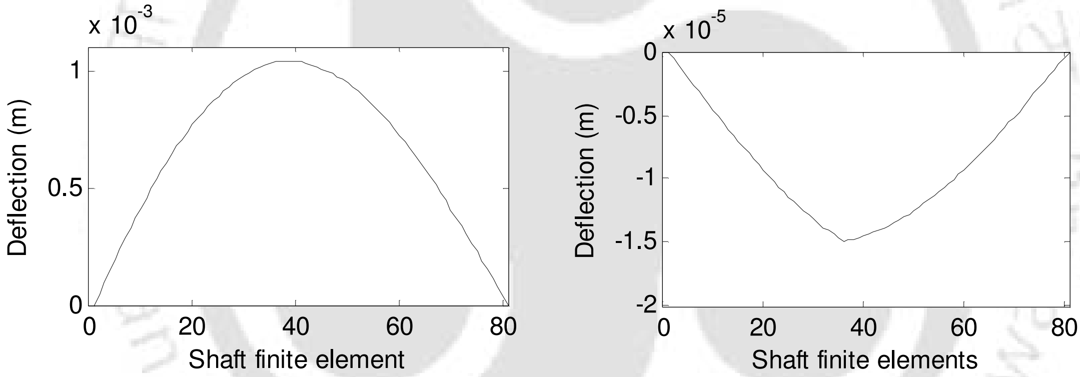

(a) Vertical response

(a) Horizontal response

Figure 5.13: Cracked shaft responses for the crack orientation angle of 45° for a single crack of the crack depth ratio 0.6.

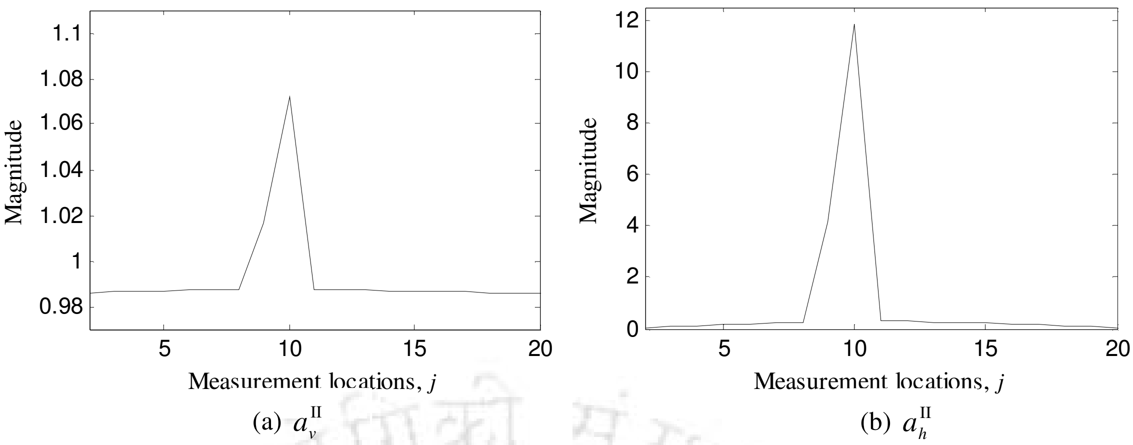

(a) a_v^{II} (b) a_h^{II}

Figure 5.14: Coefficients a_v^{II} and a_h^{II} at the excitation frequency of 100 rad/s.

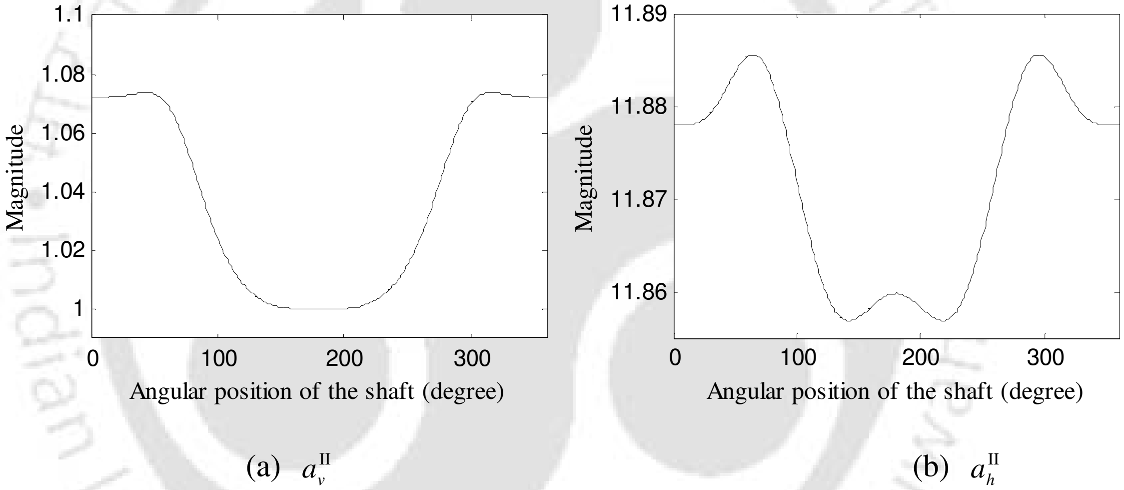

(a) a_v^{II} (b) a_h^{II}

Figure 5.15: Peak value variations in coefficients a_v^{II} and a_h^{II} at the excitation frequency of 110 rad/s.

From Figure 5.12 and Figure 5.15, it can observed that the variation of the peak value in co-efficients a_v^{II} and a_h^{II} with the shaft angular position are similar to that of the stiffness of the cracked element, $K_{i,j}$.

5.4.2 Detection and Localization of Breathing Cracks

In this section, the MCDLA of Section 3.2 is tested for breathing cracks using the numerical simulation. In the first simulation example, a single crack of crack depth ratio 0.6 and crack orientation angle 45° is considered. The location of crack is taken to be finite element number 21. *CPF*s of the simulation example are given in Figure 5.16. Crack probability functions for a shaft with two cracks of the crack depth ratios 0.6 (at finite element number 21 and crack orientation angle of 10°) and 0.7 (at element number 35 and crack orientation angle of 45°) are shown in Figure 5.17. In both the simulation example, the algorithm detects cracks very well as peaks in the *CPF* values comes at crack locations.

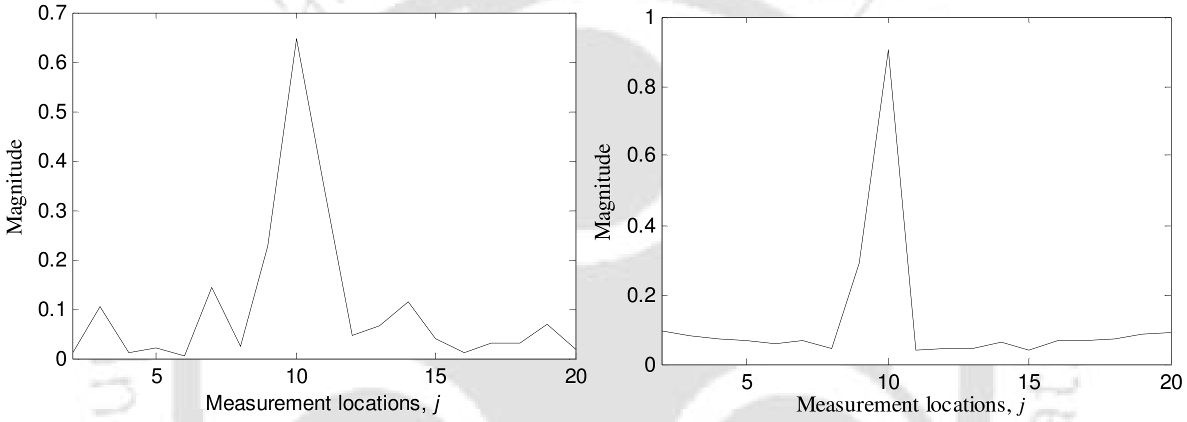

(a) CPF_v (b) CPF_h.

Figure 5.16: Crack probability functions for a shaft with a crack of the crack orientation angle, 45°.

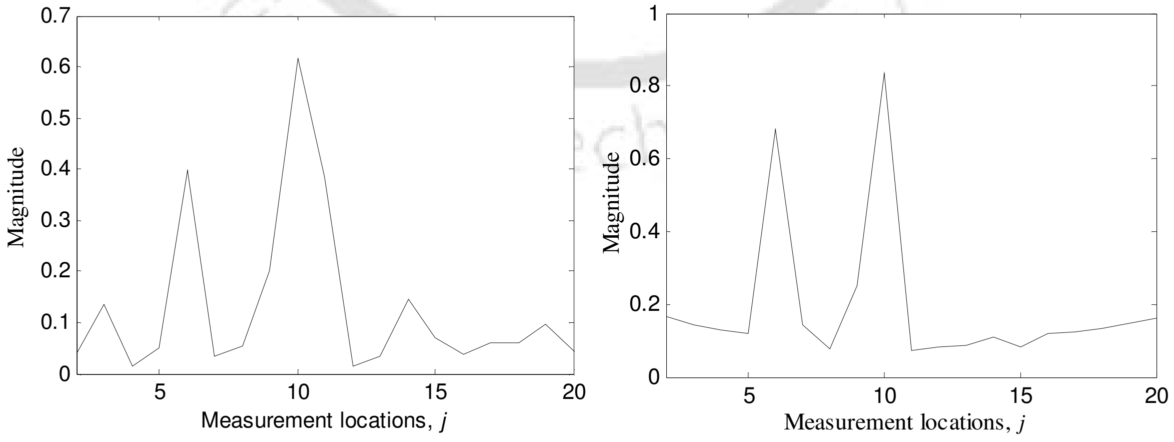

(a) CPF_v (b) CPF_h.

Figure 5.17: Crack probability functions for a shaft with two cracks.

In the next section, an algorithm is presented for estimating the crack orientation angle of the breathing cracks. Estimation of crack orientation angle is important for the optimization problem given in Section 4.6.

5.4.3 Estimation of Crack Orientation Angle of Breathing Cracks

The estimation of crack orientation angle for open cracks was presented in Section 5.3.1. In the present section, an algorithm is presented for estimation of the crack orientation angle of breathing cracks. Presence of a crack in the shaft causes a slope discontinuity in the elastic line of the shaft (Section 3.2). This slope discontinuity has different values for different orientations of the crack. This information is used to find out the crack-orientation angle of cracks present in the shaft. Coefficients a_v^{II}, for a shaft with single crack at finite element number 35 is are plotted in Figure 5.18 (a). Crack depth ratio and the crack orientation angle of the crack is taken to be 0.7 and of 0°, respectively. Peak in coefficients a_v^{II} is present at the location of crack. The location of crack over the shaft length can be obtained from crack probability functions also.

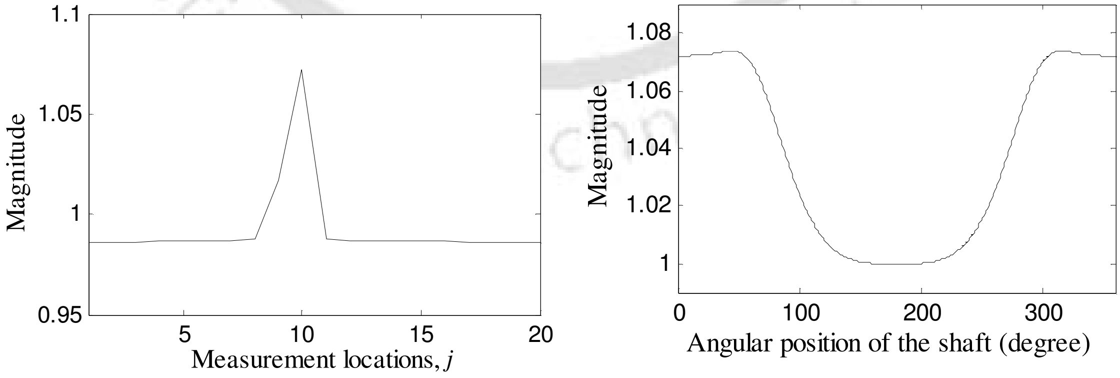

(a) (b)

Figure 5.18: Coefficients a_v^{II} for a shaft with a single crack at 50 rad/s of excitation frequency, (a) variation with the shaft length, (b) variation of peak value in a_v^{II} with the angular position of the shaft.

Since the amount of slope discontinuity due to the crack depends upon the orientation of the crack, the magnitude of the coefficient a_v^{II} has different values for different orientations of the crack. Variation of the peak value of coefficient a_v^{II} with respect to the angular position of the shaft is plotted in Figure 5.18(b). It is obtained by plotting the magnitude of a_v^{II} at 10th measurement location for different angular position of the shaft, shown in Figure 5.18 (a). For Figure 5.18 (b), the crack orientation angle is 0°. Figure 5.18 (b) could be used as a database for finding out the crack orientation angle of a rotated crack. For measuring the crack orientation angle of a rotated crack, suppose that the transverse vibrations of the shaft are measured at various angular orientations of the shaft. Now, when the crack-orientation angle of the crack would have been -α° instead of 0°, the pattern of Figure 5.18 (b) would have started after α° rotation of the shaft. Hence, for the identification of crack orientation angle in actual measurements, if the pattern of Figure 5.18 (b) comes after α° rotation clockwise of the shaft, the crack orientation angle must be -α°.

As an example, let for the above case (i.e., for a single crack at element number of 35, and crack depth ratio of 0.7), the crack orientation angle is -90°. For this, the variation of the coefficient a_v^{II} (at measurement location 10) with respect to the shaft orientation angle is plotted in Figure 5.19.

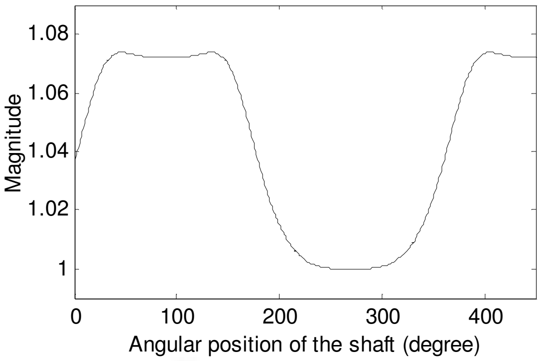

Figure 5.19: The variation of peak value in a_v^{II} with the angular position of the shaft for a crack of the crack orientation angle = -90°.

Now for the identification of the crack orientation angle from Figure 5.19, Figure 5.18 (b) should be treated as a database. In Figure 5.19, the pattern of Figure 5.18 (b) starts after 90° rotation of the shaft. Hence the crack orientation angle of the crack should be -90°.

The crack orientation angle can be determined even if more than one breathing crack is present in the shaft. To demonstrate this, a shaft with two breathing cracks is considered. System parameters (other than the crack orientation angles) are taken to be same as those of Simulation-I of Table 3-1 and Table 3-2.

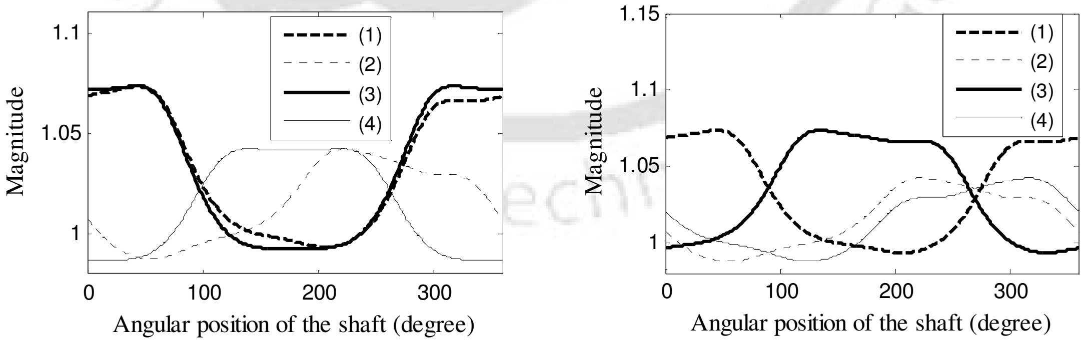

(a) (b)

Figure 5.20: Variation of peak values of the coefficients a_v^{II} with the angular position of the shaft (a) Crack orientation angle of the second crack is changed (b) Crack orientation angle of the first crack is changed.

The variation of the peak value of the coefficient a_v^{II}, at 50 rad/s of excitation frequency, is plotted in Figure 5.20. For Figure 5.20 (a) and Figure 5.20 (b), legends (1) and (2) together refer to one set of data while legends (3) and (4) together refer to another set of data. Description of the legends in Figure 5.20 (a) is as follows.

(1) – First crack, *crack orientation angle* - 0°
(2) – Second crack, *crack orientation angle* - 90°
(3) – First crack, *crack orientation angle* - 0°
(4) – Second crack, *crack orientation angle* - 180°.

Description of legends in Figure 5.20 (b) is as follows.

(1) – First crack, *crack orientation angle* - 0°
(2) – Second crack, *crack orientation angle* - 90°
(3) – First crack, *crack orientation angle* - 180°
(4) – Second crack, *crack orientation angle* - 90°.

In Figure 5.20(a), initially, the crack orientation angles of the first crack and the second crack are kept at 0° and 90°, respectively. After that the crack orientation angle of the first crack is kept same but for the second crack it is changed to 180° (i.e., rotated by 90°). It can be seen from Figure 5.20 (a) that the curve corresponding to the second crack also shifts, with some distortion, by 90°. The curve corresponding to the first curve is almost unaffected. Similarly, for a second example shown in Figure 5.20(b), the crack orientation angle for the second crack is kept same while for the first crack it is changed to 180°. The corresponding curve also shifts by 180°. Hence, it shows that for the multi-cracked shaft, the crack orientation angle of one crack could be found out independent of crack parameters of other cracks. For methods based on natural frequencies, the changes in natural frequencies are a combined effect of crack parameters of all the cracks present in the shaft.

5.4.4 Identification of Crack Size

Assuming that approximate locations of the cracks are known using the MCDLA presented in Section 3.2, the location and size of cracks can be obtained using the multi-objective genetic algorithm described in Section 4.6. The number of decision variables per crack is same, because it is assumed that the crack orientation angle is obtained from the procedure outlined in Section 5.4.3.

A double-cracked shaft is considered for the numerical simulation example. The crack depth ratio, location, and crack orientation angle of the first crack are 0.6, 21, and 45° respectively. For the second crack, the crack depth ratio, location and crack orientation angle are 0.7, 35, and 90° respectively. Other parameters are same as Simulation-I in Table 3-1. Simulation results are presented in Figure 5.21. For the simulated example, converged results for crack parameters are $(\beta_1, \beta_2, \beta_3, \beta_4)_{31} = (21, 35, 0.60, 0.70)$. These results are matching with actual crack parameters, as finite elements corresponding to the two cracks are 21 and 35, and the crack depth ratio of the two cracks were chosen to be 0.6 and 0.7.

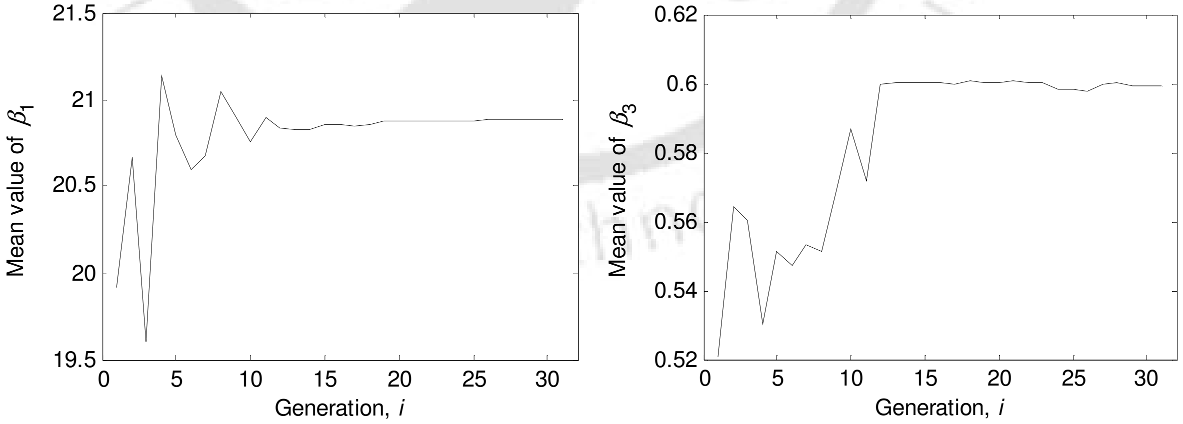

(a) First crack location, β_1 (b) First crack size, β_3

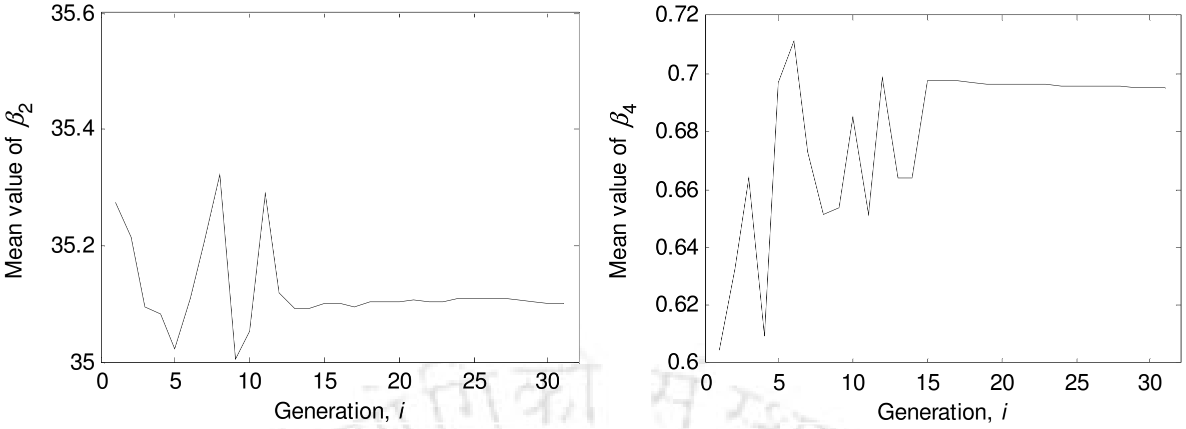

(c) Second crack location, β_2 (d) Second crack size, β_4

Figure 5.21: Convergence of crack parameters for numerical Simulation-I.

In Sections 5.2 and 5.4, the MCDLA (Section 3.2) is tested for rotated cracks. Both the open crack model as well as the breathing crack model is used to get the stiffness of rotated crack at any crack orientation angle. Methods are suggested for estimating the crack orientation angle. Finally optimization problem (Section 4.6) is used to get the size and location of rotated cracks.

The MCDLA is based upon detecting the slope discontinuity present in the elastic line of the shaft. However, steps present in a shaft will also produce slope discontinuity in the elastic line of the shaft. Hence, it would be appropriate to see the working of the MCDLA for a stepped shaft. In the next section, the MCDLA is tested for a stepped shaft.

5.5 Detection and Localization of Cracks in a Stepped Shaft

Steps in a shaft are provided to fulfill different requirements such as mounting the gears, sprockets, pulleys and bearings. This causes stress concentration in the shaft near the steps. Occurrence of cracks is more favorable near the region of stress concentration. This necessitates the study of detecting cracks in stepped shaft, especially the situation when crack is near a step, since these (step) locations are more favorable for the occurrence of cracks.

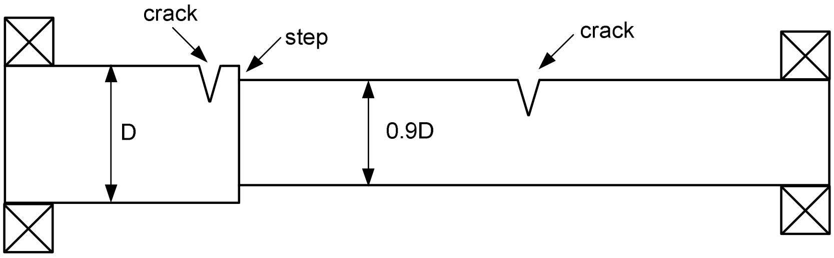

Figure 5.22: A stepped shaft with two cracks.

In a numerically simulated example, a stepped shaft (shown in Figure 5.22) of 0.01m diameter and 1 m length is considered. Although the MCDLA (Section 3.2) works with responses measured at several frequencies, for explaining the working of the algorithm for stepped shaft, initially a single frequency forcing is used for the shaft excitation and also the measurement noise is not considered. Next, the identification examples are taken with responses at several frequencies and noise added in it (to mimic the actual experimentation).

In the first example, a stepped shaft is considered with a single crack. The step in the shaft is considered near the 7th measurement location while the crack is taken near the 12th measurement location. Hence, for this case the crack is located far from the step. The size of step is given in Figure 5.22. The crack depth ratio and the crack orientation angle for the crack are taken to be $\alpha_1 = 0.6$ and $\phi_1 = 0°$, respectively. Coefficients a^{I}_{cv} and a^{I}_{wcv}, obtained at 50 Hz of excitation frequency, are plotted in Figure 5.23(a). Normalized coefficients, a^{II}_{v}, are plotted in Figure 5.23(b). It is evident from Figure 5.23(a) that the effect of step is not there in the normalized coefficients. From Figure 5.23(a), since the slope discontinuity at the location of step is almost same in both the shafts (intact as well as the cracked) its effect is canceled during normalization. But at the location of the crack, only the cracked shaft has the slope discontinuity which gives a peak in the normalized coefficients at the location of crack. For the application of the algorithm to real cracked shaft, presence of step in the shaft would be known; hence it can be taken into account while modeling the shaft for getting the intact shaft response.

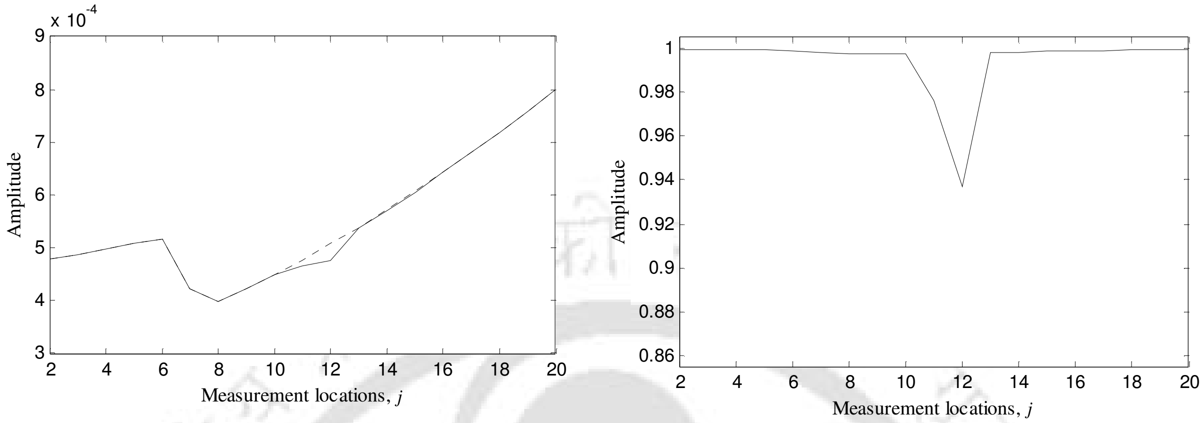

(a) Coefficients a_{cv}^{I} (-) and a_{wcv}^{I} (--)

(b) coefficients, a_{v}^{II}

Figure 5.23: Quadratic coefficients for the first example (step near 7th location, one crack of crack depth ratio 0.6 near the 11th measurement location).

In the second example, two cracks are considered. While keeping all other parameters same as in the above example, the second crack is chosen to be very near to the step. Resulting values of coefficients a_{cv}^{I} and a_{wcv}^{I} are plotted in Figure 5.24(a), and normalized coefficients a_{v}^{II} are plotted in Figure 5.24(b). For the crack located far from the step, the normalization is similar to previous example. For the crack near the step, the slope discontinuity in both shafts are not same and hence the slope discontinuity of the cracked shaft is not canceled out completely while normalization. Hence, it gives a peak near the location of the crack. In the above two examples the crack orientation angles for the two cracks are taken to be zero. Next, the above two examples are presented with measurement noise added in the shaft response.

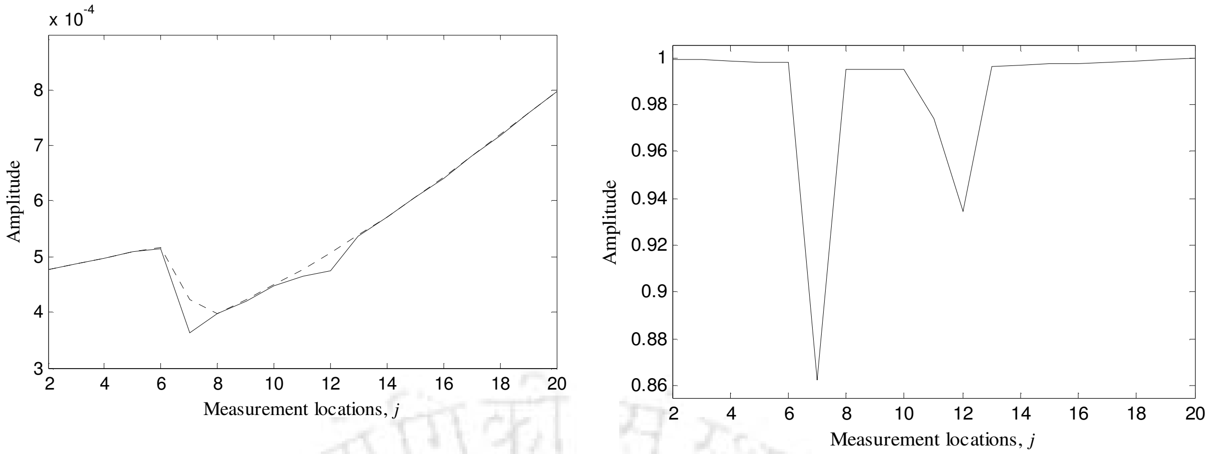

(a) Coefficients a^{I}_{cv} (-) and a^{I}_{wcv} (--)

(b) coefficients, a^{II}_{v}

Figure 5.24: Quadratic coefficients for the second example (step near 7th location, two cracks of crack depth ratios 0.6 each and located near the 7th and11th measurement location.

In Figure 5.23 and Figure 5.24, a single excitation frequency is used for explaining the working of the algorithm. In actual case, the measurement of shaft responses would be contaminated with measurement noise. Hence, to mimic the actual experimentation, 1% noise (Appendix D) is added in the shaft response. In presence of measurement noise, the presence of cracks is not evident from the plot of normalized coefficients at a single frequency. It is evident from the plot of normalized coefficients in Figure 5.25. Hence, the identification algorithm uses shaft response at several frequencies to reduce the effect of noise in the measurements. Now the crack probability functions are obtained using several excitation frequencies (5, 10, …, 110 Hz).

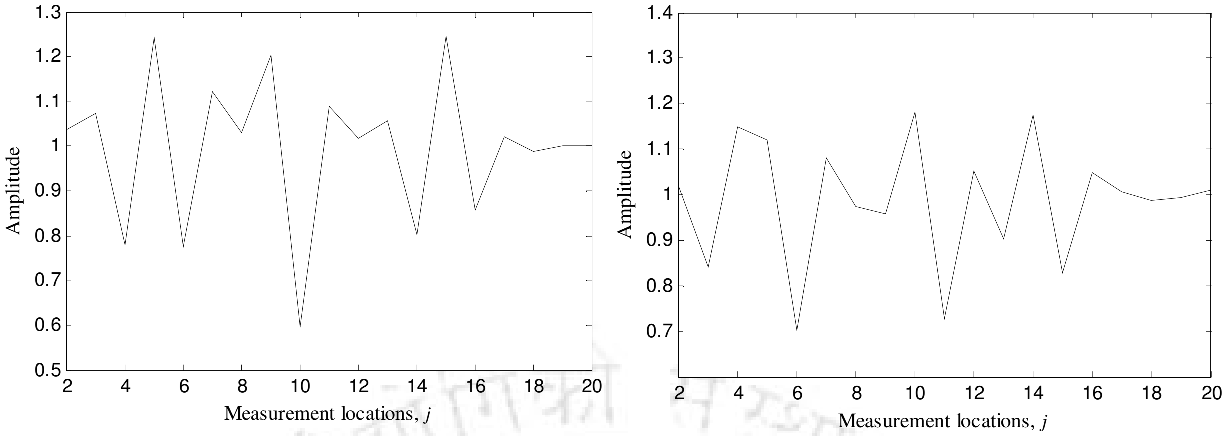

(a) Coefficients, a_v^{II} for the first example with one crack.

(b) Coefficients, a_v^{II} for the second example with two cracks.

Figure 5.25: Normalized quadratic coefficients for (a) the first example (b) the second example.

Crack probability functions for the first example (crack near measurement location 12 and step near the measurement location 7) are given in Figure 5.26(a). The crack orientation angle for the crack is taken to be 10°. For the second example (first crack near the measurement location 7 and the second near the measurement location 12 with step in the shaft near the measurement location 7) is given in Figure 5.26(b). Crack orientation angles for the first and the second crack are taken to be 10° and 45°, respectively. For both the cases the identification algorithm identifies the presence of cracks properly.

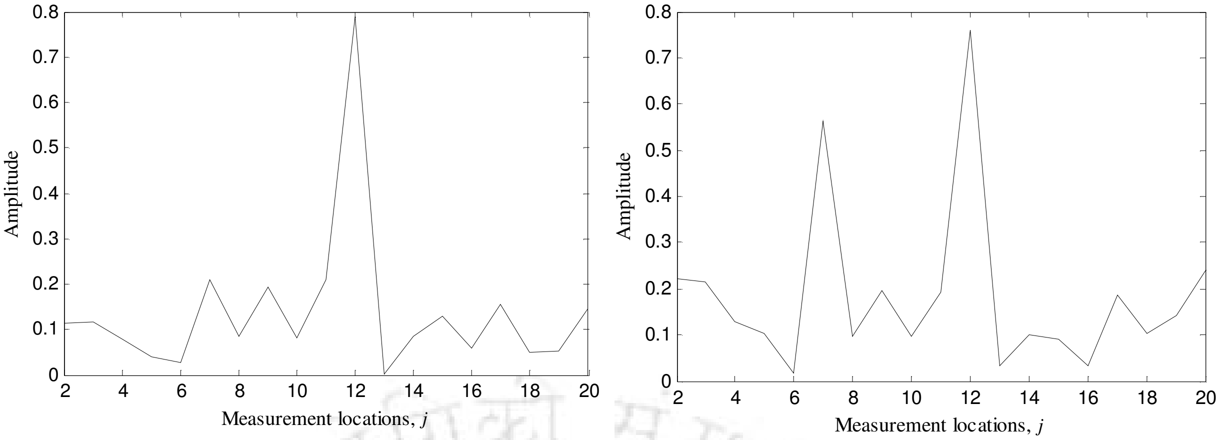

(a) *CPF* for the with one crack. (b) *CPF* for the second example with two cracks.

Figure 5.26: Crack probability functions for (a) first example (b) second example.

The MCDLA presented in Section 3.2 is based on finding the slope discontinuity in the elastic line of the shaft, caused by the presence of crack in the shaft. Although the presence of step in the shaft is also producing a slope discontinuity but its effect is neutralized during normalization because of similar slope discontinuity in the intact shaft. The special normalization technique used in the algorithm is capable of keeping only that the slope discontinuity which is arising from the crack and it is in contrast with techniques based upon the wavelet transform which will show a slope discontinuity at the location of step also.

Up to now, in Chapters 3, 4, and 5, the MCDLA (Section 3.2) and the MCLSA (the optimization problem, Section 4.6) are tested with the response of a cracked shaft obtained from the numerical simulation (FE modeling of the cracked shaft). The measurement noise is added in the shaft response to mimic the actual shaft response. In the next chapter, working of the MCDLA is tested with the measurements of the forced response from a real shaft. The procedure of experimentation on the real shaft and the results are presented in next chapter.

6 EXPERIMENTAL VERIFICATION OF THE MCDLA

6.1 Introduction

In Chapter 3, the MCDLA is presented and the algorithm is tested with numerically simulated responses of the cracked shaft. Noise was added to the cracked shaft response to mimic the actual experiments. In the present chapter, validation of the algorithm with measured responses from real cracked shaft is attempted. Experimentations were done at the vibration and acoustics laboratory at IIT Guwahati. The test setup consists of a shaft with artificially introduced cracks (slits) and supported at ends over rolling bearings. In the first attempt to verify the algorithm, proximity sensors are used to measure the responses. In the second attempt, the laser vibrometer is used to measure the shaft responses. Crack probability functions are obtained from the shaft responses from vertical direction (i.e., direction of forcing) only. The coupled horizontal direction motion would be possible if the system is excited by a non-contacted exciter (e.g. magnetic bearings), which is not attempted in the present work.

6.2 Experimental Setup and Instrumentation

The experimental setup consists of following parts:

1. Experimental setup
2. Excitation unit
3. Signal generator and power amplifier
4. Proximity probes and its amplifier
5. Rotational laser vibrometer
6. Data acquisition system

These are described in following sections in more detail.

6.2.1 Experimental Setup

The set-up used for the experimentation is shown in Figure 6.1. A mild steel shaft of circular cross-section is used for the experimentation. The shaft is supported by deep-groove ball bearings at both ends as shown in Figure 6.2. The bearings are accommodated in specially fabricated split-type bearing housings (made from rectangular mild steel plates), which provided a firm support and simple means for mounting/dismounting of bearings as well as of the shaft. A stringer is used to connect the modal exciter with the shaft. It prevents the shaft from rotation while application of the transverse force. The shaft is excited by the sine-sweep force with the help of the exciter. Transverse cracks are introduced in the shaft artificially by using a saw. Cracks made by this procedure are open cracks, i.e., the cracks will remain open for any crack orientation angle (Figure 6.3).

Figure 6.1: The test rig for the experimental crack detection.

Figure 6.2: A close view of one end of the shaft, supported by a deep-groove ball bearing.

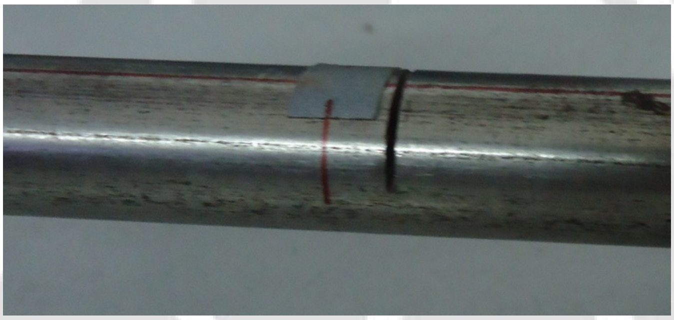

Figure 6.3 A close view of the slit-type crack.

The modal exciter is placed under the shaft at a suitable location. The exciter is placed away from locations of cracks since it is expected that effect of crack on responses would be more if the exciter is near to the crack and accordingly crack identification would be expected to be better. However, in real situation it is less likely that placement of exciter happens to be near the unknown crack location. A sensor stand is designed and fabricated to mount proximity sensors. Provisions were made to slide the sensor stand in the axial direction of the beam at various locations over the beam length.

6.2.2 The Excitation Unit

An electromagnetic exciter (B&K, Type 4808) is used in the present experiment (Figure 6.4). In an electromagnetic exciter the supplied input signal is converted to an alternating magnetic field by means of a coil which is attached to the drive part of the device (Sujatha, 2009). A force sensor is used to measure the force applied by the exciter. The exciter has force rating of 112 N sine peak (or 187 N with the cooling). The working frequency range is 5 Hz to 10 kHz and the first axial resonance is 10 kHz.

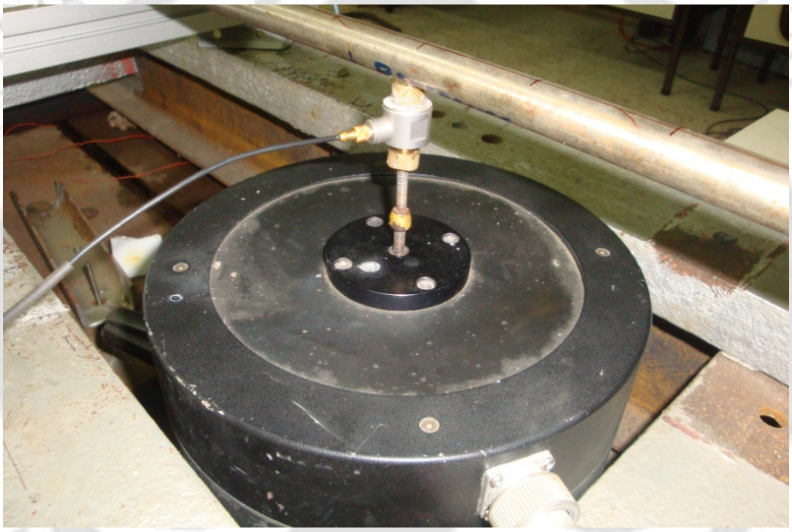

Figure 6.4: An electromagnetic exciter connected to the shaft through a stringer via a transducer.

6.2.3 Signal Generator and Power Amplifier

The necessary excitation to the shaft system is given by a modal exciter, which is operated by a signal generator module of the B&K Pulse software through a power amplifier. The generator module (B&K, Type 3107) can be used for generating various kinds of signals. The generator is designed around a digital signal processor and a 16-bit D/A converter. The frequency range is 0 to 102.4 kHz. Output levels are adjustable from 1 mV to 5V. In terms of waveforms, single and dual superimposed sine waves can be generated. Sweep-sine (continuously changing the frequency of the signal) can be used for both the sine and dual sine signals. The power amplifier - B&K, Type 2719 - is used in the present experimentation to drive the vibration exciter. It has 180VA power output, adjustable RMS output-current limit and low or high output impedance.

6.2.4 Force Transducer

The force transducer is installed directly between the exciter and the test structure being excited. The piezoelectric type of transducers is suited for measuring tensile and compressive forces. The transmitted force, or a known fraction of it, is applied directly across the crystal, which generates a corresponding charge, proportional to the force. The following are features of the force transducer (B&K, Model 2311-1), which is used in the present experiment. It is designed for the modal exciter, and to measure the compression and tension excitations. It has low impedance output and its force sensitivity is 0.227 mV/N and the maximum frequency range is 75 kHz.

6.2.5 Proximity Transducers

Bently-Nevada® 3300 eddy current probes (along with amplifiers and condition monitoring) are used for measuring the shaft displacements (Figure 6.5). They are non-contact type of sensors. They provide a voltage signal proportional to the gap between the probe tip and the shaft. It comprises of a probe, a length of extension cable and an oscillator demodulator. The proximity probe sensitivity is 7874 V/m.

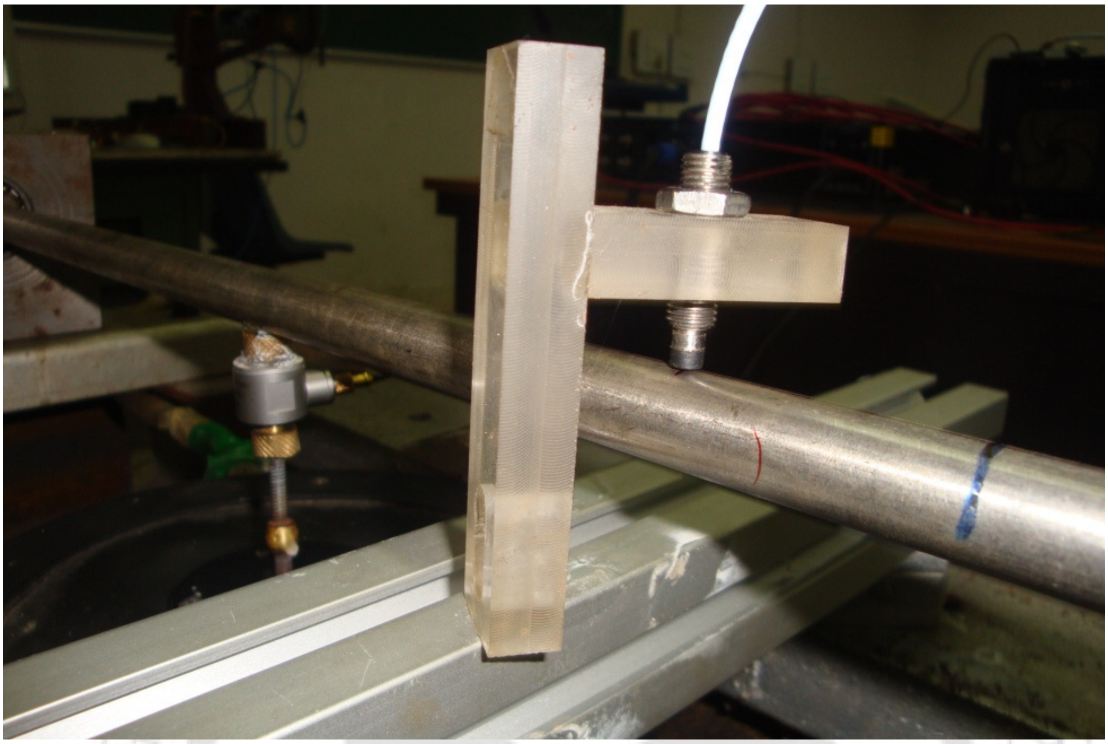

Figure 6.5: Measurement of shaft displacements using proximity sensors.

The probe stand is a specially fabricated by Perspex sheet, which had threaded holes. Proximity sensors are screwed in these holes. The stand can be fixed at any required axial position of the shaft for transverse displacement measurements.

6.2.6 Laser Vibrometer

In the second attempt to improve the accuracy of measurements, rotational laser vibrometer (RLV) is used to measure transverse vibrations of the shaft. Rotational laser vibrometer is a laser optical instrument for non-contact acquisition of rotational vibrations on rotating parts. It can be used to measure vibrations of a non-rotating part also. The RLV is made up of the controller RLV-5000 and the sensor head RLV-500. The optical measurement principle for the rotational vibrometer is based on laser interferometry. Dynamic acquisition of rotational vibrations is possible in a frequency range from 0Hz to 10 kHz.

For rotation measurements, the sensor head of the rotational vibrometer contains two interferometers aligned in parallel which acquire the translational velocity components in the direction of the respective laser beam. For translation measurements, only one channel of the rotational vibrometer is used. Also, it needs reflecting film to be applied on the surface of vibrating body. In the present work, translational vibrations are measured with single channel of the vibrometer. The rotational laser vibrometer used in the experiment is shown Figure 6.6.

Figure 6.6: Laser head of the rotational laser vibrometer.

6.2.7 Data Acquisition System

Pulse analyzer® (B&K, 3560C) is used for the purpose of data acquisition of measured forced responses. It is a PC-based sound and vibration analysis system and it consists of a PC with LAN interface, software, Microsoft® Windows® operating system, and data acquisition front-end hardware. The system has both the time capture and the FFT analyzer for recording the real-time data. The algorithm is tested for both single-cracked shafts and double-cracked shafts. Stages for conducting the experiments are discussed in the following section.

6.3 Stages for Conducting the Experiments

Two mild steel shafts, namely Shaft-I and Shaft-II are used for the experimental verification of the MCDLA. First, a single crack is introduced in each of the shafts and the algorithm is tested for a single-cracked shafts. Next, one more crack is introduced in the shafts and the algorithm is tested for doubled-cracked shafts. Physical parameters of the two shafts are given in Table 6-1. Crack orientation angles of all cracks are 0°. The location of exciter for the case of Shaft-II with two cracks is 670 mm from the left end support (58th node of FE model). For all other cases, it is 294 mm from the left end support (25th node of FE model).

Table 6-1: Physical parameters of the cracked shaft for the experimentation.

S. No.	Parameters	Values (Shaft-I)	Values (Shaft-II)
1	Diameter of the circular shaft, D (in mm)	16.3	16.3
2	Shaft length, L (in mm)	940	940
3	Young's modulus of the beam material, E (N/m^2)	2.06×10^{11}	2.06×10^{11}
4	Density of the beam material, ρ (kg /m^3)	7800	7800
3	Number of measurement locations	19	19
4	Location of the first crack from the left end support (in mm)	468	570
5	Location of the second crack from the left end support (in mm)	652	274
6	Size of the first crack (in mm)	4	6
7	Size of the second crack (in mm)	4	6

First, measurements have been performed with the proximity sensor; however, after not getting satisfactory results with the proximity sensors, the rotational laser vibrometer has been used. Procedure for conducting experiments using proximity sensors, along with required signal processing is discussed in following sections.

6.4 Experimentation using Proximity Sensors

6.4.1 Procedure

The MCDLA needs both actual test measurements from the real (cracked) shaft and numerically simulated responses from the intact shaft. For the finite element modeling of the intact shaft, the shaft is discretised into 80 elements, but the shaft deflection at 21 (equidistant) measurement locations are taken for the algorithm. In the real shaft also, we need to know the shaft deflections at these 21 measurement locations. Out of these 21 locations, shaft displacements at two ends are known to be zero (due to boundary conditions). Hence, it remains to measure shaft displacements at remaining 19 measurement locations. These 19 measurement locations are marked on the cracked shaft (Figure 6.1). A harmonic forcing is applied for the external excitation of the shaft. The frequency of excitations are 2, 4, 6,…,50 Hz. The forcing applied to the shaft is measured through the force transducer. Both responses and the forcing are measured at each of the excitation frequencies and at all the measurement locations. When the displacement sensor is stationed at a particular measurement location, measurement at all the frequencies are taken one by one. After taking measurements at all the excitation frequencies for a given location, the sensor (displacement sensor) is moved to another measurement location. In this way, measurements are taken at all the measurement locations. Signal Processing of Measured Signals

The measured forcing time history and the response time history are stored in separate files for further processing in the MATLAB environment. A sample forcing time history, measured by force transducer, is given in Figure 6.7 and a sample of response time history measured using the displacement sensor is given in Figure 6.8.

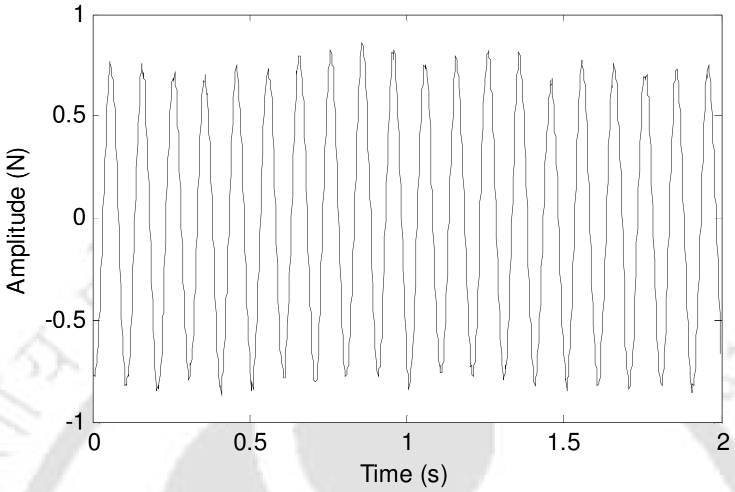

Figure 6.7: A sample forcing time history at 10 Hz.

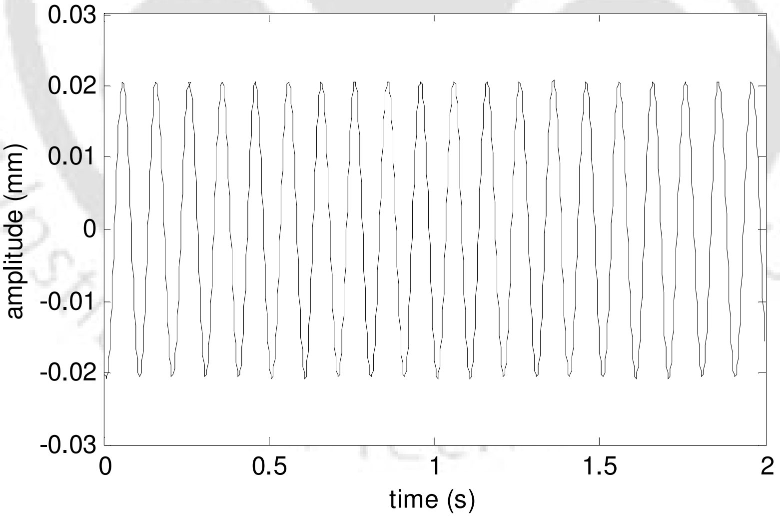

Figure 6.8: A sample response time history at the 9th measurement location and the excitation frequency of 10 Hz.

There are different sources of noise in electronic instruments. Both the forcing signal and the response signal (in Figure 6.7 and Figure 6.8) contain noise. Hence, filters are used to reduce the effect of noise in the measurement. It also eliminates any DC component in the signal. Filter has been designed using the '*Filter design and analysis tool'* from MATLAB toolbox. A band-pass filter is designed using the Butterworth method and the order is taken to be 4. The sampling frequency is obtained from the measured signal and cut-off frequencies are selected based upon the excitation frequency. The filtered and unfiltered signals for the sample forcing time history (shown in Figure 6.7), for small time interval, is given in Figure 6.9. The symbol *star* in the plots indicates the maxima and minima of the filtered signal. Similarly, filtered and unfiltered signal for the sample response time history (shown in Figure 6.8) is given in Figure 6.10. A sample filter characteristics for excitation at 20 Hz is given in Figure 6.11.

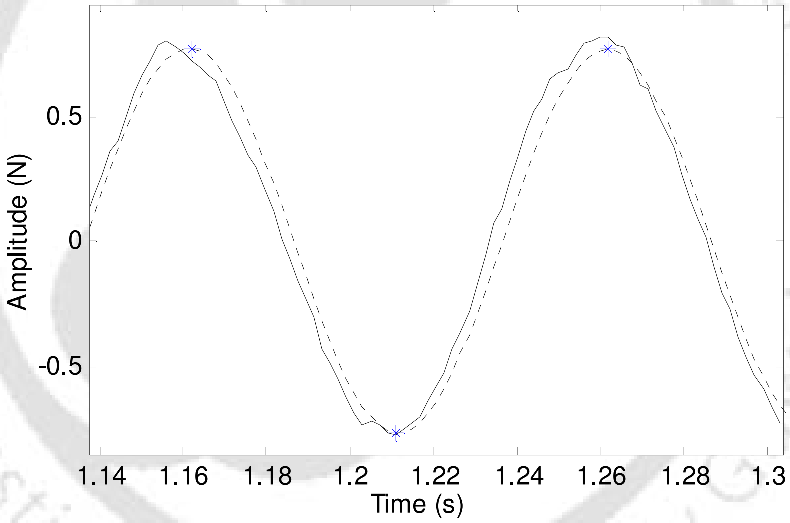

Figure 6.9: The filtered (- -) and unfiltered (-) signals for the sample forcing time history of Figure 6.7.

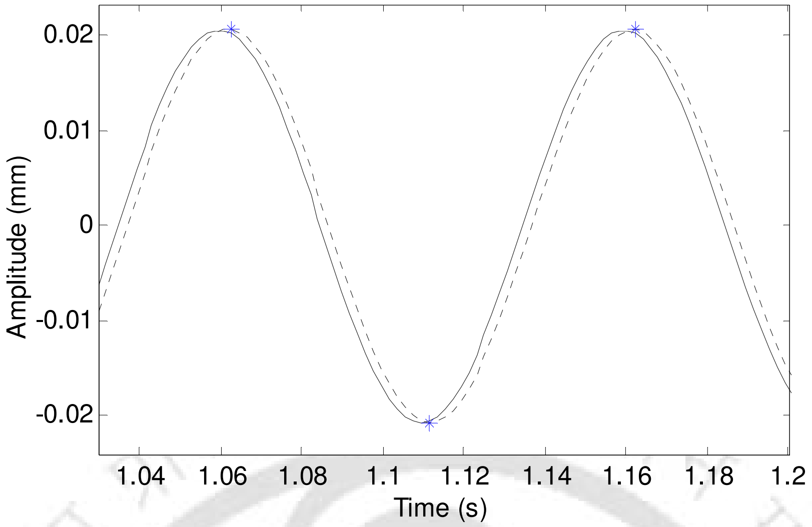

Figure 6.10: The filtered (- -) and unfiltered (-) signals for the sample response time history of Figure 6.8.

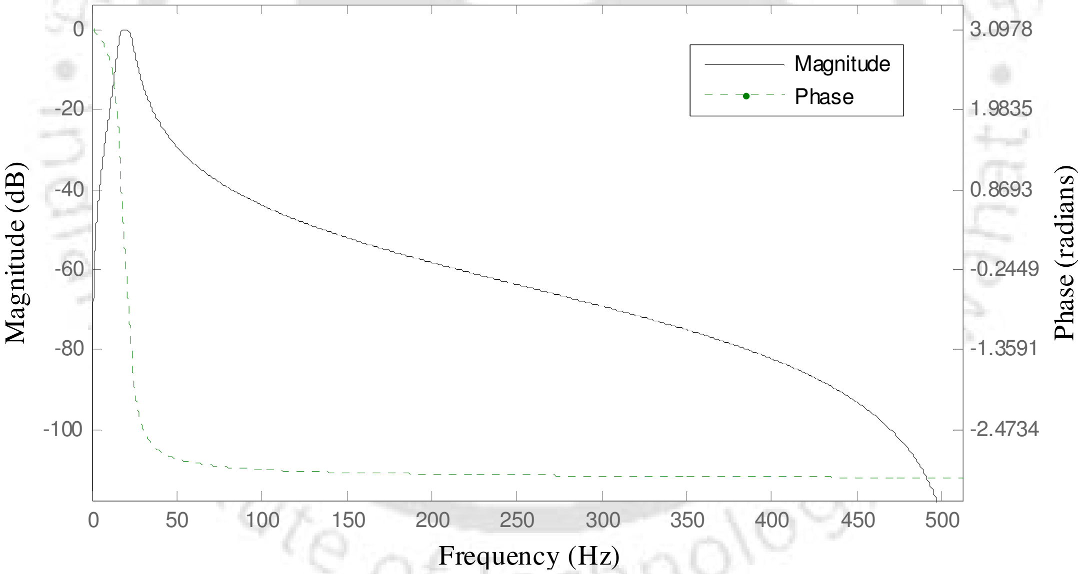

Figure 6.11: A sample filter characteristics for excitation at 20 Hz.

For both the measurements (i.e., the force and the response), filtered signals are used for the experimental verification of the MCDLA. A computer code has been written in MATLAB to find out one pair of adjacent maxima and minima from the filtered response time history. Similarly, the maxima and the minima are obtained for the filtered data of forcing time history also.

After choosing a particular maxima from the response time history, the maxima from the forcing time history is chosen in such a way that the two maxima (i.e., one in the force and another in the response) are located closest in terms of the time instance. The two maxima are separated by the phase between the forcing and the response. Similarly, the two minima are separated by the phase between the forcing and the response. The response amplitude, $X^{'}$, is found out as follows

$$X^{'} = \frac{\text{Maxima in response time history} - \text{Minima in response time history}}{2} \tag{6.1}$$

Similarly, the force amplitude, F, is found out as follows

$$F = \frac{\text{Maxima in force time history} - \text{Minima in force time history}}{2} \tag{6.2}$$

Now, the response per unit force, X is calculated by

$$X = \frac{X^{'}}{F} \tag{6.3}$$

The response per unit force, X, is calculated for all excitation frequencies and at all the measurement locations. The response per unit force, X, is used for the verification of the proposed algorithm. The shaft deflection is obtained from calculating X at all the measurement locations. A sample shaft deflection for Shaft-I, at the excitation frequency of 24 Hz, is plotted in Figure 6.12.

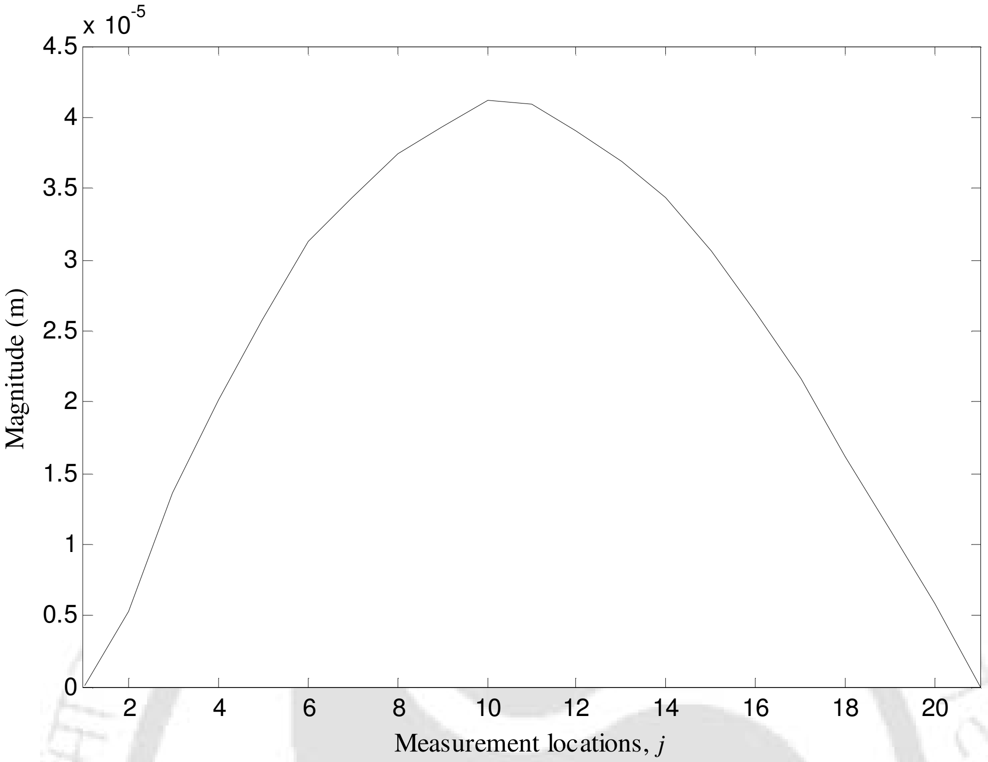

Figure 6.12: The cracked shaft deflections at 24 Hz.

6.4.2 Experimental Results

For experimentations, initially a single crack is introduced near the middle of Shaft-I. The crack is near to 11th measurement location (between 11th and 12th measurement locations). The crack depth ratio of the crack is 0.4. Two sets of measurements are taken. Crack probability functions (*CPFs*) for the first set of measurement is given in Figure 6.13, while those for the second set of measurement is given in Figure 6.14. Excitation frequencies of 4, 6, 8, …, 24 Hz are used to test the MCDLA for both measurement sets.

In Figure 6.13, for the first measurement set, peaks in *CPF* values came at 6th, 10th and 14th measurement locations. Peaks in *CPF* values (Figure 6.14) from the second measurement set came at 10th measurement location. Whereas, the peak in *CPF* value was expected to come at 11th measurement location, since the crack is near to 11th measurement location.

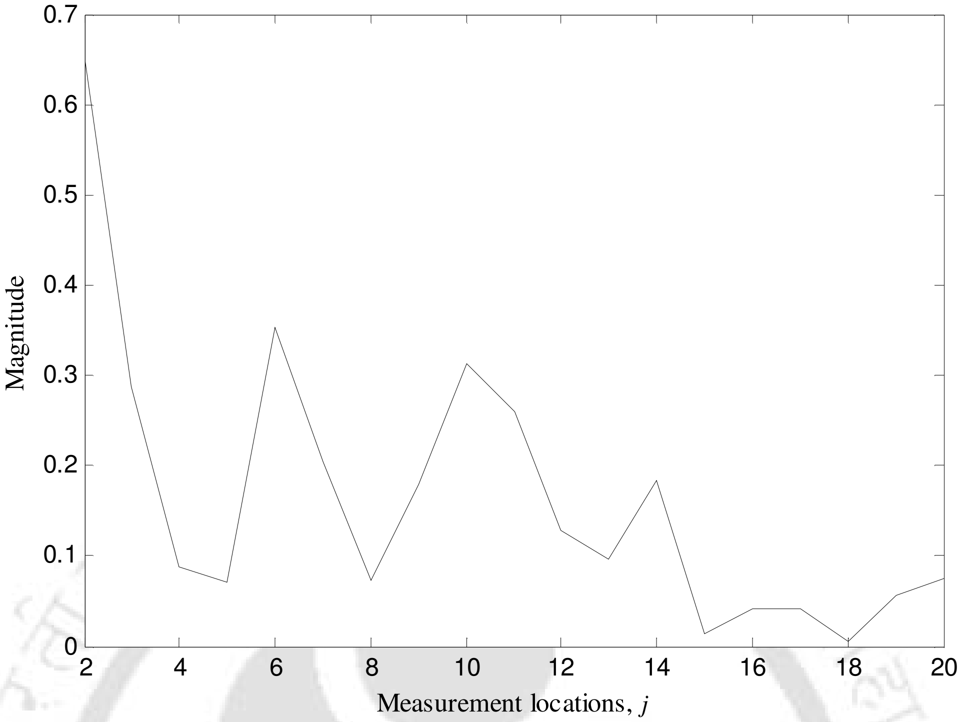

Figure 6.13: The crack probability functions for Shaft-I with single crack neat 11th measurement location (first set of measurements).

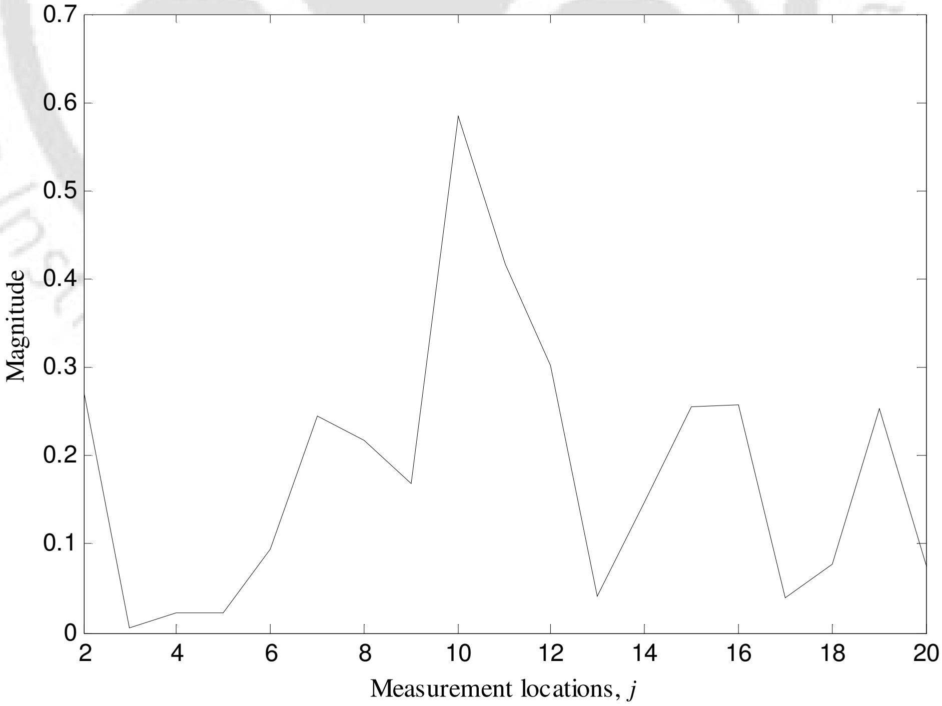

Figure 6.14: The crack probability functions for Shaft-I with single crack near 11th measurement location (second set of measurements).

For the measurement taken from displacement transducers, size of the sensors is considerably big and it is difficult to position the sensor exactly over the mark that is marked as measurement location. Also there is a chance of improper positioning of the transducer because of the high curvature of the shaft surface, as the shaft diameter is less (i.e., 0.0163 m). The effect of curvature of shaft surface would have been less had the shaft diameter been more. Hence to improve the accuracy, the laser vibrometer is used for measuring the shaft deflection. The laser beam in laser vibrometer is sharp and it can be focused over a small mark (meant for measurement locations). The procedure used for measurements with laser vibrometer is discussed in the next section.

6.5 Experimentation using Laser Vibrometer

6.5.1 Procedure

The laser vibrometer (LVM) is used to measure the forced responses. A reflecting film is applied at the measurement locations on the shaft (shown in Figure 6.15) for the measurement of responses. It reflects back the incident beam from laser beam source to the beam receptor of the LVM. The laser beam is sharp and hence it is possible to focus the beam over small point marks. But there are some problem focusing the beam over point marks: (1) the point mark is not visible due to glare in the beam and (2) it is advised not to stare at the laser beam for long. To overcome these two difficulties, it is planned to focus the laser beam over the measurement locations by visual alignment of a line and the laser beam. Two perpendicular marking lines are drawn for each measurement location (red colored lines in Figure 6.15). If the laser beam is focused properly over the point, the laser beam and a particular marking line will be seen aligned when viewed along that particular marking line. This way, proper focusing is achieved by aligning the laser beam along both marking lines. The sensor for measuring the forcing remained the same. Now, a sine-sweep of 1 Hz/s is used to excite the shaft. After taking measurements at a particular measurement location, the sensor (i.e., the Laser head) is moved to another measurement location while keeping the location of exciter unchanged. Advantage with the sine-sweep is that for a particular measurement location, the response of the shaft at several frequencies can be obtained in a single run. While for the discrete excitation (excitation at a particular frequency), number of measurements would be more. At the same time, effort would be needed to extract the forcing and the response at a particular frequency, from the sine-sweep forcing and the corresponding response.

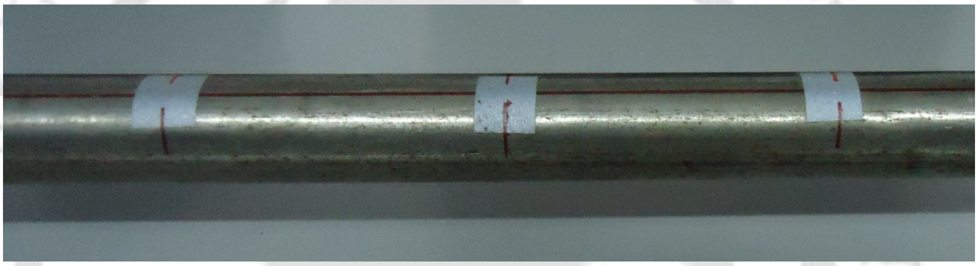

Figure 6.15: Reflecting films on the shaft surface for response measurements using the laser vibrometer.

6.5.2 Signal Processing of the Measured Signal

The forcing time history and the response time history are stored each in a separate file for further processing in the MATLAB environment. A sample forcing time history is given in Figure 6.16 and the corresponding response time history is given in Figure 6.17.

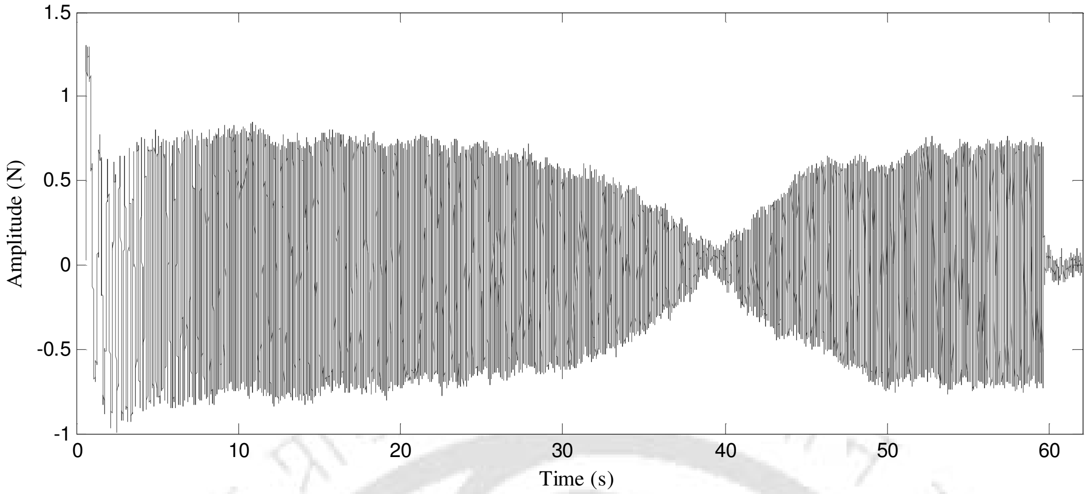

Figure 6.16: A sample sine-sweep forcing.

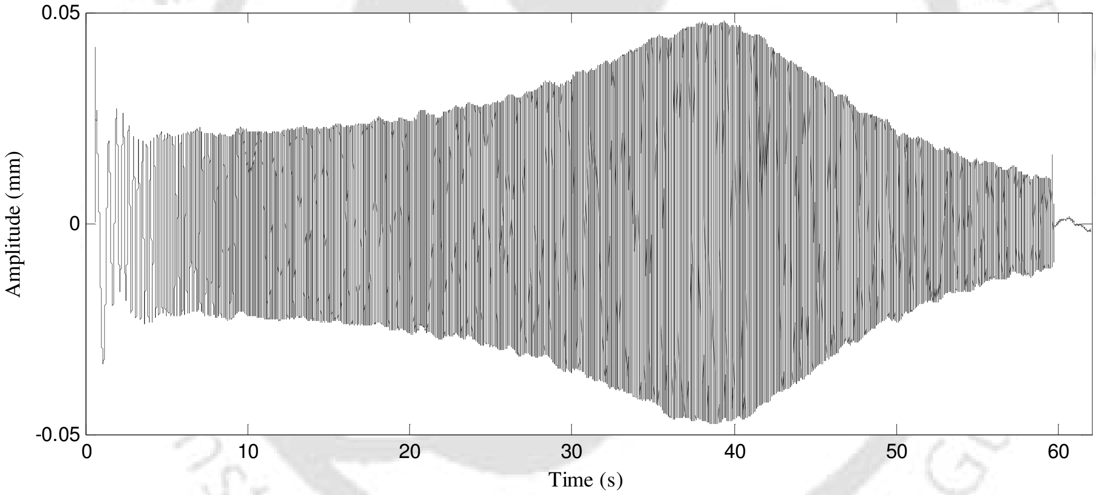

Figure 6.17: A sample response to a sine-sweep forcing.

Again filters are used to remove the noise from the forcing and response signals. After filtering the signal, all the maxima and minima from a time history are identified. In contrast to the discrete frequency excitation used while taking measurements using displacement sensors, now the excitation frequency is varying continuously for the sine-sweep excitation. Therefore all the maxima and minima in the signal are identified from the filtered forcing signal. A pair of maxima and minima is formed from the forcing time history by selecting a minima just next to a maxima. Now the force amplitude F is calculated using Eqn. (6.2) for all the pair of maxima and minima form the forcing signal. Similarly, response amplitude is calculated using Eqn. (6.1) for all the pair of maxima and minima in the response signal. Now all force amplitudes are fitted in the polynomial of degree 20, to further smooth the curve and it is shown in Figure 6.18. The response amplitude is plotted in Figure 6.19. Response amplitudes at some more measurement locations are shown in Figure 6.20.

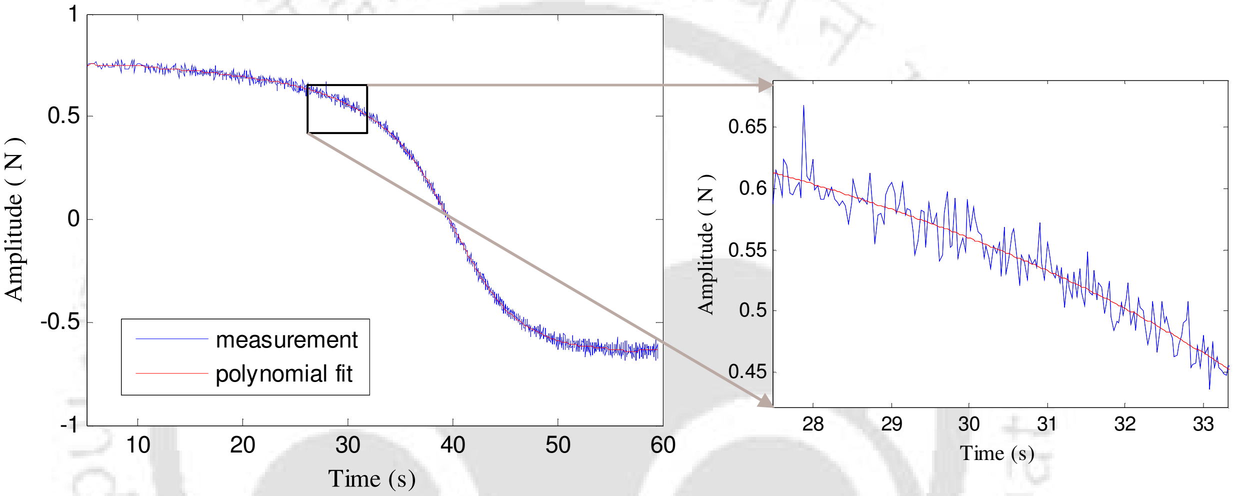

(a) The force amplitude for the complete measurement time

(b) The force amplitude for small portion of measurement time (Zoomed portion from Figure 6.18 (a))

Figure 6.18: Variation of force amplitude with time.

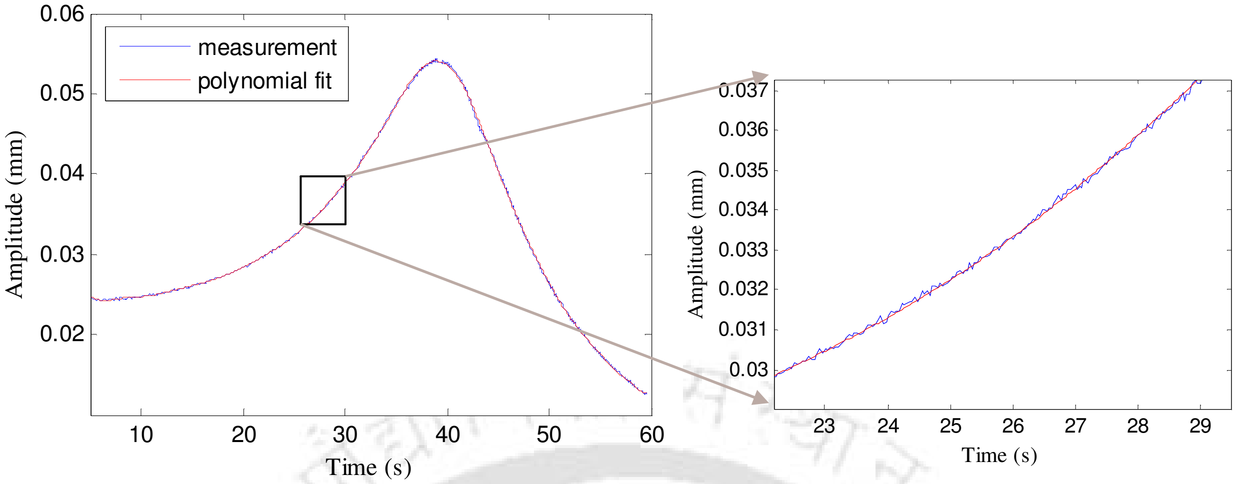

(a) Response amplitude for the complete measurement time

(b) Response amplitude for a small portion of measurement time (Zoomed portion from Figure 6.19 (a))

Figure 6.19: A sample response amplitude at 6th measurement location.

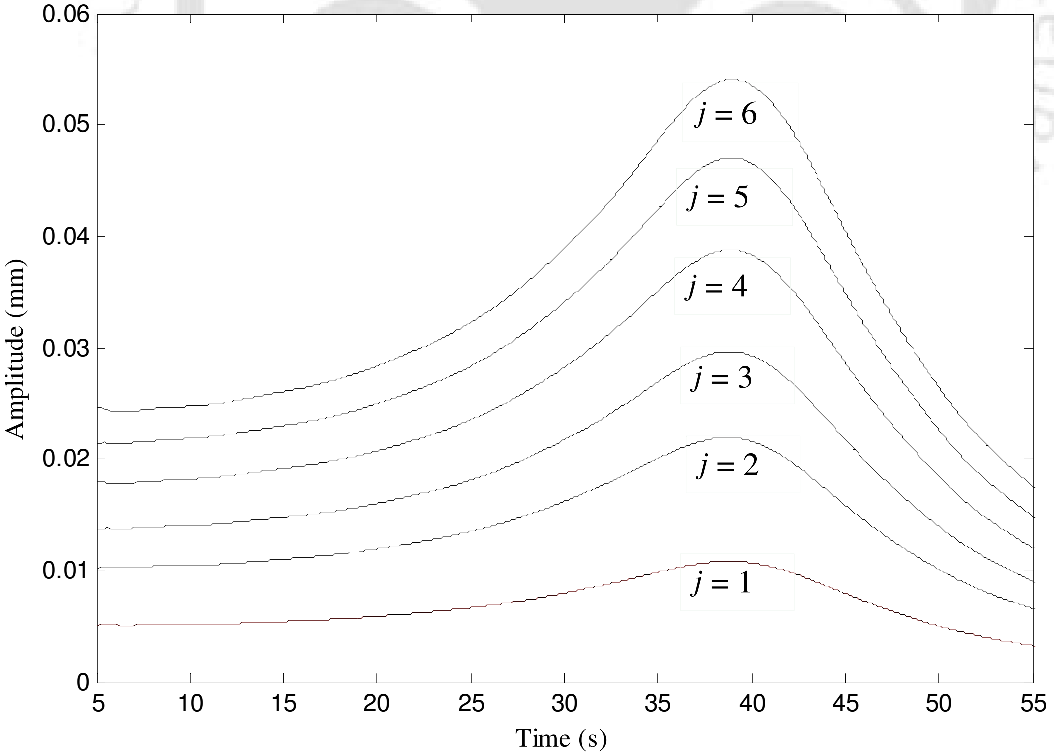

Figure 6.20 The response amplitude at various measurement locations, *j*.

Now the response per unit force (FRF) is obtained by dividing the response amplitude by the corresponding force amplitude. With the known sweep rate of 1 Hz/s, the response per unit force is obtained as a function of frequency. The response per unit force, for the measurement location 4, is shown in Figure 6.21.

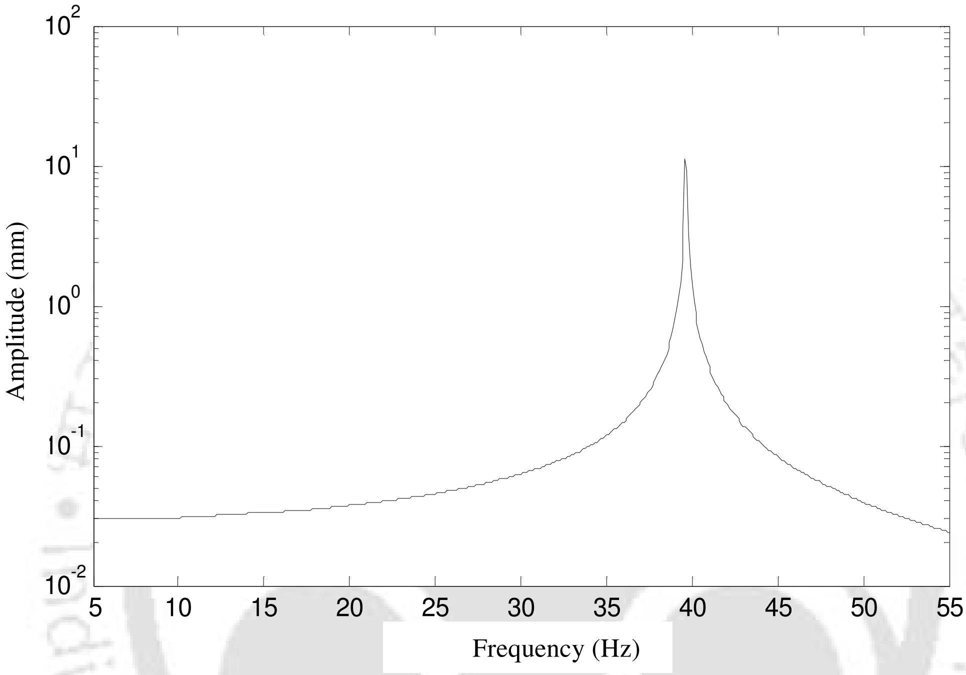

Figure 6.21 The response per unit force at the measurement location 4.

Similar response per unit force was obtained at all the measurement locations. For all these measurement locations, the location of exciter was same. The shaft deflection at a particular frequency is obtained from the response per unit force at all these measurement locations. The shaft deflection at 20 Hz of excitation frequency is plotted in Figure 6.22.

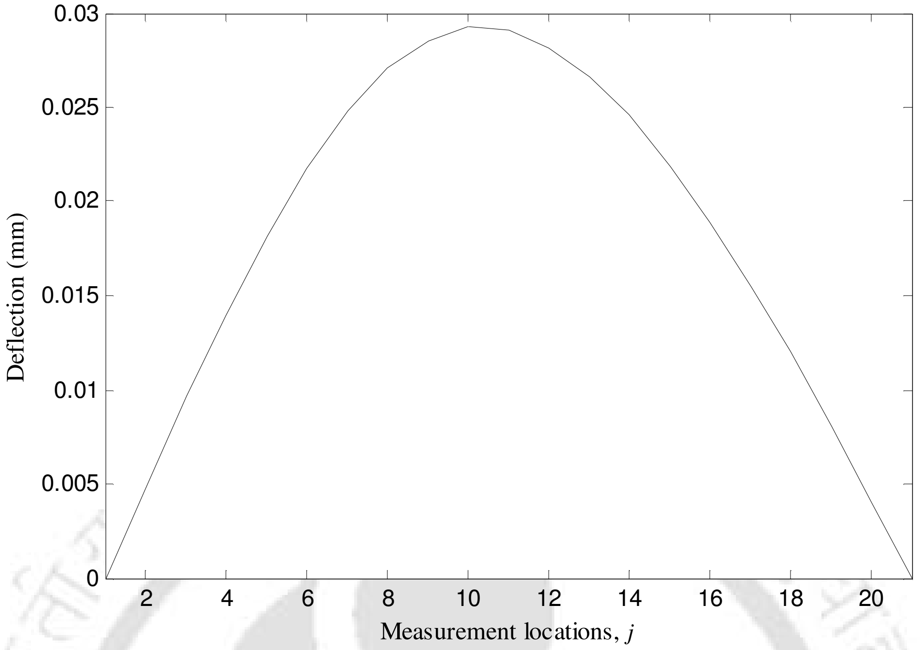

Figure 6.22: The shaft deflection at the excitation frequency of 20 Hz.

Now the measurement data is in the form which can be used in the proposed MCDLA. Experimental results using the measurements from the Laser vibrometer is presented in the following section.

6.5.3 Experimental Results from the Laser Vibrometer

First, measurements are taken over Shaft-I. It has a single crack near the middle of the shaft. The *CPF* from the first measurement set is given in Figure 6.23. The location of the single crack is near 11th measurement location while the peak in the *CPF* values appears at 17th measurement location. *CPF* values for the Shaft-I for the second set of measurements are given in Figure 6.24. Peaks appear at 10th and 14th measurement locations. Hence, the algorithm is not effectively detecting the presence of crack for this case.

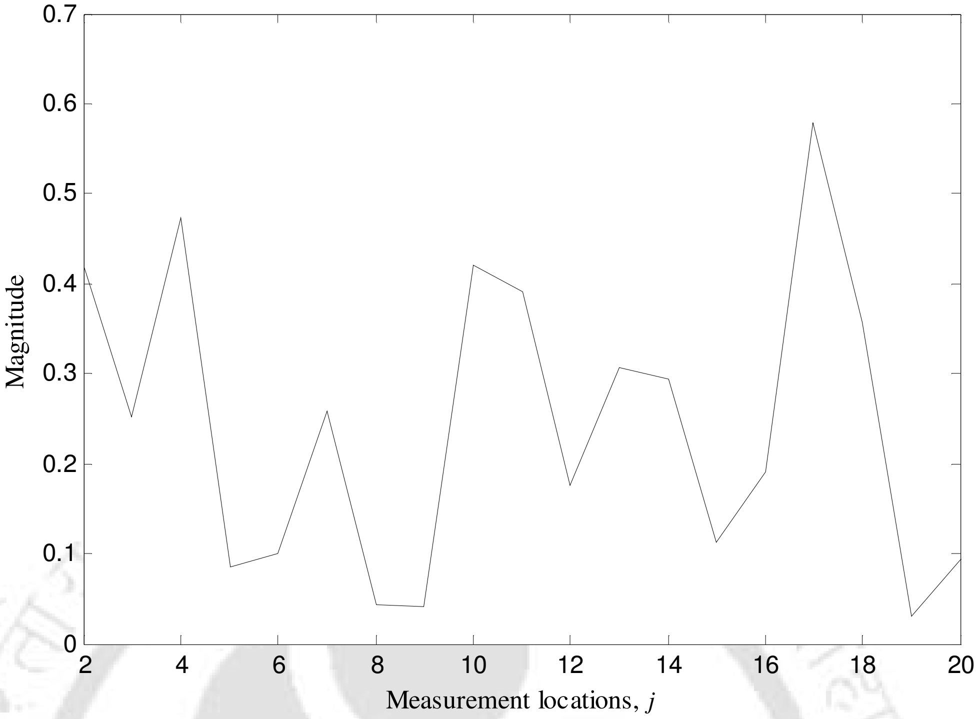

Figure 6.23: Crack probability functions for the Shaft-I with a crack near 11th measurement location (first set of measurements).

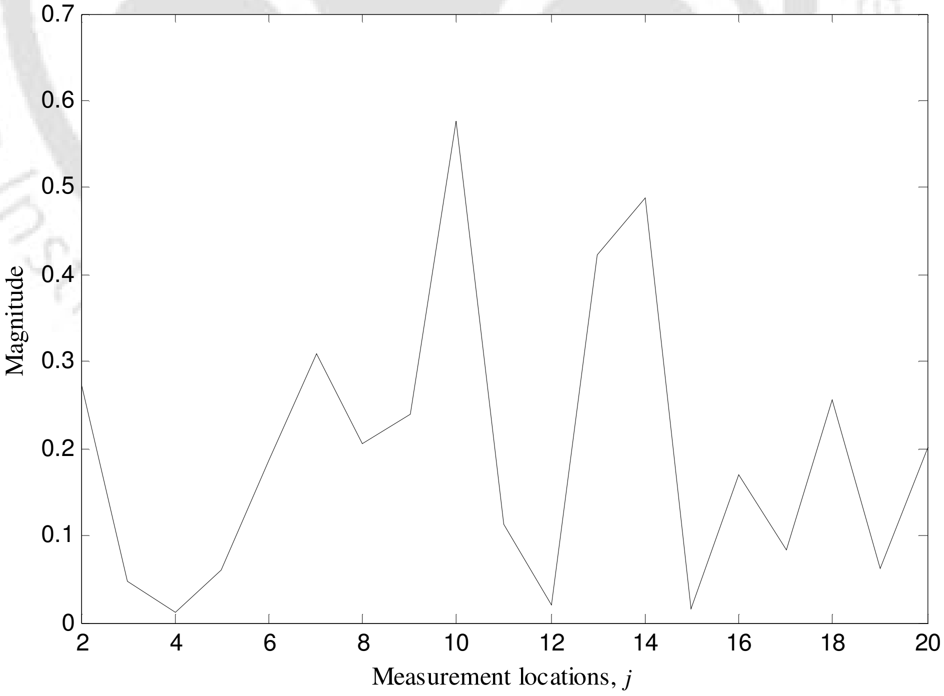

Figure 6.24: Crack probability functions for the Shaft-I with a crack near 11th measurement location (second set of measurements).

Now the algorithm is tested for the second shaft, i.e., Shaft-II. A single crack is made near the 13th measurement location. The *CPF* values from the first measurement set are given in Figure 6.25. Here, two predominant peaks occur, one peak is at the 8th measurement location and the other peak is at the 13th measurement location. Hence, there is a peak in the *CPF* values near the location of crack. But then there is another peak at 8th measurement location also, where there is no crack. Crack probability functions for the second set of measurements are given in Figure 6.26. There is a predominant peak at the 13th measurement location. Hence, the algorithm identifies the presence of cracks in Shaft-II for both the measurement sets.

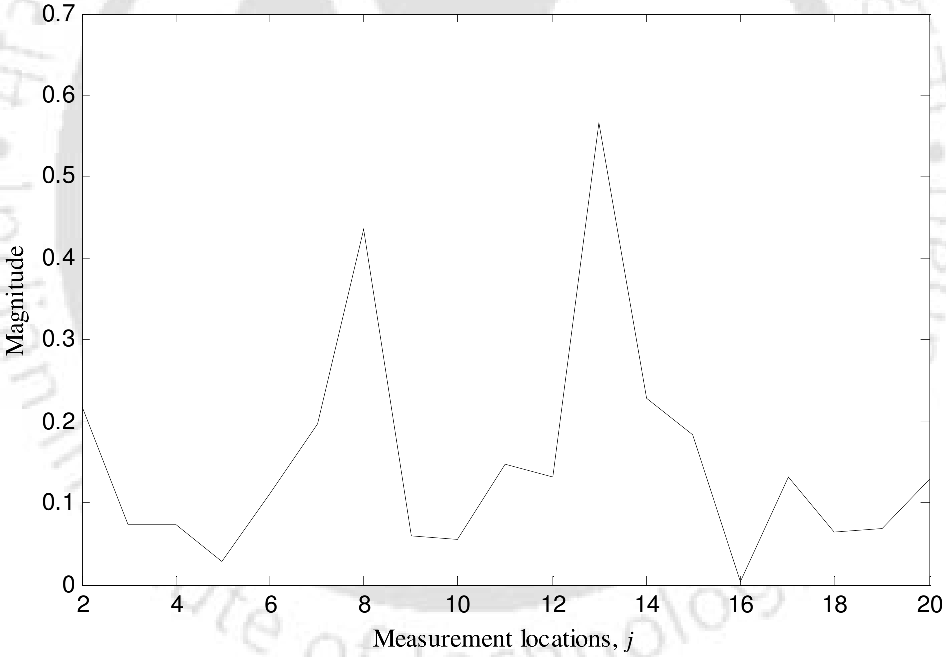

Figure 6.25: Crack probability functions for the Shaft-II with a single crack near 13th measurement location (first set of measurements).

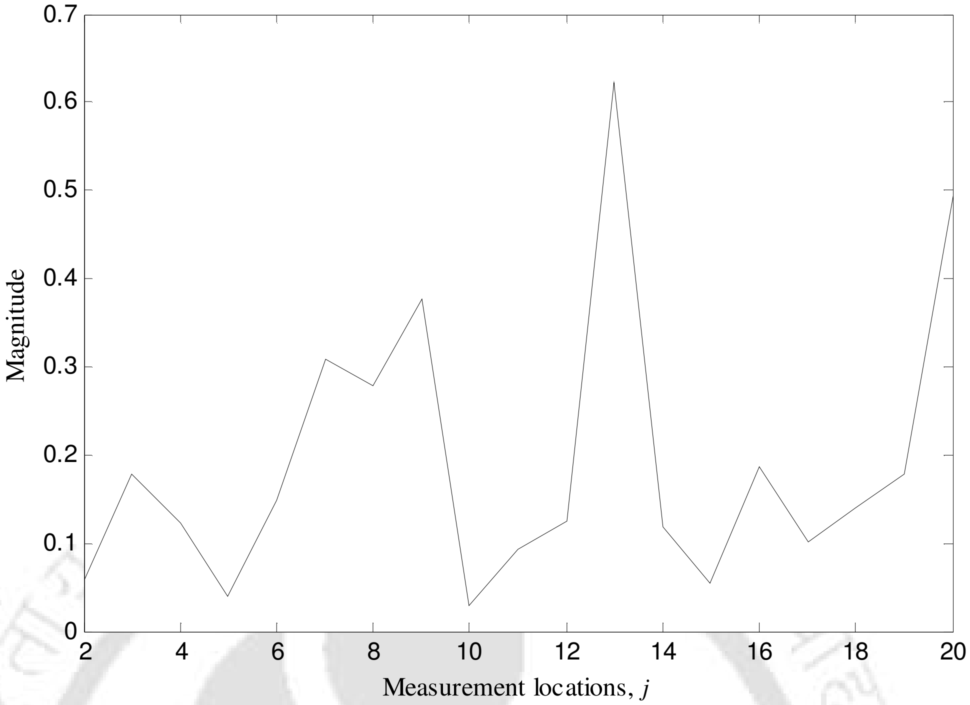

Figure 6.26: Crack probability functions for the Shaft-II with a single crack near 13th measurement location (second set of measurements).

The algorithm is tested for shafts with two cracks also. A second crack is introduced near 15th measurement location in the Shaft-I. The *CPF* values obtained from the first set of measurement are plotted in Figure 6.27 while those obtained from the second set of measurements are plotted in Figure 6.28. The two cracks in the shaft are at 11th and 15th measurement locations. From Figure 6.27, there is no peak in the *CPF* values at either of the locations whereas a single peak at 11th measurement location appears in Figure 6.28.

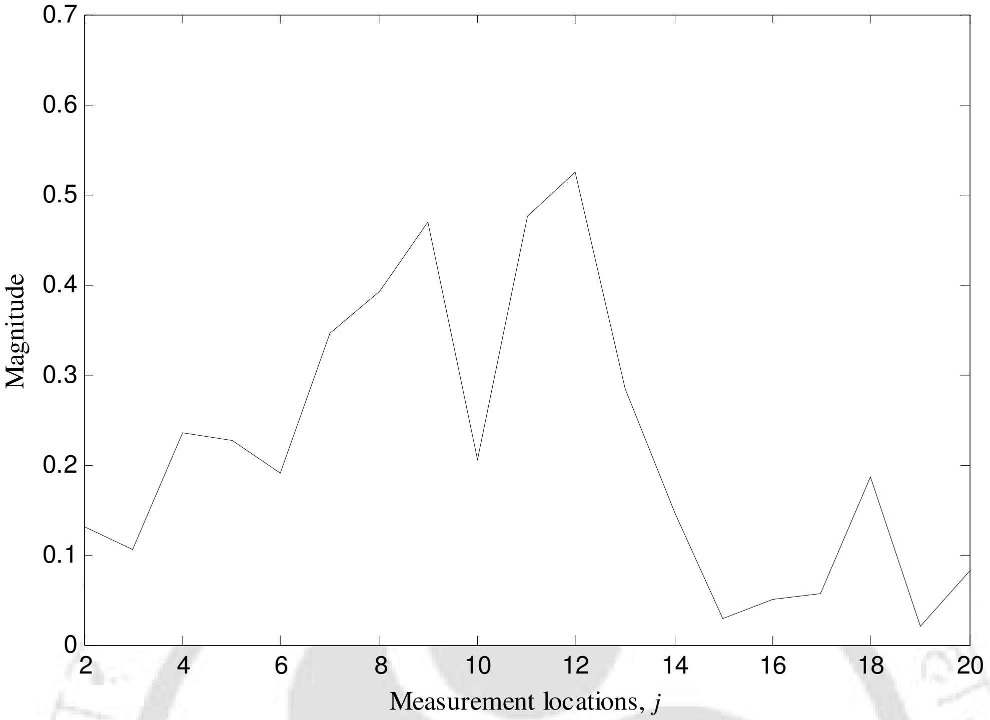

Figure 6.27: Crack probability functions for the Shaft-I with two cracks (one near 11th measurement location and the other near 15th measurement location, first set of measurements).

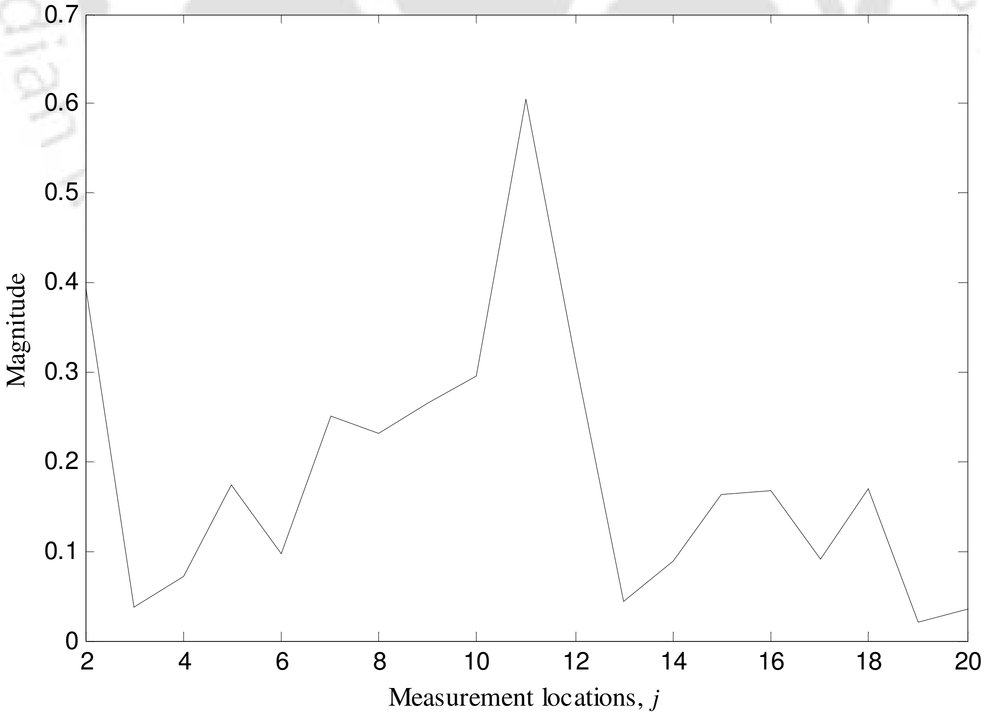

Figure 6.28: Crack probability functions for the Shaft-I with two cracks (one near 11th measurement location and the other near 15th measurement location, second set of measurements).

For the Shaft-II, a second crack is introduced near the measurement location 7. *CPF* values from the first measurement set, for the Shaft-II with two cracks, are presented in Figure 6.29. The algorithm identifies both the cracks present in the shaft as there are two peaks in the *CPF* plot, one at 7th measurement location and the other at 13th measurement location. Although there is another peak at 19th measurement location, however there is no crack at this measurement location. *CPF* values (from the second measurement set) for the Shaft-II with two cracks are presented in Figure 6.30. The crack at 13th measurement location is identified. But, there is no peak at 7th measurement location.

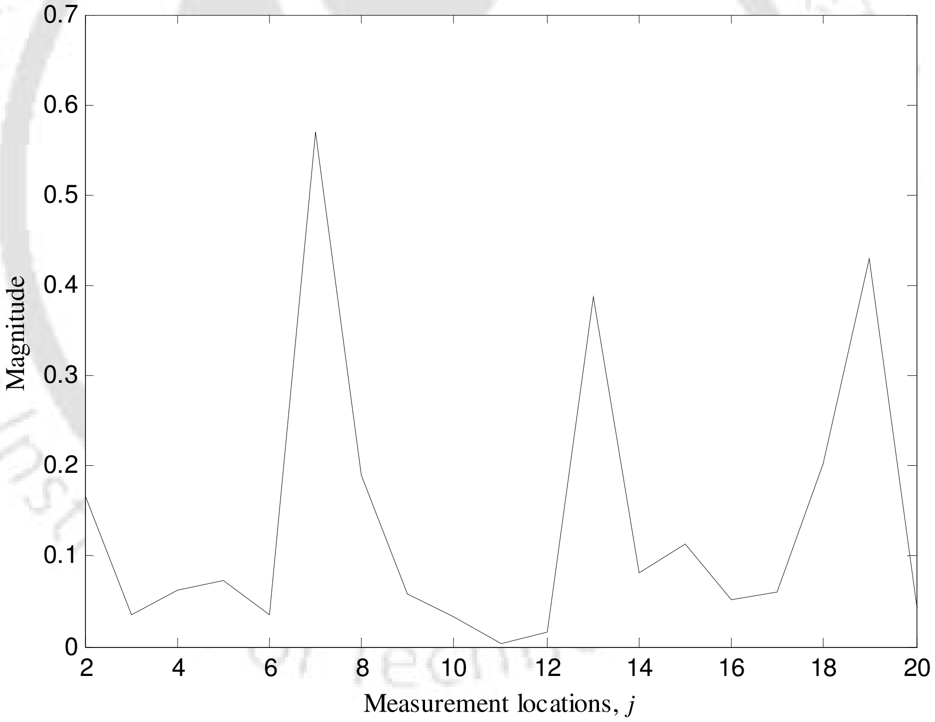

Figure 6.29: Crack probability functions for the Shaft-II with two cracks (one near 13th measurement location and the other near 7th measurement location, first set of measurement).

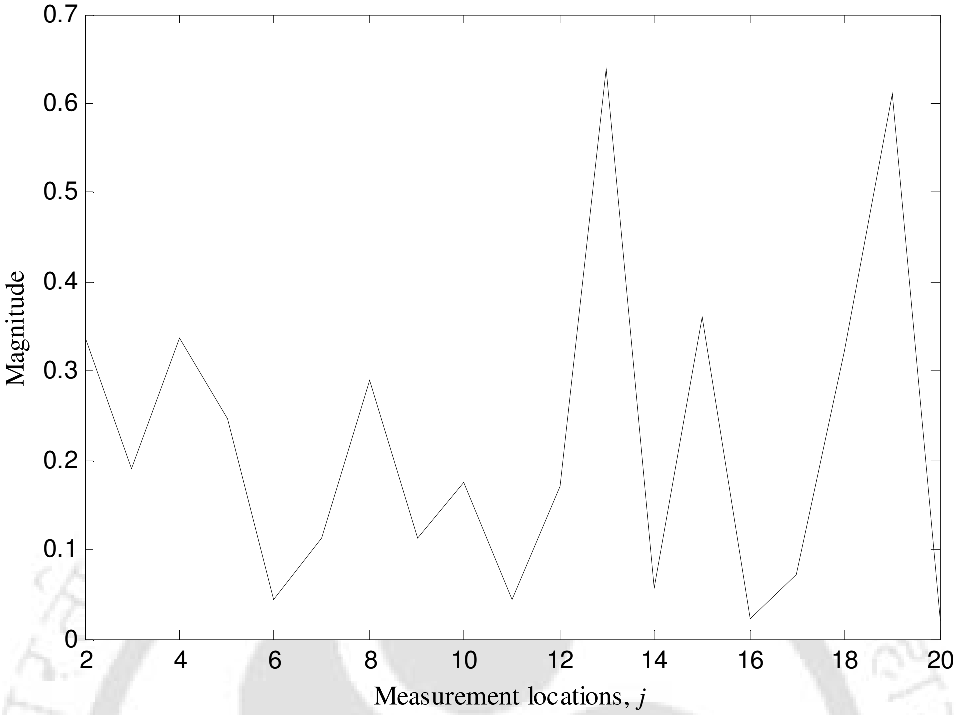

Figure 6.30: Crack probability functions for the Shaft-II with two cracks (one near 13th measurement location and the other near 7th measurement location, second set of measurement).

From the above *CPF* plots (Figure 6.23 to Figure 6.30), it can be observed that the algorithm is not effectively detecting the crack(s) for Shaft-I. For Shaft-II with a single crack, the algorithm identifies the presence of crack for both measurement sets. For the Shaft-II with two cracks, the algorithm is detecting the crack at 13th measurement location (which is near to middle of the shaft) in both the measurement sets. Good performance of the algorithm for the Shaft-II may be attributed to bigger size of the cracks. As from Table 6-1, size of the cracks for Shaft-II were more than that for the Shaft-I. A bigger crack size is expected to give more slope discontinuity.

In the numerical experiment (Section 3.3), 1% white noise was added to mimic the actual experimentation. So, probable reasons for poor performance of the algorithm are expected to be (1) type of noise and its level is different in the measurements as compared to the numerical simulation and (2) the bias error due to the modeling error. In the next section, a scheme is presented to estimate the quadratic coefficients more accurately.

6.6 Scheme for Better Estimation of the Quadratic Coefficients

The MCDLA uses double derivative of the shaft deflection (with respect to the shaft length). In the proposed scheme, effect of noise in the estimation of double derivatives are reduced by reducing the number of measurement locations for a given shaft length. Reducing the number of measurement locations would result in longer distances between the consecutive measurement locations.

6.6.1 The Scheme

In Figure 6.31 , let y_r $(r = 1,2,\ldots 5)$ be the actual shaft deflection at the axial distance of x_r. For estimating the slope of the shaft at distance x_2, let the measured deflection y'_r $(r = 1,3,4,5)$ at locations x_r are used. Let e the measurement error at x_1 and x_4. Similarly, $-e$ be the measurement error at x_3 and x_5. Thus, the magnitude of the error is considered to be same at all locations. Because of the measurement error, the measured value of shaft deflection at location x_1 and x_4 would be $(y'_1 = y_1 + e)$ and $(y'_4 = y_4 + e)$, respectively. Similarly, the measured value of the shaft deflection at locations x_3 and x_5 would be $(y'_3 = y_3 - e)$ and $(y'_5 = y_5 - e)$, respectively. In Figure 6.31, the solid line will give the actual slope which we have to estimate while the dashed line will give the estimated slope. Now it can be observed that slope (at location x_2) of the shaft is more accurate when it is calculated using deflections at x_1 and x_3 compared to when it is calculated using deflections at x_4 and x_5. Although the MCDLA uses the double-derivative (d^2y/dx^2), the effect of 'distance between two measurement locations' over the accuracy of estimated slope is explained for first derivative (dy/dx) only.

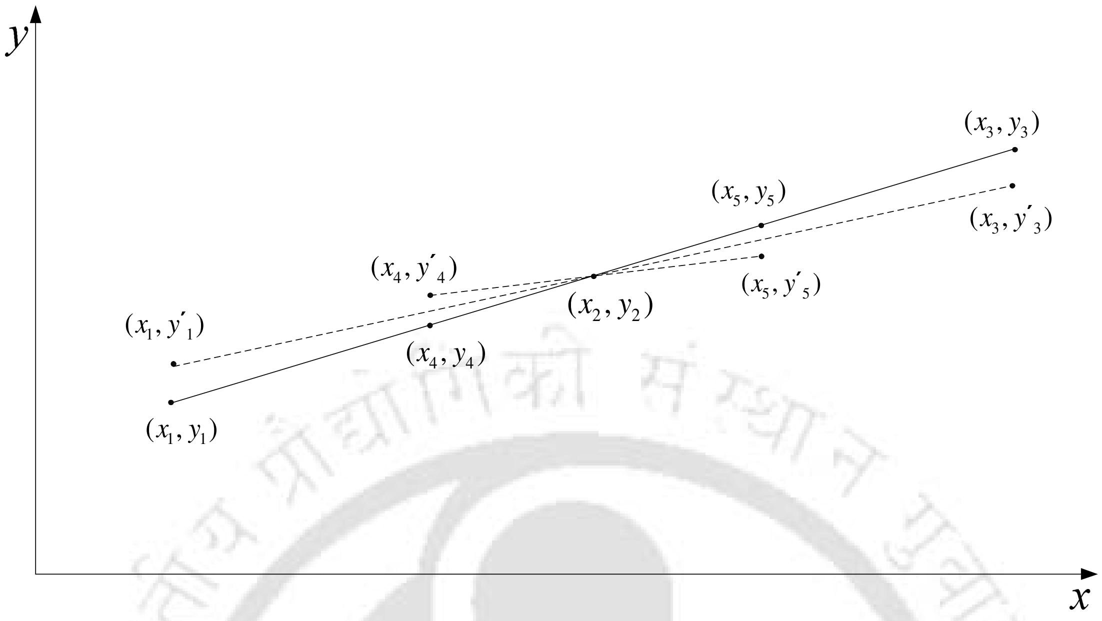

Figure 6.31: Estimation of the slope from measured shaft deflections.

In the following sections, working of the scheme is explained with numerical simulation examples. Thereafter the scheme is implemented to the actual measurements.

6.6.2 Numerical Simulation of the Scheme

Numerical simulations are presented to show the effect of 'distance between measurement locations' on the 'accuracy of estimated quadratic coefficients'. A simply supported shaft of length 1 meter and diameter 10 cm is considered. Excitation frequency is taken to be 50 rad/s. Two cases are considered (a) distance between measurement locations equal to 10 cm, and (b) distance between measurement locations equal to 5 cm. Estimated coefficients are plotted in Figure 6.32. Estimated coefficients with distance between measurement locations equal to 10 cm are closer to actual coefficients.

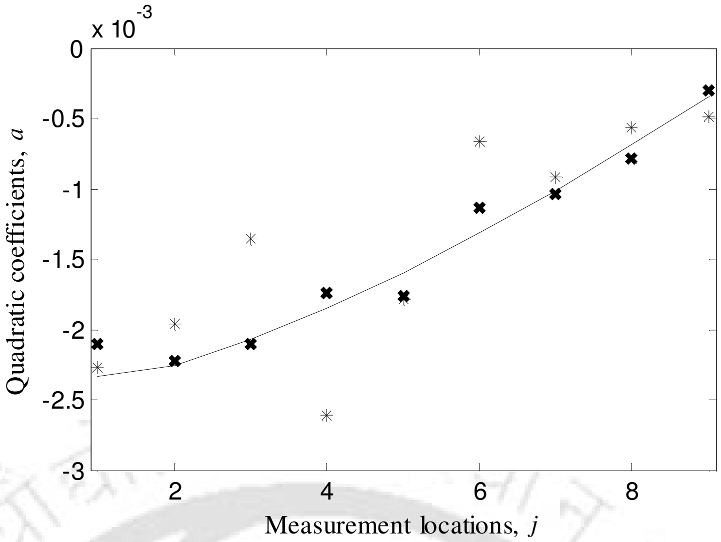

Figure 6.32: Estimation of quadratic coefficients, (actual values, without noise: —), (1% noise and distance between measurement locations is 5 cm: $*$), (1% noise and distance between measurement locations is 10 cm: $\times$) .

It is expected that the MCDLA will work better if estimation of quadratic coefficients are more accurate. Now, numerical simulations are presented to show the effect of 'distance between measurement locations' on the working of the MCDLA. A simply supported shaft with a single crack is considered for the numerical simulations. The MCDLA is used for three situations. The different settings for the measurement noise and the number of measurement locations are presented in Table 6-2. First two natural frequencies of the intact shaft are 126.78 rad/s and 506.93 rad/s.

Table 6-2: Different parameters for numerical simulations.

Parameters	Values for Simulation A	Values for Simulation B	Values for Simulation C
Number of measurement locations	21	21	11
% of noise	1	5	5
Depth of the crack	0.0035 m	0.0035 m	0.0035 m
Number of finite elements	80	80	80
Location of the cracked element	31	31	31
Excitation frequencies, ω_i (in rad/s)	5,10,…,110	5,10,…,110	5,10,…,110

In simulation A, the noise is taken to be 1% and the number of measurement locations is taken to be 21. The presence of crack in the shaft is at 31st finite element i.e., the crack is near 9th measurement location. There is a peak in the plot of *CPF* values at 9th measurement location (Figure 6.33). Hence the algorithm identifies the presence of crack. When the noise is increased from 1% to 5% (in simulation B), keeping all other parameters unchanged, the algorithm is not able to identify the presence of crack in the shaft (Figure 6.34).

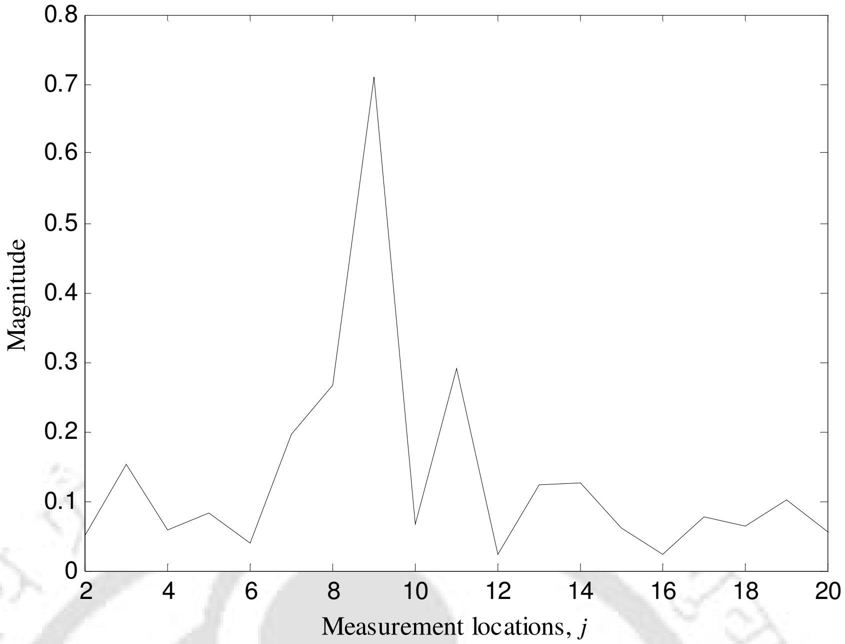

Figure 6.33: Crack probability functions for simulation A (19 measurement locations and 1% noise).

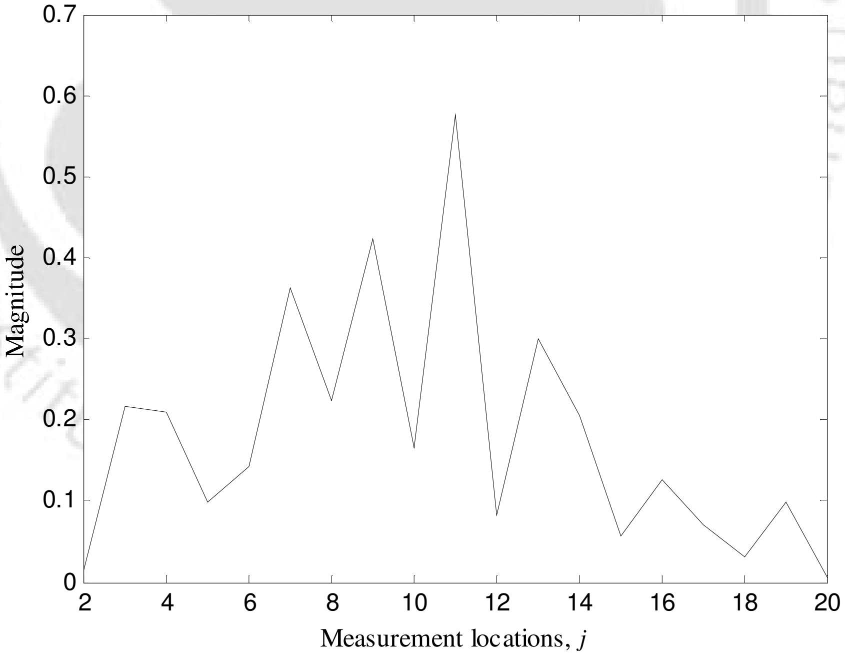

Figure 6.34: Crack probability functions for simulations B (19 measurement locations and 5% noise).

In Simulation 3, the % of noise is kept to be same, i.e., 5%. Now, the number of measurement locations is reduced thereby increasing the distance between two measurement locations. Now the distance between two measurement locations is double of the previous value. From Figure 6.35, there is a peak at the location of crack. Hence, the algorithm identified the presence of crack when the distance between two measurement locations is increased. In the next section, the scheme is implemented for actual measurements on the shaft.

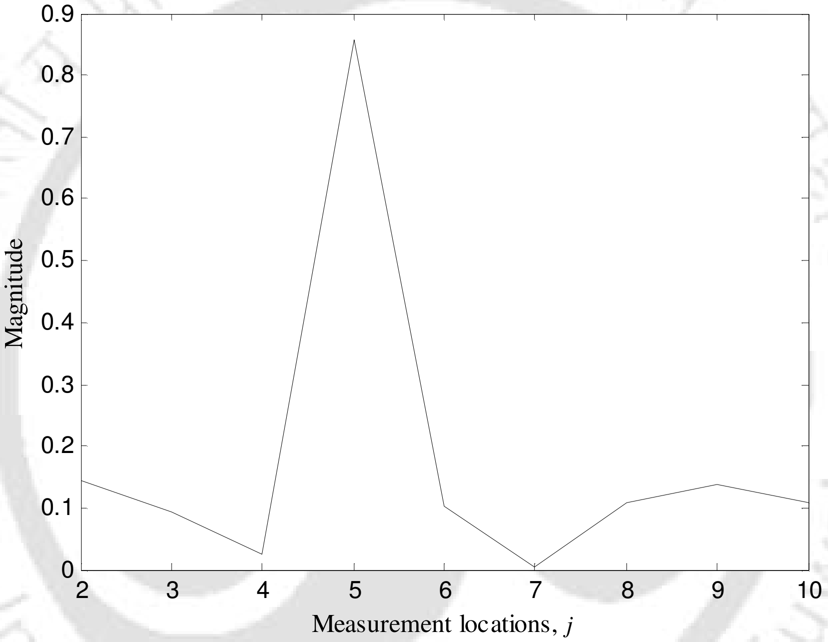

Figure 6.35: Crack probability functions for simulation C (9 measurement locations and 5% noise).

For the verification of the MCDLA, presented in Section 6.5, a total of 21 measurement locations are taken. Now the algorithm is attempted again with 11 measurement locations only. Hence, distance between two measurement locations is doubled now.

6.7 Implementation of the Scheme to Actual Measurements

The MCDLA is attempted with 11 measurement locations. Earlier in Section 6.5, shaft deflections are obtained at 21 measurement locations. From those measurements, shaft deflections at alternate measurement locations are taken out for the verification of the algorithm. Excitation frequencies for the algorithm are taken to be ω_i = 10-26, 42-54 Hz at 2 Hz interval. The natural frequency of the system is around 39 Hz. The single crack in Shaft-I is now near the 6th measurement location (i.e., near the mid-span of the shaft). The resulting *crack probability functions* are given in Figure 6.36. There is a peak at 6th measurement location. Two small peaks are present at 3rd and 9th measurement locations although there is no crack at these locations.

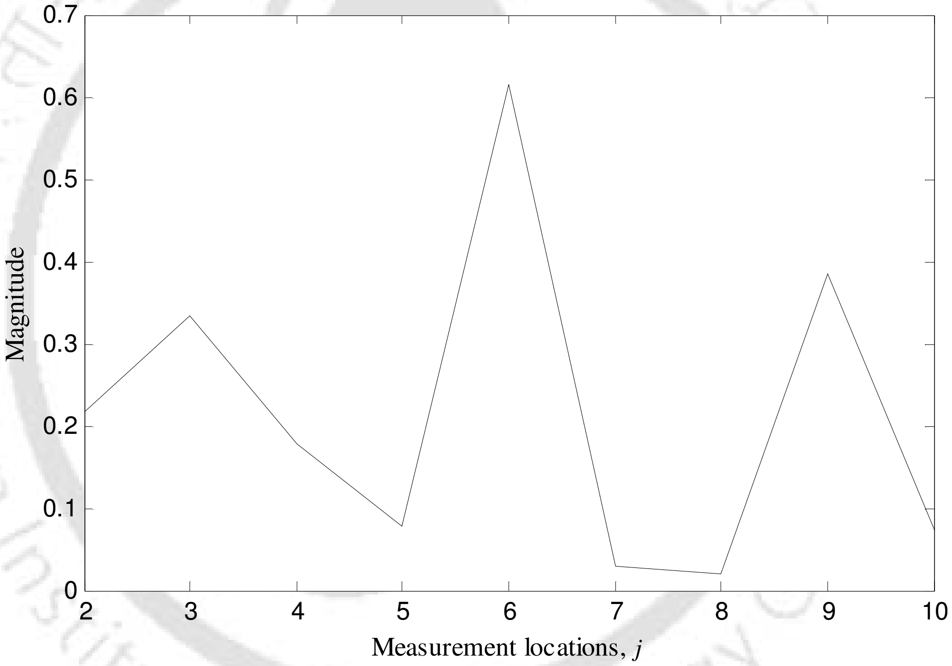

Figure 6.36: Crack probability functions for the Shaft-I with a single crack near 6th measurement location (first set of measurements).

The *crack probability functions* for the second set of measurements over Shaft-I with a single crack near 6th measurement locations are given in Figure 6.37. Here, a single peak comes at the 6th measurement location. Hence, again the algorithm identifies the presence of crack over the shaft. Moreover, if we see the *CPF* plots for both set of measurements (Figure 6.36 and

Figure 6.37); it is more clear that there is a crack in the shaft near the 6th measurement location. And there is no crack in the shaft near the measurement locations 3 and 9.

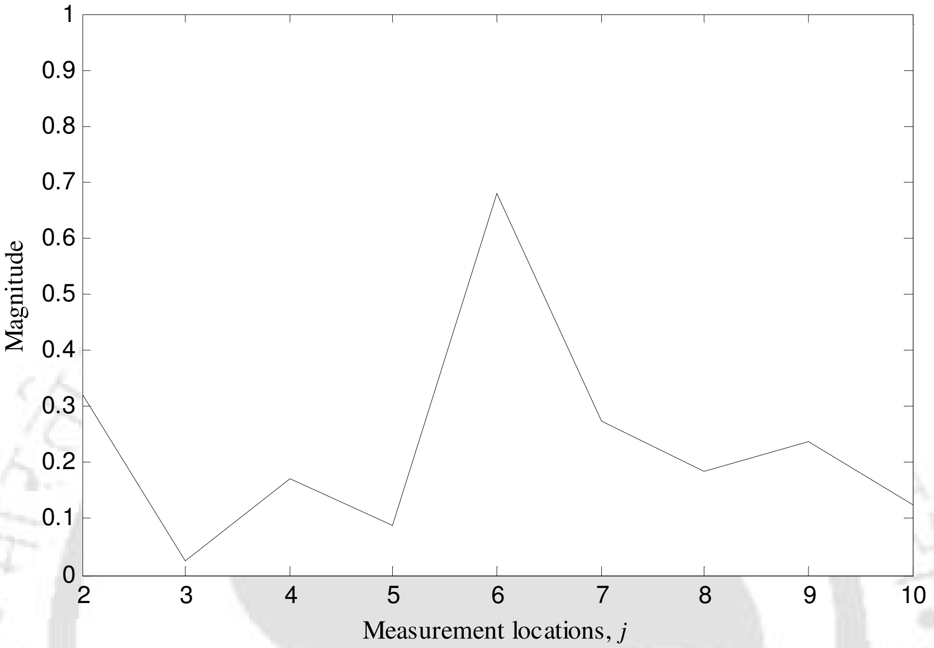

Figure 6.37: Crack probability functions for the Shaft-I with a single crack near 6th measurement location (second set of measurements).

For the second shaft, the crack is now near the measurement location 7. The crack probability function for this case is given in Figure 6.38. There is a big peak at the crack location (7th measurement location) and one small peak at 9th measurement location.

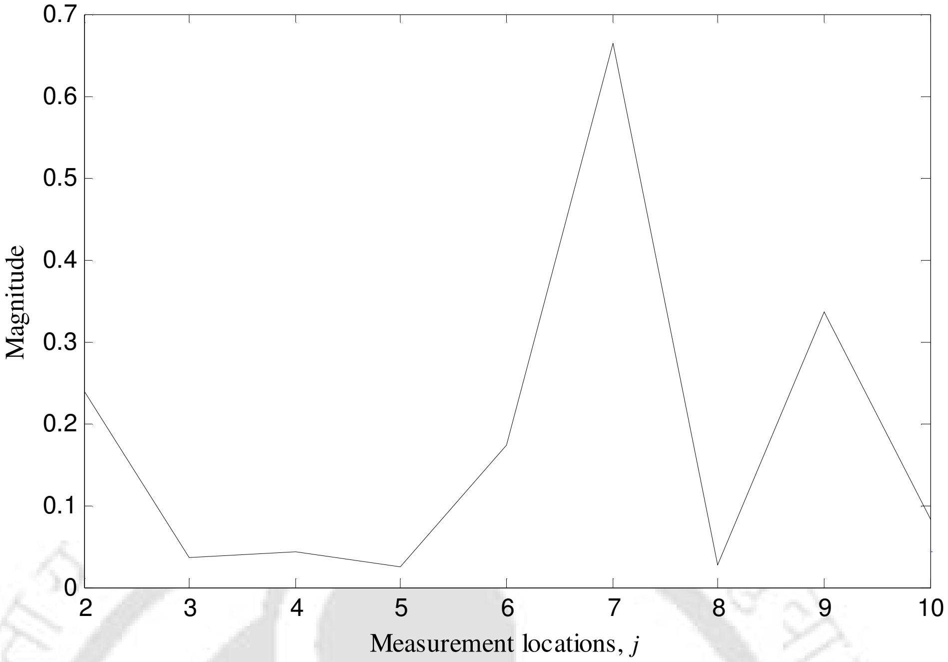

Figure 6.38: Crack probability functions for the Shaft-II with a single crack near 7th measurement location of the shaft (first set of measurements).

*CPF*s obtained from the second set of measurement for the same condition (Shaft-II with single crack at 7th measurement location) are given in Figure 6.39. Now there is a single peak in the *CPF* plots at the 7th measurement location. Hence, the algorithm is identifying the presence of crack in the shaft properly. Again, comparing the *CPF* plots from the two set of measurements (Figure 6.38 and Figure 6.39), it can be concluded that there is a crack in the shaft near 7th measurement location.

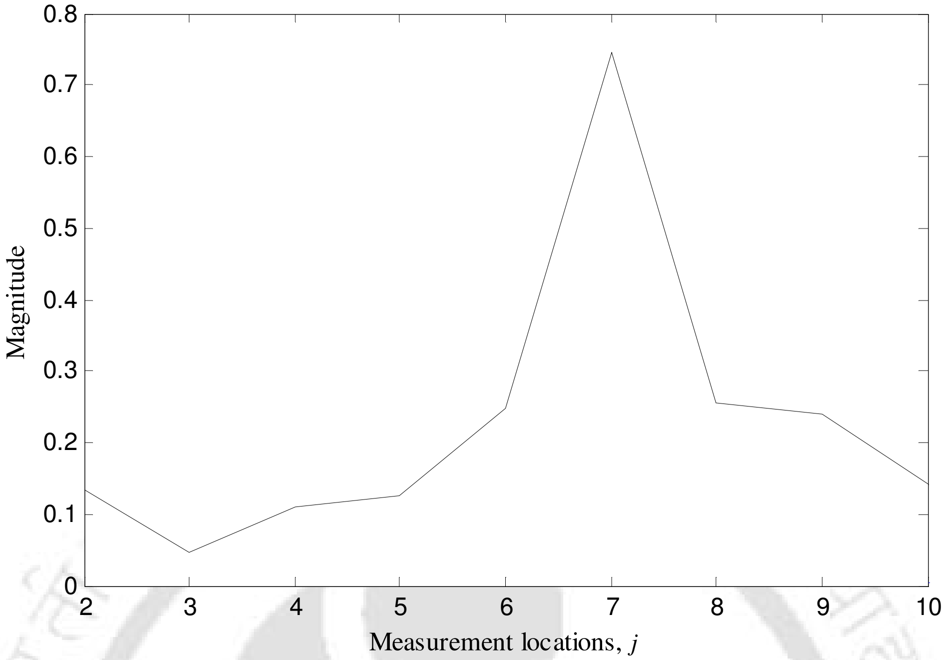

Figure 6.39: Crack probability functions for the Shaft-II with a single crack near 7th measurement location of the shaft (second set of measurements).

After observing the working of the MCDLA for the single cracked shaft, the algorithm is applied to Shaft-I with two cracks. With 11 measurement locations, now the two cracks are at 6th and 8th measurement locations. The crack probability functions obtained from the first and the second set of measurements are presented in Figure 6.40 and Figure 6.41, respectively. The crack near the middle of the shaft is identified in both the plots. There is no clear peak near the second crack location.

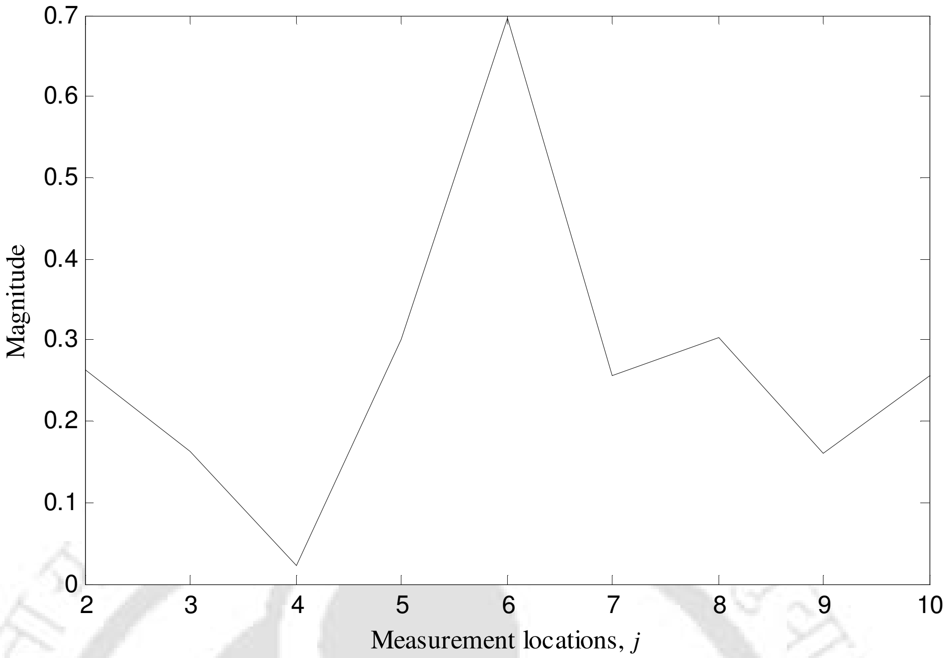

Figure 6.40: Crack probability functions for the Shaft-I with two cracks. First crack near 6th measurement location and the second crack near the 8th measurement location (first set of measurements).

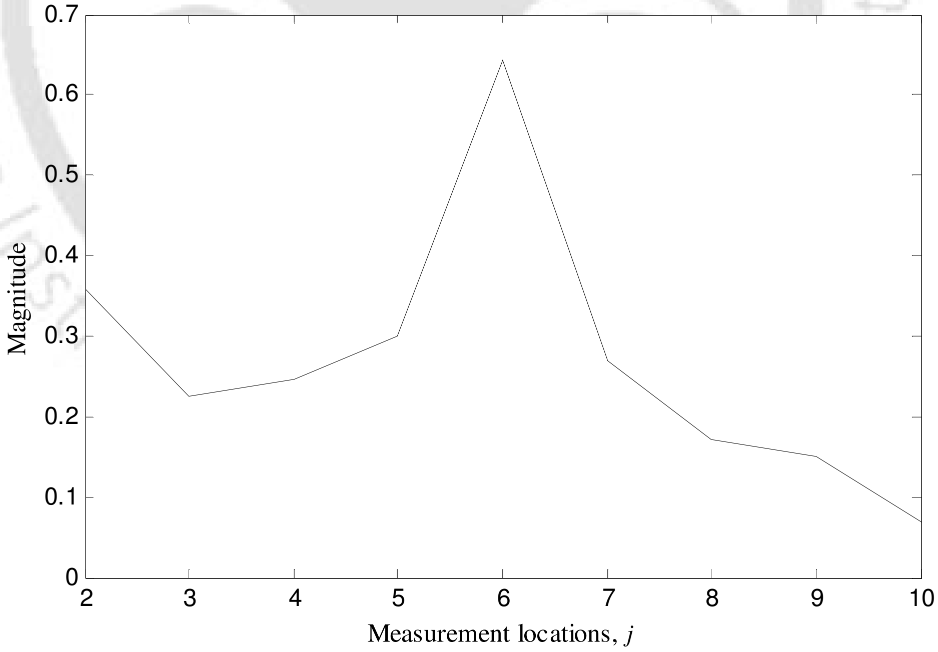

Figure 6.41: Crack probability functions for the Shaft-I with two cracks. First crack near 6th measurement location and the second crack near the 8th measurement location (second set of measurements).

Now the Shaft-II is used for the verification of algorithm. Now the first crack and the second crack are near to the 7th and 4th measurement locations, respectively. The crack probability functions obtained from the first and the second set of measurements are presented in Figure 6.42 and Figure 6.43, respectively. The two cracks in the Shaft-II are identified in both the measurement sets.

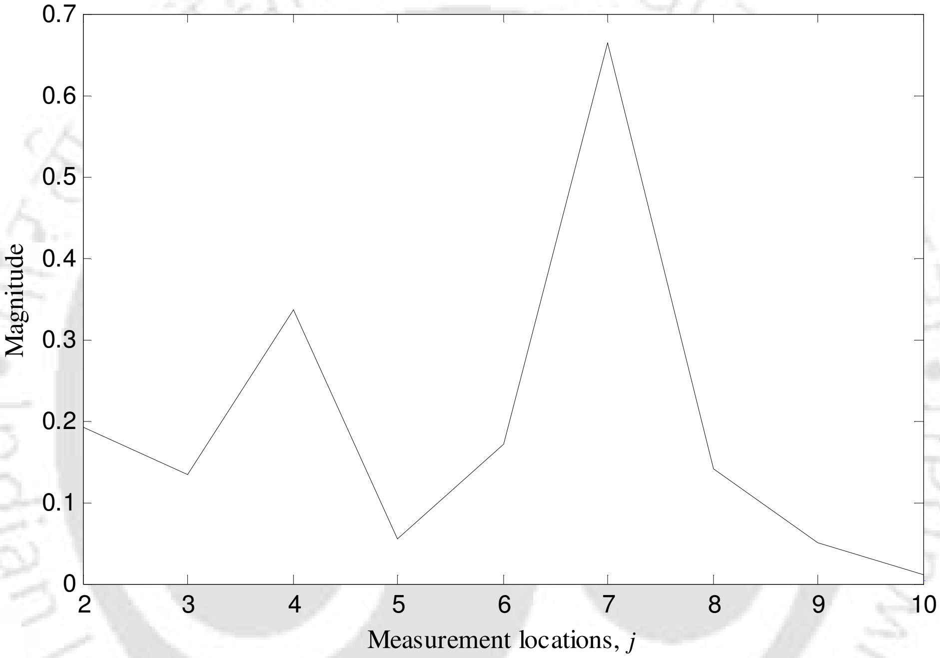

Figure 6.42: Crack probability functions for the Shaft-II with two cracks. First crack is near the 7th measurement location and the second crack is near the 4th measurement location (first set of measurements).

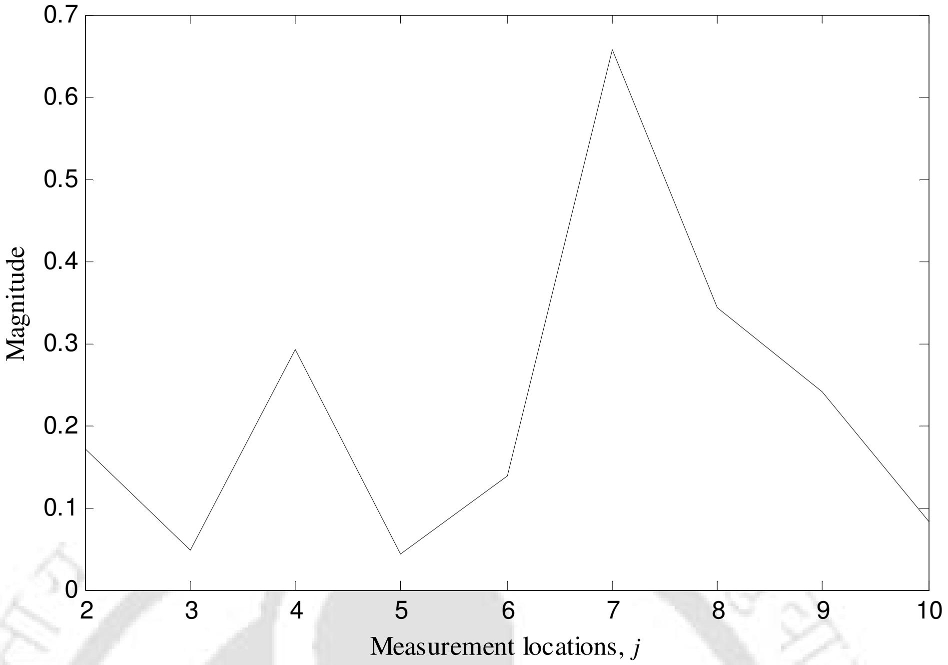

Figure 6.43: Crack probability functions for the Shaft-II with two cracks. First crack near 7th measurement location and the second crack near the 4th measurement location (second set of measurements).

The *CPF* plots, from Figure 6.23 to Figure 6.30 and *CPF* plots from Figure 6.36 to Figure 6.43 are obtained from the same measurements (i.e., the same forcing time history and the same response time history). Hence by comparing these two sets of *CPF* plots, it can be ascertained that the MCDLA is working better with the scheme. But definitely at the cost of reduced resolution with which the location of a crack is known along the shaft length. If the measurement noise is less, the algorithm can be used with more number of measurement locations and the location of a crack will be known with higher resolution.

From Figure 6.36 to Figure 6.43, it can be observed that the algorithm works well for all the cases except for Shaft-I with two cracks. The algorithm is not able to detect the presence of the second crack in Shaft-I, which is near the 8th measurement location. This may be attributed mainly to smaller size of the second crack in Shaft-I. Also, although the location of the second crack from the end support is same for both the shafts (i.e., Shaft-I and Shaft-II), distance between the two cracks is less in case of Shaft-I.

Overall the MCDLA was tested for two shafts, namely, Shaft-I and Shaft-II. First a single crack was made in each of the two shafts and the algorithm was tested for single-cracked shafts. Thereafter another crack was introduced in the shafts and the algorithm was tested for double-cracked shafts. These four cases are, (i) Shaft-I with single crack (ii) Shaft-II with single crack (iii) Shaft-I with two cracks, and (IV) Shaft-II with two cracks. Results from two measurement set are presented for each of the four cases. The algorithm is found to be working for all the cases except for the case (iii). For case (iii) the algorithm is able to detect only one crack out of the two cracks present in the shaft in both the measurement sets. This is attributed to small size of the crack and its proximity to the end support. Hence, out of 8 results presented, the algorithm is working perfectly in six results and partially in remaining two results. This way the experimental verification of the algorithm has shown good repeatability.

The MCDLA is robust against measurement noise. As explained in Sections 6.5.1, if the measurement noise is more, distance between measurement locations should be more. Effect of increasing 'the distance between measurements locations' over 'the working of the MCDLA' is explained by numerical simulation in Section 6.6 and by experimentation in Section 6.7.

Some more characteristics of the algorithm need to be tested experimentally, such as: (1) performance of the algorithm for cracks near the end supports, (2) Minimum size of a crack that the algorithm can detect, and (3) performance of the algorithm for rotated cracks. Since the working of the algorithm is affected by the measurement noise, measurement techniques should be improved to reduce this noise. One feasible way for better measurement accuracy would be to incorporate some mechanism for precision positioning of the sensors over the shaft.

In the present chapter, the MCDLA has been verified experimentally. The algorithm is tested for the single- as well as double-cracked shafts. A scheme is proposed to reduce the effect of measurement noise by increasing the distance between consecutive measurement locations. The algorithm is able to detect the presence of cracks in the shaft.

7 CONCLUSIONS AND SCOPES FOR FUTURE WORK

7.1 Conclusions

A new multi-crack identification methodology has been developed for a shaft system. The methodology is based upon forced responses of the cracked shaft at several frequencies. It gives the number of cracks, its size and location, and crack orientation angle of cracks in a shaft.

Initially the MCDLA is developed, in which displacements at three consecutive axial locations are fitted in quadratic polynomial to get coefficients of a quadratic polynomial. Quadratic coefficients from the cracked shaft responses are normalized by those obtained from the intact shaft responses. The algorithm uses several excitation frequencies to increase the signal–to–noise ratio in the signal. Working of the MCDLA is illustrated with numerically simulated cracked shaft response. The algorithm defines the *crack probability functions*, an indicator of presence of cracks in a shaft. Peaks in plots of *crack probability functions* versus measurement locations appear at crack locations.

Then, the MCLSA has been developed which gives the size and accurate locations of the cracks. It involves a multi-objective optimization problem that is solved by NSGA-II. Objective functions of the optimization problem is based upon the difference of FEM predicted cracked shaft responses and the measured cracked shaft responses. Number of cracks and their approximate locations, obtained from the MCDLA, defines the decision variable space for the optimization problem. Numerical simulation examples are presented to demonstrate the working of the algorithm. A modification to the normalization procedure is proposed by defining the *equivalent reduced stiffness*. It improves the normalization procedure in the MCDLA.

Subsequently, the restriction on the alignment of crack front with the forcing direction is relaxed and the crack front is assumed to be displaced at some angular position from the forcing direction. For these rotated cracks, the crack flexibility function is calculated by the open crack model as well as for the breathing crack model. Methods have been developed to find out the crack orientation angles of open cracks as well as breathing cracks. It shows that the crack orientation angle of a particular crack could be determined independently of crack parameters of other cracks, which are present in the shaft. The MCDLA and the MCLSA have been tested for rotated cracks with numerically simulated shaft forced responses.

Steps in a shaft also cause slope discontinuity in the elastic line of the shaft. Effectiveness of the MCDLA is demonstrated for the stepped shaft also. Cracks were considered both near the step and far from the step. The algorithm identifies the presence of cracks in both the cases.

Lastly, experimentations have been done with real cracked shafts to verify the MCDLA. Two shafts were taken for experimentations. Initially, shaft deflections were measured with the eddy current displacement sensor. However, due to measurement errors the detection was not effective. Then to improve quality of the measurements a laser vibrometer was used for measuring the shaft deflections. With these measurements the detection capabilities of the algorithm were improved, however, still some improvement in the detection was expected. To improve experimental predictions further, a scheme is proposed for the better estimation of the double derivative of shaft deflections. The scheme consists of increasing the distance between two measurement locations to reduce the effect of measurement noise while estimating the double derivative. Experimental results were improved further after the scheme was implemented. Major conclusions from the present work are summarized below.

Major Conclusions and Recommendations from the Present Work:

- The presence of crack in a shaft causes a slope discontinuity in the shaft elastic line. The resulting slope discontinuity is localized and it is difficult to find the slope discontinuity because of the measurement noise.
- The MCDLA is developed for the initial detection and localization of the cracks present in a shaft. It is based upon detecting the slope discontinuity in the elastic line of the shaft. It defines *crack probability functions* as an indicator of presence of cracks in a shaft.
- The MCLSA is developed for the estimation of accurate location and size of cracks present in a shaft. It consists of a multi-objective optimization problem which is solved by NSGA-II.
- Methods are proposed for the estimation of crack orientation angle of rotated cracks. Both open crack model as well as breathing crack model is considered for the mathematical modeling of the rotate cracks.
- Numerical simulation examples are presented to show the working of the algorithms developed in the present work.
- For the experimental verification of the MCDLA, first the eddy current displacement sensor is used for the measurement of shaft deflections. But this does not give good results because of measurement noise.
- Next, to reduce the measurement noise, laser vibrometer is used for measuring the shaft deflections which improves the performance of the algorithm.

7.2 Limitations and Applicability

All the algorithms in the present work are based upon measuring the forced vibration of the shaft at regular axial locations of the shaft. However, for a real shaft all the measurement locations may not be accessible because of the mountings over the shaft, such as bearings, sprockets, gears, blades, and pulleys. The shaft curvature, in the present work, is obtained from as the quadratic coefficients (unlike central difference schemes, Pandey et al., 1991) which gives flexibility in choosing the measurement locations. Hence, the real challenge would be to improve the method with limited measurements with the help of reduction and expansion schemes. The algorithms developed in the present work can be applied to other areas such as condition monitoring of bridges, aircraft wings, etc.

7.3 Scopes for the Future Work

- In real machines, a shaft is subjected to mountings and complex loading. Testing of the algorithm in these more realistic situations would give a better evaluation of its performance.
- Some more characteristics of the algorithm could to be tested, such as:
  (1) Performance of the algorithm for cracks near the end supports,
  (2) Minimum size of a crack that the algorithm can detect,
- Presence of cracks in a rotating shaft is also expected to cause slope discontinuity in the shaft elastic line. An extension of the present work would be to apply the algorithms to rotating shafts.
- Performance of the algorithm is sensitive to the measurement noise. It would be appropriate to improve the measurement techniques so as to reduce the noise in measurements.

- Validation of the MCLSA could be performed experimentally.
- More analytical study would be needed to understand (i) the stepwise variation of the coefficients a_h^{II} and (ii) the dependence of the angle 23° with the crack depth and shaft diameter.
- Along with cracks other rotor faults like unbalance, misalignment, bent shaft, etc. could be detected and diagnosed.

APPENDIX

Appendix A: Flexibility Coefficients of an Open Crack

The Dimensionless terms of the flexibility matrix $[\bar{C}]$ (Figure 2.2) are given by Papadopoulos and Dimarogonas (1987),

$$\bar{C}_{22} = \frac{\pi E R^3 C_{22}}{(1-\nu^2)} = 4\int_0^{\bar{a}}\int_0^{\bar{b}} \bar{y} F_{III}^2(\bar{h})\,d\bar{z}\,d\bar{y}\,; \qquad \bar{C}_{33} = \frac{\pi E R^3 C_{33}}{(1-\nu^2)} = 4\int_0^{\bar{a}}\int_0^{\bar{b}} \bar{y} F_{II}^2(\bar{h})\,d\bar{z}\,d\bar{y}\,;$$

$$\bar{C}_{44} = \frac{\pi E R^3 C_{44}}{(1-\nu^2)} = 32\int_0^{\bar{a}}\int_0^{\bar{b}} \bar{z}^2 \bar{y} F_1^2(\bar{h})\,d\bar{z}\,d\bar{y}\,;$$

$$\bar{C}_{45} = \bar{C}_{54} = \frac{\pi E R^2 C_{45}}{(1-\nu^2)} = 64\int_0^{\bar{a}}\int_0^{\bar{b}} \bar{z}\,\bar{y}\,\sqrt{1-\bar{z}^2}\,F_1(\bar{h})F_2(\bar{h})\,d\bar{z}\,d\bar{y}\,;$$

$$\bar{C}_{55} = \frac{\pi E R^3 C_{55}}{(1-\nu^2)} = 64\int_0^{\bar{a}}\int_0^{\bar{b}} \bar{y}(1-\bar{z}^2) F_2^2(\bar{h})\,d\bar{z}\,d\bar{y}\,; \tag{A.1}$$

where,

$$\bar{z} = z/R, \qquad \bar{a} = d/R, \qquad \bar{y} = y/R, \qquad \bar{b} = b/R, \qquad \bar{h} = h/R. \tag{A.2}$$

$$F_1\left(\frac{\alpha}{h}\right) = \sqrt{\frac{\tan\lambda}{\lambda}}\left[0.752 + 2.02\left(\frac{\alpha}{h}\right) + 0.37(1-\sin\lambda)^3\right]\Big/\cos\lambda$$

$$F_2\left(\frac{\alpha}{h}\right)=\sqrt{\frac{\tan\lambda}{\lambda}}\left[0.923+0.199(1-\sin\lambda)^4\right]\Big/\cos\lambda.$$

$$F_{II}\left(\frac{\alpha}{h}\right)=\left[1.122-0.561\left(\frac{\alpha}{h}\right)+0.085\left(\frac{\alpha}{h}\right)^2+0.18\left(\frac{\alpha}{h}\right)^3\right]\Big/\sqrt{1-\left(\frac{\alpha}{h}\right)}.$$

$$F_{III}\left(\frac{\alpha}{h}\right)=\sqrt{\frac{\tan\lambda}{\lambda}}.$$

and

$\lambda=\dfrac{\pi\alpha}{2h}$ as given in Tada et al. (2000) (A.3)

where R is the radius of the beam of circular cross section, h is the height of assumed elemental strip, a is the crack depth, $2b$ is the width of the elemental strip and α is the local crack depth which varies along the cross section (refer Figure 2.2).

Appendix B: Rayleigh damping

The relation between damping ratio, ζ, and natural frequency, ω_n, is expressed as Clough and Penzien (1993)

$$\zeta_n=\frac{a_0}{2\omega_n}+\frac{a_1\omega_n}{2} \tag{B.1}$$

where a_0 and a_1 are Rayleigh damping factors and this can be evaluated by the solution of a pair of simultaneous equations, if the damping ratios ζ_m and ζ_n associated with two specific known frequencies ω_m and ω_n. Writing equation (B.1) for each of these two cases and expressing them in the matrix form leads to

$$\begin{Bmatrix} \zeta_m \\ \zeta_n \end{Bmatrix} = \frac{1}{2} \begin{bmatrix} 1/\omega_m & \omega_m \\ 1/\omega_n & \omega_n \end{bmatrix} \begin{Bmatrix} a_0 \\ a_1 \end{Bmatrix} \tag{B.2}$$

from Equation (B.2), a_0 and a_1 can be obtained as,

$$\begin{Bmatrix} a_0 \\ a_1 \end{Bmatrix} = 2\frac{\omega_m \omega_n}{\omega_n^2 - \omega_m^2} \begin{bmatrix} \omega_n & -\omega_m \\ -1/\omega_n & 1/\omega_m \end{bmatrix} \begin{Bmatrix} \zeta_m \\ \zeta_n \end{Bmatrix} \tag{B.3}$$

where ω_m and ω_n are the system fundamental and highest natural frequencies of interest.

Appendix C: Elemental Mass and Stiffness Matrices for Transverse Vibrations

C.1: Elemental Mass Matrices

The element mass matrix $[M]^{(e)}$ consists of the translational mass matrix $[M_T]^{(e)}$ and the rotational mass matrix $[M_R]^{(e)}$, which is given as

$$[M]^{(e)} = [M_T]^{(e)} + [M_R]^{(e)} \tag{C.1}$$

with

$$[M_T]^{(e)} = [M_T]_0 + \Phi [M_T]_1 + \Phi^2 [M_T]_2$$

and

$$[M_R]^{(e)} = [M_R]_0 + \Phi [M_R]_1 + \Phi^2 [M_R]_2$$

The element translational mass matrix $[M_T]^{(e)}$

$$[M_T]_0 = \frac{\rho A l}{420(1+\Phi)^2}\begin{bmatrix} 156 & & SYM. & \\ 22l & 4l^2 & & \\ 54 & 13l & 156 & \\ -13l & -3l^2 & -22l & 4l^2 \end{bmatrix};$$

$$[M_T]_1 = \frac{\rho A l}{420(1+\Phi)^2}\begin{bmatrix} 294 & & SYM. & \\ 38.5l & 7l^2 & & \\ 126 & 31.5l & 294 & \\ -31.5l & -7l^2 & -38.5l & 7l^2 \end{bmatrix}$$

$$[M_T]_2 = \frac{\rho A l}{420(1+\Phi)^2}\begin{bmatrix} 140 & & SYM. & \\ 17.5l & 3.5l^2 & & \\ 70 & 17.5l & 140 & \\ -17.5l & -3.5l^2 & -17.5l & 3.5l^2 \end{bmatrix} \tag{C.2}$$

The element rotational mass matrix $[M_R]^{(e)}$

$$[M_R]_0 = \frac{\rho I_d}{(1+\Phi)^2}\begin{bmatrix} 6/5l & & SYM. & \\ 1/10 & 2l/15 & & \\ -6/5l & -1/10 & 6/5l & \\ 1/10 & -l/30 & -1/10 & l/15 \end{bmatrix};$$

$$[M_R]_1 = \frac{\rho I_d}{(1+\Phi)^2}\begin{bmatrix} 0 & & SYM. & \\ -1/2 & l/6 & & \\ 0 & 1/2 & 0 & \\ -1/2 & -l/6 & 1/2 & l/6 \end{bmatrix};$$

$$[M_R]_2 = \frac{\rho I_d}{(1+\Phi)^2}\begin{bmatrix} 0 & & SYM. & \\ 0 & l/3 & & \\ 0 & 0 & 0 & \\ 0 & l/6 & 1/2 & l/6 \end{bmatrix} \tag{C.3}$$

C.2: The element stiffness matrix $[K_{wf}]^{(e)}$

The element stiffness matrix $[K_{wf}]^{(e)}$ can be expressed as

$$[K_{wf}]^{(e)} = [K_{wf}]_0 + \Phi[K_{wf}]_1 \tag{C.4}$$

where

$$[K_{wf}]_0 = \frac{EI}{(1+\Phi)l^3}\begin{bmatrix} 12 & & SYM. & \\ 6l & 4l^2 & & \\ -12 & -6l & 12 & \\ 6l & 2l^2 & -6l & 4l^2 \end{bmatrix};$$

$$[K_{wf}]_1 = \frac{EI}{(1+\Phi)l^3}\begin{bmatrix} 0 & & SYM. & \\ 0 & l^2 & & \\ 0 & 0 & 0 & \\ 0 & -l^2 & 0 & l^2 \end{bmatrix}$$

$$\Phi = \frac{12EI}{k_{sc}GAl^2} \qquad \text{and} \qquad k_{sc} = \frac{6(1+\nu)}{7+6\nu}$$

where *EI* is the flexural rigidity of the beam, *l* is the element length, *A* is the cross sectional area of the beam, *G* is the modulus of rigidity of the beam material, ρ is the mass density of the beam material, k_{sc} is the shear correction factor for the circular cross section and ν is the Poisson's ratio .

C.3 Elemental Displacement Vector for Transverse Vibrations

The element displacement vector $\{q\}^{(e)}$

The element displacement vector for transverse vibrations can be written as

$$\{q\}^{(e)} = \{v_1 \quad \theta_1 \quad v_2 \quad \theta_2\}^T \tag{C.5}$$

Appendix D: Addition of noise to simulated cracked shaft deflection

Let $\{q\}$ and $\{r\}$ be the shaft deflection vector and the measurement noise vector, respectively. Vector $\{q\}$ is obtained from the finite element modeling of the cracked shaft (Eqn. (2.12)) and the vector $\{r\}$ is obtained from the random noise generator, function *randn.m*, in MATLAB. Element q_j of vector $\{q\}$ is the shaft deflection at measurement location *j*. The size of both the vectors is same. Noise in the simulated cracked shaft response $\{q\}$ is added according to the following expression

$$\{q'\} = \{q\} + \frac{\text{Noise percentage}}{100} \times \frac{1}{2 \times \max(\text{abs}\{r\})} \times \{q\} \times \{r\}^T \tag{D.1}$$

where the vector $\{q'\}$ is the shaft deflection with measurement noise.

REFERENCES

Abraham, O. N. L., and Brandon, J. A., The modelling of the opening and closure of a crack, *Journal of Vibration and Acoustics* 1995; 117, 370-377.

Adams, R. D., Cawley, P., Pye, C. J. and Stone, B. J., A Vibration Technique for Non-Destructively Assessing the Integrity of Structures, *Journal of Mechanical Engineering Science* 1978; 20, 93-100.

Al-Shudeifat., M. A., and Butcher, E. A., New breathing functions for the transverse breathing crack of the cracked rotor system: Approach for critical and subcritical harmonic analysis, *Journal of Sound and Vibration* 2011; 330, 526-544.

Babu, T. R., Srikanth, S., and Sekhar, A. S., Hilbert–Huang transform for detection and monitoring of crack in a transient rotor, *Mechanical Systems and Signal Processing* 2008; 22 (4), 905-914.

Bachschmid, N., Pennacchi, P., and Vania, A., Identification of multiple faults in rotor systems, *Journal of Sound and Vibration* 2002; 254 (2), 327-366.

Bachschmid, N., Pennacchi, P., Tanzi. E., and Audebert S., Transverse crack modelling and validation in rotor systems including thermal effects, *International journal of rotating machinery* 2004; 10 (4), 253-263.

Bachschmid, N., Pennacchi, P., and Tanzi, E., *Cracked Rotors: A Survey on Static and Dynamic Behaviour Including Modelling and Diagnosis*, Springer-Verlag Berlin Heidelberg, 2010.

Carneiro, S. H. S., and Inman, D. J., Continuous Model for the Transverse Vibration of Cracked Timoshenko Beams, *Transactions of the ASME Journal of Vibration and Acoustics* 2002; 124, 310-320.

Chang, C. C., and Chen, L. W., Vibration damage detection of a Timoshenko beam by spatial wavelet based approach, *Applied Acoustics* 2003; 64 1217-1240

Changhe, L., Bernasconi, O., and Xenophontidis, N., A generalised approach to the dynamics of cracked shafts, *Journal of Vibration, Acoustics, Stress and Reliability in Design* 1989; 111, 257-263.

Chondros, T. G., Dimarogonas, A. D., and Yao, J., A consistent cracked bar vibration theory, *Journal of Sound and Vibration* 1997; 200 (3), 303-313.

Chondros, T. G., Dimarogonas, A. D., and Yao, J., A continuous cracked beam vibration theory, *Journal of Sound and Vibration* 1998; 215 (1), 17-34.

Christides, S., and Barr, A. D. S., One-dimensional Theory of Bernoulli-Euler beams, *International Journal of Mechanical Science* 1984; 26 (11-12) 639-648.

Christides, S., and Barr, A. D. S., Torsional vibration of cracked beams of non-circular cross-section, *International Journal of Mechanical Science* 1986; 28, 473-490.

Changhe, L., Bernasconi, O., and Xenophontidis, N., A generalised approach to the dynamics of cracked shafts, *Journal of Vibration, Acoustics, Stress and Reliability in Design* 1989; 111, 257-263.

Chasalevris, A. C., and Papadopoulos, C. A., Identification of multiple cracks in beams under bending, *Mechanical Systems and Signal Processing* 2006; 20, 1631-1673.

Chasalevris, A. C., and Papadopoulos, C. A., Coupled horizontal and vertical bending vibrations of a stationary shaft with two cracks, *Journal of Sound and Vibration* 2008; 309, 507-528.

Chasalevris, A.C., and Papadopoulos C. A., A continuous model approach for cross-coupled bending vibrations of a rotor-bearing system with a transverse breathing crack, *Mechanism and Machine Theory* 2009; 44, 1176-1191.

Clough, R. W., and Penzien, H., *Dynamics of structures*, McGraw-Hill, Inc New York, 1993.

Darpe, A. K., Gupta, K., and Chawla, A., Dynamics of a two-crack rotor, *Journal of Sound and Vibration* 2003; 259 (3), 649-675.

Darpe, A. K., Gupta, K., and Chawla, A., Coupled bending, longitudinal and torsional vibrations of a cracked rotor, *Journal of Sound and Vibration* 2004; 269 (1-2), 33-60.

Darpe, A. K., Coupled vibrations of a rotor with slant crack, *Journal of Sound and Vibration* 2007; 305 (1-2), 172-193.

Darpe, A. K., A novel way to detect transverse surface crack in a rotating shaft, *Journal of Sound and Vibration* 2007; 305 (1-2), 151–171.

Deb, K., and Agrawal, R. B., Simulated binary crossover for continuous search space, *Complex Systems* 1995; 9, 115–148.

Deb, K., and Goyal, M. A., A combined genetic adaptive search (GeneAS) for engineering design, *Computer Science and Informatics* 1996; 26 (4) 30-45.

Deb, K., Pratap, A., Agarwal, S., and Meyarivan, T., A fast elitist multiobjective genetic algorithm: NSGA-II, *IEEE Transactions on Evolutionary Computation* 2002*;* 6 (2), 182-197.

Dharmaraju, N., Tiwari, R., and Talukdar, S., Identification of an open crack model in a beam based on force–response measurements, *Computers and Structures* 2004; 82, 167-179.

Dharmaraju, N., Tiwari, R., and Talukdar, S., Development of a novel hybrid reduction scheme for identification of an open crack model in a beam, *Mechanical Systems and Signal Processing* 2005; 19 (3), 633-657.

Di, W., and Law, S. S., Eigen-parameter decomposition of element matrices for structural damage detection, *Engineering Structures* 2007; 29 (4), 519-528.

Dilena, M., and Morassi, A., The use of anti-resonances for crack detection in beams, *Journal of Sound and Vibration* 2004; 276 (1-2), 195-214.

Dimentberg, F. M., *Flexural Vibrations of Rotating Shafts*, Butterworths, London, England 1961.

Dimarogonas, A. D., and Massouros, G., Torsional vibration of a shaft with a circumferential crack, *Engineering Fracture Mechanics* 1981; 15 (3-4), 439-444.

Dimarogonas, A. D., and Paipetis, S. A., *Analytical Methods in Rotor Dynamics*, Elsevier Applied science, London 1983.

Dimarogonas, A. D., and Papadopoulos, C. A., Vibration of cracked shafts in bending, *Journal of Sound and Vibration* 1983; 91 (4), 583-593.

Dimarogonas, A. D., Vibration of cracked structures: A state of the art review, *Engineering Fracture Mechanics* 1996; 55 (5), 831-857.

Doebling, S. W., Farrar, C. R., Prime, M. B., and Shevitz D. W., A review of damage identification methods that examine changes in dynamic properties, *Shock and Vibration Digest* 1998; 30 (2) 91-105.

Feldman, M., Hilbert transform in vibration analysis, *Mechanical Systems and Signal Processing* 2011; 25 (3), 735-802.

Friswell, M. I., Penny, J. E. T., and Garvey, S. D., A combined genetic and eigen sensitivity algorithm for the location of damage in structures, *Computers and Structures* 1998; 69, 547-556.

Friswell, M. I., and Penny, J. E. T., Crack modelling for structural health monitoring, *Structural Health Monitoring* 2002; 1 139-148.

Gasch, R., Dynamic behavior of a simple rotor with a cross-sectional crack, *Proc of I.Mech.E. Conference on Vibrations in Rotating Machinery* 1976; 123-128.

Gasch, R., A Survey of the dynamic behavior of simple rotating shaft with a transverse crack, *Journal of Sound and Vibration* 1993; 160 (2), 313-332.

Gounaris, G., and Dimarogonas, A. D., A finite element of a cracked prismatic beam in structural analysis, *Computers and Structures* 1988; 28 (3), 309-313.

Grabowski, B., The vibrational behaviour of a rotating shaft containing a transverse crack, in: O. Mahrenholtz (Ed.), Dynamics of Rotors—Stability and System Identification, *CISM Courses and Lectures*, Vol. 273, Springer, New York, 1984.

Gudmundson, P., The dynamic behaviour of slender structures with cross-sectional cracks, *Journal of the Mechanics and Physics of Solids* 1983; 31 (4), 329-345.

Guo, H. Y., and Li, Z. L., A two-stage method to identify structural damage sites and extents by using evidence theory and micro-search genetic algorithm, *Mechanical Systems and Signal Processing* 2009; 23 (3), 769-782.

Han, J. G., Ren, W. X., and Sun, Z. S., Wavelet packet based damage identification of beam structures, *International Journal of Solids and Structures* 2005; 42, 6610-6627.

Han, Q., and Chu F., Local flexibility of an elliptical cracked shaft under bending and tension, *Mechanical Systems and Signal Processing* 2011; 25 (8) 3198-3203.

Hadjileontiadis, L. J., Douka, E., and Trochidis, A., Fractal dimension analysis for crack identification in beam structures, *Mechanical Systems and Signal Processing* 2005; 19 (3), 659-674.

Heng, A., Zhang, S., Tan, A. C. C., and Mathew, J., Rotating machinery prognostics: State of the art, challenges and opportunities, *Mechanical Systems and Signal Processing* 2009; 23 (3) 724-739

Holland, J. H., *Adaptation in Natural and Artificial Systems*, University of Michigan press, Ann Arbor 1975.

Hong, J. C., Kim Y. Y., Lee H. C., Lee Y. W., Damage detection using the Lipschitz exponent estimated by the wavelet transform: applications to vibration modes of a beam, *International Journal of solids and structures* 2002; 39 (7) 1803-1816.

Horn, J., Nafpliotis, N., and Goldberg, D. E., A niched pareto genetic algorithm for multi-objective optimization, *Proceedings of the first IEEE conference on evolutionary computation, IEEE world congress on computational intelligence,* Piscataway, NJ, 1994; 82-87.

Imam, I., Azzaro, S. H., Bankert, R. J., and Scheibel, J., Developement of an on-line rotor crack detection and monitoring system, *ASME Journal of Vibration, Acoustics, Stress & Reliability in Design* 1989; 111, 241-250.

Irretier, H., Mathematical foundations of experimental modal analysis in rotor, *Mechanical Systems and Signal Processing* 1999; 13 (2) 183-191.

Irwin, W. J., Analysis of stress and strains near the end of a crack traversing a plate, *Journal of Applied Mechanics*1957; 24, 361-364.

Jaishia, B., and Ren, W. X., Damage detection by finite element model updating using modal flexibility residual, *Journal of Sound and Vibration* 2006; 290 (1-2), 369-387.

JianPing, J., and Guang, M., A novel method for multi-fault diagnosis of rotor system, *Mechanism and Machine Theory* 2009; 44 (4) 697-709.

Jun, O. S., Dynamic behavior analysis of cracked rotor based on harmonic motion, *Mechanical Systems and Signal Processing* 2012; 30, 186-203.

Karthikeyan**,** M.**,** Tiwari, R., and Talukdar, S., Crack localization and sizing in a beam based on the free and forced response measurements, *Mechanical Systems and Signal Processing* 2007; 21 (3), 1362-1385.

Karthikeyan, M., Tiwari, R., and Talukdar, S., Development of a novel algorithm for a crack detection, localization, and sizing in a beam based on forced response measurements, *Transactions of ASME, Journal of Vibration and Acoustics* 2008; 130 (2) 021002-(1-14).

Karthikeyan, M., R. and Tiwari, R., Detection, localization, and sizing of a structural flaw in a beam based on forced response measurements - An Experimental Investigation, *Mechanism and Machine Theory* 2010; 45 (4), 584-600.

Khiem, N. T., and Lien, T. V., A simplified method for natural frequency analysis of a multiple cracked beam, *Journal of Sound and Vibration* 2001; 245 (4), 737-751.

Khiem, N. T., and Lien, T. V., Multi-crack detection for beam by the natural frequencies, *Journal of Sound and Vibrations* 2004; 273 (1-2) 175-184.

Kim, D., and Lee. S., Structural damage identification of a cantilever beam using excitation force level control, *Mechanical Systems and Signal Processing* 2010; 24 (6) 1814–1830.

Kirmsher, P. G., The effect of discontinuities on the natural frequency of beams, *Proceedings of American Society of testing and Materials* 1944; 44, 897-904.

Law, S. S., and Lu, Z. R., Crack identification in beam from dynamic responses, *Journal of Sound and Vibration* 2005; 285 (4-5), 967-987.

Lee, C. W., Yun, J. S., and Jun, O. S., Modeling of a simple rotor with switching crack and its experimental verifications, *Transactions of ASME, Journal of Vibration and Acoustics* 1992; 114, 217-225.

Liebowitz, H., Vanderveldt, H., and Harris, D. W., Carrying capacity of notched columns, *International Journal of Solids & Structures* 1967; 3 (4), 489-500.

Liu, J. K., and Yang, Q. W., A new structural damage identification method, *Journal of Sound and Vibration* 2006; 297 (3-5), 694-703.

Loutridis, S, Douka, E., and Trochidis, A., Crack identification in double-cracked beams using wavelet, *Journal of Sound and Vibration* 2004; 277 (4-5) 1025-1039.

Mayes, I. W., and Davies, W. G. R., The vibrational behaviour of a rotating shaft system containing a transverse crack, Paper C168/76, *Proc. of I.Mech.E. Conference on Vibrations in Rotating Machinery* 1976, 53-64.

Mayes, I. W., and Davies, W. G. R., Analysis of the response of a multi-rotor-bearing system containing a transverse crack in a rotor, *ASME Journal of Vibration, Acoustics, Stress, and Reliability in Design* 1984; 106 (1), 139-145.

Maynard, K. P., Trethewey, M. W., and Groover, C., Application of torsional vibration measurement to shaft crack monitoring in power plants, *Proceedings of the 55th Meeting of the Society for Machinery Failure Prevention Technology,* Virginia Beach, VA, 2001; April 2–5.

Mazanoglu, K., and Sabuncu, M., A frequency based algorithm for identification of single and double cracked beams via a statistical approach used in experiment, *Mechanical Systems and Signal Processing* 2012; 30, 168-185.

Messina, A., Williams, E. J., and Contursi, T., Structural damage detection by a sensitivity and statistical-based method, *Journal of Sound and Vibration* 1998; 216 (5), 791-808.

Michalewicz, Z., *Genetic Algorithm + Data Structure = Evolution Programs*, Springer-Verlag Berlin Heidelbreg, New York, 1992.

Morassi, A., Crack-Induced changes in eigen parameters of beam structures, *Journal of Engineering Mechanics ASCE* 1993; 119 (9), 1798-1803.

Morassi, A., Damage detection and generalized Fourier coefficients, *Journal of Sound and Vibration* 2007; 302 (1-2), 229-259.

Nahvi, H., and Jabbari, M., Crack detection in beams using experimental modal data and finite element model, *International Journal of Mechanical Sciences* 2005; 47 (10), 1477-1497.

Nelson, H. D., and Nataraj, C., The dynamics of a rotor system with a cracked shaft, *Journal of Vibration, Acoustics, Stress and Reliability in Design* 1986; 108 (2), 189-196.

Nguyen, K. V., and Tran, H.T., Multi-cracks detection of a beam-like structure based on the on-vehicle vibration signal and wavelet analysis, *Journal of Sound and Vibration* 2010, 329, 4455-4465.

Okamura, H., A cracked column under compression, *Engineering Fracture Mechanics* 1969; 1 (3), 547-564.

Ono, I., and Kobayashi, S., A real-coded genetic algorithm for function optimization using unimodal normal distribution crossover, *Proceedings of the Seventh International Conference on Genetic Algorithms,* Morgan Kaufmann, San Mateo, CA 1997; 246-253.

Owolabi, G. M., Swamidas, A. S. and Seshadri**,** J. R., Crack detection in beams using changes in frequencies and amplitudes of frequency response functions, *Journal of Sound and Vibration* 2003; 265 (1), 1-22.

Pandey, A. K., Biswas, M., and Samman, M. M., Damage detection from changes in curvature mode shapes, *Journal of Sound and Vibration* 1991; 145 (2), 321-332.

Papadopoulos, C. A., and Dimarogonas A. D., Coupled longitudinal and bending vibrations of rotating shaft with an open crack, *Journal of Sound and Vibrations* 1987; 117, 81-93.

Papadopoulos, C. A., and Dimarogonas A. D., Stability of the cracked rotors in the coupled vibration mode, *ASME Journal of Vibration, Acoustics, Stress, and Reliability in Design* 1988; 110 (3), 356-359.

Papadopoulos, C. A., The strain energy release approach for modeling cracks in rotors: A state of the art review, *Mechanical system and signal processing* 2008; 22 (4), 763-789.

Patel, T. H., and Darpe, A. K., Influence of crack breathing model on nonlinear dynamics of a cracked rotor, *Journal of Sound and Vibration* 2008; 311 (3-5), 953-972.

Patil, D. P., and Maiti, S. K., Experimental verification of a method of detection of multiple cracks in beams based on frequency measurements, *Journal of Sound and Vibration* 2005; 281 (1-2), 439-451.

Perera, R., and Ruiz, A., A multistage FE updating procedure for damage identification in large-scale structures based on multi objective evolutionary optimization, *Mechanical Systems and Signal Processing* 2008; 22 (4), 970-991.

Pennacchi, P., Bachschmid, N., and Vania, A., A model-based identification method of transverse cracks in rotating shafts suitable for industrial machines, *Mechanical Systems and Signal Processing* 2006; 20 (8), 2112-2147.

Pennacchi, P., Vania, A., and Bachschmid, N., Increasing the robustness of fault identification in rotor dynamics by means of M-estimators, *Mechanical Systems and Signal Processing* 2007; 21 (8), 3003-3029.

Quek, S., Wang Q., Zhang, L., and Ang, K., Sensitivity analysis of crack detection in beams by wavelet techniques, *International Journal of Mechanical Sciences* 2001; 43 2899-2910.

Rajab, M. D., and Al-Sabeeh, Vibrational characteristics of cracked shafts, *Journal of Sound Vibration* 1991; 147 (3), 465–473.

Rao, J. S., *Design optimisation of active magnetic thrust bearing system using multi-objective genetic algorithms*, PhD thesis, Department of Mechanical Engineering, Indian Institute of technology Guwahati, India 2010.

Rucka, M., and Wilde, K., Application of continuous wavelet transform in vibration based damage detection method for beams and plates, *Journal of Sound and Vibration* 2006, 297, (3-5), 536-550.

Rucka, M., and Wilde, K., Crack identification using wavelets on experimental static deflection profiles, *Engineering Structures* 2006; 28 (2), 279-288.

Rytter, A., *Vibration based inspection of civil engineering structures*, Ph. D. Dissertation, Department of Building Technology and Structural Engineering 1993; Aalborg University, Denmark.

Sabnavis, G., Kirk, R.G., Kasarda, M., and Quinn, D., Cracked shaft detection and diagnostics: a literature review, *The Shock and Vibration Digest* 2004; 36 (4), 287-296.

Salawu, O. S., Detection of structural damage through changes in frequency: a review, *Engineering Structures* 1997; 19 (9), 718-723.

Saridakis, K. M., Chasalevris, A. C., Papadopoulos, C. A., and Dentsoras, A. J., Applying neural networks, genetic algorithms and fuzzy logic for the identification of cracks in shafts by using coupled response measurements, *Computers and Structures* 2008; 86 (11-12), 1318–1338.

Sawicki, J. T., Friswell, M. I., Kulesza, Z., Wroblewski, A., and Lekki, J. D., Detecting cracked rotors using auxiliary harmonic excitation, *Journal of Sound and Vibration* 2011; 330 (7), 1365-1381.

Schaffer, J. D., Multiple objective optimization with vector evaluated genetic algorithms, *Proceedings of the first international conference on genetic algorithms and their applications,* J. J. Grefenstette (Ed.) Pittsburg 1985; July 24-26, 93-100.

Sekhar, A. S., and Prasad, B. P., Dynamic analysis of a rotor system considering a slant crack in the shaft, *Journal of Sound and Vibration* 1997; 208 (3), 457-473.

Sekhar, A. S., Vibration characteristics of a cracked rotor with two open cracks, *Journal of Sound and Vibration* 1999; 223 (4), 497-512.

Sekhar, A. S., and Srinivas, B. N., Vibration characteristics of slotted shafts, *Journal of Sound and Vibration* 2002; 251 (4), 621-630.

Sekhar, A. S., Crack identification in a rotor system: a model-based approach, *Journal of Sound and Vibration* 2004; 270 (4-5), 887-902.

Sekhar, A. S., detection and monitoring of cracks in a coast-down rotor supported on fluid film bearings, *Tribology International* 2004; 37(3), 279–287.

Sekhar, A. S., Model-based identification of two cracks in a rotor system, *Mechanical Systems and Signal Processing* 2004; 18 (4), 977-983.

Sekhar, A. S., Mohanty, A. R., and Prabhakar, S., Vibrations of cracked rotor system: transverse crack versus slant crack, *Journal of Sound and Vibration* 2005; 279 (3-5), 1203-1217.

Sekhar, A. S., Multiple cracks effect and identification, *Mechanical System and Signal processing*, 2008; 22, 845-878.

Shen, M. H. H., and Pierre, C., Natural Modes of Bernoulli-Euler beams with symmetric crack, *Journal of Sound and Vibration* 1990; 138 (1), 115-134.

Shifrin, E. I., and Ruotolo, R., Natural frequencies of a beam with an arbitrary number of cracks, *Journal of sound and vibration* 1999; 222 (3), 409-423.

Sinha, J. K., Friswell, M. I., and Edwards, S., Simplified models for the location of cracks in beam structures using measured vibration data, *Journal of Sound and Vibration* 2002; 251 (1), 13-38.

Solbeck, J. A., and Ray, L. R., Damage identification using sensitivity-enhancing control and identified models, *Transactions of the ASME, Journal of Vibration and Acoustics* 2006; 128 (2), 210-220.

Springer, W. T., Lawrence, K. L., and Lawley, T. J., The effect of a symmetric discontinuity on adjacent material in a longitudinally vibrating uniform beam, *Experimental Mechanics* 1987; 27 (2), 168-171.

Srinivas, N., and Deb, K., Multiple objective optimization using nondominated sorting in genetic algorithms, *Evolutionary Computation* 1994; 2 (2), 221-248.

Sujatha, C., *Vibrations and Acoustics*, Tata McGraw-Hill 2009.

Sukumar, N., Moes, N., Morn, B., and Belytschko, T., Extended finite element method for three-dimensional crack modeling, *International Journal for Numerical methods in Engineering* 2000; 48 (11), 1549-1570.

Tada, H., Paris, P. C., and Irwin, G. R., *The Stress Analysis of Cracks Handbook. 3rd ed.*, New York: ASME 2000.

Thomson, W. J., Vibration of slender bars with discontinuities in stiffness, *Journal of applied mechanics* 1943; 17, 203-207.

Tiwari, R., and Dharmaraju, N., Development of a condensation scheme for transverse rotational degrees of freedom elimination in identification of beam crack parameters, *Mechanical Systems and Signal Processing* 2006; 20 (8), 2148-2170.

Tsutsui, S., Yamamura, M., and Higuchi, T., Multi-parent recombination with simplex crossover in real-coded genetic algorithms, *Proceedings of the Genetic and Evolutionary Computation Conference (GECCO-1)* 1999; 657-664.

Vyas, N. S., and Satishkumar, D., Artificial neural network design for fault identification in a rotor-bearing system, *Mechanism and Machine Theory* 2001; 36 (2), 157-175.

Wang, W. Q., Golnaraghi M.F., and Ismail F., Prognosis of machine health condition using neuro-fuzzy systems, *Mechanical Systems and Signal Processing* 2004; 18 (4), 813-831.

Wauer, J. Dynamics of cracked rotors: A literature review, *Applied Mechanics Reviews* 1990; 43 (1), 13-17.

Wauer, J., Modelling and formulation of equations of motion for cracked rotating shafts, *International Journal of Solids and Structure* 1990; 26 (8), 901-914.

Wu, M., and Huang, S., Vibration and crack detection of a rotor with speed-dependent bearings, *International Journal of Mechanical Sciences* 1998; 40 (6), 545-555.

Yang, B., Suh, C. S., and Chan, A. K., Characterization and detection of crack induced rotary instability, *Transactions of the ASME, Journal of Vibration and Acoustics* 2002; 124 (1), 40-48.

Yang, Q. W., A new damage identification method based on structural flexibility disassembly, *Journal of Vibration and Control* 2011; 17 (7), 1000-1008.

Zhong, S., and Oyadiji, S. O., Crack detection in simply supported beams without baseline modal parameters by stationary wavelet transform, *Mechanical Systems and Signal Processing* 2007; 21 (4), 1853-1884.

Publications from the Present Work

Journals:

1. S. K. Singh and R. Tiwari, Identification of Multiple Crack in a Shaft System using Transverse Frequency Response Functions, *Mechanism and Machine Theory* 2010; 45 1813-1827.
2. S. K. Singh and R. Tiwari, Detection and Localisation of Multiple Cracks in a Stepped Shaft, *Fatigue and Fracture of Engineering Materials and Structures* 2012; doi: 10.1111/j.1460-2695.2011.01653.x

Book chapter:

1. S. K. Singh, R. Tiwari and S. Talukdar, A Multi-Crack Identification Algorithm Based on Forced Vibrations from a Shaft System, *IUTAM Symposium on Emerging Trends in Rotor Dynamics IUTAM* Bookseries 2011; Volume 1011, 505-513, DOI: 10.1007/978-94-007-0020-8_42.

Conference:

1. S. K. Singh and R. Tiwari, A Novel Normalization Procedure of Quadratic Coefficients in a Multi-Crack Identification Algorithm for a Shaft System, *IFToMM International Conference on Rotor Dynamics*, Sept. 12-15, 2010, KIST, Seoul, South Korea.
2. S. K. Singh and R. Tiwari, Multi-crack Identification using Forced Responses from a Rotor System, *International Conference on Vibration Engineering and Technology of Machinery, VETOMAC-VI,* Dec. 13-15, 2010, IIT Delhi, New Delhi, India.